The Electrobat

Final Report

Group 20

Chris Nieuwboer	5063663	Easwaar Alagesen	4644441
Erik Schröter	5000467	Lennart Krieg	4862120
Max Snoodijk	4454367	Niels van Mierlo	4872029
Niels Prins	4840895	Sheharyar Ali	4798791
Thijs van Lith	4874536	Wessel Kruidenier	4834232

Delft University of Technology

TU Delft

This page is intentionally left blank.

The Electrobat

Final Report

by

Group 20

Chris Nieuwboer	5063663	Easwaar Alagesen	4644441
Erik Schröter	5000467	Lennart Krieg	4862120
Max Snoodijk	4454367	Niels van Mierlo	4872029
Niels Prins	4840895	Sheharyar Ali	4798791
Thijs van Lith	4874536	Wessel Kruidenier	4834232

Project duration: May 16, 2022 – June 21, 2022

Course coordinators:
Ir. R. N. H. W. Van Gent, TU Delft, tutor
Ir. L.T. Lima Pereira, TU Delft, coach
Ir. Z. Wang, TU Delft, coach

TU Delft Delft University of Technology

Executive overview

Project Overview

As climate change becomes more and more apparent, it is necessary to find sustainable methods for future aviation. The battery industry is rapidly developing, allowing for batteries with more power density which make more electric aviation possible. As the average aerobatic flight is only 30-40 minutes, it is the perfect category to test these new electric methods. By using this information, the following mission need and project statement can be formulated.

Mission need statement *To demonstrate the applicability of electric propulsion in aerobatic flights with an originally designed electric-powered aerobatic aircraft.* From this mission need statement, the following project objective can be formulated.

Project objective statement *To design an aerobatic electric aircraft capable of having a 40 minutes endurance including reserves and able to withstand +8 / -6 G, by 10 students in 10 weeks.*

In order to get a better understanding of the overall performance of an aerobatic aircraft, a flight profile is constructed, which can be seen in Figure 1. The flight profile makes a distinction between the different flight phases, estimates the duration of a particular phase and approximates the power setting of the motor to propel the aircraft expressed in percentages. This flight profile will be used later as a foundation for the battery design.

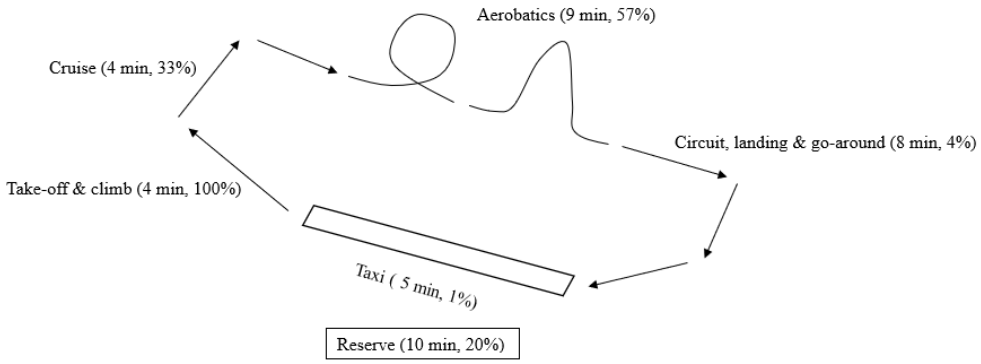

Figure 1: *Flight profile of the Electrobat*

It is envisioned that the aircraft will be aimed at both beginners, casual and competitive aerobatic pilots. After having performed a market analysis, it has been found that there are currently four electrically powered aerobatic aircraft on the market. The following aircraft already exist:

1. The Extra 330LE developed by Extra Aircraft with Siemens, MT-Propeller and Pipistrel
2. The Hamilton aEro electric plane powered by Siemens
3. The Magnus eFusion by Siemens and Magnus Aircraft
4. The integral E by Aura-Aero powered by Safran

These existing aircraft all follow a conventional design of aerobatic aircraft. Therefore, a gap in the market was found since there are no extreme aerobatic aircraft of that take advantage of new electric propulsion systems, to explore innovative solutions such as ducted fan design, with low noise and high thrust characteristics.

With this design in mind, several requirements were set up that will drive the design of the aircraft. These requirements should be met at the end of the design in order to make the aircraft feasible for the market. The following driving requirements were set up.

- EFLY-STK-APER-06: The aircraft shall have limit loads $+8$ and $-6\,\mathrm{G}$.
- EFLY-STK-COST-01: The aircraft shall have a maximum production cost of $595.000\,€$.
- EFLY-STK-USE-01: The aircraft shall seat 2 persons.
- EFLY-STK-GPER-03: The aircraft shall have a flight endurance of $40\,\mathrm{minutes}$ including reserves.
- EFLY-STK-USE-03: The aircraft shall have a turn-around time of $3\,\mathrm{hours}$.
- EFLY-STK-GPER-04: The aircraft shall be able to operate from a grass or tarmac runway of $500\,\mathrm{m}$.

Preliminary Design

The initial weight of the aircraft was determined through a class I weight estimation analysis, of which the results are given in Table 2. This analysis consisted of several comparable aircraft found in the market analysis and an average airframe weight computed as $345\,\mathrm{kg}$. Then, using an iterated flight profile resulting in $40\,\mathrm{min}$ of total flight time, an initial battery weight could be estimated at $287\,\mathrm{kg}$ using an energy density of $236\,\mathrm{Wh/kg}$. Furthermore, the $33\,\mathrm{kg}$ electric motor from Saluqi was included as well as a $20\,\%$ margin on the total aircraft. The breakdown of the power and energy usage is outlined in Table 1 This gave an OEM of $790\,\mathrm{kg}$ and MTOM of $888\,\mathrm{kg}$ and $978\,\mathrm{kg}$ for single and dual pilot operations respectively.

Table 1
Power settings per flight phase

Phase	Time [min]	Power [%]	Energy [Wh]	% of Total
Taxi	5	1	215	0.4
Take-off & Climb	4	100	17194	29.9
Cruise (To and From)	4	33	5674	9.9
Aerobatics	9	57	21786	37.8
Circuit, Landing & Go-around	8	4	1376	2.4
Reserve	10	20	8597	14.9
Total	40	-	54842	95.2
5% Margin	42	-	57584	100

Table 2
Initial mass estimations

Part	Mass [kg]	% of Total
Structure	345	35.3
Batteries	287	29.3
Motor	33	3.4
OEM reference	665	68.0
20% margin	133	13.6
OEM	798	81.6
Pilot	90	9.2
MTOM (pilot only)	888	90.8
Passenger	90	9.2
MTOM (both)	978	100

Table 3
CG location for the given take-off masses

	Mass [kg]	CG [m]	% of LEMAC
OEW	786.0	3.86	24.0
1 occupant front	876.0	3.76	17.0
1 occupant rear	876.0	3.91	27.0
2 occupants	966.0	3.81	21.0

The class II weight estimation determines the mass of the main components of the aircraft using averages of multiple methods, using the Class I result as a basis. Additionally, the initial wing position and CG location are determined using the expected moment arms and masses of the main components. The wing is positioned $3.50\,\mathrm{m}$ from the nose and CG locations are presented in Table 3.

The preliminary sizing of the wing is done using a constraint analysis in which the constraining performance requirements are used to determine the wing area required. These constraints included those relevant for a stall, take-off, landing, climb rate, climb gradient and manoeuvring performance. Consequently, the most constraining requirements were those for a stall speed of $50\,\mathrm{kts}$ in landing configuration as well as the $2.5\,\mathrm{G}$ sustained turn performance. These resulted in an optimal design point with a wing loading corresponding to $778\,\mathrm{N/m^2}$. Using the class II weight estimate of MTOM gives a required wing area of $12.3\,\mathrm{m^2}$.

Aerodynamics

Following the initial sizing of the wing, the rest of the wing is sized resulting in Table 4. Using considerations from various sources the desired lift distribution increasing aerodynamic efficiency and thus reduced power consumption was achieved using a taper ratio of 0.45. Additionally, winglets were incorporated to further improve the aerodynamic performance of the wing by approximately $4\,\%$ allowing again a reduction in power consumption and thus the battery weight. The main wing measurements are visualised in Figure 2.

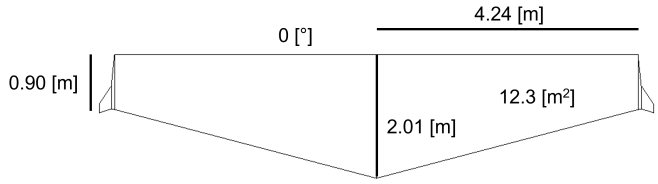

Figure 2: *Wing planform drawing*

Table 4
Wing planform design parameters

Parameter		Value
Wing area	[m^2]	12.3
Wing span	[m]	8.48
Aspect ratio	[-]	5.8
Taper ratio	[-]	0.45
Leading edge sweep	[°]	0
Mean aerodynamic chord	[m]	1.46

With the main wing designed, the high lift devices are sized to meet performance targets, namely, stall speed of $50\,\mathrm{kts}$. This resulted in a flapped wing surface of $11\,\mathrm{m}^2$ corresponding to $91\,\%$ of the wing surface area described in Table 5. These flapped surfaces were distributed into five separate surfaces, two on each wing and one on the fuselage. The flapped sections on the wing were divided into two separate surfaces, with the tips deflecting to a lesser $20°$, to improve the lift distribution during landing and reduce the tendency for tip stall.

Table 5
Flaperon sections.

Parameter		Section 1	Section 2	Section 3
Half-span position	[m]	0-0.34	0.51-3.39	3.39-4.03
Flap chord	[m]	0.48	0.47-0.28	0.28-0.24
Deflection	[°]	30	30	20

Landing Gear

The design of the landing gear was based on the methods detailed by Roskam [1]. Using the loads on the wheels, the diameter and width of the main landing gear wheel can be determined. The nose is chosen to be $70\,\%$ of the size of the main landing gear wheel. This resulted in the wheel size shown in Table 6.

The height of the landing gear is based on two reference aircraft. The longitudinal tip-over criteria were satisfied by making use of the CG range from the weight estimations. Based on this, the longitudinal ground clearance criteria were checked. This resulted in the values depicted in Figure 3. The parameters and corresponding values of the landing gear design are also given in Table 6.

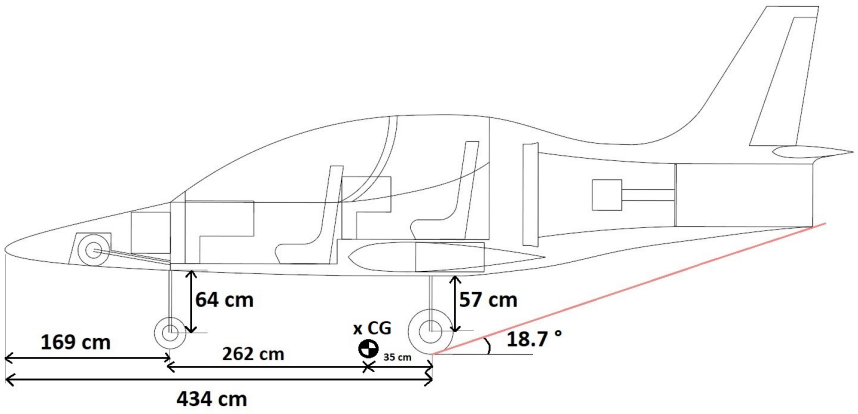

Figure 3: *Landing gear size and position*

Table 6
Tables showing the values of the main parameters of the undercarriage

(a) *Size specification of the landing gear*

Parameter		Value
Height of main struts	[mm]	571
Height of nose gear strut	[mm]	640
Distance CG to main wheel	[mm]	348
Distance CG to nose wheel	[mm]	2,620
Diameter nose wheel	[cm]	33
Width nose wheel	[cm]	12
Diameter main wheel	[cm]	45
Width main wheel	[cm]	20

(b) *Fuselage parameters with corresponding values*

Parameter		Value
X-Position of main gear	[m]	4.34
X-Position of nose gear	[m]	1.69
Distance between main landing gear	[m]	1.09
Scrape angle	[°]	18.7
Nose loading	[%]	11.7
Load per wheel on main landing gear	[kg]	426.3
Load on nose landing gear	[kg]	113.5

Fuselage

The design of the aircraft is shown in the three plan view given in Figure 4. This gives the side, front and top view. In Figure 5 a side view of the 3D model is shown.

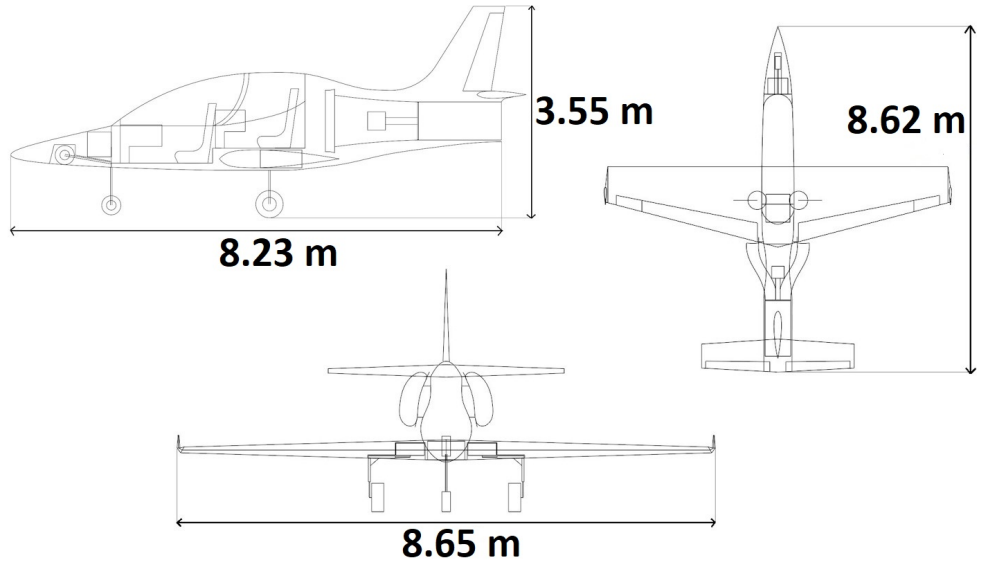

Figure 4: *Three plan view of the Electrobat*

Figure 5: *Side view in 3D of the Electrobat*

Inside the fuselage, the landing gear, batteries, fan and motor are efficiently positioned. For the placement of the batteries, the CG is taken into account resulting in $40\,\%$ of the batteries in the nose and $60\,\%$ in the wing. In addition, the empennage is placed in a manner such that it is safe for stalls. The horizontal tail is placed such that during a stall of the main wing, the aircraft maintains pitch control. The vertical tail is placed such that during a spin, the area that is blanked is not more than 1/3 of the entire vertical tail area.

The drag has been determined for the landing gear, canopy and fuselage, resulting in a value of 0.0017, 0.0039 and 0.0156, respectively.

Propulsion System

The extreme concept has an electrically driven ducted fan as a key feature for the propulsion. The fan was sized using a python program. This program computed every possible combination of fan diameter, expansion ratio and RPM to deliver the thrust required at all critical conditions in take-off, clean and landing configuration at $0\,\mathrm{ft}$ and $6{,}000\,\mathrm{ft}$. From all the possible combinations, a final design was chosen which would also work in the RPM range of the electric motor. The values for the thrust can be found in Table 7 and the final sizing of the ducted fan can be found in Table 8.

Table 7
Propulsion requirements based on the constraint analysis

Constraint		value
Power required	[kW]	260
Thrust clean (2.5G) 0 ft	[N]	2,001
Thrust clean (2.5G) 6000 ft	[N]	1,967
Thrust take-off 0 ft	[N]	1,344
Thrust take-off 6000 ft	[N]	1,321
Thrust landing 0 ft	[N]	1,593
Thrust landing 6000 ft	[N]	1,566

Table 8
Propulsion characteristics

Parameter		Value
Diameter	[m]	0.63
Area	[m^2]	0.31
ε_d	[-]	1.00
Max RPM	[2π/min]	7,600
Min RPM	[2π/min]	5,000
Max Power propeller	[kW]	216
Max power engine	[kW]	257
η_f	[-]	0.885
η_e	[-]	0.95

The efficiencies in Table 8 are from the propeller of the UL-39 and the motor that will power the aircraft. As can be seen in Table 7 the power required of the motor is $260\,\mathrm{kW}$. The engine that fits best in the design is the P200T6 from Saluqi motors. This motor weighs $33\,\mathrm{kg}$ and is $30\,\mathrm{cm}$ in diameter and has a length of $30\,\mathrm{cm}$ as well. Due to this powerful, light and compact motor, it is possible to power this aircraft.

Inlet and duct

The following flow properties of the ducting for the propulsion system of the Electrobat are calculated and shown in Table 9:

Table 9
Computed flow properties for the Electrobat's engine duct system

Station		0	1	2	3	4
Duct Area	[m^2]	0.466	0.420	0.302	0.302	0.296
Flow Velocity	[m/s]	77	85	119	125	127
Total Pressure	[kPa]	105	105	104	111	111
Static Pressure	[kPa]	101	100	96	101	100
Total Temperature	[K]	291	291	291	296	296
Static Temperature	[K]	288	287	284	288	288

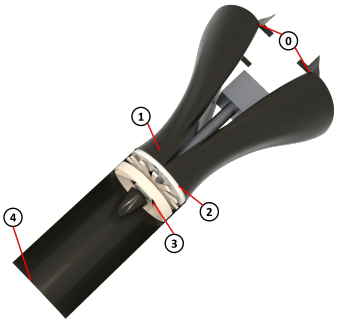

Figure 6: *Station numbering of duct model*

Iterations of the calculations were made by varying the supposed thrust that should be produced by the fan and in Figure 7 and Figure 8 the behaviour of the total thrust in comparison with the fan and exhaust

thrust is shown. The green dotted line shows the minimum required thrust of T = 2,001 N at the Electrobat's operations velocity, V_0 = 77.17 m/s.

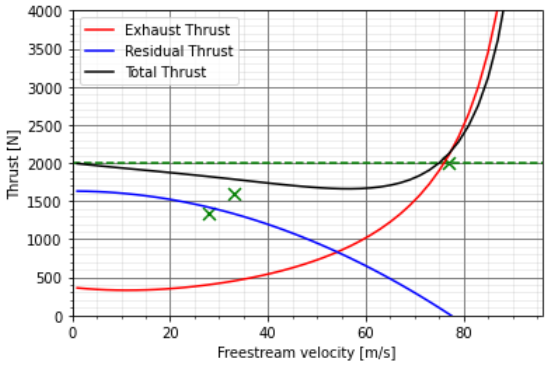

Figure 7: *Shows the variation in residual exhaust, and total thrust at sea level condition.*

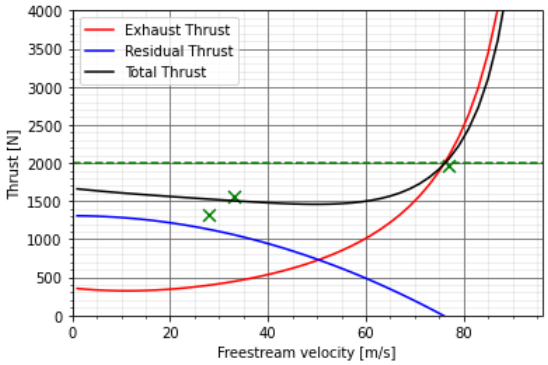

Figure 8: *Shows the variation in residual exhaust, and total thrust at an altitude of* 6,000 ft.

Iterations were done until the total thrust value was in the range of the required thrust as tabulated in Table 7. The finalised total thrust generated by the Electrobat is T = 2,137 N. Higher thrust values are possible, but this would require a more in-depth analysis of the fan itself to have a meaningful result.

Given that the geometry of the duct is sized via the varying cross-sectional areas, the dimensions of the inlet can also be computed to aid the fuselage design of the Electrobat. With some aerodynamic considerations, it was decided that the inlets should be embedded into the fuselage with a splitter plate to avoid low-speed air within the boundary layer that developed on the fuselage skin upstream of the inlet.

With the fan dimensions known, it is possible to give an estimation of the noise produced. This calculation is necessary in order to check if the requirement is met. As the aircraft is electrically propelled, the main noise source is the fan and the interaction between the stator and the fan. The calculated SPL was 90.62 dB at 1,000 ft. From literature, it was found that, if the aircraft is flying overhead, the reduction factor is 19.27 dB[2]. This will reduce the noise to 71.35 dB. After this reduction there is an A-level reduction of 14 dB, this is the reduction due to the perceived noise at the listener. After this reduction, the perceived noise will be 57.35 dB at 1,000 ft. Keep in mind that this calculation is only for a single fan in a duct. The aircraft has two stators, which will reduce the noise generated even more.

Power System

To power the propulsion system, high-performance batteries are used. The batteries provide direct current to every system in the aircraft except the motor. To power the motor, an inverter is required to change the direct current to alternating current. The battery pack in the aircraft will be on a 500 V system. This voltage is necessary to output the required power of the motor. The battery that will be used is the ELEO size 35 performance module. A total of ten battery packs is enough to satisfy the requirements.

As can be seen from the table, the total mass of the batteries will be 276 kg. The ELEO 35 performance module is expected to last 500 to 1,500 cycles. As there is no degradation data publicly available, a conservative estimate of 500 cycles is assumed.

For the energy recovery system, two energy recovery systems were considered. The first option was to install generators on the main landing gear. After quick calculations, it was found that in an optimal case only 0.2 % of the battery capacity will be recharged. This is not a feasible option as the added mass and complexity are not worth the benefit. The second option was to use the ducted fan as a turbine. Because all the hardware is already in place, it is potentially worth it to use the electric motor as a generator during flight. It was calculated that the energy recovered will be around 11 % of the battery capacity. Therefore, it is feasible to use the ducted fan as a turbine during flight as an energy recovery system.

Wing Structure

The wing structure of the Electrobat is designed for 1.5 times the critical loads exerted on the wing during a $8\,\mathrm{G}$ manoeuvre, performed at the manoeuvring speed of $150\,\mathrm{kts}$. To carry this load, a fully-composite three-spar, two-cell wing box was designed. The main spar of this design is located at $30\,\%$ chord at the location of maximum airfoil thickness and close to the aerodynamic centre. This spar carries the largest part of the vertical load. A rear spar is located at $75\,\%$ chord, coinciding with the hinge line of the flaperon. Lastly, with the front spar located at $10\,\%$ of the chord, the leading edge of the wing is not considered structural. The leading edge could be damaged by a bird strike or impact of debris, so as a non-structural component, it poses less risk and is easier to repair or replace. Ribs and z-stringers split up the spar webs and skin panels. Through iterations, the number and locations of these ribs and stringers as well as the thicknesses of each of the created panels were optimised. The final design parameters of the wing box are shown in Table 10. Following this, the wing weight is estimated at $136\,\mathrm{kg}$. This includes correction factors of the flaperon, leading-edge bodywork and landing gear reinforcements.

Table 10
Wing structure design parameters

Span section [m]	Front spar thickness [mm]	Main spar thickness [mm]	Rear spar thickness [mm]	Cell 1 skin top/bottom thickness [mm]	Cell 2 skin top/bottom thickness [mm]	Nr. of stringers top
0-0.3	2.08	2.72	2.56	1.92	2.24	19
0.3-0.65	2.08	2.72	2.56	1.76	2.24	19
0.65-1.1	2.08	2.72	2.40	1.76	1.92	19
1.1-1.65	2.08	2.56	2.24	1.6	1.92	19
1.65-2.7	1.92	2.56	1.92	1.28	1.6	19
2.7-4.24	1.44	1.92	1.44	1.28	1.6	11

Fuselage Structure

The fuselage structure was designed for the shear force and bending moments on the aircraft at $+12$ and $-9\,\mathrm{G}$, incorporating a safety factor of 1.5 compared to the maximum loads on the aircraft. Only the fuselage section above the wing, which is a constant cross-section and located between $3.696\,\mathrm{m}$ and $4.996\,\mathrm{m}$ from the nose, was analysed. The structure consists of composite z-stringers and skin. Frames have not been added to this structure yet, as skin buckling was not analysed. The analysed fuselage section was split into four parts. This was done because the loads on the fuselage reduce towards the tail, allowing for a thinner skin. Table 11 shows fuselage structure characteristics resulting from the analysis.

Table 11
Fuselage structural dimensions

		Section 1	Section 2	Section 3	Section 4
Range	[mm]	3,696 - 3,815	3,815 - 4,165	4,165 - 4,450	4,450 - 4,996
Skin thickness	[mm]	0.32	1.28	0.48	0.32
Stringer width	[mm]	10	15	10	10
Flange thickness	[mm]	0.80	1.60	0.96	0.80
Web thickness	[mm]	0.80	1.44	0.96	0.80
Stringer height	[mm]	10	20	10	10
Stringer area	[mm^2]	25.28	81.41	30.64	25.28
# stringers	[-]	12	12	12	12
Weight section	[kg]	0.27	3.04	0.93	1.24

Stability and Control

To determine the stability and control of the aircraft, a Python script was written. The program can determine the responses of the aircraft based on geometry and exported lift and drag curves from the XFLR program. During verification, a few minor errors were corrected and validation showed the drag prediction is underestimated. Other parameters in the program could be improved as well, but it was also apparent that the model used did not entirely correspond to the actual aircraft and other deviating parameters

Using the calculated eigenvalues of each mode, Table 12 was constructed. It can be seen that for a lightweight, highly manoeuvrable aircraft, the Electrobat fulfils the criteria for all modes, apart from the spiral. The spiral is marginally unstable, indicating it will be harder to control for a pilot, but also more manoeuvrable. During the flight, testing can be determined if additional damping is desired. The program also gave the control rates per flight phase, as shown in Table 13. It can be seen that with these rates, the aircraft will remain controllable during take-off and landing, and extremely manoeuvrable during aerobatics. The equations are used only to compare the control derivative to the aerodynamic damping effect, so these rates will likely be lower in reality.

Table 12
Eigenvalue parameters for the Electrobat

	λ_{re} [-]	λ_{im} [-]	ζ [-]	ζ_{req}[-]	ω [rad/s]	ω_{req} [rad/s]
Short-period	-0.86	2.52	0.32	0.20 - 2.00	2.38	0.37 - 5.96
Phugoid	-0.01	0.34	0.03	0.00 >	0.34	-
Aperiodic roll	-2.34	-	-	-	-	-
Spiral	0.07	-	-	-	-	-
Dutch Roll	-0.11	2.19	0.05	0.02 >	2.19	0.40 >

Table 13
Control rates for different configurations and corresponding velocities.

Configuration	Velocity [m/s]	Roll [deg/s]	Pitch [deg/s]	Yaw [deg/s]
Take-off / landing	33	115	102	97
Clean	77	571	484	427

Analysis of Final Design

As an aerobatic aircraft, the Electrobat has to be able to deliver sufficient performance for the following flight phases: take-off/landing, climb, glide, cruise, and aerobatics. For take-off, landing, and climb, the following climb rates and flight path angles were obtained for the corresponding flight speeds as shown in the table below.

Table 14
Climb rates (R/C) with corresponding velocities (V_∞) and flight path angles (γ) for different configurations at maximum thrust

(a) *Two occupants (mass = 966 kg)*

Configuration	R/C [m/s]	V_∞ [m/s]	γ [°]
Clean	16.0	77	12.0
Take-off	9.3	51	10.5
Landing	5.7	33	9.9

(b) *One occupant (mass = 876 kg)*

Configuration	R/C [m/s]	V_∞ [m/s]	γ [°]
Clean	17.8	77	13.3
Take-off	10.6	50	12.2
Landing	6.7	33	11.7

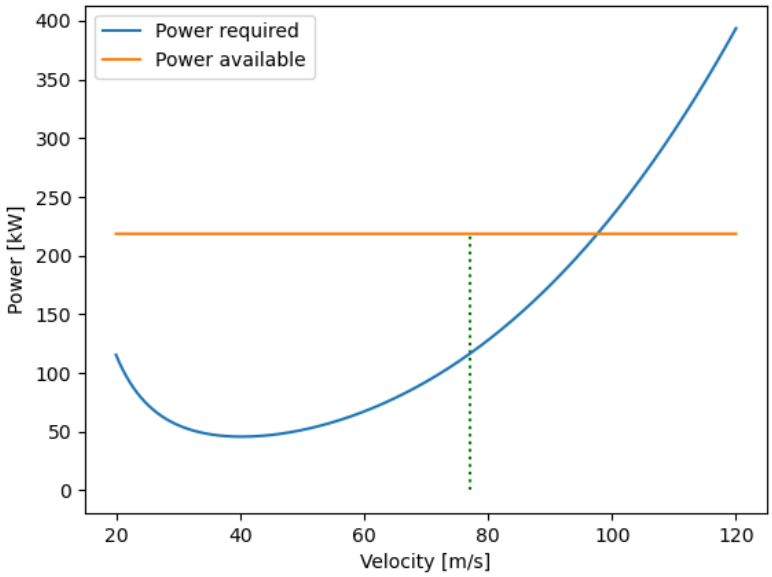

Figure 9: *Power curve of the Electrobat*

When cruising, the Electrobat has enough excess power to operate at higher operational velocity, after accounting for the complete range of velocities the Electrobat should be able to operate in. For aerobatics, on the other hand, it was deemed that if Electrobat can perform a complete loop without stalling with a yaw and roll input, it should be able to perform the other required manoeuvres as stated in the technical requirements. It was obtained that the Electrobat is able to sustain a $5\,\mathrm{Gs}$ full loop without stalling with cruising thrust setting.

Cost

The Electrobat is set to have varying costs of roughly €548.000 and fixed costs of roughly €243.000. This means that the Electrobat will have a total unit cost of €792.000. Accounting for a profit margin of 10%, based on the market price of the other aerobatic aircraft, the market price of the Electrobat is €871.000. On top of this, given that the life cycle of the Electrobat is around 10-15 years, the lifecycle cost of the Electrobat is €1.347.000. Below is a comparison of cost per hour between the Electrobat and an aerobatic aircraft powered by internal combustion (insurance cost is not accounted for at this stage).

Table 15
Direct Operating Cost Overview for 125 flight hours a year

	Electrobat [€/hour]	**Combustion [€/hour]**
Maintenance	13,60	21,60
Storage	33,60	33,60
Fuel	202,21	195,50
Inspection	4,75	4,75
Insurance	-	-
Total	253,91	255,45

Design Rationale

The sustainability of the design ensures the future viability of the design and its continued usage through environmental and socio-economic aspects throughout the aircraft's life cycle. For brevity, the report limits the discussion of sustainability to the two most critical design components, the carbon fibre airframe and lithium-ion batteries. Overall sustainability philosophy is to maximise efficiency and minimise waste. These values are embedded in LEAN principles of manufacturing and a circular economy aircraft life-cycle in which parts are reused. Moreover, carbon fibre components are either reused or recycled by either pyrolysis or mechanical methods into lower structural grade components. Similarly, for lithium-ion batteries, hydrometallurgy is used to recover battery materials for reuse.

An effort has been made to ensure the system will comply with most of the technical requirements stated at the start of this project. In terms of performance, propulsion and structures, the requirements are met. At this stage in the design, the non-requirements like the battery charging position and compliance with regulations can only be verified after the design is finalised. As this is still the preliminary design phase, these requirements are still marked 'TBD' in terms of compliance.

Project Outlook

When the Electrobat is coming to the market, a production plan has to be made. The production plan outlines how the aircraft will be built. The aircraft will be built using assembly. Assembly is the integration of several subassemblies. The different subassemblies are the nose, cockpit, tail, empennage, wing, exterior duct, interior duct and undercarriage. These subassemblies will be joined together by either the manufacturing division or the mounting division.

The development logic for the continuation of the design incorporates the steps to be done leading up to the certification and aircraft delivery to market. In brief, preliminary design steps have been completed thus far and further steps include continuation into its detailed design. Additionally, verification tests of subsystems must be conducted to ensure reality meets the estimated performance. Moreover, production steps and certification are to be developed before the delivery of the aircraft.

Contents

Nomenclature

Abbreviations

AC	Aerodynamic Centre
A	Analysis
AC	Alternating Current
ADSB	Automatic Dependent Surveillance-Broadcast
AE	Aerodynamic Efficiency
AIAA	American Institute of Aeronautics and Astronautics
AP	Aerobatic Performance
APER	Aerobatic Performance
AR	Aspect ratio
BPF	Blade Passing Frequency
C	Coefficient
CBS	Cost Breakdown Structure
CFD	Computational Fluid Dynamics
CG	Centre of Gravity
CO	Control
COST	Cost
CPIT	Cockpit
CS	Control System
CS-23	Certification Specifications 23
CTRL	Control
D	Demonstration
DC	Direct Current
DOC	Direct Operating Cost
DOC	Documentation
DSE	Design Synthesis Excercise
EFLY	E-Flyer
ELT	Emergency Locator Transmitter
ENV	Environment
EQP	Equipment
ERS	Energy Recovery System
FBD	Functional breakdown Diagram
FBW	Fly-by-wire
FFD	Functional flow diagram
FL	Flight
G	Gravitational
GC	Gantt Chart
GFRP	Glass Fibre Reinforced Polymer
GHG	Green House Gas
GM	Ground Manoeuvring
GPER	General Performance
GR	Ground
HLD	High-Lift Devices
I	Inspection
ICAO	International Civil Aviation Organization
IN	Instrument
IT	International Technology
KTAS	Knots True Air Speed
LCC	Lifecycle Cost
LE	Leading Edge
LLT	Lifting Line Theory
LO	Long Term
MAC	Mean Aerodynamic Chord
MLM	Maximum Landing Mass
MTOM	Maximum Take-Off Mass
MTOW	Maximum Take-Off Weight
N/A	Not Applicable
OEM	Operational Empty Mass
OEW	Operational Empty Weight
OPER	Operations
P	Probability
PE	Performance
PED	Primary Energy Demand
PERF	Performance
PROD	Productions
RAMS	Reliability, Availabilty, Maintainability and Safety
rCFRP	recycled Carbon-Fibre-Reinforced Polymer
RE	Requirement
REG	Regulatory
RI	Risk
RPM	Rounds Per Minute
S	Severity
SAFE	Safety
SC	System Complexity
SM	Safety Margin
SPL	Sound pressure level
STAB	Stability
STK	Stakeholder
STR	Structure
SU	Sustainability
SYS	System
T	Test
TBD	to be determined
TE	Technical
TL	Top-Level
TOP	Take-off Parameter
UDP	Uniform Daylight Period

USE	Usage
vCFRP	virgin Carbon-Fibre-Reinforced Polymer
vf	volume fraction
VLM	Vortex Lattice Method
WBS	Work Breakdown Structure
WFD	Work Flow Diagram

Greek Symbols

α	Angle of attack	rad
β	Sideslip angle	rad
δ	Derivative	$-$
δ_a	Ailerons deflection	rad
δ_e	Elevator deflection	rad
δ_r	Rudder deflection	rad
δ_T	Boundary layer thickness	m
ϵ	Downwash angle	rad
η	Imaginary part of eigenvalue	$-$
η_e	Engine energy efficiency	$-$
η_f	Fan energy efficiency	$-$
Γ	Dihedral angle	rad
γ	Flight path angle	rad
λ	Taper ratio	$-$
$\lambda_{c/2}$	Sweep half chord	rad
$\lambda_{c/4}$	Sweep quarter chord	rad
μ	Dimensionless mass	$-$
μ_∞	Free-stream dynamic viscosity	kg/ms
ν	Poisson ratio	
ϕ	Angle of twist	rad
ϕ	Roll angle	rad
ψ	Yaw angle	rad
ρ	Density	kg/m^3
ρ_∞	Free-stream density	kg/m^3
σ	Sidewash angle	rad
$\sigma_{cc}^{(i)}$	Crippling stress	N/mm^2
σ_x	Bendig stress around x-axis	N/mm^2
σ_y	Yield stress	N/mm^2
τ	Shear strength	MPa
θ	Pitch angle	rad
ε_d	Duct expansion ratio	$-$
ξ	Real part of eigenvalue	$-$
ζ	Damping ratio	$-$
A_i	Flange area	mm^2
V_h	Horizontal tail volume coefficient	mm^2
V_v	Vertical tail volume coefficient	mm^2

Latin Symbols

$\bar{c}_w$	wing chord length	m
$\bar{V}_h$	horizontal tail volume coefficient	$-$
$\bar{V}_v$	vertical tail volume coefficient	$-$
$\bar{x_{ac}}$	aerodynamic center of the aircraft less tail	m
$\bar{x_{cg}}$	center of gravity of the aircraft less tail	m
$\Delta C_{D_{canopy}}$	Total canopy drag coefficient	$-$
ΔC_{D_s}	Drag coefficient dependent on Mach number	$-$
$\dot{m}$	Mass flow	kg/s
$\frac{V_h}{V_\infty}$	Tail/wing speed ratio	$-$
$\overline{c}$	Mean aerodynamic chord	m
A_4	Exit area of duct	m^2
A_R	Propeller rotor area	m^2
A_{max}	Frontal area of canopy	m^2
$A_{stringer}$	Stringer area mm^2	
B	Number of blades	$-$
b	Skin panel lenght	mm
b_e	Elevator span	m
b_h	Horizontal tail span	m
B_p	Number of blades	$-$
b_r	Rudder span	m
b_v	Vertical tail span	m
b_w	wing span	m
b_1	Lower flange width	mm
b_2	Upper flange width	mm
B_i	Boom area	mm^2
c	Speed of sound at altitude	m/s
c_1	Inner diameter shaft	m
c_2	Outer diameter shaft	m
c_e	Elevator chord position	%
c_r	Rudder chord position	%
C_{d_0}	Zero-lift drag	$-$
$C_{D_{emp}}$	drag coefficient of the empennage	$-$
$C_{D_{fus}}$	Fuselage drag	$-$
$C_{D_{gear_{CL=0}}}$	Zero-lift landing gear drag coefficient	$-$
$C_{D_{gear}}$	Landing gear drag coefficient	$-$
C_{D_h}	drag coefficient of the horizontal tail	$-$
C_{D_v}	drag coefficient of the vertical tail	$-$
$C_{L_{\alpha_{A-h}}}$	aircraft less tail lift gradient	$1/rad$
$C_{L_{\alpha_h}}$	tail lift gradient	$1/rad$
$C_{L_{land}}$	Landing lift coefficient	$-$
$C_{L_{max}}$	Maximum lift coefficient	$-$
C_{l_p}	Roll rate derivative coefficient	$-$
$C_{L_{TO}}$	Take-off lift coefficient	$-$

C_l	Roll moment coefficient	$-$
C_m	Pitch moment coefficient	$-$
C_n	Yaw moment coefficient	$-$
c_r	Root chord	m
C_X	Directional force coefficient	$-$
C_Y	Sideforce coefficient	$-$
C_Z	Downforce coefficient	$-$
D	Wheel diameter	cm
d	Diameter	m
D_R	Diameter of the propeller	m
E	Youngs modulus	MPa
e	Oswald efficiency number	$-$
h	Height	m
h	Stringer height	mm
I	Moment of inertia	M^4
i	Incidence angle	$^\circ$
I_{XX}	Moment of inertia around X axis	mm^4
I_{XZ}	Product of inertia around X axis	mm^4
I_{YY}	Moment of inertia around Y axis	mm^4
I_{ZZ}	Moment of inertia around Z axis	mm^4
J	Polar moment of inertia	m^4
k_q	Torque coefficient	$-$
k_t	Thrust coefficient	$-$
l	Length	m
l_h	horizontal tail moment arm	m
l_v	Vertical tail moment arm	m
m	Mass	kg
M_t	Tip speed mach	$-$
M_x	Moment around x-axis	Nmm
M_y	Moment around y-axis	Nmm
n	Revolutions per second	rev/s
N_p	Number of propellers	$-$
n_p	Rotational speed of the propeller	rad/s
p	Factor accounting for reduced drag due to lift	$-$
p	Roll rate	rad/s
$p_{0,i}$	Total pressure at station i	Pa
P_{br}	Shaft brake horse power	
P_{ENG}	Power required of engine	W
p_i	Static pressure at station i	Pa
P_m	Load on individual main landing wheel	N
P_n	Load on nose landing gear	N
P_q	Torque power	W
P_{REQ}	Power required of propeller	W
Q	Torque	N
q	Pitch rate	rad/s
$q_{s,0}$	Resultant shear flow	N/mm
q_s	Shear flow	N/mm
r	Yaw rate	rad/s
r_p	Distance from observer	m
Re	Reynold's number	m
S	Wing surface area	m^2
S_e	Elevator area	m^2
S_h	Horizontal tail area	m^2
S_r	Rudder area	m^2
S_v	Vertical tail area	m^2
S_w	Wing area	m^2
S_{gear}	Landing gear surface area	m^2
S_y	Shear force in y-direction	N
S_z	Shear force in z-direction	N
T	Thrust	N
t	Thickness of hollow shaft	m
t_d	Skin thickness	mm
$T_{0,i}$	Total temperature at station i	K
t_1	Flange thickness	mm
t_2	Web thickness	mm
T_i	Static temperature at station i	K
V	Velocity	m/s
V_3	Velocity after rotor	m/s
V_4	Duct exit velocity	m/s
V_∞	Free stream velocity	m/s
w	Wheel width	cm
w	width	m
W/P	Power loading	N/W
W/S	Wing loading	N/m^2
W_{FG}	Weight of the fuselage group	kg
W_{WG}	Weight of the wing group	kg
x	Length from nose to splitter plate	m
$x_{CG,FG}$	CG position of the fuselage group	m
$x_{CG,OE}$	CG position of the OEW	m
x_{LEMAC}	Leading edge of the MAC position	%
y_r	Distance from neutral z-axis	mm
y_{MLG}	Distance between main landing gear wheels	m
z_r	Distance from neutral y-axis	mm

1

Introduction

For decades, general aviation aircraft have been using large combustion engines to obtain the required performance. In aerobatics, this is significantly worse, and most of these aircraft still use leaded petrol [1]. This outdated concept has never been sustainable, and it is about time changes are made, especially with the climate change becoming increasingly apparent. With this, the Electrobat has the potential to drastically revolutionise the design philosophies previously employed for aerobatic aircrafts. Instead of a heavy, polluting combustion engine, it will use electric propulsion, which is far more efficient and emission-free. The objective of this project is to work out this concept in sufficient detail to examine its feasibility.

The aim of this report is to present a multidisciplinary preliminary design of an electric aerobatic aircraft, the Electrobat, and to evaluate whether the stakeholder's needs can be realised with this concept. To accomplish this within the limited time span of ten weeks, the aircraft has been divided into subsystems according to each discipline and evaluated using physical and empirical models. The primary disciplines are aerodynamics, structures, stability and control, propulsion and power, and performance. To ensure each model is realistic, each of them has been verified and validated. Non-technical aspects are evaluated as well, like risk, cost, and sustainability.

The report is outlined as follows. Chapter 2 to Chapter 5 cover the preparation of the project, as a proper understanding of the target market and clear overview of the requirements is vital to a successful product. Chapter 6 to Chapter 11 cover the technical analysis of this report. Each discipline is worked out in detail and all the findings are presented in the respective chapter. Chapter 12 and Chapter 13 discuss the final stage of this project with the expected requirement compliance and project outlook after this report. A summary of the final design with the recommendation can be found in Chapter 14.

[1] URI: https://www.shell.com/business-customers/aviation/aviation-fuel/avgas.html [Accessed 20 June 2022]

2

Project Overview

This chapter will outline the project objectives of the Design Synthesis Exercise (DSE) and the stakeholder requirements. The project objective is discussed in Section 2.1 and will state the main goal of this DSE project. The stakeholder requirements are discussed in Section 2.2. These requirements must be met in order to satisfy the stakeholders of this project.

2.1. Project Objectives

With the ever-increasing demand for new sustainable ways to live, it is necessary to find non-polluting alternatives for current technologies. The battery industry is developing at a rapid rate, and this creates a gap in the market for developing new electric aircraft [1]. At the moment, battery capacity is still low for commercial long haul flights. It is, however, possible to design electric aircraft that do not have to fly multiple hours on end. Therefore, an aerobatic aircraft is the perfect aircraft to test and develop these new technologies, as the average duration of an aerobatic flight is only 30-$40\,\mathrm{minutes}$ and performance is prioritized over flight duration. With the design goal in mind, it is possible to construct a mission need statement and project objective statement.

Mission need statement
To demonstrate the applicability of electric propulsion in aerobatic flights with an originally designed electric powered aerobatic aircraft.

From the mission need statement, a project objective statement can be formulated and is as follows.

Project objective statement
To design an aerobatic electric aircraft capable of having a $40\,\mathrm{minutes}$ *endurance including reserves and able to withstand* $8/-6\,\mathrm{G}$*, by* 10 *students in* 10 *weeks.*

2.2. Stakeholder Requirements

Five stakeholders have been identified, each having different demands of the final product:

- Operators, mainly concerned with costs and reliability;
- Aerobatic pilots, demanding a manoeuvrable aircraft;
- Regulatory bodies, enforcing safety;
- Environment, reducing waste and emissions generated during the aircraft lifespan;
- People living close to the airport, demanding low noise emissions.

With these stakeholders in mind, along with the pre-defined mission requirements, the stakeholder requirements have been set up, as shown in Table 2.1. The majority of the requirements follow from performance, as the aircraft has to perform a variety of aerobatic manoeuvres at a high G-load. The environmental requirements are in place to satisfy the sustainability objective of this project. In these tables each requirements has an identifier and a verification method, in which A stands for analysis, T for testing, D for demonstration and I for inspection.

[1] URL: https://www.afar.com/magazine/electric-planes-are-coming-sooner-than-you-think [Accessed 20 June 2022]

Table 2.1
Stakeholder requirements

Identification	Requirement	Verif.
EFLY-STK-COST-01	The aircraft shall have a maximum unit cost of €595.000.	A
EFLY-STK-USE-01	The aircraft shall seat 2 persons.	A
EFLY-STK-USE-02	The aircraft shall have an operational life of at least 20 years.	A
EFLY-STK-USE-03	The aircraft shall have a turn-around time of 3 hours.	A
EFLY-STK-USE-04	The aircraft shall have a service interval greater than 500 flight hours.	A
EFLY-STK-GPER-01	The aircraft shall have an operational speed of 150 [kts].	T
EFLY-STK-GPER-02	The aircraft shall have a stall speed of 50 [kts] in the landing configuration.	D
EFLY-STK-GPER-03	The aircraft shall have a flight endurance of 40 minutes including reserves.	D
EFLY-STK-GPER-04	The aircraft shall be able to operate from a grass or tarmac runway of 500 [m].	D
EFLY-STK-APER-01	The aircraft shall be able to perform an aileron roll.	D
EFLY-STK-APER-02	The aircraft shall be able to perform a barrel roll.	D
EFLY-STK-APER-03	The aircraft shall be able to perform a snap roll.	D
EFLY-STK-APER-04	The aircraft shall be able to perform a spin.	D
EFLY-STK-APER-05	The aircraft shall be able to perform a loop.	D
EFLY-STK-APER-06	The aircraft shall have limit loads +8 / -6 G.	T
EFLY-STK-APER-07	The aircraft shall be able to perform a tail slide.	D
EFLY-STK-APER-08	The aircraft shall be able to perform a Cuban Eight.	D
EFLY-STK-APER-09	The aircraft shall be able to perform an Immelmann.	D
EFLY-STK-APER-10	The aircraft shall be able to perform inverted flight.	D
EFLY-STK-SAFE-04	The aircraft shall be longitudinally stable.	T
EFLY-STK-CPIT-01	The noise level within the cockpit shall be below 70 [dB].	T
EFLY-STK-CPIT-02	The pilot shall have a total field of view of 220 [deg].	I
EFLY-STK-REG-01	The aircraft shall comply with the CS-23 aerobatic regulations.	All
EFLY-STK-REG-02	The aircraft shall comply with ICAO annex 16 noise regulations.	T
EFLY-STK-ENV-01	The aircraft shall be electrically propelled.	I
EFLY-STK-ENV-02	The aircraft shall have less than 10% material waste at the end of life.	A
EFLY-STK-ENV-03	The aircraft shall be emission-free during operation.	D
EFLY-STK-ENV-04	The aircraft shall produce no more than 60 [dB] noise at 1000 [ft].	T

3

Market Analysis and Risk Analysis

At the beginning of the conceptual design phase, it is vital for the economic success of a design that it is competitive with similar products in the market space. Therefore, it is useful to conduct a market analysis in which the performance of existing and in-development aerobatic and electric aircraft are considered. Consequently, this allows the target cost and performance parameters to be outlined, which would give the aircraft design a competitive edge when coming to the market. First, the market forecast and target performance are explained in Section 3.1 and Section 3.2, respectively. Then, a technical risk analysis including a risk map is presented in Section 11.2.

3.1. Market Forecast

It is envisioned that the electric aerobatic aircraft be aimed at both beginner recreational and competitive aerobatic pilots alike. This would suit the aircraft for ownership by as well flight schools as private owners, and may even allow the development of an individual electric aerobatic class of aircraft.

There are currently four existing electric aerobatic aircraft, namely:

1. The Extra 330LE developed by Extra Aircraft and Siemens, MT-Propeller and Pipistrel [1]
2. The Hamilton aEro electric aircraft powered by Siemens [2]
3. The Magnus eFusion by Siemens and Magnus Aircraft [3]
4. The integral E by Aura-Aero powered by Safran [4]

To conduct a market analysis, a database of approximately 80 piston-driven aerobatic aircraft and these four electric aerobatic aircraft was generated. This database is depicted in Figure 3.1, with the aforementioned electric aerobatic aircraft highlighted in yellow. The result showed an expected reduced performance of the electric aircraft in comparison to the conventionally-driven aircraft. This is largely related to technological performance factors of electric motors and batteries. Moreover, the four electric aerobatic aircraft all demonstrate comparable performance parameters to the initial design requirements (i.e. $6/-4.5\,\mathrm{G}$, $150\,\mathrm{KTAS}$, 1-2 seats, and approximately $40\,\mathrm{min}$ of total endurance). This demonstrates a non-competitive target market for such a design but offers a market gap for a better performing and expanded-envelope class of electric aerobatic aircraft. Hence, the cost and performance parameters are adjusted to meet this market gap. These changes can be seen in Table 3.1.

Table 3.1
Modified top-level requirements

Identification	Initial Requirement	Revised Requirement
EFY-TL-REQ-PERF.12	The aircraft shall have limit loads +6/ -4.5 G.	The aircraft shall have limit loads +8/-6 G.
EFY-TL-REQ-COST.1	The aircraft shall have a maximum production price of € 300,000.	The aircraft shall have a maximum production price of € 595.000

[1] URL: https://www.aerospace-technology.com/projects/extra-330le-electric-aircraft/ [Accessed 10 June 2022]
[2] URL: https://www.lugaro.com/successful-launch-hamilton-aero-electric-aircraft-made-aerobatics/ [Accessed 10 June 2022]
[3] URL: https://www.magnusaircraft.com/ [Accessed 10 June 2022]
[4] URL: https://aura-aero.com/en/integral/integral-e/#testimonials [Accessed 10 June 2022]

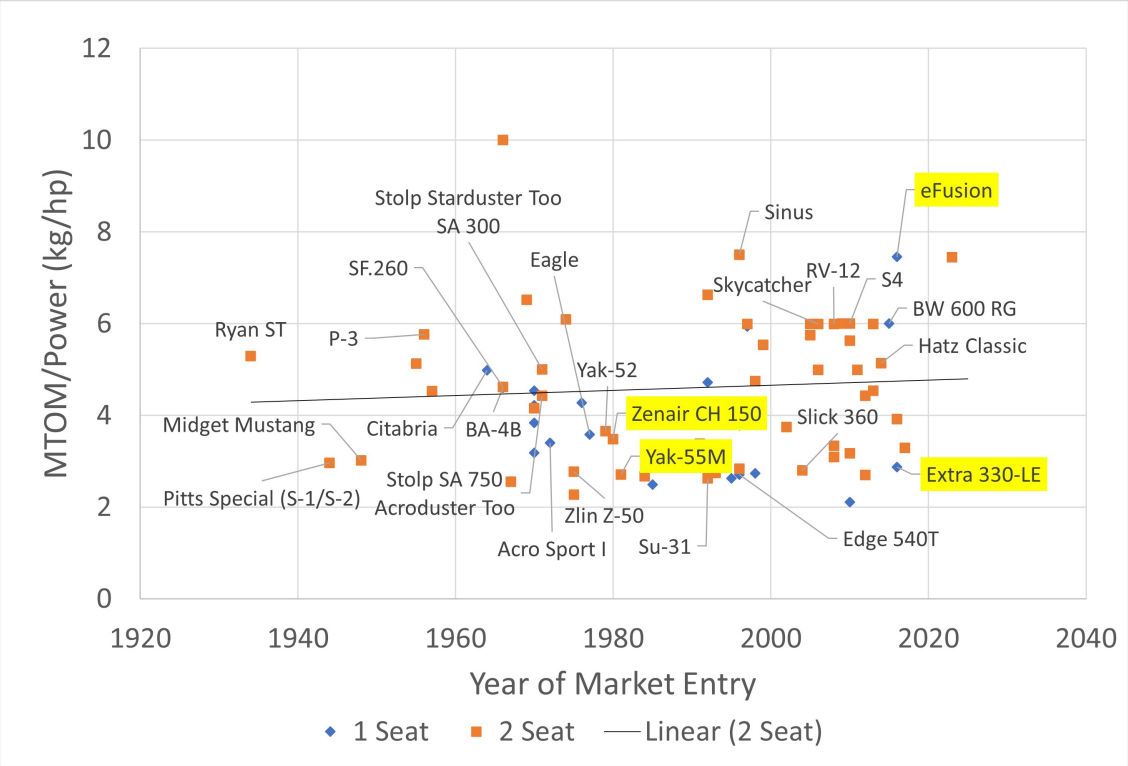

Figure 3.1: *Two-seater Maximum Take-off Mass and Power Ratio (MTOM/Power)*

3.2. Target Performance and Cost

Appeal, safety, performance and expense are factors to be considered in order to create a marketable design. Consequently, using the market analysis database, an initial baseline estimate of performance parameters for an estimated entry into the market in 2027 was generated. This can be seen in Table 3.2 and includes a 25 % margin.

Then, using a fully-composite modern aerobatic aircraft of similar aerobatic performance as the target parameters, a budget cost estimate could be generated as seen in Table 3.3. The prices were originally quoted in US dollars and at the time of conception, the conversion rate of US dollar to Euro was approximately one-to-one. Hence, for the consistency of the rest of the report, these prices are given in Euros. An estimate was made by removing the cost of the engine and utilising initial cost estimates for the batteries, and the electric motor.

Table 3.2
Initial baseline performance estimate

Parameter		Value
MTOM	[kg]	890
OEM	[kg]	544
Maximum wing loading	[kg/m^2]	57
Wing area	[m^2]	15.6
Aspect ratio	[-]	7
Power required	[kW]	126

Table 3.3
Budget cost breakdown

Description	Value Estimation (€)
GB1 Gamebird Manufacturer's Quote [5]	515.000 (+)
Lycoming AE10-580-B1 Quote [6]	116.000 (-)
GB1 without Engine	399.000
Battery Cost Estimate (2022)[7]	15.000 (+)
Electric Motor Cost Estimate (180 kW)[8]	62.000 (+)
25% Cost Margin	119.000 (+)
Total Production Cost Estimate (2027)	595.000

[5] URL:https://gamecomposites.com/configure/ [Accessed 10 May 2022]
[6] URL:https://www.airpowerinc.com/aeio-580-b1a [Accessed 10 May 2022]
[7] Based on Li-ion price density of 181 $/kWh (2018): https://ourworldindata.org/battery-price-decline [Accessed 10 May 2022]
[8] Pipistrel 60 kW electric power train upscaled: https://www.pipistrel-prices.com/configurator/configure/647/ [Accessed 10 May 2022]

4

Requirements

This chapter states all the technical and non-technical requirements for the Electrobat. These requirements are discussed in Section 4.1 and Section 4.2 respectively. An extra column is added in the tables for the specific verification method per requirement. This verification method is important as it determines whether the requirement is met.

4.1. Technical Requirements

The technical requirements are given in Table 4.1 and Table 4.2. The first part is directly derived from the stakeholder requirements, as given in Table 2.1. The second part has been set up using a requirement discovery tree. Taking into account each flight phase, operations, production, and maintenance, the requirements were discovered and added as technical requirements the aircraft has to fulfil. A verification method was used to distinguish 4 different ways to verify whether the requirements are actually met: Demonstration (D), Testing (T), Inspection (I) and Analysis (A). The chosen method per requirement is given in each table as well. Section 12.2 gives an overview of the requirements' compliance.

Table 4.1
Technical Requirements part 1/2

Identification	Requirement	Verif.
EFLY-PERF-01	The aircraft shall have an operational speed of 150 [kts].	D
EFLY-PERF-02	The aircraft shall have a stall speed of 50 [kts] in the landing configuration.	D
EFLY-PERF-03	The aircraft shall have a flight endurance of 40 minutes including reserves.	T
EFLY-PERF-04	The aircraft shall be able to operate from a grass or tarmac runway of 500 [m].	D
EFLY-PERF-05	The aircraft shall be able to perform a barrel roll.	D
EFLY-PERF-06	The aircraft shall be able to perform an aileron roll.	D
EFLY-PERF-07	The aircraft shall be able to perform a snap roll.	D
EFLY-PERF-08	The aircraft shall be able to perform a Cuban Eight.	D
EFLY-PERF-09	The aircraft shall be able to perform a loop.	D
EFLY-PERF-10	The aircraft shall be able to perform an inverted flight.	D
EFLY-PERF-11	The aircraft shall be able to perform a tail slide.	D
EFLY-PERF-12	The aircraft shall be able to perform a spin.	D
EFLY-PERF-13	The aircraft shall be able to perform an Immelmann.	D
EFLY-PERF-14	The aircraft shall have limit loads +8 / -6 G.	T
EFLY-PERF-15	The aircraft shall have a <TBD> glide angle.	D
EFLY-PERF-16	The aircraft shall be able to accelerate to 20 [kts] on the ground without external support.	D
EFLY-PERF-17	The aircraft shall be recoverable from a stall.	D
EFLY-PERF-18	The aircraft shall be able to land with a maximum crosswind of 15 [kts].	D
EFLY-PERF-19	The aircraft shall be able to decelerate to the stall velocity without gaining altitude.	D
EFLY-PERF-20	The aircraft shall be able to accelerate to the operation velocity without losing altitude.	D
EFLY-PERF-21	The aircraft shall have a service ceiling of at least 10,000 [ft].	D
EFLY-STAB-01	The aircraft shall be longitudinally stable.	T + A

Table 4.2
Technical Requirements part 2/2

Identification	Requirement	Verif.
EFLY-STAB-02	The aircraft shall have convergent Dutch Roll eigenmotion.	T + A
EFLY-STAB-03	The aircraft shall have convergent short aperiodic eigenmotion.	T + A
EFLY-CTRL-01	The aircraft shall be operable by a single pilot.	D
EFLY-CTRL-02	The aircraft shall be controllable in roll during all normal flight operations.	D
EFLY-CTRL-03	The aircraft shall be controllable in pitch during all normal flight operations.	D
EFLY-CTRL-04	The aircraft shall be controllable in yaw during all normal flight and ground operations.	D
EFLY-CTRL-06	The aircraft shall have a minimum roll rate of 360 [deg/s] at the operational speed at sea level conditions, with maximum control deflection.	D
EFLY-CTRL-08	The aircraft shall have a maximum pitch rate of 45 [deg/s] at the stall speed at standard sea level conditions, with maximum control deflection.	D
EFLY-CTRL-10	The aircraft shall have a maximum yaw rate of 30 [deg/s] at the stall speed at standard sea level conditions, with maximum control deflection.	D
EFLY-STR-01	The aircraft structure shall withstand all maximum nominal loads without permanent deformation.	T + A
EFLY-STR-02	The aircraft shall be able to withstand an ultimate load factor of 12 and −9 G including a safety factor of 1.5 and 1 occupant	T + A
EFLY-STR-03	The aircraft shall not experience flutter within the flight envelope.	T + A
EFLY-STR-04	The aircraft shall not be affected by moderate rain conditions.	T
EFLY-STR-05	The aircraft shall protect the occupants from smoke and fire for at least 10 minutes.	T
EFLY-STR-06	The aircraft shall withstand a bird strike without catastrophic failure.	T
EFLY-EQP-01	The aircraft shall provide means of communication with air traffic control.	T
EFLY-EQP-02	The aircraft shall communicate all electrical system faults to the pilot.	T
EFLY-EQP-03	The aircraft shall have controls accessible from the pilot position.	I + D
EFLY-OPER-01	The aircraft shall have a tow-bar connection.	I
EFLY-OPER-02	The aircraft shall have a battery charging connection.	I
EFLY-OPER-03	The aircraft shall fit in a general aviation hangar.	D
EFLY-OPER-04	The aircraft shall be movable on the ground by a single person without power.	D
EFLY-OPER-05	The aircraft shall be able to be tied to the ground.	D
EFLY-OPER-06	The aircraft turn around time shall be less than 3 hours.	D
EFLY-PROD-01	All subassemblies shall fit in a standard ISO shipping container.	D
EFLY-PROD-02	The propulsion and power subassembly shall be provided by subcontractors.	D

4.2. Non-technical Requirements

A similar method has been applied for the non-technical requirements. Initially, all the tables listing the requirements related to the CS-23 regulations were in this section as well, but have been left out due to their lengthiness. In Section 12.2 they have been addressed, as the final design will have to comply with these regulations.

Table 4.3
Non-technical requirements

Identification	Requirement	Verif.
EFLY-ECON-01	The aircraft shall have a production cost of at most €595.000.	A
EFLY-ECON-02	The aircraft shall seat 1 person	D
EFLY-ENV-01	The aircraft shall be electrically propelled.	I
EFLY-ENV-02	The aircraft shall be emission-free during operation.	D
EFLY-ENV-03	The aircraft shall have less than 10% material waste at the end of life.	A

5

Mission Analysis

The mission analysis entails everything the aircraft will encounter during its operational lifetime. It is useful to construct such an analysis as it will influence the design of the aircraft. First, the mission profile is discussed in Section 5.1. Then the function flow and functional breakdown diagram are stated in Section 5.2 and Section 5.3 respectively. Section 5.4 will go in to the operations and logistics. To end this chapter, Section 5.5 will showcase the communication flow diagram

5.1. Mission Profile

The mission profile consists of the flight phases that the aircraft will encounter during its operational life. The mission profile consists of the flight profile and the V-n diagram. These are discussed in Subsection 5.1.1 and Subsection 5.1.2 respectively.

5.1.1. Flight Profile Diagram

To get a good understanding of the different phases of flight of the Electrobat, a flight profile diagram is constructed. This flight profile diagram shows how long these phases take, and what the average thrust setting is during this phase. The time per phase and thrust setting are crucial parts of determining what the required battery capacity is. The flight profile can be seen in Figure 5.1

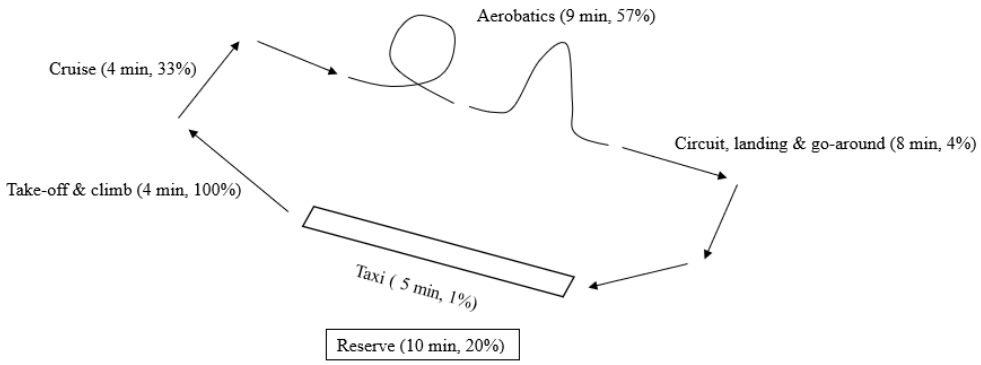

Figure 5.1: *Flight profile of the Electrobat*

The battery capacity allocated to aerobatics in the flight profile was computed by estimating the time per maneuver and power setting required Table 5.1. The main source for these estimations were based on literature review of online videos. Furthermore, considerations for transitions between each maneuver are represented by the parameter 'rest'.

Table 5.1
Energy distribution of aerobatic maneuvers

Maneuver	Time allocation [s]	Power setting [%]	Energy [Wh]	Energy distribution [%]
Aileron Roll	15	45	492	2
Barrell Roll	15	45	492	2
Snap roll	15	45	492	2
Spin	30	45	983	5
Loop	100	45	3,278	15
Tailslide	30	81	1,750	8
Cuban Eight	150	67	7,250	33
Immelmann	45	81	2,625	12
Inverted	15	45	492	2
Rest	120	45	3,933	18
Total	535		21,786	

5.1.2. V-n Diagram

The V-n diagram showcases the flight envelope of the aircraft. It defines the strength limitations of the aircraft. The flight envelope outlines the loads the aircraft can encounter at different airspeeds. The V-n diagrams for both one and two occupants are displayed in Figure 5.2 and Figure 5.3. Next to the displayed flight envelope, the gust-loading is also integrated into the V-n diagram and is indicated by the yellow line. From the flight envelope it can be seen that the dive speed is $187.5\,\mathrm{kts}$, 1.25 times the cruise speed [1].

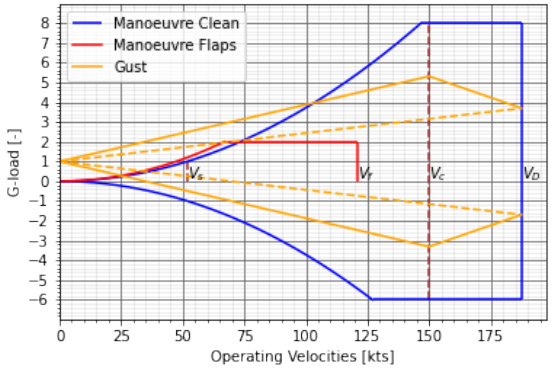

Figure 5.2: *V-n diagram of the Electrobat for one occupant*

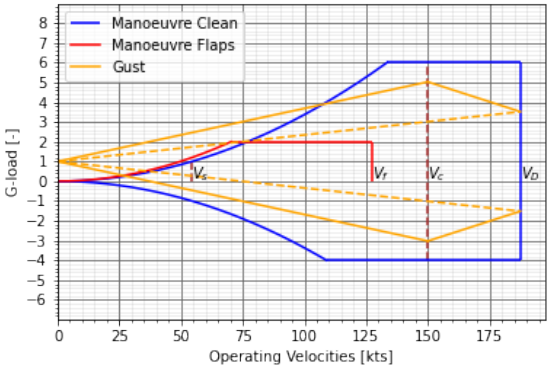

Figure 5.3: *V-n diagram of the Electrobat for two occupants*

5.2. Functional Flow Diagram

The functional flow diagram (FFD) showcases the tasks the aircraft will undergo and perform during its lifetime and can be seen in Figure 5.6. The FFD is in chronological order and starts at the design phase of the aircraft, where all the parameters are determined. After this, the aircraft will be produced and certified. The aircraft will undergo these tasks only a single time. After this process, the aircraft will be delivered to its owner who will operate the aircraft. The ”deliver aircraft” function can occur multiple times during the lifetime of the owner who wants to fly at different airstrips. The ”operate aircraft” function will reoccur the most, as this will be done until the end of life of the aircraft. Then, the aircraft will be disposed of. Multiple levels are indicated with different colours. These levels are added in the FFD to provide a more in-depth view of what the aircraft will undergo and perform.

5.3. Functional Breakdown Diagram

To get a broader look at all the tasks that the aircraft will encounter, the functional breakdown diagram (FBD) is needed. These tasks are, unlike the FFD, not in chronological order. The tasks are grouped to get a clear overview of what needs to be done. The difference between the FFD and the FBD is that some tasks need

to be performed during the whole mission instead of in sequential steps. It is for this reason that these tasks are not incorporated into the FFD. Again, the colours show the different levels of detail in the FBD.

5.4. Operations and Logistics

The aircraft operations can be broken down into two subcategories: day-to-day use and maintenance. It is useful to construct an operational flow diagram for these two cases in order to get an easy and clear understanding of what the aircraft will encounter. The operational flow diagram for day-to-day operations and maintenance are given in Figure 5.4 and Figure 5.5, respectively.

For day-to-day operations the following four steps need to be taken into consideration:

- **Prepare for take-off**: The aircraft should be easily inspected prior to take-off;
- **Taxiing**: The aircraft should be easily operable on the ground and can be preferably moved by one person;
- **Park aircraft**: The aircraft should be easily embarked and disembarked from additional equipment in order to store the aircraft;
- **Charge battery**: The aircraft needs a charging station in the hangar. With more airport development, this will become more feasible [1].

For maintenance, the following 3 steps should be considered during the design:

- **Perform inspection**: The aircraft batteries can be placed such that they can be straightforwardly inspected or exchanged. Next to that, the propulsion system, wings and other subsystems need to be easily inspectable;
- **Repairs and End-Of-Life**: The aircraft parts can be made reusable, making them more sustainable; Furthermore, the aircraft can be made out of materials or components that can be reused and replaced such that it makes repairs more convenient;
- **Transport**: The aircraft should be able to be transported on a trailer if it is necessary to travel greater distances than the aircraft can fly [2].

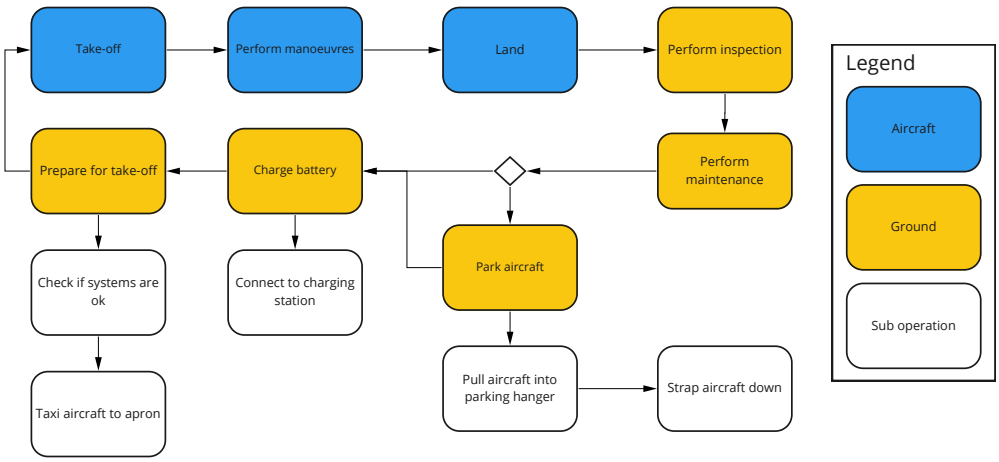

Figure 5.4: *Operational flow diagram for the day-to-day operations*

[1] URL: https://www.airport-technology.com/news/swedavia-electric-aircraft-charging-stations/ [Accessed 20 June 2022]
[2] URL: https://www.aviaircraft.com/products-and-prices/trailers [Accessed 20 June 2022]

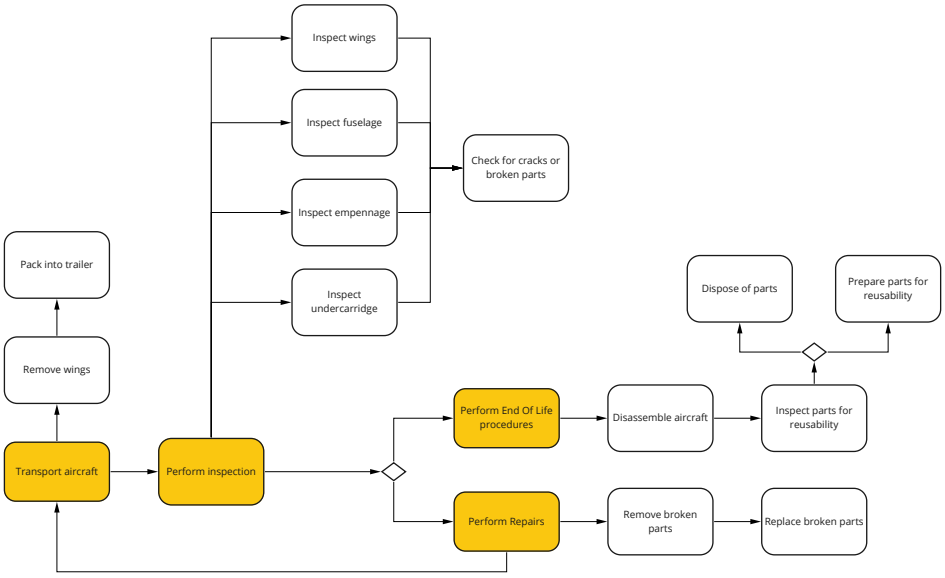

Figure 5.5: *Operational flow diagram for the maintenance operations*

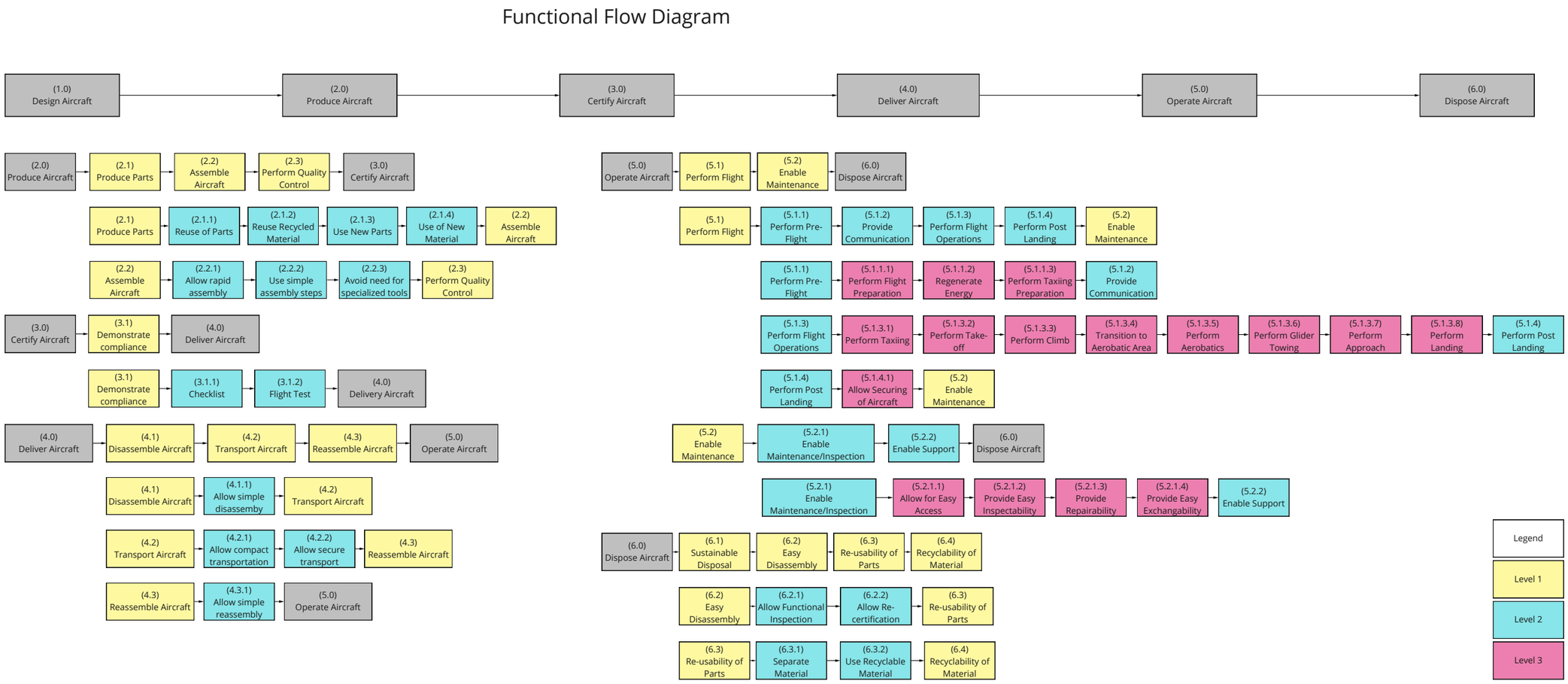

Figure 5.6: *Functional flow diagram of the Electrobat*

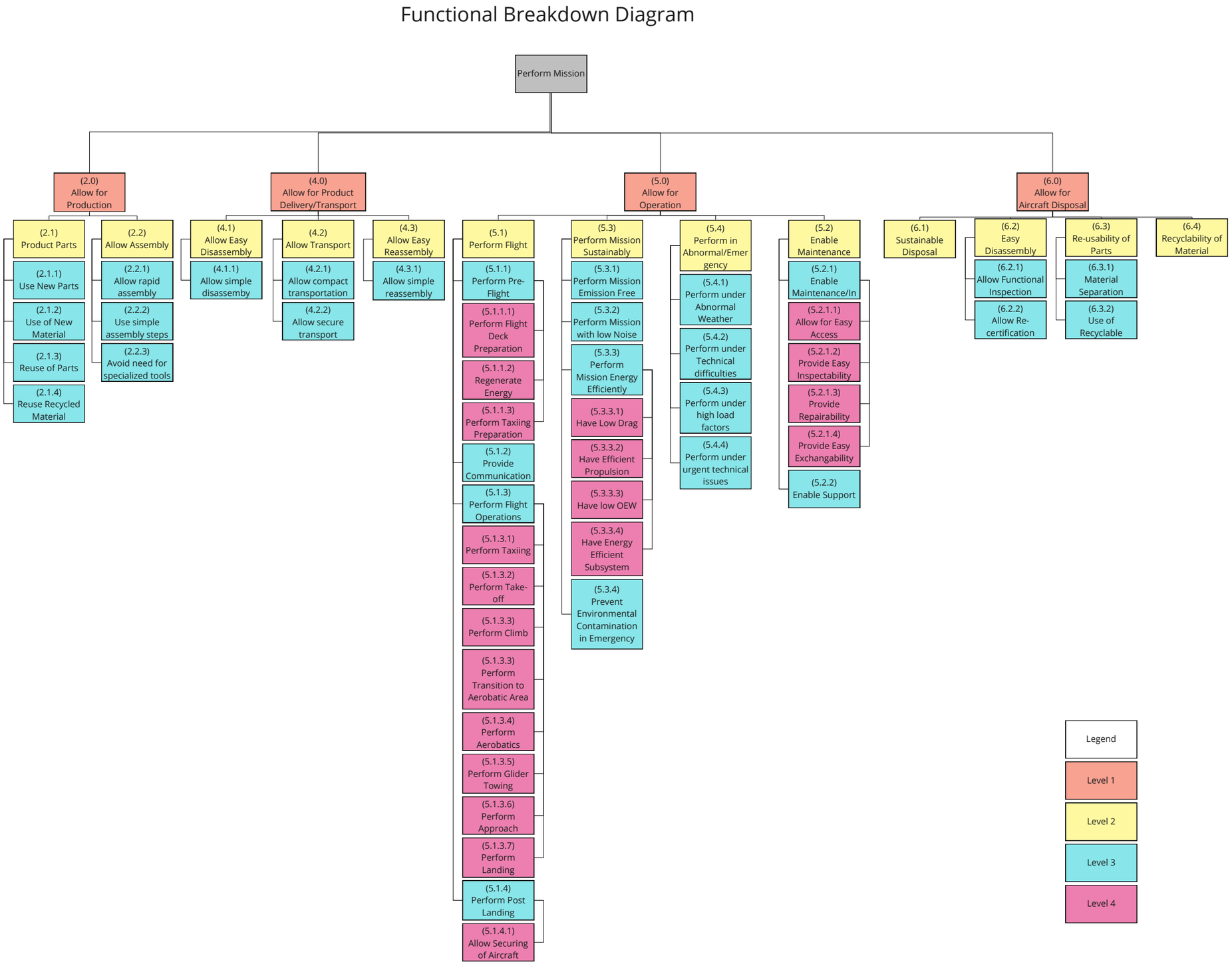

Figure 5.7: *Functional breakdown structure of the Electrobat*

5.5. Communication Flow

The data handling and communication flow diagram illustrates the flow of data through the aircraft, and towards and from its environment Figure 5.8. The data handling diagram and communication flow diagrams are combined as their subsystems are interrelated. The communication flow includes the pilot, air traffic and aircraft state measurement interactions. Notably, all pilot control inputs are interpreted by one of two flight computers, for redundancy, which then generates executable commands. These commands may result in deflection of the control surfaces by two redundant actuators per surface, or operations of the landing gear motor, throttling of the motor, or battery. Additionally, controllers serve to distribute commands and read the state of the relevant device. Furthermore, measuring instruments such as the angle-of-attack vane and pitot tube allows an analysis of the environment to derive the aircraft's state. This state is then used to activate the Emergency Locator Transmitter (ELT) if a crash G-load is exceeded or alternatively, to communicate aircraft altitude, velocity and position via the Automatic Dependent Surveillance-Broadcast (ADSB) transponder. All relevant information is presented to the pilot visually via the avionics.

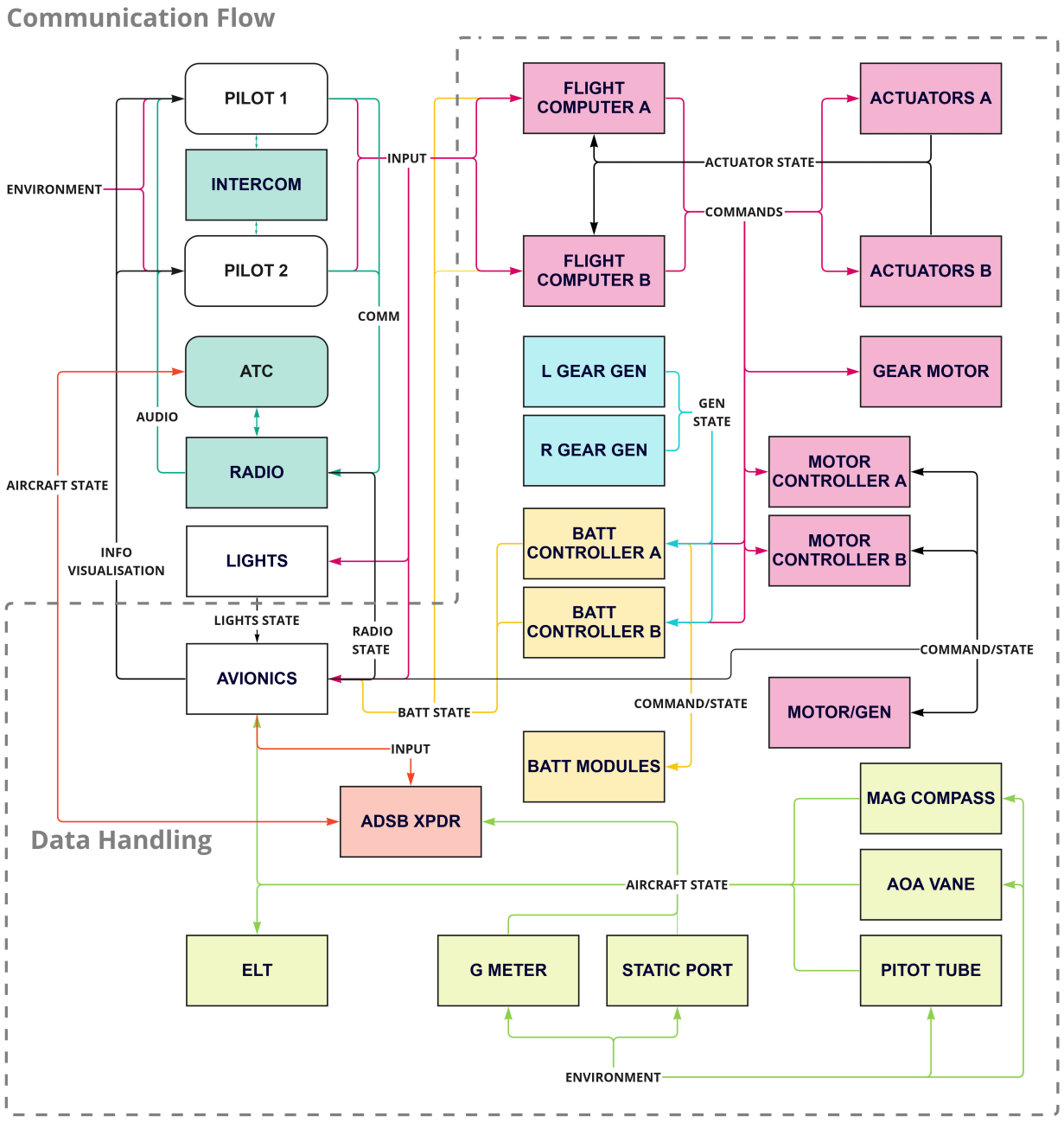

Figure 5.8: *Data handling and communication flow diagram of the Electrobat*

6

Preliminary Design

This chapter covers the preliminary design of the aircraft. This includes the design options and final concept, as discussed in Section 6.1 and Section 6.2. Section 6.3 shows the N2 chart used in the design process of the Electrobat. Furthermore the weight estimations are discussed in Section 6.4 and Section 6.5. Section 6.6 includes the initial positioning of the wing and the centre of gravity location.

6.1. Design Options

Before coming up with a final design concept, a design option tree was made for the different subsystems of the aircraft. The design option tree is an OR-tree which displays all possible combinations for a specific subsystem [3]. This diagram is useful to construct as it gives an overview of all the options and makes it more noticeable if an option is missing. Every possibility that is in the design option tree was put in a trade-off table. The trade-off table was then used to compare each option against different criteria. These criteria were weighted and for each option a final score was obtained [3]. Doing this for every subsystem, all the best options were determined. It was seen that the best options were all subsystems that are used in conventional aircraft, which is logical, however it does not mean that combining all the best options together would result in the best aircraft. The interaction between these subsystems is crucial for the performance of the aircraft and so, three possible design options were constructed in order to see which concept would be the best suited for the given requirements.

6.2. Design Concepts

As stated before, three design concepts were constructed with the design options from the trade-off tables. The three options are referred to as conventional, advanced and extreme and can be seen in Figure 6.1. This Venn diagram showcases the subsystems that were chosen for each concept.

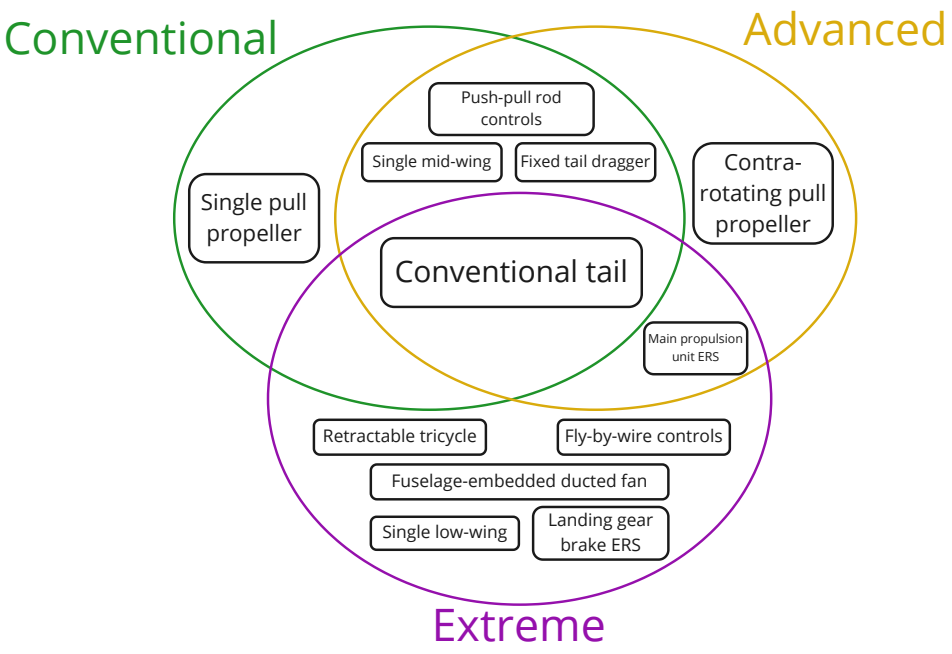

Figure 6.1: *Venn diagram of the shared design options between the 3 concepts and the design options that are unique to each of them*

With the three design concepts determined, a final trade-off table was constructed to determine the best concept for the given requirements. The concepts that came out of the trade-off are worked out in greater detail in this report. The trade-off tables can be seen in Table 6.2 and Table 6.3. The tables are constructed based on the results of the design option trade-offs, the risk assessment and the operations and logistics concepts. Per criteria, a colour is assigned to evaluate the performance. The legend is in Table 6.1.

Table 6.1
Legend for Table 6.2 and Table 6.3

Excellent	Nominal	Correctable deficiencies	Unacceptable

Table 6.2
Final trade-off between concepts 1/2

Option	Propulsive performance	Mass performance	Controllability
Weight	*20%*	*20%*	*20%*
Conventional	Standard propeller	Lightweight	Control rods
Advanced	Added propeller	Increased complexity	Control rods
Extreme	Increased efficiency	Increased complexity	Fly-by-wire

Table 6.3
Final trade-off between concepts 2/2

Option	Noise performance	Development cost	Development risk
Weight	*20%*	*10%*	*10%*
Conventional	Exposed propeller	Proven design	Proven design
Advanced	Turbulent wake	Propulsion system	Propulsion system
Extreme	Ducted	Innovative systems	Innovative systems

The conventional aircraft scores nominal on almost everything except the noise performance. This is due to the exposed propeller. The Advanced concept is not acceptable as the contra-rotating propeller will definitely exceed the $60\,\mathrm{dB}$ noise requirement. This leaves the extreme concept which has excellent scores on three criteria while the other three criteria are satisfied with acceptable margins. After evaluation with the team, the decision has been made to continue with the extreme concept for the following reasons:

- **Performance**: With effective use of each subsystem, the extreme concept can exceed the performance of the conventional design. In the conventional design, each subsystem works independently of one another which has benefits in terms of safety and redundancy, but not with regards to efficiency. Having a single integrated electric system has the potential to weigh less with the same performance.
- **Controllability**: The fly-by-wire system forms the basis on which future subsystems can be added. Basic safety factors, like maximum G-loads, can already be implemented without the need for multiple mechanical actuators and sensors [1]. Secondly, as mentioned previously, it allows for an integrated system design which ultimately weighs less. Thirdly, with regard to the market analysis, a simple feedback gain can be implemented to make the aircraft appealing to both beginner and experienced pilots. The product can thus be appealing to both flight schools and private owners, covering a large market. In future versions, additional systems can be implemented such as dynamic control in terms of trim, auto-recovery systems and autopilots. This does require additional sensors, adding mass to the aircraft. Lastly, the extreme concept uses a tricycle landing gear instead of a taildragger. This improves ground manoeuvrability tremendously and removes the risk of tip-over during excessive braking.
- **Noise**: The noise requirement of $60\,\mathrm{dB}$ is driving for the propulsion system, and it is unsure if the other concepts can meet this [4, 5]. Next to the increased efficiency, the noise of a ducted fan is reduced because the noise source is shielded and of a higher number of blades are spinning at faster RPM.

[1] URL: https://onboard.thalesgroup.com/how-fly-by-wire-flight-controls-are-increasingly-enhancing-aircraft-performance-and-safety/ [Accessed 20 June 2022]

- **Innovation**: Both the conventional and advanced designs have already been tested and implemented in the current market. Making an aircraft which is almost identical to the competition does not help in terms of brand recognition. The innovative extreme concept can distinguish itself from the competitors in terms of aesthetics, performance, and sustainability. Exploring this concept also builds a new knowledge base for an electrically powered ducted fan propulsion system for an aircraft.
- **Risk**: The extreme concept is associated with higher risks compared to the other two other concepts, mainly in terms of costs and certification. Costs are increased due to the innovative propulsion and electric system. Instead of an outside unit, the propulsion system has to be integrated into the fuselage and will undoubtedly cost more (high complexity). Flight management computers and added redundancy require both expensive hardware and software, and these components are likely to cost more than their mechanical counterparts. The added complexity also implies an extensive certification process in a conservative industry, further adding costs. These drawbacks cannot be mitigated and have to be accepted. From the trade-offs made, the advantages mentioned earlier have a realistic potential to exceed these drawbacks and further analysis will follow to check if this is indeed the case.

The extreme concept will consist of a ducted fan with a fuselage-embedded propeller. It will also have retractable landing gear, an energy recovery system and fly-by-wire controls. The exact design will be worked out in more detail in the coming chapters.

6.3. N2 chart

In the design phase, it is essential to have an overview of the relations between the different subsystems. The N2 charts outlines the required inputs for a specific subsystem design and displays the outputs that are obtained after the design. These outputs are then used for different subsystems, which result in an iteration cycle. Diagrams like this are helpful to get an understanding on how to approach the design of the aircraft.

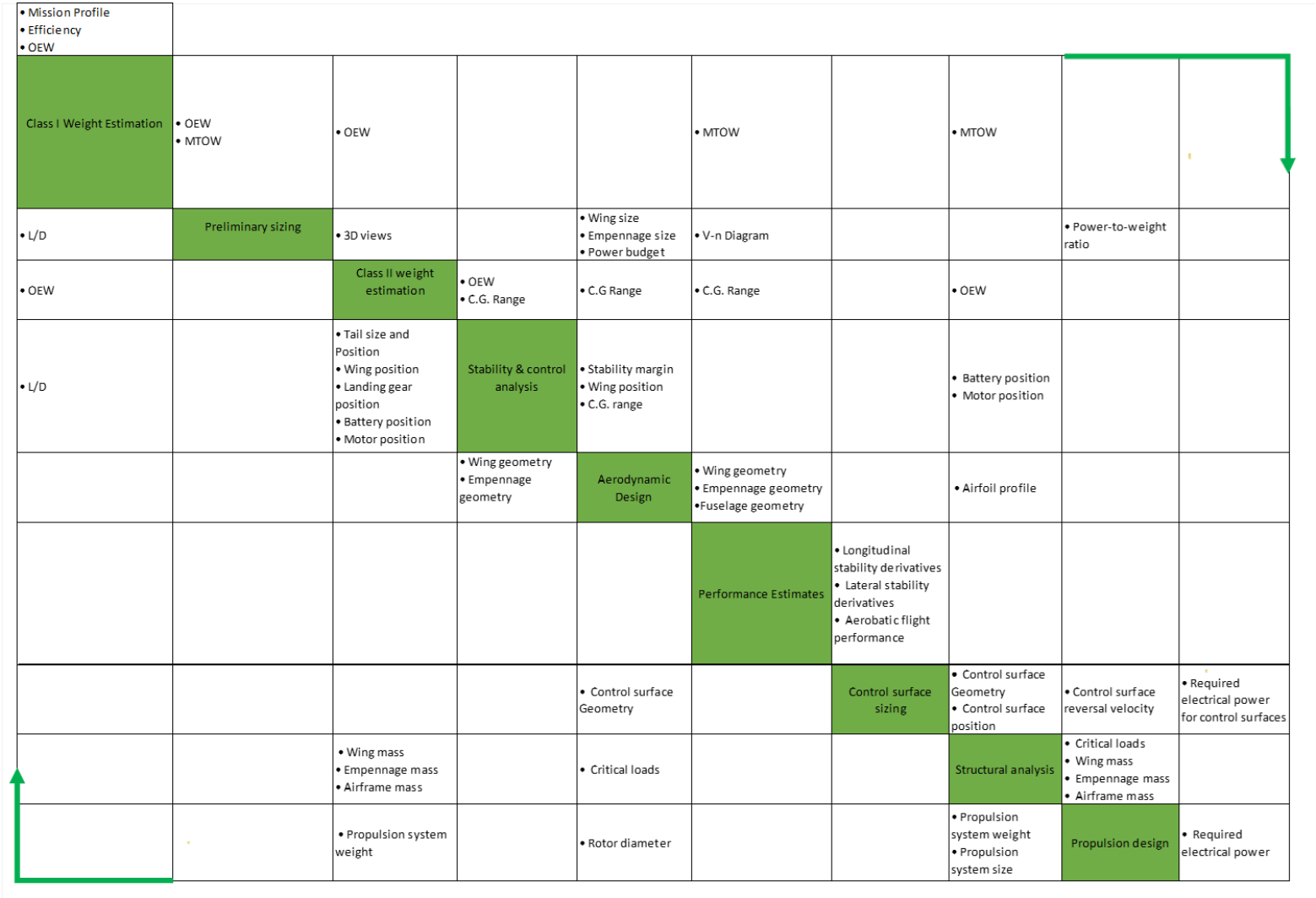

Figure 6.2: *N2 chart of the Electrobat*

6.4. Class I Weight Estimation

The initial weight of the aircraft was determined during the class I weight estimation analysis. This consisted of a number of comparable aircraft that were found during the market analysis. The weights of these aircraft were corrected for the engine weight and an average value for the structural mass was determined. This value was calculated to be $345\,\mathrm{kg}$ and excludes the batteries and motor of the aircraft. Using an iterated flight profile, a flight time of approximately $40\,\mathrm{min}$ and total energy of $56\,\mathrm{kWh}$ was found. With an initial energy density estimate of $236\,\mathrm{Wh/kg}$ for the lithium-ion battery, the battery weight was estimated to be $281\,\mathrm{kg}$ [2]. The electric motor weight was taken to be $33\,\mathrm{kg}$ according to Saluqi's datasheet [3]. Adding a $20\,\%$ margin resulted in an Operational Empty Mass (OEM) of $790\,\mathrm{kg}$. The pilots, estimated at $90\,\mathrm{kg}$ each ($80\,\mathrm{kg}$ for the pilot and $10\,\mathrm{kg}$ for a parachute), result in a Maximum Take-Off Mass (MTOM) of $880\,\mathrm{kg}$ and $970\,\mathrm{kg}$ for single and dual pilot operations respectively [1]. This class I weight estimate was obtained via iterations to ensure convergence of the MTOM.

Using this iterated initial weight estimate, a second iteration was performed in order to ensure convergence of power-loading, battery weight and thus MTOM. A completely converged MTOM of $978\,\mathrm{kg}$ is achieved within six iterations. This results in the power settings flight profile as seen in Table 6.4, resulting in $58\,\mathrm{kWh}$ of energy, including a $5\,\%$ margin for maximum charge capacity. This then results in a mass build up as described in Table 6.5, providing a MTOM of $888\,\mathrm{kg}$ and $978\,\mathrm{kg}$ for single and dual pilots respectively.

Table 6.4
Power settings per flight phase using a maximum power of $260\,\mathrm{kW}$

Phase	Time [min]	Power [%]	Energy [Wh]	Percentage [%]
Taxi	5	1	215	0.4
Take-off & Climb	4	100	17194	29.9
Cruise (To and From)	4	33	5674	9.9
Aerobatics	9	57	21786	37.8
Circuit, Landing & Go-around	8	4	1376	2.4
Reserve	10	20	8597	14.9
Total	40	-	54842	95.2
5% Margin	42	-	57584	100

Table 6.5
Initial mass estimations

Part	Mass [kg]	Percentage [%]
Structure	345	35.3
Batteries	287	29.3
Motor	33	3.4
OEM reference	665	68.0
20% margin	133	13.6
OEM	798	81.6
Pilot	90	9.2
MTOM (pilot only)	888	90.8
Passenger	90	9.2
MTOM (both)	978	100

6.5. Class II Weight Estimation

A class II weight estimation follows the class I weight estimation and requries some initial design parameters. Together with these parameters and the weight calculated during the class I weight estimations, it is possible to determine the main component weights of the aircraft. There are different class II weight estimation methods, but all methods are based on empirical formulas. The methods used for this design are: Cessna, Raymer, Torenbeek and USAF, which can be found in the Roskam and Snorri book [1, 6]. These methods

[2] URL: https://www.cei.washington.edu/education/science-of-solar/battery-technology/ [Accessed 20 June 2022]
[3] URL: https://www.saluqimotors.com/products/ [Accessed 17 June 2022]

are not necessarily made for small aerobatic aircraft, which means that a critical evaluation is required to determine if the values are reasonable. The final values calculated with the different methods for the given components are presented in Table 6.6 below. These are the final values after some correction factors were implemented to obtain more reasonable values. The wing is one of the components that has been given a correction factor because the methods used are not designed to estimate the weight of composit components. The use of composits could reduce the weight of the wing up to $70\,\%$ compared to aluminium and a correction factor of implemented.[4]. This factor was equal to 0.5 to be a bit conservative. The final component values that are used for this design are the average values of the methods just mentioned and give a general indication of how much the systems should approximately weigh. The final mass value for two occupants can be seen in the table below as being $966\,\mathrm{kg}$. This means that the MTOM of with one occupant is equal to (966-90 =) $876\,\mathrm{kg}$.

Table 6.6
Calculated component masses in kg for different methods

	Wing	H-tail	V-tail	Fuselage	Gear	Control	Electric	Misc	Batteries	Motor	Occupants	Totals
Cessna	144.0	51.0	14.0	26.0	36.0	11.0	26.0	18.0	276.0	33.0	180.0	815.0
Raymer	146.0	31.0	22.0	103.0	89.0	66.0	-	27.0	276.0	33.0	180.0	973.0
Torenbeek	134.0	55.0	55.0	-	50.0	18.0	35.0	-	276.0	33.0	180.0	836.0
USAF	184.0	43.0	16.0	148.0	20.0	41.0	-	92.0	276.0	33.0	180.0	1033.0
Average [kg]	154.0	45.0	27.0	92.0	49.0	34.0	30.0	46.0	276.0	33.0	180.0	966.0
Average [%]	16.0	4.7	2.8	9.5	5.1	3.5	3.1	4.7	28.6	3.4	18.6	100.0

6.6. Center of Gravity and Wing Placement

The centre of gravity is an important design parameter of an aircraft because it plays a role in for example the placement of the wing, landing gear position and the stability of the aircraft. The Centre of Gravity (CG) position follows from the component weights as calculated in the class II weight estimation and a moment arm around the nose of the aircraft, which was determined with the help of the fuselage design. The wing placement could then be determined with Equation 6.1 [3]. This formula gives the location of the leading edge of the wing and was calculated to be $3.5\,\mathrm{m}$ from the nose of the aircraft. The formula depends on the CG position of the fuselage and a correction based on the weight and CG position of the wing and fuselage group.

$$x_{LEMAC} = x_{CG,FG} - x_{CG,OE} + \frac{W_{WG}}{W_{FG}}\left(x_{CG,FG} - x_{CG,OE}\right) \tag{6.1}$$

The CG location excluding the wing and the just calculated wing positioning result in a CG range that is dependent on the seating location of one or two of the occupants. A conventional aircraft also has to take into account the loading of fuel, which is simply not required for an electric aircraft. This makes the CG location relatively straight forward to determine and makes a loading diagram unnecessary. The range of the CG and the percentage of the MAC is presented in Table 6.7 below and is dependent on the number and positioning of the passengers and the total weight of the aircraft.

Table 6.7
Weight and corresponding CG positions for different seating arrangements

	Mass [kg]	CG location from nose [m]	CG location [% of LEMAC]
OEW	786.0	3.86	24.0
1 occupant front	876.0	3.76	17.0
1 occupant rear	876.0	3.91	27.0
2 occupants	966.0	3.81	21.0

[4] URL: https://discovercomposites.com/industrial/composites-vs-other-materials-in-industrial-applications/ [Accessed 1 June 2022]

7

Aerodynamics and Fuselage Design

Following the weight estimations, the wing may now be sized accordingly in Section 7.1 in order to satisfy the performance requirements outlined previously in Chapter 4. Additionally, after the sizing of the wing and the high-lift devices, the landing gear and fuselage are designed to ensure the successful integration of all subsystems into an airframe in Section 7.2 and Section 7.3.

7.1. Wing Aerodynamics

In Subsection 7.1.1 the wing planform is designed using a constraint analysis. Following this, in Subsection 7.1.2 an airfoil is selected with the most promising parameters to fit the given concept. In Subsection 7.1.3, the complete wing is analysed in XFLR to determine the lift and drag curves. Subsection 7.1.4 and Section 7.4 discuss the performance of the wing during various flight phases.

7.1.1. Wing Planform Design

To obtain a preliminary planform of the wing which satisfies the performance requirements, a constraint analysis was performed as seen in Figure 7.1. This analysis was depicted in a power loading - wing loading diagram. The constraints included those most critical to the performance of the aircraft namely, stall, take-off, landing, climb rate, climb gradient, and manoeuvring performance. The cruise phase has not been considered, as the sustained turn represented a more critical condition. To obtain the best planform design, combinations of aspect ratio and lift coefficients have been investigated, leading to the selection of the parameters seen in Table 7.1. The resulting design point provides a wing loading of $778\,\mathrm{N/m^2}$ and a power loading of $44.2\,\mathrm{N/kW}$.

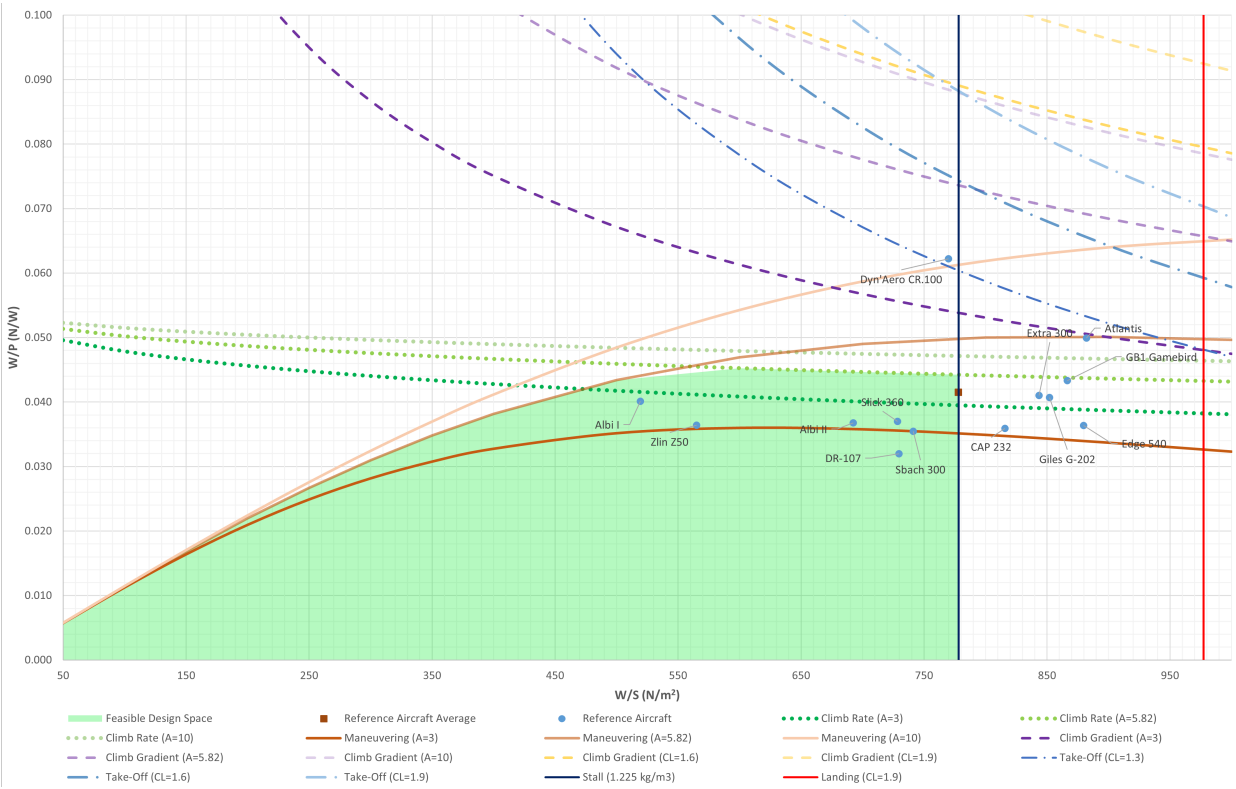

Figure 7.1: *Constraint analysis for required performance*

From this design point, the limiting constraint of stall speed of $50\,\mathrm{kts}$ at sea level requires a wing loading of $778\,\mathrm{N/m^2}$ for the double seater. When using the class II weight estimate for MTOM this gives a wing area of $12.3\,\mathrm{m^2}$. Additionally, following the design point in the constraint analysis, the span was determined in Table 7.1 and seen in Figure 7.2.

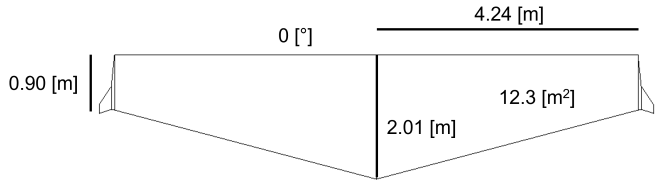

Figure 7.2: *Wing planform drawing*

Table 7.1
Wing planform design parameters

Parameter		Value
S	[m^2]	12.3
b	[m]	8.48
AR	[-]	5.8
λ	[-]	0.45
Λ_{LE}	[°]	0
$\Lambda_{c/4}$	[°]	-3.75
C_r	[m]	2.01
C_t	[m]	0.90
MAC	[m]	1.46
i	[°]	0.75

To tailor the rest of the wing design, the desired performance characteristics are considered. The stall characteristics of a wing are dependent on its lift distribution [7]. According to feedback from aerobatic pilots, “the optimal lift distribution will result in a stall that initiates on most of the wing simultaneously” [7]. Additionally, in order to reduce the number of batteries, a reduced propulsion power consumption is necessary. Therefore, an increased aerodynamic efficiency, and thus elliptical lift distribution, is prioritized. Moreover, the ease-of-handling characteristics at the stall improve as the stall initiates at the root, allowing lateral control to be maintained. The several key parameters affecting the lift distribution of a wing are the sweep, wing twist and taper ratio. However, due to the low stall speed and runway operating distance requirements the leading edge wing sweep angle is chosen to be $0°$, also simplifying the wing manufacturing. Additionally, no wing twist was selected to provide symmetrical performance in both inverted and normal flights. A report from the American Institute of Aeronautics and Astronautics (AIAA) found the taper ratio to be most effective in controlling the lift distribution [7]. Hence, by applying a taper ratio of 0.45 a nearly elliptical lift distribution is achieved over the half-span at angles of attack nearing stall as seen in Figure 7.3.

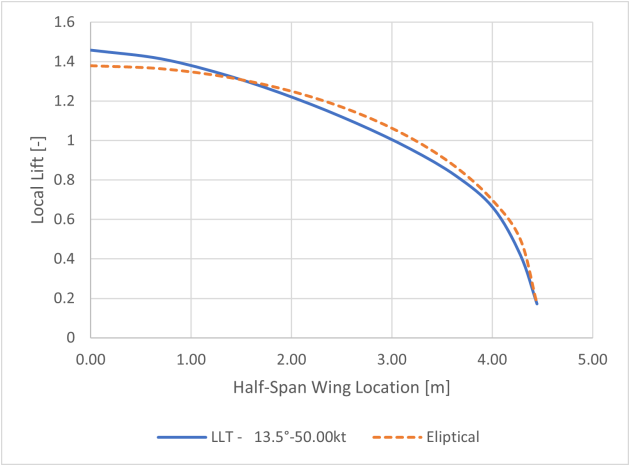

Figure 7.3: *XFLR5 half-span local lift distribution at* $\alpha = 13°$ *at* $50\,\mathrm{kts}$

In order to provide positive lift with the fuselage level, a small positive incidence angle of $0.75°$ is applied to the wing. This angle due to its magnitude still allows the similar performance of the wing while inverted.

Lastly, in order to improve the aerodynamic efficiency of the wing and thereby reduce the power required and thus the weight of the batteries, winglets are incorporated. The benefits of winglets on performance and handling qualities of general aviation aircraft were stated in a NASA report to be a $5.6\,\%$ increase in cruise speed at altitude and half power, in addition to a $6\,\%$ increase in the rate of climb [8]. This provides an increase in excess power, desirable for aerobatic manoeuvrability. Moreover, the stall speed is unchanged

and handling qualities, are reported, ”favourably affected” [8]. In designing the winglets, the airfoil section remains as the tip airfoil for ease of manufacturability. Furthermore, both outboard and inboard winglet twists were analysed in XFLR5, with $-3°$ outboard twist providing the greatest improvement in aerodynamic efficiency.

7.1.2. Airfoil Selection

Using statistical ranges for lift, drag coefficient and Oswald efficiency factor, the aerodynamic target parameters can be outlined, as seen in Table 7.2. Then adding relative-statistical finite wing correction of $15\,\%$ based on experience, the finite wing parameters were used to define the required airfoil lift coefficients.

Table 7.2
Aircraft aerodynamic target parameters

Flight configuration	C_{D_0} [-]	e [-]	$C_{L_{max}}$ [-]	C_L [-]	C_l [-]	C_D[-]
Clean (n = 1)	0.025	0.8	1.6	0.21	0.25	0.028
Clean (n = 3)	0.025	0.8	1.6	0.64	0.74	0.053
Clean (n = 6)	0.025	0.8	1.6	1.28	1.47	0.137
Clean (n = 8)	0.025	0.8	1.6	1.55	1.78	0.189
Take-Off (gear & flaps)	0.06	0.85	1.92	1.59	1.82	0.222
Landing (gear & flaps)	0.11	0.9	1.92	1.14	1.31	0.188

To begin selecting an airfoil to satisfy these target parameters, five typically used aerobatic airfoils were shortlisted and their performance analysed in XFLR5 for a Reynolds number of 7.7×10^6 at the operational speed and MAC, seen in Table 7.3. Notably, all aerobatic aircraft make use of symmetric airfoils for their symmetric aerodynamic properties in inverted flight. Using the same finite wing corrections mentioned above, the clean wing target $\mathrm{C_{L_{max}}}$ is 1.84. Comparing with the airfoils, it is apparent that only the NACA 0012, 0015 and the FX71-120 airfoils satisfy the target parameter. Additionally, as the ability to spin and snap roll better is generally desirable in an aerobatic aircraft, a variation in root and tip airfoils is used in order to promote the tendency to tip stall in clean configuration [1]. Therefore, for the ease of manufacturability as well as the wealth of aerodynamic test data, the NACA 0015 and 0012 were chosen as the root and tip airfoils respectively.

Table 7.3
Airfoil performance shortlist

Parameter		NACA 0012	NACA 0015	NACA 64-012A	FX71-120	Eppler 474	Eppler 472
Max. Thickness	[%]	12	15	12	12	14	12
Pos. Max. Thick.	[x/c]	0.3	0.3	0.4	0.25	0.22	0.18
Leading Edge Radius	[r/c]	0.016	0.025	0.008	0.024	0.013	0.014
Area	[m^2]	0.082	0.103	0.079	0.081	0.090	0.077
$C_{l_{max}}$	[-]	1.84	1.87	1.75	1.84	1.72	1.79
C_{d_0}	[-]	0.005	0.005	0.004	0.008	0.006	0.006

Validation
To validate the computed XFLR5 airfoil aerodynamic performance, wind tunnel data from Sandia National Laboratories at similar Reynolds numbers were used to compare [9]. With this, it became evident that the computed performance remained within $1\,\%$ of the wind tunnel data up to approximately $10°$ of the angle of attack.

7.1.3. Finite Wing Analysis

To verify the performance parameters of the wing, an XFLR5 analysis was performed using the previously defined planform and airfoil. This allowed a rapid initial confirmation of the wing’s performance with respect to the target parameters. Below are the drag polar in Figure 7.4, lift slope in Figure 7.5, aerodynamic efficiency in Figure 7.6 and moment coefficient slopes in Figure 7.7 computed using the non-linear Lifting Line Theory (LLT) method and Vortex Lattice Method (VLM) methods. In order to better estimate the effects of the thickness of the wing VLM was used at low angles of attack, up to approximately $5°$ angle of attack, while LLT with its non-linear method is used to provide a better estimate at higher angles of attack.

[1] URL: https://www.modelflying.co.uk/stall-school [Accessed 10 June 2022]

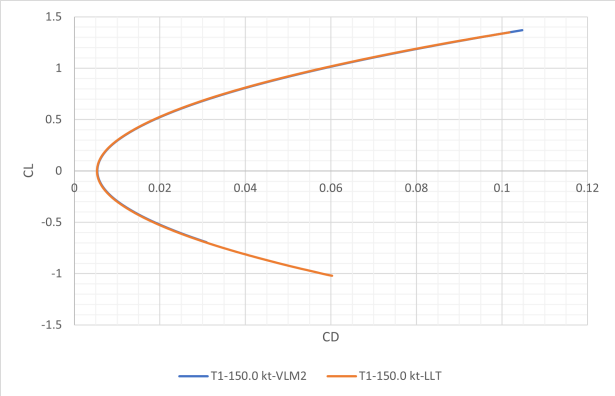

Figure 7.4: *Drag polar at* $150\,\mathrm{kts}$

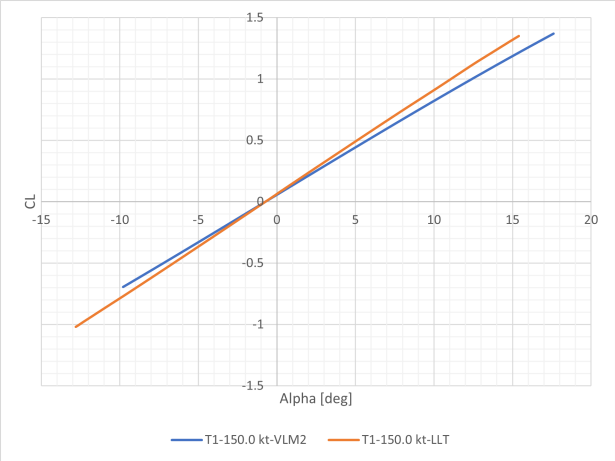

Figure 7.5: *Lift slope of the wing at* $150\,\mathrm{kts}$

From, the drag polar the zero-lift drag C_{D_0} of the wing was determined to be 0.005. Additionally, at C_L = 0.21 of clean configuration a drag coefficient of 0.008 is achieved. Furthermore, from the lift slope, the finite lift slope C_{L_α} was determined to be $4.85\ 1/\mathrm{rad}$ and the zero-lift angle of attack α_{0L} is $-0.7°$. Due to limitations of XFLR5, the non-linearity of the stall and near-stall conditions was not considered and hence analytical methods will be used to determine these parameters.

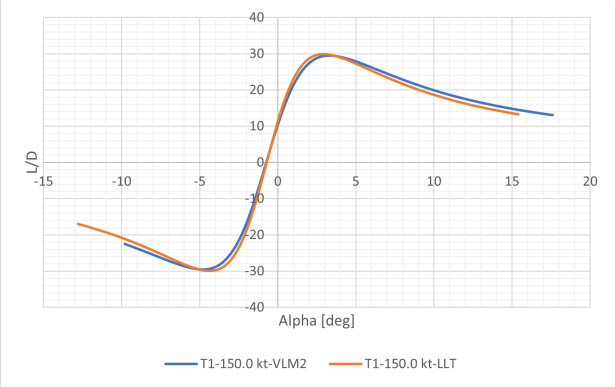

Figure 7.6: *Aerodynamic Efficiency of the wing at* $150\,\mathrm{kts}$

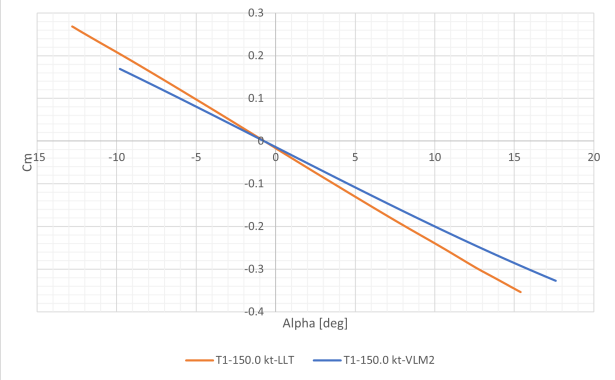

Figure 7.7: *Moment coefficient slope of the wing at* $150\,\mathrm{kts}$

Then from the aerodynamic efficiency curves, a maximum aerodynamic efficiency $(L/D)_{max}$ was determined to be 29.5. Additionally, the zero-lift moment coefficient C_{m0} was determined to be -0.001, and the moment coefficient slope C_{m_α} was found to be $-1.28\ 1/\mathrm{rad}$ at the wing leading edge.

Using the equation for $C_{l_{max}}$ of subsonic aircraft with a moderate sweep from Raymer, the stall lift coefficient of the wing can be estimated using Equation 7.1 from [10]. In consideration of reference subsonic aircraft, a quarter-chord sweep angle greater than $3.5°$ is generally considered moderate.

$$C_{L_{max}} = 0.9 C_{l_{max}} \cos \Lambda_{c/4} \tag{7.1}$$

Using, the infinite maximum lift-coefficient analysed for the NACA 0015 of 1.79 and the quarter-chord sweep of $\Lambda_{c/4}$ $-3.74°$, the finite maximum lift lift-coefficient of the wing is estimated at $C_{L_{max}}$ 1.61. This maximum lift coefficient is in line with the aerodynamic target parameters for the wing in clean configuration, validating the performance parameters of our main wing. Similarly, the stall angle of attack equation for high aspect ratio wings Equation 7.2 can be used from [10].

$$\alpha_{C_{L_{max}}} = \frac{C_{Lmax}}{C_{L_\alpha}} + \alpha_{0L} + \Delta\alpha_{C_{l_{max}}} \tag{7.2}$$

Using the data from Figure 7.5 a finite lift slope of C_{L_α} $0.0847\ 1/°$ and the zero-lift angle of attack is used.

The angle of attack maximum lift increment $\Delta\alpha_{C_{l_{max}}}$ is computed to be $2.4°$ from Raymer and is a function of leading edge sharpness factor and the leading edge sweep [10]. This then provides a finite stall angle of attack $\alpha_{C_{L_{max}}}$ of $20.6°$.

Limitations

It should be noted that the limitations of XFLR impact the results, namely, viscosity, modelling methods and wake [11]. Here, VLM methods interpolate 2D viscous drag estimation from local wing lift [11]. However, LLT non-linear methods utilise 2D viscous data obtained from airfoils. Consequently, the lift is a linear function of the angle of attack when using VLM panel methods. Hence, the potential flow model is valid only in conditions of limited flow separation [11]. This limits the analysis to high Reynolds numbers, low angles of attack and low flap deflections in order to obtain the most accurate results [11]. Furthermore, as panel methods interpolate 2D viscous drag from local wing lift, cross-flow effects are ignored and therefore these methods underestimate the total drag while over-estimating the glide ratio [11]. Additionally, the use of uniform vortex strength on each panel means that areas of sharp pressure gradients are not adequately modelled [11]. The best mitigation method is increasing panel density, particularly at discontinuities, changes, and edges.

Validation

In order to validate the accuracy of the computed results, they are compared with real-world aircraft data from [12]. According to Nicolai and Carichner, the "maximum L/D is a major design parameter" and is important to be checked [12]. This comparison relates the span and wetted area to the maximum aerodynamic efficiency. Assuming an initial fuselage width estimate of $1.6\,\mathrm{m}$, results in a wetted area S_{wet} of $18.6\,\mathrm{m}^2$. Thus, the span over square-root of wetted area is 2.0 resulting in a range of maximum aerodynamic efficiencies 25 to 32 and average of 29 using Figure 7.8. This is in line with the values computed for the wing planform with XFLR5.

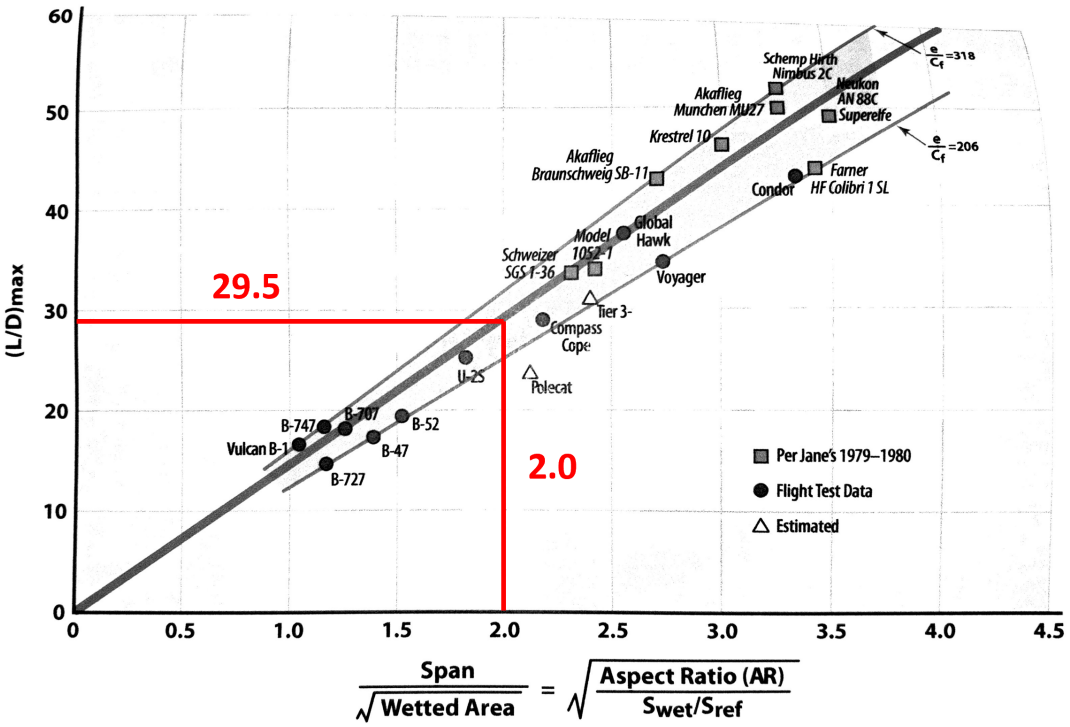

Figure 7.8: *Maximum aerodynamic efficiency check [12]*

For aerobatics a certain wing loading is achieved at the maximum maneuver load factor requiring then an aerobatic lift coefficient $C_{L_{ac}}$ outlined in Table 7.4, with '1' indicating a single occupant and '2' indicating both occupants. Here the operational speed of $150\,\mathrm{kts}$ is converted to $77\,\mathrm{m/s}$ and furthermore, the summarized parameters are compared with the widely known Extra 300 for validation [2].

[2]URI: https://www.extraaircraft.com/docs/service/POH%20EA%20300%20CUS%202006-09-20.pdf [Accessed 20 June 2022]

Table 7.4
Maneuver wing loadings and required C_L

Parameter		Electrobat (1)	Electrobat (2)	Extra 300 (1)	Extra 300 (2)
W/S	[N/m^2]	704	778	751	798
V	[m/s]	77	77	81	81
n_{max}	[-]	8	6	10	8
Wn_{max}/S	[N/m^2]	5636	4668	7514	6380
$C_{L_{ac}}$	[-]	1.545	1.285	1.857	1.577

7.1.4. High-Lift Devices Design

In order to achieve the required performance on the wing during take-off and landing phases, high lift devices must be incorporated into the wing design. Furthermore, due to weight and manufacturing considerations, the functions of the flaps and ailerons were combined to form flaperons [3].

To increase the efficiency of the design, the flaperons on the wing are split into an outboard and inboard set. During landing and take-off, the outboard flaperons would function mainly as ailerons but also as flaps, deflecting to $20°$, while the inboard flaperons act mainly as flaps and deflect $30°$. A single flaperon deflected to $30°$ generates a lift distribution which increases the wing loading, thereby posing a larger potential for tip stalls during critical phases of flight. However, during all other phases, the two flaperons sections will function as a single flaperon to provide greater controllability and manoeuvrability. Furthermore, in order to satisfy the target maximum lift coefficient parameter in take-off and landing configuration of 1.92, an additional body flap deflecting to $30°$ is positioned at the portion of the wing underneath the fuselage. Note this flap does not function as an aileron and is only used during take-off and landing. This concept is experimental and has to be verified during flight testing, as the fuselage wake behind the flap might become excessive. To size the flaperon sections, the equation for maximum lift coefficient increment with flaps from Raymer is used Equation 7.3 [10].

$$\Delta C_{Lmax} = 0.9 \Delta C_{lmax} \left(\frac{S_{flapped}}{S_{ref}} \right) \cos \Lambda_{HL} \tag{7.3}$$

ΔC_{lmax} in Equation 7.3 is obtained from the difference between the clean and flapped airfoils from the XFLR5 airfoil analysis. For the NACA 0015 with $30°$ flap deflection at $75\,\%$ hinge point, a ΔC_{lmax} of 0.41. For the NACA 0012 with $20°$ flap deflection at $75\,\%$ chord, a ΔC_{lmax} of 0.33 can be expected. With these, the flaperon sections are sized as seen in Figure 7.9 and described in Table 7.5. The first two sections closest to the wing provide the extra required C_l for landing, while the most outboard sections provide roll control during landing. The area of this section is assumed to be large enough to provide sufficient roll control, but will be checked in Chapter 10 to ensure that the aircraft is manoeuvrable during landing and take-off. This then results in a C_{D0} of 0.048 for the flapped wing at $50\,\mathrm{kts}$ using LLT. Additionally, at $C_{Lto} = 1.59$ and $C_{Llanding}$ = 1.14, a drag coefficient of 0.167 and 0.103 is achieved respectively.

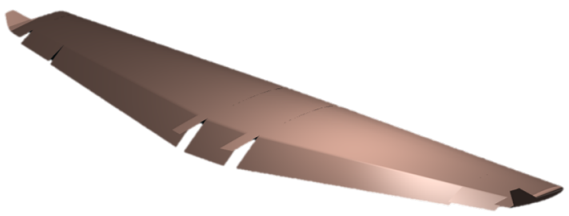

Figure 7.9: *Isometric view of the flaperons*

[3] URL: https://backcountrypilot.org/forum/conventional-flaps-vs-flaperons-6188 [Accessed 20 June 2022]

Table 7.5
Flaperon sections.

Parameter		Section 1	Section 2	Section 3
Half-span position	[m]	0-0.34	0.51-3.39	3.39-4.03
Flap chord	[m]	0.48	0.47-0.28	0.28-0.24
Deflection	[°]	30	30	20
Λ_{HL}	[°]	0	-11	-11

7.2. Landing Gear Design

In this section, the design of the landing gear is discussed. The section starts off with Subsection 7.2.1, elaborating on the methods used to size the landing gear. Afterwards, in Subsection 7.2.2, the general layout of the landing gear is elaborated upon, including all relevant parameters with their corresponding value.

7.2.1. Methodology

Landing gear design is based on the methods detailed by Roskam [1]. The essence of landing gear design is ensuring that the aircraft has enough clearance and that it is stable when on the ground. The first stability criterion is the longitudinal tip-over criteria for tricycle gears, as illustrated by Figure 7.10. The angle between the centre of the main landing gear and the centre of gravity must be greater than or equal to $15°$. The second criteria to satisfy is the longitudinal ground clearance criteria, shown in Figure 7.11. There must be a minimum of $15°$ between the bottom of the wheel of the main landing gear and the thickest part of the empennage section of the fuselage. This ensures that during take-off, the aircraft will not be scraping the runway.

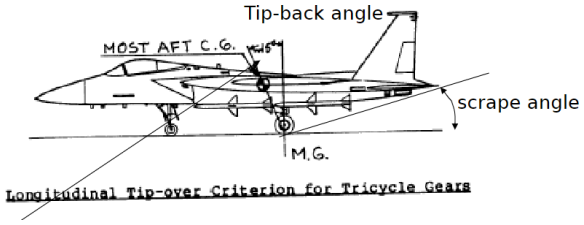

Figure 7.10: *Longitudinal tip-over criteria for tricycle landing gears [1]*

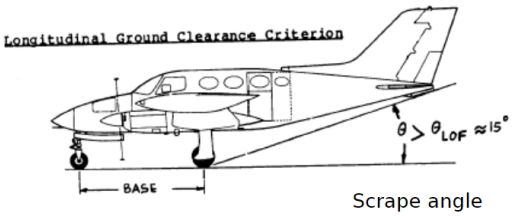

Figure 7.11: *Scrapeback criteria that the landing gear needs to satisfy [1]*

The last stability criterion to account for is the lateral tip-over, which is shown in Figure 7.12. This dictates that the overturn angle for the landing gear must be less than or equal to $15°$. Based on the geometry of the gear, one can design the landing gear such that Equation 7.4 is satisfied. The meanings of all the symbols in Equation 7.4 are detailed in Figure 7.13.

$$y_{MLG} > \frac{l_n + l_m}{\sqrt{\frac{l_n^2 \tan^2 \psi}{z^2} - 1}} \tag{7.4}$$

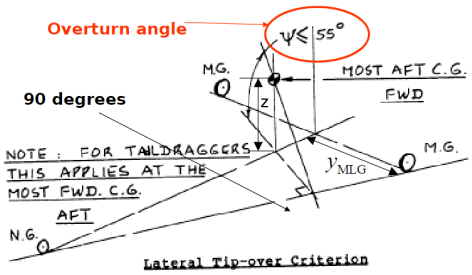

Figure 7.12: *Lateral tip over criteria for tricycle landing gears [1]*

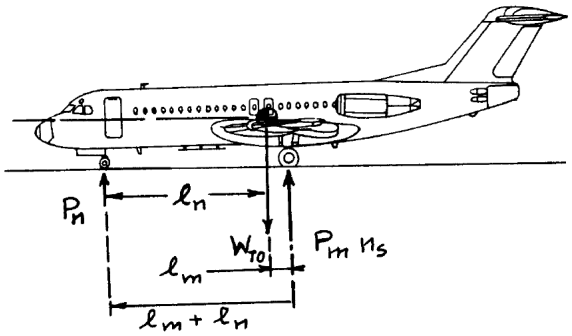

Figure 7.13: *Parameters used in Equation 7.4*

A structural consideration is that the nose gear must not experience excessive loading in order to function properly. It is suggested that the loading of the nose wheel must be between 8 and $16\,\%$ of the MTOM [1]. The loads on the landing gears can be calculated using Equation 7.5 and Equation 7.6, where P_n and P_m are the respective loadings on the nose and main wheel respectively and n_s is the number of struts on the main landing gear. Using these equations, the loads are calculated to be $113.5\,\mathrm{kg}$ and $426.3\,\mathrm{kg}$ for the nose and main gear, respectively. Note that the value given is only for a single main gear. This corresponds to a load fraction of $11.8\,\%$ for the nose gear, which is within the suggested bounds.

$$P_n = \frac{W_{TO} l_m}{l_m + l_n} \tag{7.5}$$

$$P_m = \frac{W_{TO} l_n}{n_s\,(l_m + l_n)} \tag{7.6}$$

Since it is expected that the aircraft will be operating out of grass airfields, the aircraft must have significant ground clearance. As such, reference aircraft with similar operating conditions were investigated to find initial estimates for the height of the landing gear. These include the Pilatus PC24 business jet and the Aero L39 Albatross [4] [5]. While the PC24 is a business jet, it is also designed to operate out of grass fields and is thus comparable in that regard to the Electrobat. The distances between the bottom of the fuselage for the PC24 and the L39 are $0.84\,\mathrm{m}$ and $0.93\,\mathrm{m}$ respectively, which will be used to determine the ground clearance required for the Electrobat.

The final consideration for the landing gear is the size of the wheels. The size of the wheels is dependent on the load exerted on each of the wheels, calculated in Equation 7.5 and Equation 7.6. The size is based on a statistical approach for similar aircraft. The main wheel's diameter (D) and width (w) in cm can be calculated with Equation 7.8 and Equation 7.7 respectively [10]. Resulting in a main wheel diameter of $46\,\mathrm{cm}$ and width of $20\,\mathrm{cm}$ for the Electrobat. The nose tire is assumed to be $70\,\%$ of the size of the main tire, resulting in a diameter of $32\,\mathrm{cm}$ and width of $14\,\mathrm{cm}$ [10]. From this estimation, a tyre is chosen out of The Aircraft Tire DataBook [6]. The tyres that are chosen are type III, which are common for general aviation aircraft [6]. This results in the main wheel size of $8.00-4$ and nose wheel size $5.00-4$. The diameters and widths are given in Table 7.6.

$$D = 5.1 Pm^{0.394} \tag{7.7}$$

$$w = 2.3 Pm^{0.312} \tag{7.8}$$

7.2.2. Landing Gear Layout

The first element of the landing gear that was decided was the height of the landing gear based on the two reference aircraft mentioned in Subsection 7.2.1. An initial value of $0.8\,\mathrm{m}$ for the gear height is used to ensure enough clearance while keeping the weight of the landing gear to a minimum. The nose wheel is positioned underneath the start of the cockpit, as this ensures loads of the gear would be distributed into the cockpit wall. The load-carrying elements of the cockpit and the nose gear are therefore merged into a single load, reducing complexity and weight.

[4] URL: https://skybrary.aero/aircraft/pc24 [Accessed 10 June 2022]
[5] URL: https://skybrary.aero/aircraft/l39 [Accessed 10 June 2022]
[6] URL: https://www.goodyearaviation.com/resources/pdf/Aviation-Databook-2022.pdf [Accessed 20 June 2022]

The position of the main landing gear is heavily dictated by the stability criteria discussed in Subsection 7.2.1. Firstly, the longitudinal tip-over criterion is satisfied by using the CG range from the weight estimations and creating a list of all possible longitudinal positions for the wheel. Based on this, and the height of the aircraft, the longitudinal ground clearance criterion is satisfied as well. With all the lengths detailed in Figure 7.13 known, the horizontal distance between the main gears is determined by Equation 7.4. All the values stated have been iterated multiple times due to the design of the fuselage changing throughout the design process. The final values for the undercarriage are visualized in Figure 7.14 and given in Table 7.6.

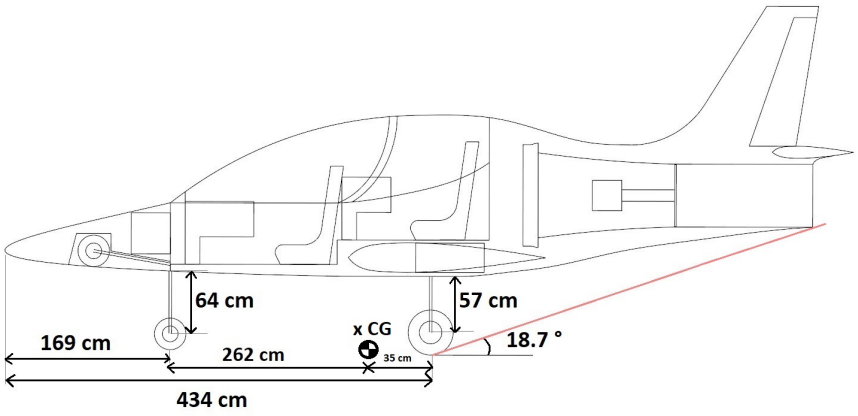

Figure 7.14: *Landing gear size and position*

Table 7.6
Tables showing the values of the main parameters of the undercarriage

(a) *Size specification of the landing gear*

Parameter		Value
Height of main struts	[mm]	571
Height of nose gear strut	[mm]	640
L_m	[mm]	348
L_n	[mm]	2620
D_{nose}	[cm]	33
w_{nose}	[cm]	12
D_{main}	[cm]	45
w_{main}	[cm]	20

(b) *Fuselage parameters with corresponding values*

Parameter		Value
X-Position of main gear	[m]	4.34
X-Position of nose gear	[m]	1.69
y_{MLG}	[m]	1.09
Scrape angle	[°]	18.7
Nose loading	[%]	11.7
P_m	[kg]	426.3
P_n	[kg]	113.5

As can be seen in Table 7.6, the scrape angle is greater than the required $15°$ but it is still lower than the maximum angle of attack during landing. This could be remedied by either moving the main gear more aft or by increasing the length of the landing gear. Moving the gear more aft has adverse effects on the ground stability as well as producing issues with the packaging. Moving the gear backwards would mean that the landing gear would no longer be in the wing and would need to fit into the fuselage which interferes with the position of the duct.

Increasing the landing gear length also has similar effects i.e. the nose gear would no longer fit inside the nose and the main gear would no longer fit inside the wing. Furthermore, to aid in the packaging, the y_{MLG} would need to increase which would mean adding more stiffeners away from the root.
Therefore, the best option is to add a skid plate to the bottom of the fuselage near the tail. This means that in case of a tail strike, the bottom of the fuselage can be protected. This option does not adversely affect stability and has minimal effect on weight since the plate can be quite thin and can be replaced when it gets damaged [7]

[7] URL: https://www.boeing.com/commercial/aeromagazine/articles/qtr_1_07/article_02_1.html [Accessed 20 June 2022]

7.3. Fuselage and Empennage Design

This section describes the design of the fuselage. It starts off with the 2D and 3D views of the aircraft in Subsection 7.3.1 and Subsection 7.3.2 respectively. Thereafter, the method and internal configurations are discussed in Subsection 7.3.3 and Subsection 7.3.4. The section ends with the empennage placing in Subsection 7.3.5 and drag estimates for the canopy and landing gear in Subsection 7.3.6 and Equation 7.10.

7.3.1. 2D views

The figures below show the side-view, top-view and front-view of the aircraft respectively in Figure 7.15, Figure 7.16 and Figure 7.17. Some important subsystems such as the batteries, landing gear and duct design are highlighted to show the positions more clearly.

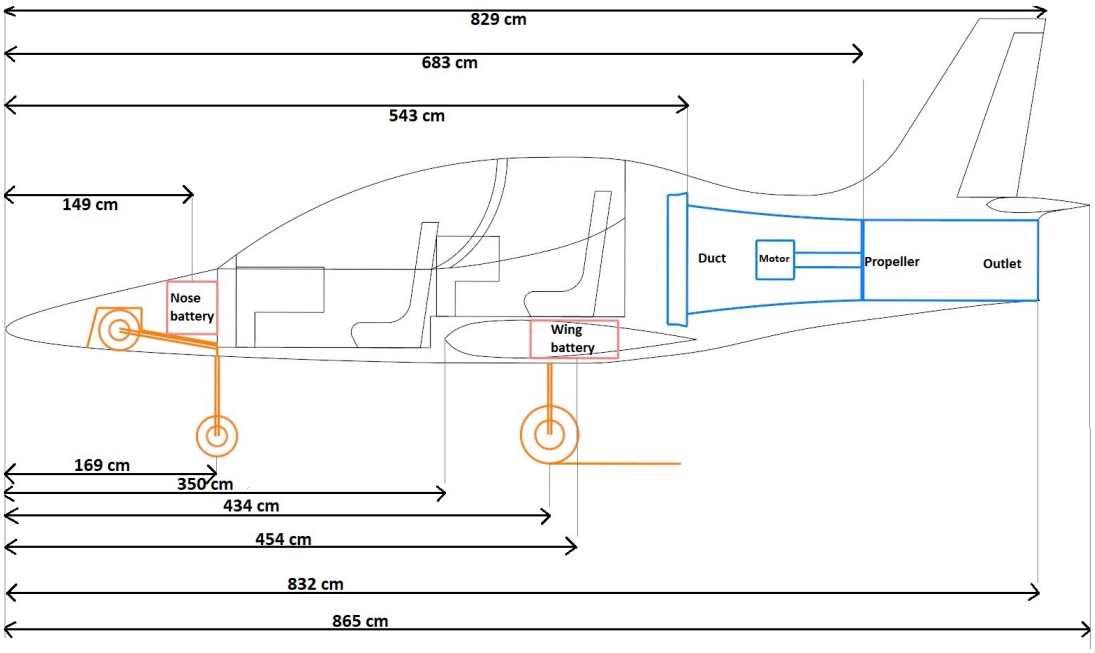

Figure 7.15: *Side-view of the design of the Electrobat*

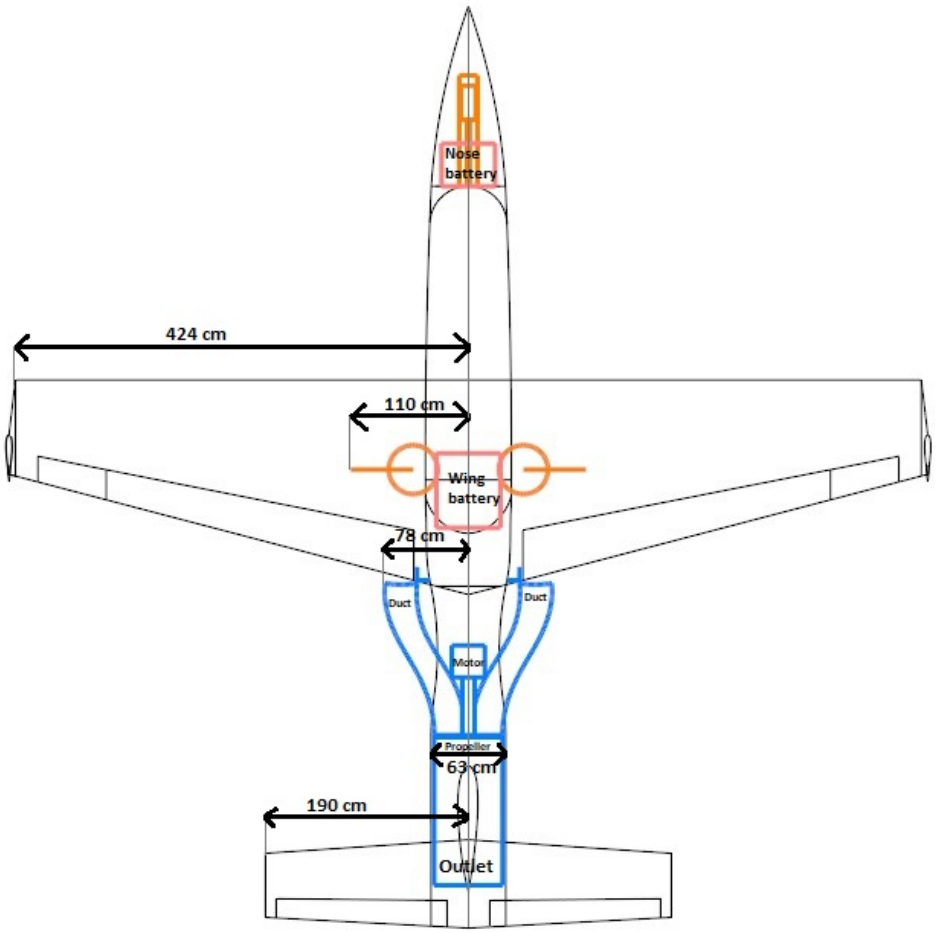

Figure 7.16: *Top-view of the design of the Electrobat*

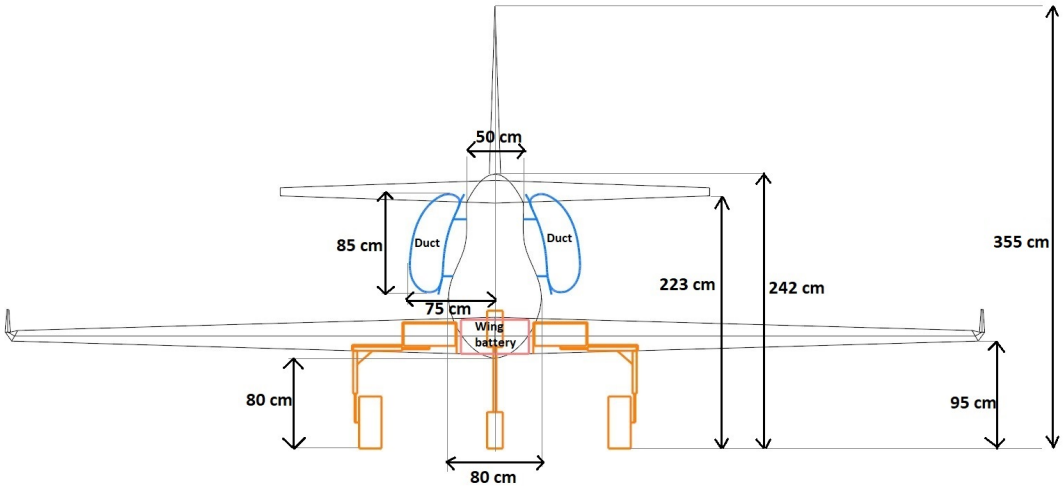

Figure 7.17: *Front-view of the design of the Electrobat*

7.3.2. 3D Model

The 2D views of the aircraft were used to construct a 3D model of the aircraft, which are shown in this subsection. The front, side, top and landing view can be seen in Figure 7.18a, Figure 7.18b, Figure 7.18c and Figure 7.18d respectively.

(a) *Front view of the Electrobat*

(b) *Side view of the Electrobat*

(c) *Top view of the Electrobat*

(d) *Landing configuration of the Electrobat*

Figure 7.18: *Front (a), side (b), top (c) and landing (d) view of the electrobat*

7.3.3. Methodology

During the design of each type of aircraft, there is a common and important parameter: keeping the weight as low as possible in order to minimize the cost. This is why packaging the entire aircraft tightly and efficiently while ignoring certain commercial aspects like comfort is paramount. The conventional design methods, as described in Roskam, had to be adapted to realise such a design. These adapted equations were used to size the cockpit [1]. From the requirements, it is known that the aircraft needs to seat two pilots and that the pilots have certain viewing angle requirements. The specific viewing angle requirements used for the sizing of the cockpit are stated below:

- EFLY-STK-CPIT-02-2-1: The pilot shall have a total vertical field of view of 135 deg;
- EFLY-STK-CPIT-02-2-2: The pilot shall have an over the nose vertical field of view of 15 deg;
- EFLY-STK-CPIT-02-2-3: The pilot shall have a rearward vertical view of 30 deg;
- EFLY-STK-CPIT-02-2-4: The pilot shall have an over the side vertical view of 40 deg.

Note, here the Electrobat is assumed to be flown with a centre stick instead of a side stick. This is because it is easier and more ergonomic to perform manoeuvres with a central stick than with a side stick [8]

The first step is to determine the initial dimensions and relative distances between the components within the cockpit. These dimensions are related to for example the seats, clearances and position of the instruments. These dimensions were obtained from literature and result in the illustrated cockpit design as can be seen in Figure 7.19 [1, 13].

Figure 7.19: *Side and front view of the cockpit and fuselage of the Electrobat*

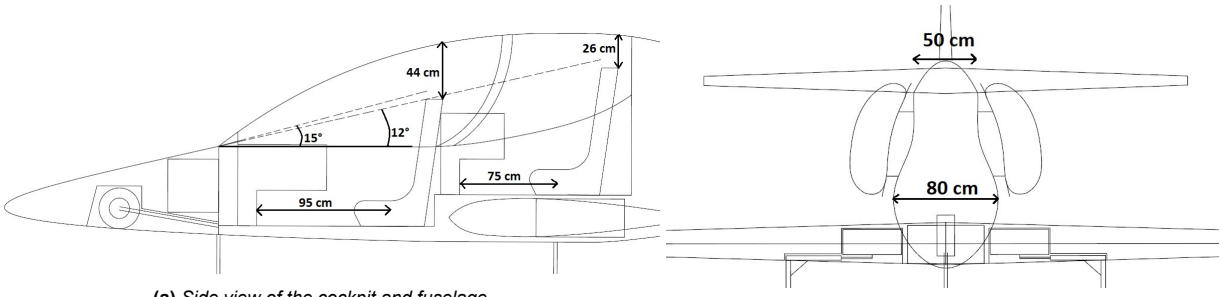

(a) *Side view of the cockpit and fuselage*

(b) *Front view of the cockpit and fuselage*

The clearance between the seat and the canopy is for each pilot a minimum of $25\,\mathrm{cm}$ and the leg room is at least $75\,\mathrm{cm}$. In addition, as can be seen from Figure 7.19a, the pilot in the front seat has an over-the-nose vertical view of $15\,\mathrm{deg}$. For the pilot in the back, the over-the-nose vertical view is $12\,\mathrm{deg}$. The canopy of the cockpit extends all the way around the cockpit, with only the canopy bow potentially blocking the view. The over-the-side viewing angles will remain equal around the cockpit, and thus the rearward vertical view requirement is met as well. The canopy bow is located right behind the first pilot, such that it does not hinder the view of any of the two pilots.

The next step is to obtain the length of the fuselage. This is done by using statistical relations between the diameter of the fuselage and the length. For military trainer aircraft, which this aircraft can be compared to, the ratio of the diameter of the fuselage and its length is usually between 5.4 and 7.5 [1]. Since this aircraft needs more space compared to conventional aircraft to package all the components, a ratio value of 7.5 has been selected and a diameter of $80\,\mathrm{cm}$ is used for the entire fuselage. This gives an initial fuselage length of $600\,\mathrm{cm}$. During later iteration stages, it became apparent additional space is required to fit all the components. The final fuselage length after iteration was determined to be $8.23\,\mathrm{m}$ which was mostly due to a longer required duct and an extended nose to include the nose wheel and batteries.

7.3.4. Internal Configuration

With the fuselage size determined, the components can be positioned inside the fuselage. The major components are the landing gear, batteries and the motors and fan. These components will be discussed in this

[8] URL: https://www.smithsonianmag.com/air-space-magazine/outrageous-adolescence-f-16-180949491/ [Accessed 19 June 2022]

section.

Landing gear The nose gear will retract into a compartment in the nose cone, below the batteries. The main landing gear will retract into a compartment, which is partly in the wing and fuselage. A margin is taken into account between the landing gear and the compartment. This margin was chosen to be $5\,\%$ of the width of the landing gear, which is a reasonable spacing according to literature [12]. The extended and retracted position of the landing gear can be seen in Figure 7.20 below.

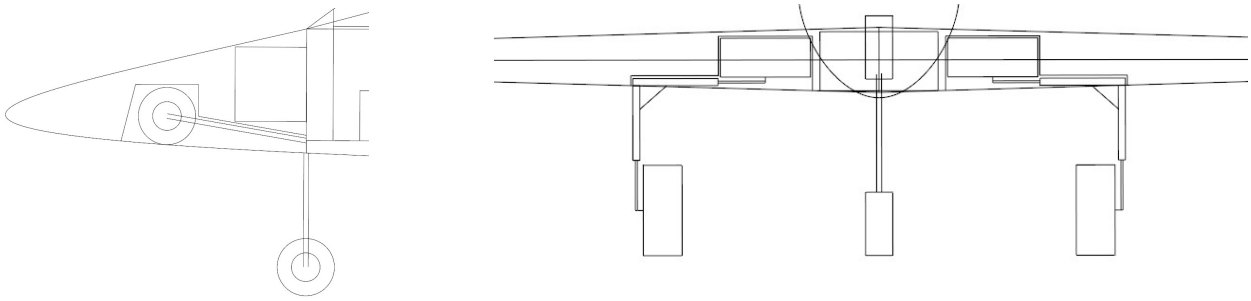

(a) *Side view of nose landing gear storage*

(b) *Front view of nose and main landing gear storage*

Figure 7.20: *Landing gear storage configuration*

Batteries For the purpose of weight distribution and safety, the batteries are split up into two different blocks. This provides redundancy in case one block fails and is therefore considered safer. For optimal mass distribution, $40\,\%$ of the batteries are located in the nose and $60\,\%$ in the root of the wing. The cockpit is shielded from fire by the means of a firewall. These walls are placed between the battery compartments and the cockpit to protect the passengers in case a battery pack catches fire.

The battery characteristics are discussed in detail in Section 8.3. Following this, each battery module weighs $27.7\,\mathrm{kg}$ and its dimensions are $0.864\,\mathrm{m}$ by $0.303\,\mathrm{m}$ by $0.08\,\mathrm{m}$ [9]. This results in the aircraft needing 10 batteries and a total battery volume of $0.21\,\mathrm{m}^3$. In order to place the batteries, $0.084\,\mathrm{m}^3$ of space in the nose and $0.13\,\mathrm{m}^3$ of space in the wing root is required. The wing root batteries are placed as a cuboid module of dimensions $0.698\,\mathrm{m}$x$0.600\,\mathrm{m}$x$0.300\,\mathrm{m}$. In the nose, a similar cuboid configuration is used with dimensions of $0.418\,\mathrm{m}$ by $0.400\,\mathrm{m}$ by $0.501\,\mathrm{m}$. The positions of the batteries are shown in Figure 7.16.

Fan and Motor The fan is placed inside the duct and as low as possible. This is done to keep the thrust in line with the vertical position of the centre of gravity. Since most of the heavier structures, like the wings and batteries, are placed lower in the fuselage, the centre of gravity will likewise be lower. The duct itself has been lowered until it lies just above the wing. The motor is connected to a driveshaft and placed in line with the fan. This can be seen best in the side and top-view as shown in Figure 7.15 and Figure 7.16 respectively.

7.3.5. Empennage Placing and Drag

The desired positioning of the empennage is as far aft as possible for stability and control to have a large moment arm. This could result in lower tail areas, leading to a lower structural mass. There are however several other criteria to keep in mind when placing the empennage, which is explained in the next paragraphs.

Firstly, the vertical location of the horizontal tail is considered. For the vertical position of the horizontal wing, the position of the main wing relative to the horizontal stabilizer is of importance due to the wake generated by the main wing. To reduce the area of the horizontal tail that is blanked when the wing has stalled, the horizontal tail is placed outside a specified region. This region lies between the $60°$ vertex of the leading edge and the $30°$ vertex of the trailing edge. The position of this region and the horizontal tail can be seen in Figure 7.21a.

The vertical tail size and positioning are largely determined by the spin recovery requirement. In a spin, the aircraft is spinning around the vertical axis and to stop this spin, a sufficient rudder input is required. The wake of the horizontal tail during a spin blanks the vertical tail and thereby reduces the ability to recover from a spin. This effect must be minimised to have sufficient lateral control in order to escape the spin [12]. The analysis is performed graphically, drawing a line of $60°$ from the leading edge of the horizontal tail and a line

[9] URL: https://eleo.tech/solutions/battery-modules/size-35 [Accessed 10 June 2022]

of $30°$ from the trailing edge [12]. It is desired that not more than $\frac{1}{3}$ of the area of the vertical tail falls within that region. As can be seen in Figure 7.21b, less than $\frac{1}{3}$ of the vertical tail area is placed inside that region.

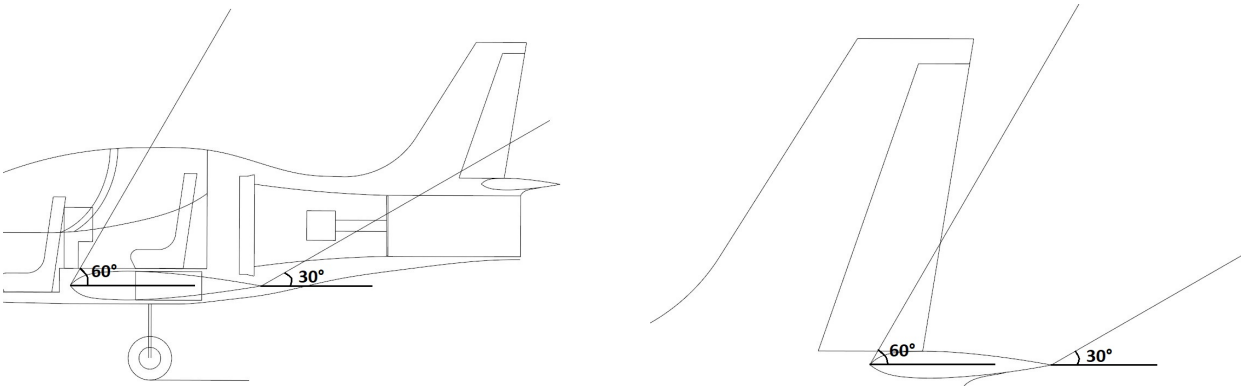

(a) *Wake of main wing affecting the horizontal tail* **(b)** *Wake of horizontal tail affecting the vertical tail*

Figure 7.21: *Vertical position of empennage*

The drag of the empennage is determined by extracting C_{D_0} from the drag polars. These values are corrected with $\frac{S_h}{S_w}$ and $\frac{S_v}{S_w}$ for the horizontal and vertical tail. This is required to sum the values with the other drag components of the aircraft. C_{D_h} is equal to 0.0022 and C_{D_v} is 0.0005. These two values summed represent the empennage drag, which is thus 0.0027. It should be noticed that the drag of the horizontal tail is significantly higher compared to the vertical tail, due to the $-4°$ incidence angle.

7.3.6. Fuselage Drag

The design of an aerobatic aircraft requires the use of a canopy in order to increase the field-of-view. A method based on experimental data is used to estimate the drag due to the canopy [1]. The drag is a function of the Mach number and is estimated during level flight and at operational speed. The drag naturally depends on the aerodynamic design of the canopy. Figure 7.22a provides typical shapes of the canopy, of which the shape with identifier C_2 is the approximated shape for the canopy of the Electrobat. The canopy drag formula is presented in Equation 7.9, where $\Delta C_{D_{canopy}}$ is the total canopy drag, ΔC_{D_s} the drag coefficient dependent on Mach number, A_{max} the frontal area of canopy and S_w the wing area [6].

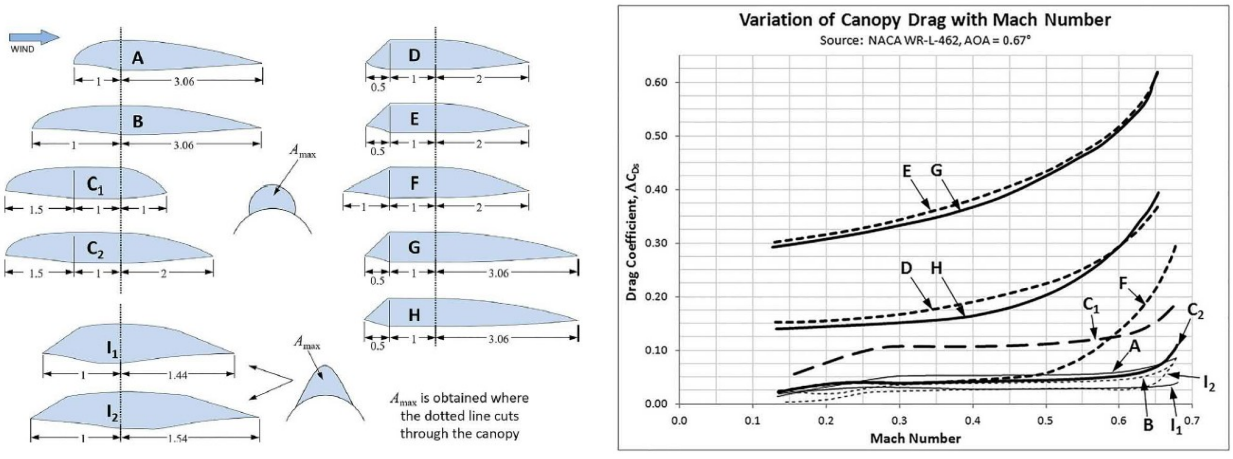

(a) *Typical canopy types* **(b)** ΔC_{D_s} *values for a given mach number*

Figure 7.22: *Canopy types and Conapy drag [6]*

$$\Delta C_{D_{canopy}} = \Delta C_{D_s} \frac{A_{max}}{S_w} \tag{7.9}$$

Using Figure 7.22b, the value for ΔC_{D_s} can be retrieved. The parameters with their corresponding values and the total canopy drag $\Delta C_{D_{canopy}}$ are given in Table 7.7. The drag for the remainder of the fuselage has been approximated with an empirical estimation from [14]. This resulted in value for $C_{D_{fus}}$ of 0.0156.

Table 7.7
Parameters and corresponding values canopy drag

Parameter		Value
ΔC_{D_s}	[-]	0.045
A_{max}	[m^2]	0.463
$C_{D_{canopy}}$	[-]	0.0017

7.3.7. Landing Gear Drag

The drag of the landing gear is estimated using Roskam's method and depends on the lift generated by the wing [1]. More lift results in a higher pressure on the bottom of the wing and thereby a reduced airflow, where the main landing gear is positioned. The drag of the main landing gear thus decreases with increasing lift [1]. According to Roskam, the drag for 'i' landing gears can be estimated with Equation 7.10 below.

$$C_{D_{gear}} = \sum_i \left[\left(C_{D_{gear_{CL=0}}} + p_i C_{L_{land}} \right) \left(\frac{S_{gear_i}}{S_w} \right) \right] \tag{7.10}$$

where $C_{D_{gear_{CL=0}}}$ is the zero-lift drag coefficient, p_i a factor accounting for the reduced drag due to lift, $C_{L_{land}}$ the landing lift coefficient, S_{gear_i} the landing gear surface area and S_w the wing surface area.

Starting off with the main landing gear, $C_{D_{gear_{CL=0}}}$ can be determined from Figure 7.23a and p_i from Figure 7.23b. $C_{L_{land}}$ can be retrieved from Subsection 7.1.2.

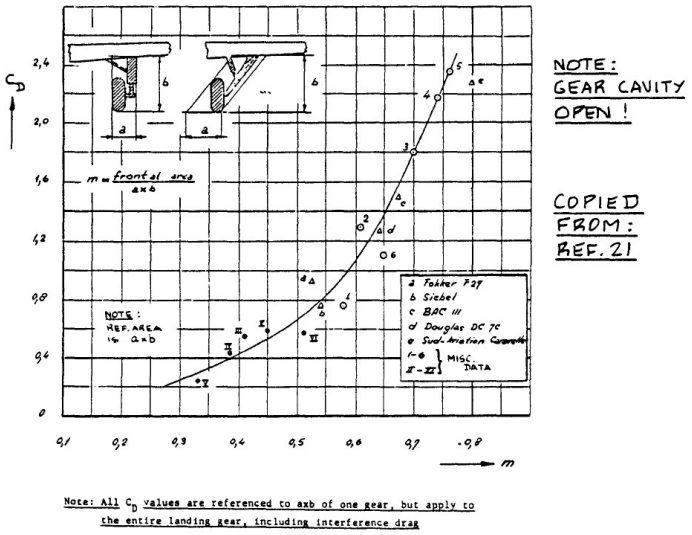

(a) *Zero-lift drag coefficient for a retractable main gear*

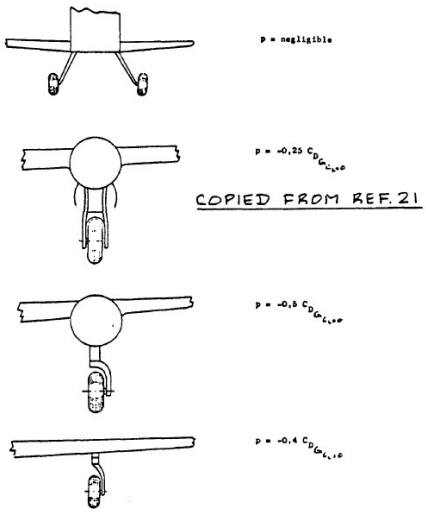

(b) *P-values for different landing gear configurations*

Figure 7.23: *Figures used to determine main landing gear drag [1]*

It should be noted that, when calculating the zero-lift drag coefficient in Figure 7.23a, the gear cavity is assumed to be open. The landing gear configuration, in order to determine the p-value, can be approximated to be the bottom configuration in Figure 7.23b. Finally, S_{gear} can be calculated by multiplying the width of the wheels with the diameter given in Subsection 7.2.1.

Secondly, the nose gear drag is estimated. In order to calculate the zero-lift drag coefficient of the nose landing gear, the distance from the nose to the landing gear, the diameter of the wheel and the length of the strut are required. The ratio of these two values is used to estimate the zero-lift drag from Figure 7.24. The two values can be found in Subsection 7.2.1.

It should be noted that this method assumes the nose gear cavity to be *closed*, contrary to the main landing gear. For this design, the nose gear cavity during landing is opened, resulting in slight inaccuracies using this method. Finally, the value of p for the nose landing gear is naturally 0, since no pressure difference of the wing, is experienced by this wheel. All values obtained are indicated in Table 7.8. Applying Equation 7.10 gives a $C_{D_{gear}}$ of 0.0039

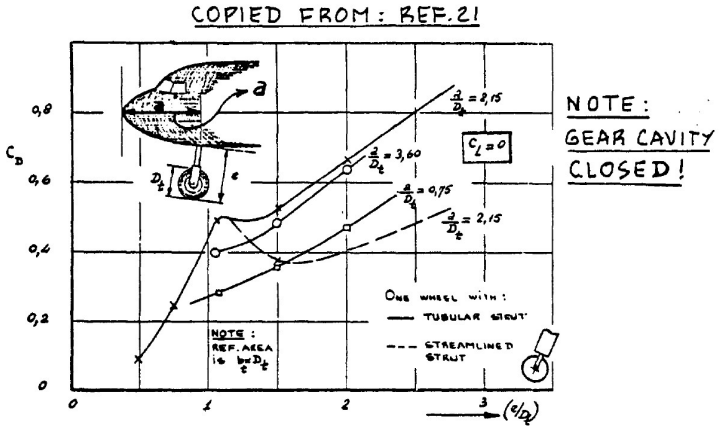

Figure 7.24: *Zero-lift drag coefficient of nose gear [1]*

Table 7.8
Landing gear drag components

Parameter		Value
$C_{D_{gear_{CL=0_{main}}}}$	[-]	0.65
$C_{D_{gear_{CL=0_{nose}}}}$	[-]	0.78
p_{main}	[-]	-0.26
p_{nose}	[-]	0
$S_{gear_{main}}$	$[m^2]$	0.0904
$S_{gear_{nose}}$	$[m^2]$	0.0443

7.4. Drag Analysis

To allow sizing of other systems, such as the required thrust, the performance of the aircraft is analysed and the drag is estimated using the wing drag curve and empirical estimations for the fuselage, as described in Subsection B.1.5. These follow from a combination of the target parameters and obtained values. As a result, the aircraft drag is estimated at both sea-level and $6{,}000\,\text{ft}$ as described in Table 7.9a.

The drag breakdown of aircraft subsystems is presented in Table 7.9b. Notably, the drag coefficient sum in clean configuration does not include the contribution of the landing gear while the take-off and landing configurations do. Comparing these drag build-ups with the target parameters in Table 7.2, the clean drag meets the target parameter with $0\,\%$ difference. Moreover, the take-off and landing parameters improve on the target drag parameters with $14\,\%$ and $32\,\%$ difference respectively. This shows that the computed drag of the aircraft is less than originally estimated for take-off and landing configuration.

Table 7.9
Drag analysis

(a) *Drag analysis of flight phases*

Flight Phase	D_{SL} [N]	D_{6000} [N]
Stall	1,671	1,642
Clean (n = 1)	1,266	1,244
Clean (n = 3)	2,386	2,345
Clean (n = 6)	6,168	6,062
Clean (n = 8)	8,497	8,351
Take-off	1,344	1,321
Landing	1,593	1,566

(b) *Drag breakdown of the aircraft subsystems*

Parameter	Value
$C_{D_{wing}}$ (clean / take-off / landing)	0.008 / 0.167 / 0.103
$C_{D_{gear}}$	0.0039
$C_{D_{fus}}$	0.0156
$C_{D_{canopy}}$	0.0017
$C_{D_{empennage}}$	0.0027
$C_{D_{total}}$	0.028 / 0.191 / 0.127

8

Propulsion and Power

In order to propel the aerobatic aircraft, a powerful motor is required to generate sufficient thrust during flight. The thrust is generated by a ducted fan. The required mass flow to generate the thrust will enter via the inlets and through the duct to the fan. Rechargeable batteries will be used to power the motor in the aircraft. These high performance batteries should provide enough continuous power to the motor during the flight. First, the sizing of the fan and the motor selection is discussed in Section 8.1. Then, the design for the inlet and duct will be determined in Section 8.2. To end this chapter, the verification of the python code will be discussed in Section 8.3.

8.1. Propulsion Characteristics

The extreme concept has the ducted fan as a characteristic feature of the aircraft. A ducted fan is essentially a shrouded propeller. This shroud prevents the formation of vortices around the tips of the propeller blade. The absence of vortices will mean that the ducted fan is more energy efficient than a conventional propeller. A second benefit of the ducted fan is that the noise generated is significantly reduced as the shroud shields the generated noise.

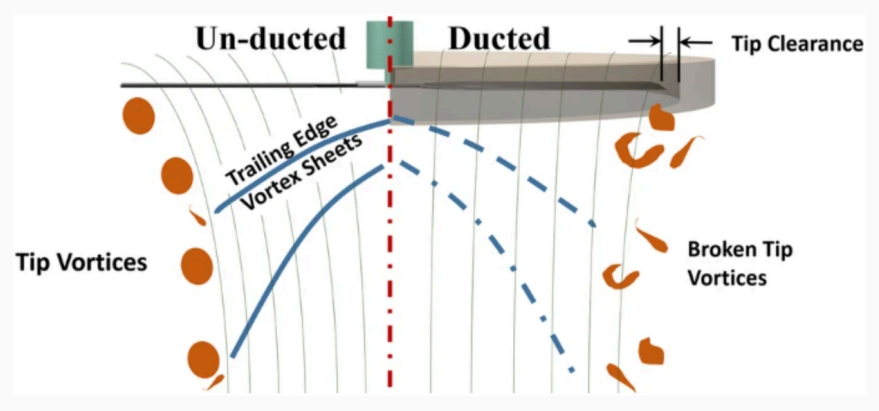

Figure 8.1: *Tip vortices generated by an open propeller vs. a ducted fan/propeller [15]*

This is contrasted by the high complexity of designing and implementing the ducted fan system. Furthermore, it also takes up more space in the fuselage compared to a conventional propeller and electric motor combination.

First the initial sizing is discussed in Subsection 8.1.1, then the general information about the propulsion system is discussed in Subsection 8.1.2. To close this section, the inlet and duct sizing is discussed in Subsection 8.1.3.

8.1.1. Fan and Engine Sizing

The main components of the propulsion system consist of the engine and the ducted fan. The thrust requirements for the different flight configurations are based on the drag obtained in the constraint analysis. The thrust is in all configurations set equal to the drag as for steady conditions are assumed. Furthermore, the design should also satisfy the power required from the constraint analysis.

The general equation for thrust and torque generated by the fan are given in Equation 8.1 and Equation 8.2, respectively. In these equations the thrust constant, k_t, and torque constant, k_q, are obtained from the UL-39[16]. The UL-39 is an ultra light, full composite ducted fan aircraft with similar performance characteristics

as the Electrobat. Furthermore, these two equations are also dependent on the rotational rate (revolutions per second), n, and the diameter of the fan, D_R.

$$T = k_t \rho n^2 D_R^4 \tag{8.1}$$

$$Q = k_q \rho n^2 D_R^5 \tag{8.2}$$

It then must be determined for which fan diameter in combination with a specific RPM, the thrust is sufficient to satisfy the required thrust for the different flight configurations. The results of this are presented in Table 8.1[6].

There are several thrust requirements and for each requirement the diameter of the fan should be the same, but the RPM will differ. A Python program is constructed which evaluated all of the combinations of RPM for the different configurations for a specific diameter [1]. The duct expansion ratio, ε_d, should be incorporated as well and therefore all these combinations are considered for varying ε_d in the range of 0.8 till 1.2.

Then the found combinations of parameters should be evaluated and be subjected to another requirement from the constraint analysis: the maximum power required. The maximum power required of the propeller to satisfy a specific thrust, T, velocity, V_∞, propeller area, A_R, and duct expansion ratio, ε_d, is calculated according to Equation 8.3[6].

$$P_{REQ} = \frac{3}{4} T V_\infty + \sqrt{\frac{T^2 V_\infty^2}{4^2} + \frac{T^3}{4 \rho A_R \varepsilon_d}} \tag{8.3}$$

After obtaining the required power for the propeller to operate appropriately, the engine power can be determined by using Equation 8.4, in which η_f and η_e are the fan and engine efficiency, respectively[6].

$$P_{ENG} = \frac{P_{REQ}}{\eta_f \eta_e} \tag{8.4}$$

The final and most important characteristics of the propeller and engine are given in Table 8.2 and a more elaborate overview of all the parameters for the different flight configurations is given in Table 8.3. It should, however, be noted that the clean configuration is the configuration in which a 2.5g sustained turn is taken as the thrust setting.

Table 8.1
Propulsion requirements based on the constraint analysis

Constraint		value
Power required	[kW]	260
Thrust clean (2.5G) 0 ft	[N]	2001
Thrust clean (2.5G) 6000 ft	[N]	1967
Thrust take-off 0 ft	[N]	1344
Thrust take-off 6000 ft	[N]	1321
Thrust landing 0 ft	[N]	1593
Thrust landing 6000 ft	[N]	1566

Table 8.2
Propulsion characteristics

Parameter		Value
Diameter	[m]	0.63
Area	[m^2]	0.31
ε_d	[-]	1.00
Max RPM	[2π/min]	7600
Min RPM	[2π/min]	5000
Max Power propeller	[kW]	216
Max power engine	[kW]	257
η_f	[-]	0.885
η_e	[-]	0.95

Table 8.3
Parameters of the propeller for different flight conditions

		CL 0 ft	CL 6000 ft	TO 0 ft	TO 6000 ft	LA 0 ft	LA 6000 ft
RPM	[2π/min]	6100	6600	5000	5400	5400	5900
Power	[kW]	204.7	205.8	72.19	129.2	154.5	99.21
Thrust	[N]	2061	2017	1385	1350	1615	1611
Torque	[Nm]	139.6	136.6	93.8	91.47	109.4	109.2

[1] URL: https://github.com/Niels-Prins/dseEflyer [Accessed 20 June 2022]

As mentioned before, the required thrust value that are tabulated in Table 8.1 are based of steady flight conditions, where no accelerations are taking place. In reality, energy is traded during flight operations, such as when landing or taking-off. This is the reason why, in Table 8.1, the apparent thrust required for take-off seems to be lower than the thrust when landing. In real life, take-off always requires more thrust, often times the maximum thrust the propulsion unit is capable of. When landing, it is often times simply trading off potential energy (loosing altitude) to gain kinetic energy to retain sufficient airspeed without requiring additional thrust.

8.1.2. General information of the propulsion system

As said in Subsection 8.1.1, the UL-39 propeller will be adapted for use in this aircraft. The UL-39 has a combination of a propeller and a stator in order to direct the flow out of the engine, so the drag in the duct is lowered. The design of the propeller and stator can be seen in Figure 8.2. The propeller and rotor have 13 and 14 blades respectively. Each rotor blade weighs $113\,\mathrm{g}$ and can withstand $23\,\mathrm{kN}$ of centrifugal force [17]. The airfoil that is used for the rotor and stator is the NACA 65 A 010 [18].

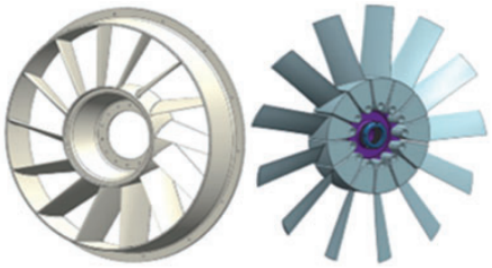

Figure 8.2: *The stator and rotor of the UL-39 [17]*

The Electrobat will have a fan in between two stators. The first stator will correct the flow from the inlets. This will allow the fan to receive clean airflow, which will increase the efficiency and the thrust generated. The stator behind the fan will also correct the flow towards the outlet of the duct. The total efficiency of the ducted fan will increase if the flow is redirected towards the duct in a clean manner.

Now that the propeller dimensions and characteristics are known, an engine can be chosen that will be sufficient for the design. The electric motor company that will suit the design best is called Saluqi motors [2]. This company is founded in 2016 and focuses on high performance, compact and light electric motors. There are 4 motors currently on the market and are outlined in Table 8.4. The max power is determined at 5000 RPM. Furthermore, the value for continuous power in Table 8.4 for the P50T4 HV, P100T4 and P150T4 motors is generated at 3500 RPM at 400 volts. For the P200T6 it is generated at 2000 RPM at 400 volts. These continuous power values are just specific points in the power curve to give an example of what the motor can deliver. In reality, the power of the motor is a function of voltage and will increase as the RPM increases. This will be discussed after this table.

Table 8.4
Available Saluqi motors and data [2]

Parameter		P50T4 HV	P100T4	P150T4	P200T6
Operating voltage	[V]	100-500	100-500	100-500	100-500
Max power (3 min)	[kW]	60	130	190	260
Continuous power	[kW]	40	80	120	125
Weight	[kg]	18	27	34	33
Max power density	[kW/kg]	3.3	4.8	5.6	7.8
Efficiency	[%]	>95	>95	>95	>95
Diameter	[cm]	20	20	20	31
length	[cm]	20	26	32	30

With the engine power required in Table 8.1, it can be seen that the P200T6 is just enough for the design as the max power is $260\,\mathrm{kW}$. Therefore, the decision was made to use the P200T6 for the aircraft design.

[2] URL: https://www.saluqimotors.com [Accessed 15 June 2022]

In order to continue with the design, Saluqi provided a datasheet with useful graphs about the power and torque of the engine. The engine should be able to provide the power and torque required throughout all the possible RPM. As can be seen in Figure 8.3, it is necessary to operate on a 500 volt system. This is due to the fact that, when the maximum engine power is required, the only option is the peak power at 500 volts. This is only used in the most demanding parts of flight, which is a $2.5\,\mathrm{g}$ sustained turn. Outside this demanding manoeuvre, the engine has more than enough power when running continuous at 500 volts.

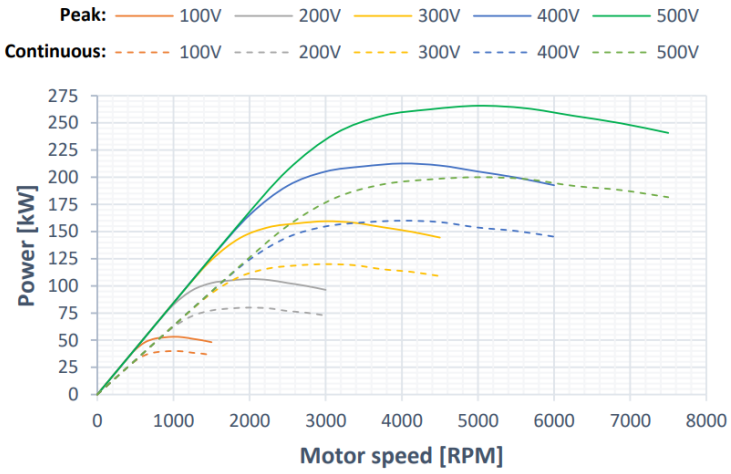

Figure 8.3: *Power against RPM graph* [2]

After knowing on which voltage the system operates it is necessary to check if the engine can keep up with the torque requirements. When looking at Figure 8.4, it can be seen that the engine provides almost triple the torque required across all the RPM ranges. This torque is also present from $0\,\mathrm{RPM}$ unlike combustion engine where the torque ramps up if the RPM get higher.

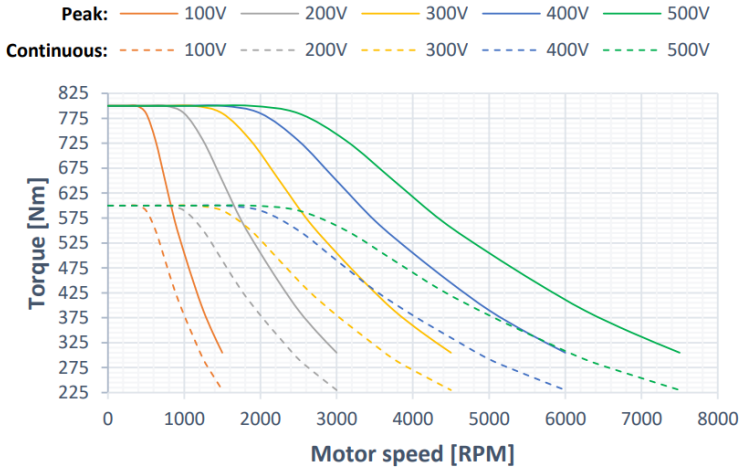

Figure 8.4: *Torque against RPM graph* [2]

Transferring this torque from the motor to the propeller requires a driveshaft. This driveshaft should be able to withstand these torque ranges easily. A safety factor of 2 was added to ensure that the driveshaft will not fail, as the maintainability of this part is rather difficult. Next to this, the angle of twist is desired to be lower than $1°$ in order to minimise the strain on the shaft. Two different materials were considered for the design of the driveshaft, namely steel and aluminium. The allowable torque is calculated with Equation 8.5 and Equation 8.6 [3]. The angle of twist is computed with Equation 8.7.

[3] URL: https://www.engineeringtoolbox.com/torsion-shafts-d_947.html [Accessed 10 June 2022]

$$J = \frac{\pi}{2}\left(c_2^4 - c_1^4\right) \quad (8.5) \qquad Q = \frac{\tau J}{c_2} \quad (8.6) \qquad \phi = \frac{TL}{EI} \quad (8.7)$$

Equation 8.5 is used in order to compute the polar moment of inertia, where c_2 and c_1 are inner and outer radius in m respectively. This polar moment of inertia is then used in Equation 8.6 where τ is the maximum allowable shear strength. This formula calculates the maximum allowable torque. With J it is possible to compute the angle of twist with Equation 8.7 where T is the torque in the shaft, L the length of the shaft, E the youngs modulus of the material and I the moment of intertia. The python program gives all the possible combinations for c_1 and c_2 where the torque of the engine is met and the angle of twist is lower than 1°, including the safety factor. The maximum diameter is capped at $6\,\mathrm{cm}$ otherwise the shaft will be too large in comparison to the propeller which will disrupt the airflow. Table 8.5 outlines the lightest option for the steel and aluminium shaft [4].

Table 8.5
Driveshaft parameter for steel and aluminium

Parameter		Steel[5]	Aluminium [6]
ρ	[kg/m^3]	1800	2710
τ	[MPa]	22.43	207
E	[GPa]	196	68.9
G	[GPa]	77.6	26.0
c_2	[cm]	3.00	3.00
c_1	[cm]	2.79	2.12
t	[mm]	2.1	8.8
m	[g]	1604	2060

As seen in Table 8.5 the steel option has a shear modulus that is 3 times higher than aluminium. The density of aluminium does not make up this deficit in the angle of twist, as this was the most constraining for the sizing. Therefore, the best option is to go with the steel drive shaft of $1{,}604\,\mathrm{g}$.

8.1.3. Propulsion Verification

The python script constructed in Subsection 8.1.1 outputs all the combinations of fan diameter, expansion ratio and RPM for which the most demanding phases of the flight are satisfied [4]. In these phases the drag should equal the thrust and are determined for take-off, clean and landing configuration at $0\,\mathrm{ft}$ and $6{,}000\,\mathrm{ft}$. The program then calculates the power required from the engine and the mass flow, which is later used in the sizing of the duct. As the formulas are the same for each phase, only the clean configuration at $0\,\mathrm{ft}$ was verified. The values used for verification can be seen in Table 8.6

Table 8.6
Values used for verification of the propulsion program

Parameter		Value
D	[m]	0.4
RPM	[2π/min]	4000
ε_d	[-]	0.8

Table 8.7
verification results of propulsion system

Parameter		Method	Python	By hand
T_{cl_0}	[N]	V & R	143.992	143.965
Q_{cl_0}	[Nm]	V & R	6.195	6.193
P_{req}	[W]	V & R	12045.57	12043.35

As can be seen in Table 8.7, the calculations by hand are almost exactly the same as the values produced by the python script. The small deficit can be explained by using a value of $1.225\,\mathrm{kg/m^3}$ for ρ instead of the calculated value by the ISA model. The ISA model calculates a more accurate value for ρ.

[4] URL: https://github.com/Niels-Prins/dseEflyer [Accessed 20 June 2022]
[5] URL:https://www.matweb.com/search/datasheet_print.aspx?matguid=71396e57ff5940b791ece120e4d563e0 [14 June 2022]
[6] URL: https://asm.matweb.com/search/SpecificMaterial.asp?bassnum=ma6061t6 [Accessed 14 June 2022]

8.2. Inlet and Duct

For a ducted fan, as the name suggests, a fan is placed in a duct. Given that a duct is only spans the pitch of the fan and is straight, the fan would operate almost exactly like a free propeller, except it will be quieter and the losses to tip vortices are reduced (similar configuration to as shown in Figure 8.1). However, when integrating with an aircraft, the ducting will inherently require some curvature at some point for sound structural integration. With curvatures present within a duct, there will be losses given the length of the ducting before and after the fan. To minimise these losses, the design of the duct and inlet has to be efficient enough and must aid the fan in generating enough thrust at the end of the duct. This can be achieved by making sure the incoming airflow is accelerated all the way through the system - inlet to fan and from fan to exhaust.

The inlet and ducting system of the Electrobat is closely related to the design of the propulsion unit (fan, motor, power required etc.). To be able to size the duct and hence the inlet, one must know the following parameters characteristics of the propulsion system:

- Engine or motor power, $P_{eng} = 260\text{kW}$
- Thrust coefficient, $k_t = 1.032914$
- Fan pressure ratio, $\Pi_{fan} = 1.0614$
- Fan efficiency, $\eta_{fan} = 0.885$
- Fan diameter, $D_{fan} = 0.63\text{m}$

The values for the thrust coefficient, fan pressure ratio, fan efficiency, and fan diameter were taken from the UL-39 aircraft since this aircraft shares a similar propulsion system as the Electrobat, except the Electrobat is driven by an electric motor [16]. The motor power (power required) was computed via Equation 8.3 and is tabulated in Table 8.2. Given all this, the next step is to compute the mass flow, $\dot{m}$, with an initial estimate of the thrust, T_{fan}, that the fan has to produce. This was computed via the following formulae, as provided by Wright Jr. [19].

$$P_{av} = T_{fan} V_0 \tag{8.8}$$

$$P_{thrust} = P_{eng} \eta_f \eta_{duct} \tag{8.9}$$

$$\dot{m} = \frac{2T_{fan}}{P_{av} - P_{thrust}} \tag{8.10}$$

The efficiency of the ducting system, η_{duct} was taken to be assumed to be $90\,\%$ and *a fan thrust of* 2060N *at sea level* with $V_0 = 77.17\text{m/s}$. Then the capture area, at station 0 was computed via mass flow rate equation [19]:

$$\dot{m} = \rho A_0 V_0 \tag{8.11}$$

$$A_0 = \frac{\dot{m}}{\rho V_0} \tag{8.12}$$

The capture area, A_0, is the area the air inlets that interacts with the freestream flow for ingestion to the fan. Depending on how many inlets is required, the capture area should be divided by the number of inlets to get the area of a single inlet, A_{0b}. Then the cross-sectional area inside the inlet duct was taken to be a converging duct to avoid internal boundary layer separation and was assumed to be $A_{1b} = 0.9A_{0b}$. Hence is the total inlet duct cross-sectional area is simply $A_1 = 2A_{1b}$, taken to be station 1. With the area known at station 1, the velocity there, V_1, can simply be computed via the continuity equation [19]:

$$A_1 V_1 = A_2 V_2 \tag{8.13}$$

To compute the velocities at the other stations of within the duct, *total and static temperatures and pressures must be computed*. The total temperature can be computed given a velocity via the isentropic relation given in Equation 8.14 [19]. Where, the isobaric specific heat is $c_p \approx 1000\text{J/kgK}$.

$$T_{0,0} = T_0 + \frac{V_0^2}{2c_p} \tag{8.14}$$

With the total temperature at station 0 computed, the total pressure at station 0 is computed via Equation 8.15 [19]. Where, the specific heat ratio is $\kappa \approx 1.4$.

$$p_{0,0} = p_0(\frac{T_{0,0}}{T_0})^{\frac{\kappa}{\kappa-1}} \quad (8.15) \qquad p_1 = p_0 + \frac{1}{2}\rho(V_0^2 - V_1^2) \quad (8.16)$$

Since no work is being done on the incoming airflow, the total temperature at station 1, $T_{0,1}$ can be considered to be same as $T_{0,0}$. Since V_1 has already been computed, the static temperature at station 1, T_1 can be computed by simply rearranging Equation 8.14. The static pressure at station 1, p_1 can also be computed given p_0, V_0, and V_1 via Bernoulli's principle. With the p_1 and T_1 known, the total pressure at station 1, $p_{0,1}$ can be computed via Equation 8.15. Another important factor that is required to analyse a ducted flow is the head losses or total pressure losses encountered within a duct. The total pressure loss throughout the duct can be computed via by first computing the Darcy friction factor, f_D, for a range of Reynolds numbers in a turbulent regime. It is important to note that considering the laminar regime assumes that no perpendicular cross currents in the flow through the duct and also " the motion of the particles of fluid is very orderly with all particles moving in straight lines parallel to the pipe walls" [20] [21]. The Darcy friction factor is obtained through the Kármán–Prandtl resistance equation, Equation 8.17, for turbulent flow in smooth pipes [22]. By solving the Kármán–Prandtl resistance equation with a Lambert W function for the correct Reynolds's number, the total pressure loss between any two stations can now be computed via the Darcy-Weisbach equation, Equation 8.18.

$$\frac{1}{\sqrt{f_D}} \approx 0.838W(0.629Re) \quad (8.17) \qquad \Delta p = f_D \frac{\rho \bar{V^2}}{2} \frac{L}{D_H} \quad (8.18)$$

Here, $\bar{V^2}$ and D_H are the mean velocity and mean hydraulic diameter between two consecutive stations. The losses were computed between all the stations (0-1, 1-2, 2-3, 3-4). To further compute the properties of the flow downstream from station 2 (through and after the fan), the total pressure loss between station 2 and 3 must be known as well as the flow properties at station 2. Once again, via Equation 8.13, V_2 is computed given V_1, A_1, and A_2 - A_2 is simply the area of the fan. To take the cross-sectional area of the driveshaft into account, it was assumed that the radius of the driveshaft, r_{hub} is 20% of the tip radius, r_{tip}[19]. The tip radius r_{tip} is simply $0.5D_{fan}$.

$$A_2 = \pi(r_{tip}^2 - r_{hub}^2) \quad (8.19)$$

With V_2 known, the static temperature, T_2 can be computed by rearranging Equation 8.14 by taking $T_{0,2}$ to be equal to $T_{0,1}$ (assume that no work is being done on the flow). Using Equation 8.16, p_2 can be computed and subsequently $p_{0,2}$ via Equation 8.15. Then to compute the losses, first the Reynold's number between station 1 and station 2 were computed given the mean velocity and mean hydraulic diameter between station 1 and station 2 with Equation 8.21.

$$Re = \frac{VD_H}{\nu} \quad (8.20)$$

The kinematic viscosity, ν, of the flow through the ducting was simply taken to be the value at sea level. With the Reynold's number computed, it can now be plugged into Equation 8.17 to obtain f_D and subsequently the total pressure loss between station 1 and 2 Δp_{1-2} via Equation 8.18. The reduced total pressure at station 2, $p_{0,2}^{'}$ is calculated as:

$$p_{0,2}^{'} = p_{0,2} - \Delta p_{1-2} \quad (8.21)$$

Since the pressure ratio of the fan, Π_{fan}, is known (as taken from the UL-39), $p_{0,3}$ and $T_{0,3}$ can be computed via:

$$p_{0,3} = \Pi_{fan} p_{0,2}^{'} \quad (8.22) \qquad T_{0,3} = T_{0,2}(1 + \frac{1}{\eta_{fan}}(\Pi_{fan}^{\frac{\kappa-1}{\kappa}} - 1)) \quad (8.23)$$

By assuming the ratio of the static pressures between station 2 and station 3 is similar to Π_{fan}, the following identity was used from Visser[23]:

$$\Pi_{fan} \approx \frac{p_3}{p_2} = (\frac{T_3}{T_2})^{\frac{\kappa}{\kappa-1}} \tag{8.24}$$

By rearranging Equation 8.24, T_3 can be computed. With the static and total temperature at station 3 known, V_3 can be obtained by rearranging Equation 8.14. The static pressure, p_3, on the other hand can be calculated by rearranging Equation 8.15. It must noted that it is assumed that the area right before and after the fan is the same, $A_2 = A_3$.

To obtain the flow properties at the exhaust of the propulsion system, it was assumed that the duct converges ever so slightly from the exit of the fan (station 3) to the exhaust (station 4). Upon extensive discussion, the decision was made to have a converging duct due to the same reason why the inlet duct was also made to converge, to reduce the internal boundary layer separation by accelerating the flow as the hydraulic diameter reduces along the length from station 3 to station 4. For the Electrobat, the cross sectional area of the exhaust was taken to be 98% of the area of the fan, $A_4 = 0.98A_3$. With A_4 now known, the exhaust velocity, V_4 of the propulsion system can be calculated via Equation 8.13.

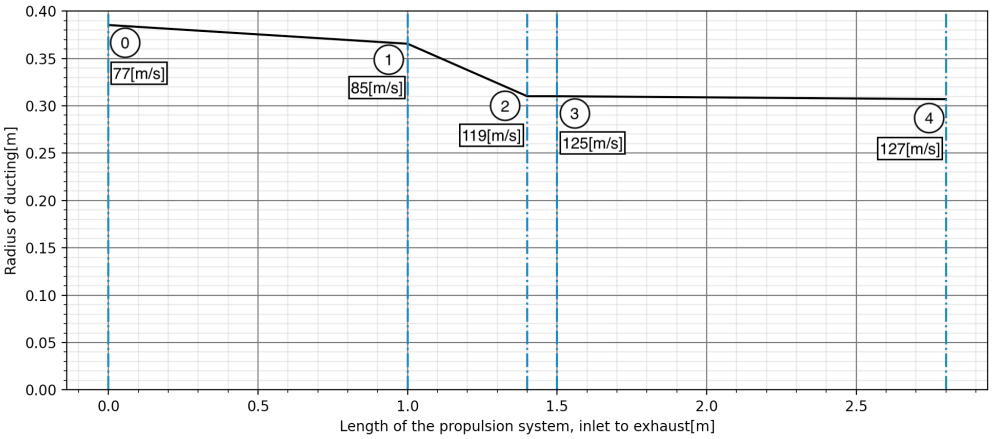

Figure 8.5: *Cross sectional change along the duct with local velocities of the airflow*

Once again, since no work is being done on the flow after the fan (between station 3 and 4), $T_{0,4}$ can be taken to be equal to $T_{0,3}$. Just like in the previous stages, T_4, p_4 and $p_{0,4}$ were all computed in exactly the same way.

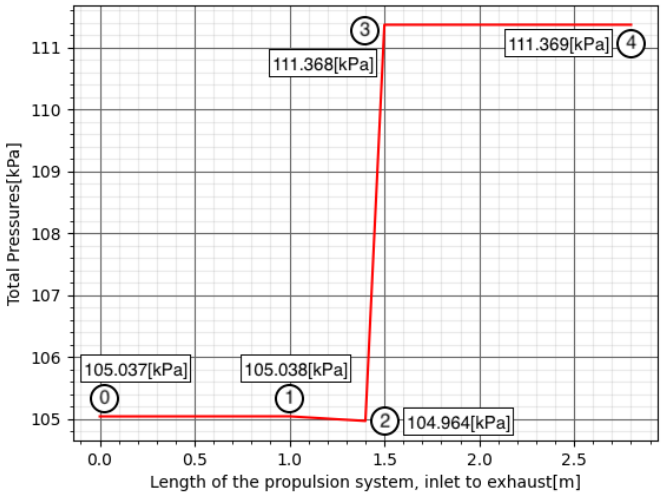

Figure 8.6: *Pressure variation throughout the length of the duct*

The *total thrust* produced by the aircraft is computed as the sum of the thrust force produced by the pressure difference (residual thrust) and the thrust force produced by the velocity difference (exhaust thrust).

$$T_{\Delta p} = A_4(p_4 - p0) \tag{8.25}$$

$$T_{\Delta V} = \dot{m}(V_4 - V_0) \tag{8.26}$$

$$T = T_{\Delta p} + T_{\Delta V} \tag{8.27}$$

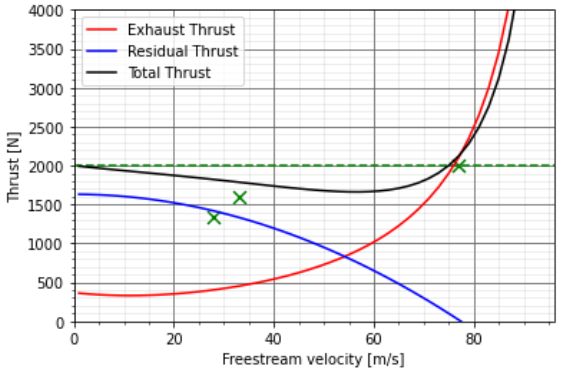

Figure 8.7: *Variation in residual exhaust, and total thrust at sea level condition*

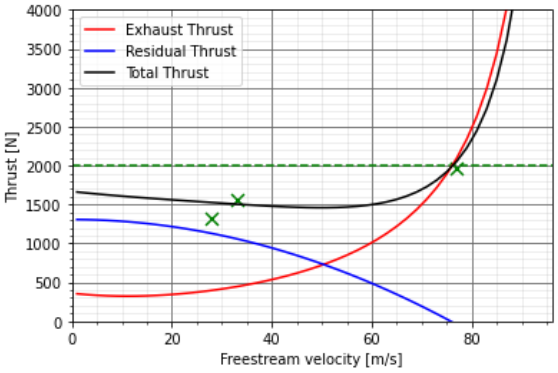

Figure 8.8: *Variation in residual exhaust, and total thrust at an altitude of* 6000ft

Upon conducting a couple of iterations by varying the initial estimate of the fan thrust (subsequently the mass flow) in Equation 8.10. The iterations were performed until the final thrust values that emerged from Equation 8.27 were in the acceptable range to meet the propulsion requirements as tabulated in Table 8.1. The final iteration yielded a thrust of $T = 2137\text{N}$, which is just slightly more than enough. The green dotted line shows the critical required thrust of $T = 2001\text{N}$ to sustain a 2.5 G horizontal turn at the Electrobat's operational velocity, $V_0 = 77.17\text{m/s}$.

Table 8.8
Computed flow properties for the Electrobat's engine duct system

Station		**0**	**1**	**2**	**3**	**4**
Duct Area	[m^2]	0.466	0.420	0.302	0.302	0.296
Flow Velocity	[m/s]	77	85	119	125	127
Total Pressure	[Pa]	105037	105038	104964	111368	111369
Static Pressure	[Pa]	101325	100469	96280	101374	100977
Total Temperature	[K]	291	291	291	296	296
Static Temperature	[K]	288	287	284	288	288

Inlet

The inlets that are required for the Electrobat are chosen based on the type of flight conditions and air flow speeds that the propulsion system will experience. Given the low subsonic conditions that the E-Flyer will be operating it, it will not have to deal with the emergence of compressible effects, like shockwaves, when ingesting the oncoming airflow. For inlets operating at subsonic speeds, it is preferred to take advantage of the streams of smooth air above the boundary layer air upstream of the inlets - usually comes from the air flow passing over the fuselage.

In Figure 8.9, do note that there is some flow separation present within the duct, after the inlet. To avoid this, the duct has to start converging towards to the fan face to accelerate the flow once again by reducing the cross-sectional area, since the mass flow will be constant (see Equation 8.13. Accelerating the flow in this manner will result in tighter streamlines, avoiding internal boundary layer separation in within the duct to have "uniform velocity distribution at the inlet plane of the fan rotor blades"[16]. The shape and size of the inlets for the Electrobat must be chosen carefully. Given the operating speeds and total conditions, the required inlet area can be easily computed via Equation 8.13.

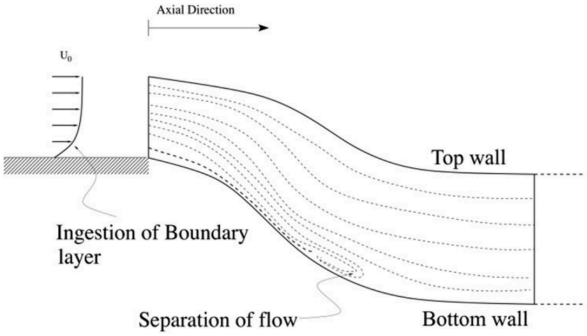

Figure 8.9: *Boundary layer ingestion for an inlet with an S-duct with flow separation [24]*

The shape of the inlet was chosen qualitatively by simply comparing different inlet aspect ratios. As mentioned previously, the Electrobat will not be encountering the formation of shockwaves at any point in its flight envelope, thus all inlet shapes that caters for this effect (ramp, variable ramp, shock cone, etc.) can be eliminated. This leaves with inlets that are derived from fuselage embedded nacelles - takes advantage of the boundary layer flow from the fuselage.

Figure 8.10: *Fuselage embedded inlets on a subsonic A-4B Skyhawk[25]*

Figure 8.11: *Ramp inlets on an F-14 Tomcat for supersonic flight regimes*[7]

The most precise and reliable method of investigating these phenomenons would be to conduct experiments and take measurements or to perform CFD analyses. However, it must be noted that with the limited time and resources at this stage in this design exercise conducting experiments or perform CFD is simply a bit too impractical.

Given the values for the required velocities and areas computed at the fan face, the *inlet areas per side* (depending on how many inlets is suitable for a given design) can be computed via continuity equation. For the Electrobat:

$$A_{inlet} = A_{0b} = \frac{A_0}{2} \tag{8.28}$$

Since it is known that a podded inlet with a high aspect ratio is suitable for the Electrobat, the inlet is essentially modelled as a semi-ellipse, where the major axis, a, was taken a the maximum allowable length along the Z-axis of the fuselage behind the cockpit (where the propulsion system starts). The semi-minor axis, b, represents the maximum cowl width of the inlet. For the Electrobat the semi-major axis was taken to be a = $0.8\,\mathrm{m}$ and the single inlet area was computed to be A_{inlet} = $0.233\,\mathrm{m}^2$ (see Table 8.8).

$$b = \frac{2A_{0b}}{\pi\left(\frac{a}{2}\right)} \tag{8.29}$$

From Equation 8.29, the maximum cowl width was computed to be $0.371\,\mathrm{m}$.

[7] URL: https://militarymachine.com/f-14-tomcat/ [Accessed 20 June 2022]

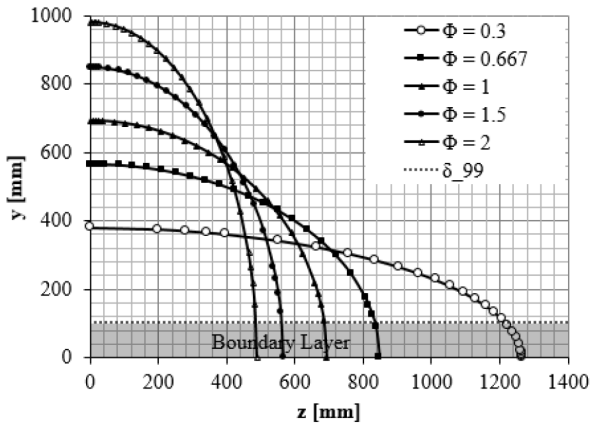

Figure 8.12: *Visualisation of different aspect ratios of inlets[26]*

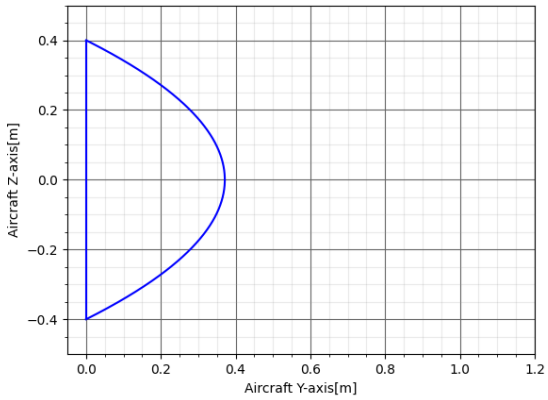

Figure 8.13: *Visualisation of the Electrobat's inlet dimensions*

Splitter Plate

A splitter plate is used in the design in order to divert the boundary layer. The distance from the fuselage to the splitter plate should have a minimum length of two times the thickness of the local boundary layer. The boundary layer thickness is shown in Equation 8.30, where δ_t is the thickness, x the length from the nose to the start of the splitter plate and Re_x the local Reynold's number [12]. As seen above, the local Reynold's number is required for calculating the boundary layer thickness. Using Equation 8.31 this Reynold's number is acquired, with ρ_∞ being the free-stream density, V_∞ the free-stream velocity and μ_∞ the dynamic viscosity [12].

$$\delta_T = \frac{0.37x}{Re_x^{0.2}} \tag{8.30}$$

$$Re_x = \frac{\rho_\infty V_\infty}{x}\mu_\infty \tag{8.31}$$

The final considerations to make is the connection point to the fuselage and the length in front of the duct. The length of the splitter plate from the connection point on-wards is two times the boundary layer thickness [12]. The attachment point is located at $30\ \mathrm{mm}$ from the start of the duct.

All the aforementioned features are shown in Figure 8.14 and Figure 8.15. The motor is visualised as a square compartment consisting of ELEO motors. This compartment is placed outside the duct to ensure that it does not interfere with the airflow within the duct.

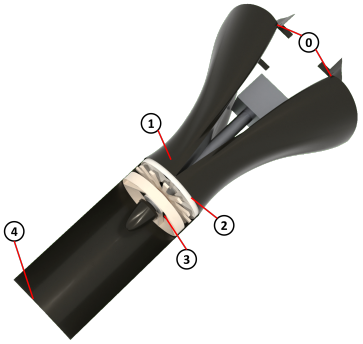

Figure 8.14: *Station numbering of the duct model*

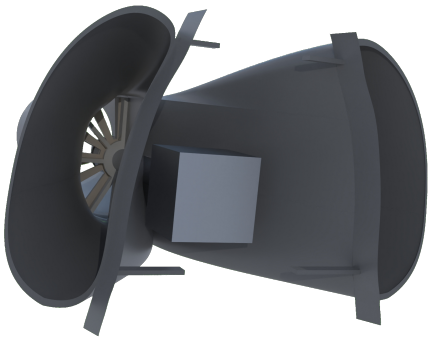

Figure 8.15: *Artist impression of the Electrobat's ducted fan propulsion unit*

Verification

The methodology used to compute the various properties of flow within the duct were mostly taken from:

- Visser: Isentropic relations to compute total and static flow properties [23];
- Wright Jr.: Relations to deduce mass flow from a given fan thrust and motor power [19];
- Rouse: Darcy-Weisbach empirical formulae for pressure loss [27].

These relations obtained from the aforementioned sources were combined to size and analyse the flow in the duct in a Python script [8]. To verify the computations performed in the script, the exact same computations were also performed by hand to make sure the equations were implemented correctly, and the correct values are defined and passed around at the right point in the code. By doing so, a robust program can be used over and over again to iterate and investigate the sensitivity of certain parameters. The selected parameters are the parameters that require the most amount of compounded relations (will contain the most amount of rounding errors) to get arrive at a value for the said parameter. Do note that the Lambert W function used in computing the Darcy friction factor has to be solved implicitly - a Scipy module was used to solve this numerically in Python. Hence the pressure loss is not accounted for in the analytical computations.

Table 8.9
Computed duct parameters from Python and analytically by hand

Parameters		Python	Analytical	Difference [%]
$\dot{m}$	[kg/s]	44.1	44.1	0.00
V_2	[m/s]	119.0	119.2	0.13
V_3	[m/s]	125.0	121.0	2.91
V_4	[m/s]	127.9	128.2	0.29
$p_{0,3}$	[Pa]	111369	111488	0.11
p_3	[Pa]	101388	102031	0.63
$T_{0,3}$	[K]	296.8	296.6	0.05
T_3	[K]	288.9	289.2	0.10
T	[N]	2138.3	2169.1	1.42

Validation
In order to validate the computational method for estimating the performance of the duct a direct comparison with the only comparable long-ducted fan aircraft is made. The values of this aircraft, which are presented in Table 8.10, were gathered from information present in various papers on it. This resulted in a static thrust of $1{,}751\,\mathrm{N}$ and a thrust at the maximum speed of the UL-39 ($80\,\mathrm{m/s}$) of $800\,\mathrm{N}$ [16]. Additionally, the mass flow through the duct was reported to be $18.4\,\mathrm{kg/s}$ [16]. The pressure ratio, isentropic efficiency, and rotational speed of the fan was reported as 1.065, 0.885, and $6{,}200\,\mathrm{RPM}$ respectively [16]. Using these values in the computational method gives the computed duct performance data of UL-39 as seen in Table 8.11.

Table 8.10
Gathered UL-39 duct performance data [16]

Stage		0	2	3	4
A	[m^2]	0.300	0.194	0.194	0.152
v	[m/s]	50	73	66	102
p	[hPa]	1,013	995	1,060	-
T	[K]	288	288	293	-

Table 8.11
Computed UL-39 duct performance data

Stage		0	2	3	4
A	[m^2]	0.300	0.194	0.194	0.152
v	[m/s]	50	77	85	109
p	[hPa]	1,013	992	1,044	1,016
T	[K]	288	286	291	289

From Table 8.10 and Table 8.11 it can be seen that the computed state parameters do not vary considerably from gathered data, the greatest difference being the air speed at station 3 with $28\,\%$ difference. Other state parameters however achieve differences on a lesser order with the next greatest difference at $7\,\%$. This inspires a good sense of confidence in the model's results. Additionally, the Mach computed at the tip of the blades is 0.53 The fan thrust was computed to be $1{,}096\,\mathrm{N}$ which when interpolating between the two thrust values reported previously appears reasonable, further reinforcing confidence in the model. Moreover, a residual thrust due to pressure expansion was computed as $41\,\mathrm{N}$, leading to a total computed thrust of $1{,}138\,\mathrm{N}$.

Sensitivity Analysis
To analyse the sensitivity of the results to variations in design parameters, the most logical output parameter to choose for this analysis was the total thrust produced. This is due to the fact that it is the most indicative parameter to check whether if the ducting is oversize or undersized. The input parameter that influences the total thrust meaningfully is the assumed fan thrust - was iterated over until the total thrust produced was in the range of required thrust values as tabulated in Table 8.3. When performing this sensitivity analysis, the

[8] URL: https://github.com/Niels-Prins/dseEflyer [Accessed 20 June 2022]

geometrical aspects of the were finalised and is only investigated for a cruise speed of $V_0 = 77.17\mathrm{m/s}$ at sea level.

Table 8.12
Shows the variation to the total thrust values if the assumed fan thrust were to be varied

Input		Output	
Fan Thrust [N]	**Variation [%]**	**Total Thrust [N]**	**Variation [%]**
1,854	-10	1,263	-41
1,936	-6	1,551	-27
1,998	-3	1,816	-15
2,039	-1	2,024	-5
2,060	0	2,138	0
2,081	1	2,261	6
2,122	3	2,536	19
2,184	6	3,036	42
2,266	10	3,943	84

8.2.1. Noise

In order to satisfy the user requirements regarding noise, considerations on elements where noise reduction or suppression may be applied are investigated. According to ICAO, Figure 8.16 depicts the distribution of typical commercial aircraft noise producing elements for both departure and arrival, segments where the aircraft is closest to the ground.

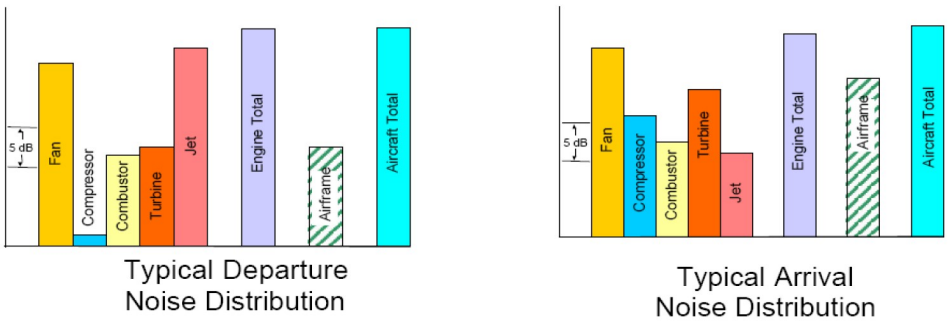

Figure 8.16: *Source noise component contributions [28]*

It should be noted that the fan, which is comparable to the ducted fan is a large source of noise component, leaded only by the jet and engine. However, considering the design incorporates an electric motor and a cold jet, these source components will be considerably less. Hence, reductions in fan noise component are most effective in limiting the aircraft's total noise. In consideration of this, particular attention is applied to reduce the noise of the propulsion system. The basic noise sources include the motor itself, the rotor-stator interaction, the rotor itself, turbulent flow, and the exhaust jet [29]. However, given the exhaust is a cold jet and the aircraft's thrust is primarily reliant on it, no considerations are made for the exhaust jet.

Rotor-stator interaction
generates tonal noise caused by the interference of wakes behind the rotor with the stator [29]. Design improvements to reduce the noise generated by these interactions include,

1. Increasing the spacing between the rotor and stator. A doubling in length reduces the noise level by 2 dB [30].
2. Increasing stator blade chord, results in more acoustic pressure wavelengths acting on the stator blades. This allows for reflected waves to interfere with incident waves reducing acoustic pressure [30].
3. Sweeping stator vanes diversifies the phase of the wakes, meaning pressure waves at different radial positions impact the stator at different times [31].
4. Leaning stator vanes increases the number of incident wakes from rotor blades acting on each stator blade [31].

Rotor noise is itself caused by multiple factors. These include its presence and rotation in turbulent flow, as well as, instable flow ingestion or boundary layer separation from the duct walls [29]. The noise generating mechanism of both is the local increase in turbulent flow intensity. A method for reducing rotor noise is with blade tip platform extensions, which reduces the tip leakage vortices that produce noise and induce aerodynamic losses [32]. Additionally, benefits are a widened range of high fan efficiencies and increased thrust [32].

Turbulent air flow inside the flow passage of the ducted fan generates broadband noise. This noise can be suppressed with either acoustic liners or stator inlet guide vanes. The acoustic liners can be applied along the duct walls of the flow passage, absorbing acoustic vibrations. Such liners differentiate between locally- and non-locally-acting liners. The difference being, that locally-acting liners do not allow acoustic waves to radiate parallel to their surface. Moreover, non-locally-acting liners are able to absorb a larger bandwidth of waves than the local. However, the application of acoustics liners complicate the interaction with the surrounding flow field and may add considerable weight to the aircraft. Additionally, stator inlet guide vanes may be applied to reflect forward-radiating noise downstream [29].

In order to check whether the ducted fan meets the noise requirement, a noise analysis is performed to estimate the noise generated by the final design. The dominant noise will come from the propeller and in order to come up with a valid estimation, a general propeller noise level is calculated, and then a reduction factor is applied due to the ducted fan.

The sound pressure level, SPL, is calculated using Equation 8.32, in which $\mathrm{M_t}$ can be obtained using Equation 8.33 [33]. In Equation 8.32, $(P_{br}$ is the shaft brake horsepower, D_R the fan diameter, B_p the number of blades, N_p the number of propellers and r_p the distance to the observer. In Equation 8.33, n_p is the rotational speed and c is the speed of sound at altitude [33].

$$SPL = 83.4 + 15.3\log_{10}(P_{br}) - 20\log_{10}(D_R) + 38.5M_t - 3\left(B_p - 2\right) + 10\log_{10}\left(N_p\right) - 20\log_{10}\left(r_p\right) \quad (8.32)$$

$$M_t = \frac{\pi D_R n_p}{60c} \quad (8.33)$$

Applying Equation 8.32 to the characteristics of the aircraft will result in a noise of $90.62\,\mathrm{dB}$ at a $1{,}000\,\mathrm{ft}$. This, however, is the formula for open propellers. Therefore, a reduction factor needs to be applied in order to find the prediction of the noise by a ducted fan. Multiple graphs were found that gave a reduction value in dB with respect to the duct length after the fan [2]. The duct lengths that were considered are $0.25D\ m$, $0.50D\ m$, $0.75D\ m$ and $1.00D\ m$. The duct length in terms of diameter of the aircraft was found to be $2.22D\ m$. A logarithmic interpolation was made between the aforementioned four graphs in order to make an estimate of the reduction value with a duct length of $2.22D\ m$. This resulted in Figure 8.17.

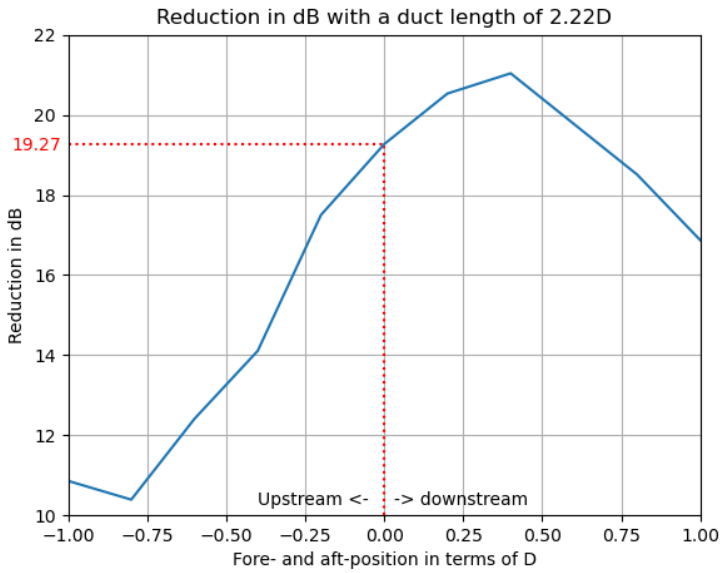

Figure 8.17: *Noise reduction due to the duct*

If the aircraft is flying exactly overhead, it can be seen that the noise reduction is $19.27\,\mathrm{dB}$. This will reduce the noise of the aircraft further down to $71.35\,\mathrm{dB}$. After this, a perceived noise reduction factor is applied. This reduction factor is a parameter called an A-level reduction with a value of $14\,\mathrm{dB}$. The final value of perceived noise will then be $57.35\,\mathrm{dB}$. Keep in mind that this is only the noise produced by the fan. The aircraft also has two stators which will decrease the sound even more as said above. Due to the time constraint it was not possible to do more research on this topic. Next to this, the estimated sound is a pure estimation, and it is important to test this once an experimental aircraft has been build to check whether the requirement is met. In order to comply with the cockpit noise requirement, both pilots will have to wear noise-cancelling headphones, as the noise too excessive otherwise. This is standard practice in smaller aircraft, as the propeller-driven aircraft generate a significant amount of noise inside the cockpit.

8.3. Electric Power System

The electrical system is the heart of the aircraft, and a complete failure of this system would be catastrophic. For this reason, critical system components are duplicated for redundancy and these are denoted with an A and a B. Additionally, the wiring will be duplicated and placed apart for additionally redundancy. As the system is based on a fly-by-wire, the complete failure of the actuators, flight management computers, or the electric wiring in between must be made as unlikely as possible within the constraints of the design. A schematic overview of the hardware and electrical system is given in Figure 8.18. These are combined as their functions in the aircraft are integrally related.

During normal operations, all the power is supplied by the main batteries. The cooling and power are regulated by the battery controller. For the main DC bus, the voltage only has to be transformed, and for the main motor, the voltage also has to be inverted to AC. All parameters will be regulated by the main motor controller in combination with the flight management computers.

The main DC bus supplies power to all the other sub-systems. If a battery pack fails, the pack-level monitoring will be able to identify and consequently remove the failed pack from the circuit. Furthermore, the compartmentalisation of the various battery packs ensures the continued supply of power to the flight management computers and the control actuators to ensure the aircraft remains controllable. All non-critical sub-systems will be disengaged by the controller to reduce energy consumption in such an event. It may also be noted that a gravity release mechanism is available to lower the landing gear.

In order for the electric propulsion system to supply the necessary power required by the aircraft, the aircraft's electric power system must be sized to meet these demands. Furthermore, the sizing and design of these subsystems allow more accurate determination of their weight components.

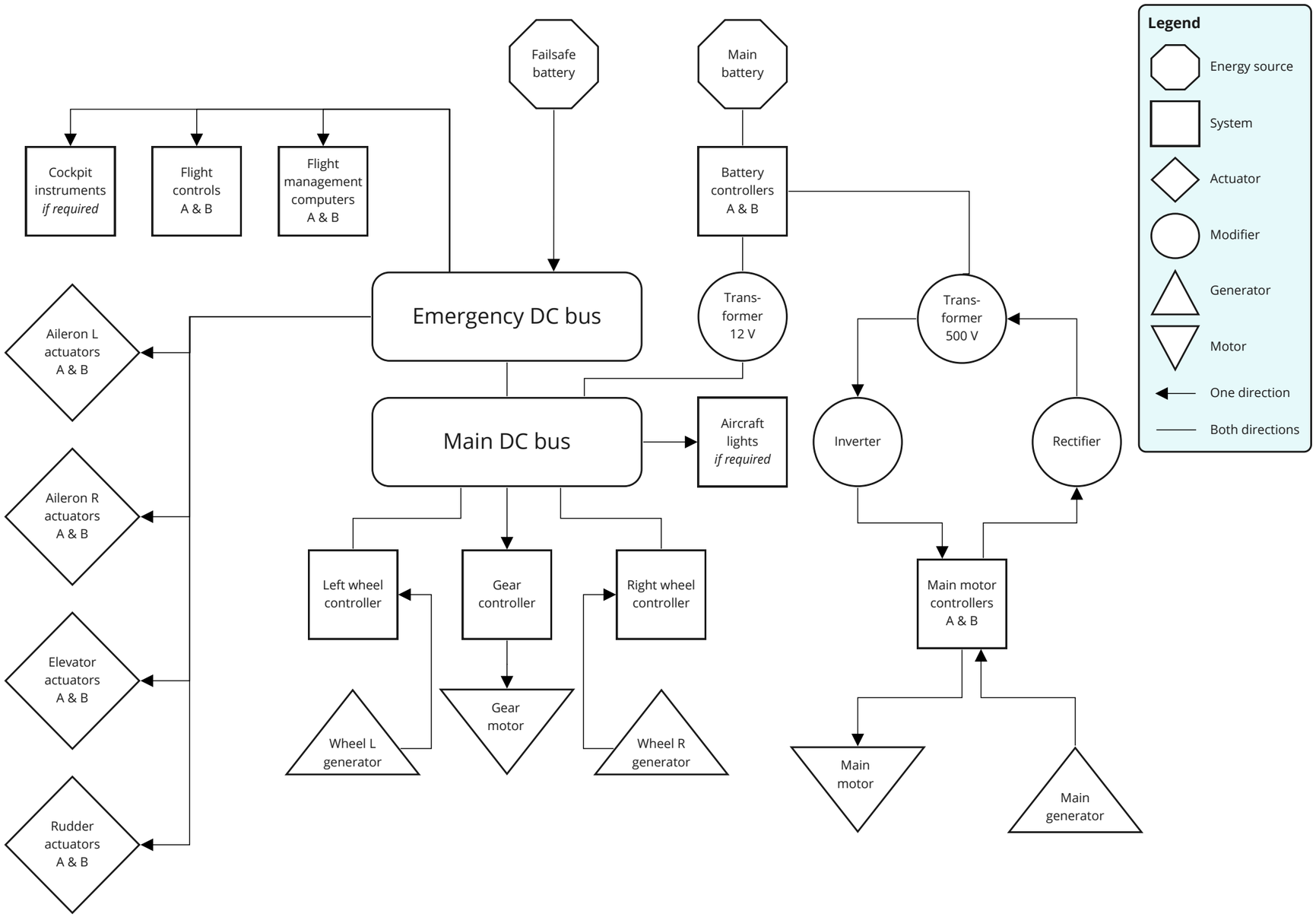

Figure 8.18: *Hardware and electrical block diagram*

8.3.1. Power storage

For the aircraft to deliver the necessary power to the electric motor, the batteries must be sized to meet both voltage, amperage, capacity and weight constraints. Here, the synergy of these parameters is investigated for the ELEO size 35 performance modules, the performance parameters of which are seen in Table 8.13. These battery modules can be customized to integrate different battery cells together and are easily scalable in both orientation and direction. This allows the achieving of desired voltage and capacity simpler. Furthermore, the modules include integrated battery management systems and cell level voltage monitoring and balancing as well as local current and temperature monitoring [9].

Additionally, in order to satisfy variations in current due to motor throttling during different phase of flight a tabular summary was generated Table 8.14. These current variations were computed on the basis of the $500\,\mathrm{V}$ power supply required by the electric motor and the engine power required for the various phases of flight. Notably, it is assumed as this stage that the power required by the fly-by-wire system of the aircraft is minimal in comparison to the motor and may be recovered by the ERS, as data for small-scale FBW systems is non-existent. In further development of this design an in-depth investigation for this shall be made.

Table 8.13
ELEO size 35 performance module (Max Continous/Peak Discharge) parameters

Variable		Value
Nom. Voltage	[V]	57.4
St. Capacity	[Ah]	103.3
St. Energy	[kWh]	5.2
St./Max Charge	[A]	51/140
Max/Peak Discharge	[A]	350/700
Weight of one battery	[kg]	27.7
Capacity density	[Ah/kg]	3.73
Energy density	[Wh/kg]	188

Table 8.14
Current variations in flight profile

Flight Phase	Current required [A]
Taxi	5
Climb	514
Cruise	169
Aerobatics	292
Landing	21
Endurance	103

Using these module performance parameters the battery subsystem build-up can be sized to provide the required combination of the aforementioned parameters, in Table 8.15. Notably, the number of modules in series provide the desired system voltage while the number of modules in parallel provide the desired amperage and system capacity. The system energy follows from the voltage and capacity.

Table 8.15
Battery subsystem build-up (Max Continuous/Peak Discharge)

Parameter		Value
No. batteries in series	[-]	8.75
No. batteries in parallel	[-]	1.14
Total No. batteries	[-]	10
Voltage of System	[V]	502
Current of System	[A]	399/798
Capacity of System	[Ah]	118
Energy of System	[kWh]	59.1
Total Weight of System	[kg]	276
System Energy Density	[Wh/kg]	214

It should be noted 8.75 batteries in series and 1.14 in parallel is required from the module size described in Table 8.13. As described earlier, the module is scalable to incorporate these fractions and deliver the desired voltage and current. Furthermore, it can be seen from Table 6.4 that the required energy of the system is obtained while achieving a total battery weight of $276\,\mathrm{kg}$. This weight is assumed to include the weight of monitoring systems of the modules provided by the values from ELEO.

This then results in a capacity distribution over the flight profile as seen in Figure 8.19. Notably, in addition

[9] URL: https://eleo.tech/solutions/battery-modules/size-35 [Accessed 20 June 2022]

to the capacity constraints derived from the flight profile, a maximum charge capacity margin of $5\,\%$ and a minimal capacity discharge of $10\,\%$ are included. The minimal capacity discharge is allocated within the reserve in order to reduce battery weight. Furthermore, as usage of the reserve is considered critical the life-time preservation of the battery at that moment is then no longer considered a priority and hence battery degradation as a result is considered acceptable. This results in a operational depth-of-discharge of $84\,\%$. Additionally, the ELEO performance batteries are expected to have a cycle life of 500 to $1{,}500$ cycles [10]. Unfortunately, no life cycle battery performance degradation data is publicly available and hence it is assumed that due to usage of maximum continuous current that 500 cycles is a conservative estimate.

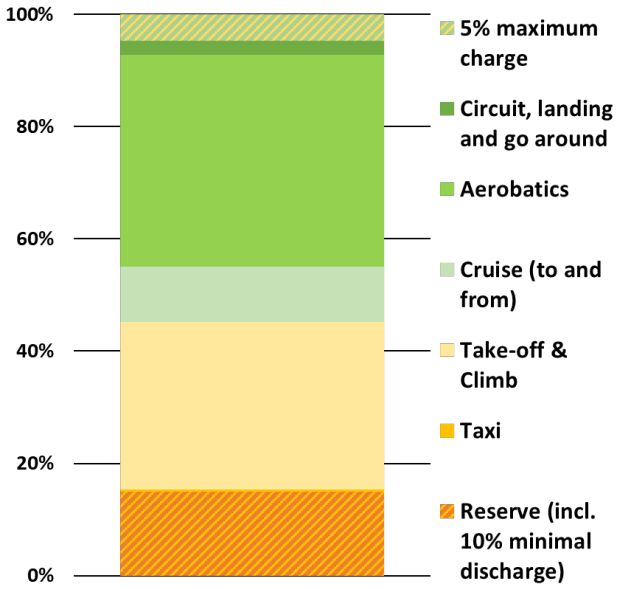

Figure 8.19: *Battery flight profile*

Furthermore, when considering the depth-of discharge and voltage of the system, the charging capacity is $94.6\,\mathrm{Ah}$. Using a standard charging current of $51\,\mathrm{A}$ for the battery packs and the 1.14 packs in series, a system charging current of $58\,\mathrm{A}$ is used. This then results in a charging time of $98\,\mathrm{min}$ [10].

As ELEO is a cell to pack integrator, they buy the latest cells and integrate these into customisable battery packs. As a result, it is expected from discussions with an electric motor engineer at Saluqi, that in the Summer 2022 ELEO will unveil new battery packs with an energy density of approximately $210-220\,\mathrm{Wh/kg}$. This shows an annual improvement of $5-7.5\,\%$ meaning an energy density of $350\,\mathrm{Wh/kg}$ could be achieved around 2030. This would result in a battery weight reduction of $102\,\mathrm{kg}$ leading to a weight of $185\,\mathrm{kg}$. Consequently, the MTOM in 2030 could reduce to $856\,\mathrm{kg}$ allowing more power to weight and thus greater performance.

8.3.2. Energy Recovery System

During the design option analysis, two energy recovery systems were considered. First, the generators in the main landing gear to recover energy during landing. A quick calculation shows the system is unable to compensate its added mass with regained energy. Assuming the aircraft weighs $978\,\mathrm{kg}$ and touches-down on the runway at $58\,\mathrm{kts}$, a total kinetic energy of $428\,\mathrm{kJ}$ is available to be converted. Assuming an ideal scenario in which all the energy is successfully converted in $17\,\mathrm{sec}$ during roll-out, this corresponds to $120\,\mathrm{Wh}$, or an equivalent of $0.6\,\mathrm{kg}$ in batteries. This accounts for $0.2\,\%$ of the total energy capacity of the aircrafts batteries. It seems therefore unfeasible the generators including connections will weigh less than this, so the system is discarded. It should be noted that if the brake system were to be replaced by the generators, this concept will be feasible, as it is energy recovery without much additional mass. The generators are, however, unlikely to provide enough stopping force to completely replace the conventional brake system.

The second recovery system considered was the energy recovery with the ducted fan in which the fan would

[10] URL: https://eleo.tech/solutions/battery-modules/size-35 [Accessed 20 June 2022]

be used as a turbine. The system would be used in flight, by converting the kinetic energy of the aircraft during excess energy phase such as diving or landing. Provided the equations used in the duct sizing, the inverse of the pressure ratio, and the isentropic efficiency are valid, the power delivered by the turbine can be calculated using Equation 8.34 [19].

$$P_{turb} = \dot{m} c_p \left(T_{0,2} - T_{0,3} \right) \tag{8.34}$$

This provides an optimistic value of $994\,\mathrm{kW}$ when operating at dive speed of $186\,\mathrm{kt}$. The actual recovered power into the batteries is estimated at $795\,\mathrm{kW}$ using an efficiency of $80\,\%$. Then by considering a conservative total ERS operation time over the flight envelope of $30\,\mathrm{s}$, the energy recovered amounts to $6.6\,\mathrm{kWh}$, the equivalent of $31\,\mathrm{kg}$ of batteries. This energy recovered amounts to about $11\,\%$ of the total energy capacity of the batteries in the aircraft. The recovered energy may be allocated to the FBW systems and its computers or used to simply recharge the batteries for later use. Furthermore, thanks to the usage of the battery few additional systems are required to make this ERS functional. Consequently, the ERS fan turbine is incorporated into the design.

9

Structural Design

The structural characteristics of the Electrobat revolve around its capability to sustain the aerodynamic loads during flight and also some loads when on the ground. The structurally most arduous phase the aircraft will endure is due to the aerodynamic loads the aircraft will experience when performing aerobatic manoeuvres. The Electrobat's airframe and wings should be able to withstand eight times the aircraft weight according to requirement [EFLY-STK-APER-06] which states that the Electrobat shall have limit loads of +8 G /-6 G. The load factors that the Electrobat will endure given a velocity are plotted in a V-n diagram, see Figure 5.2.

The type of loads that the airframe and wing should be able to withstand are shear loads and bending loads. The wings of Electrobat will generate the lifting forces required to perform the required aerobatic manoeuvres, and the airframe will maintain its structural integrity to protect the multitude of onboard components and also protect the occupants from external hazards.

9.1. Material choice

The Electrobat's structural components of the wing and fuselage of the Electrobat will be made of carbon fibre reinforced plastic. This type of material has superior specific strength and stiffness compared to traditional aircraft materials, such as aluminium 7075-T6 [34]. To be more specific, standard modulus carbon fibres have been selected. Despite having lower tensile modulus than the intermediate or high modulus categories, standard modulus fibres are between 35 to 50 percent cheaper while providing better ultimate strengths [35] [36]. An example of material properties of bidirectionally woven standard modulus carbon fibre and epoxy matrix, commonly used in general aviation, is shown in Table 9.1.

Table 9.1
Mechanical properties of Toray T700S-12K fibres with 2510 resin system prepreg [37]

Property	Symbol	Unit
Tensile strength	σ_t	1089 [MPa]
Tensile modulus	E_t	56.9 [GPa]
Compressive strength	σ_c	674 [MPa]
Compressive modulus	E_c	53.3 [GPa]
Shear strength	τ	86.2 [MPa]
Shear modulus	G	5 [GPa]
Poisson's ratio	v	0.056 [-]

Unlike metals, composite materials are not isotropic. Composites tend to have very good mechanical properties, however, for the (woven) fibre/resin layers these properties only apply in only one or two principal directions. When a laminate is a build-up of multiple of these layers in different orientations, in a so-called layup, the properties of the laminate can differ greatly from those of the individual layers. To estimate the material properties, the classical laminate theory is used [34]. This theory is derived from the general Hooke's law, with the assumption of a laminate being a thin plate in which only in-plane stresses exist.

For the design of the Electrobat however, only symmetric and quasi-isotropic layups are considered. These are layups where the ply stacking is symmetric over the laminates centre plane as well as having an equal amount of fibres in the four principal directions (0, 45, 90 and -45 degrees). By designing for such a layup, there will be no coupling between in- and out-of-plane deformation present in unsymmetrical laminates [34]. This in combination with quasi-isotropic material properties, it is assumed that classical structural analysis and design methods for isotropic materials can be applied for the design of the Electrobat, in particular for estimating buckling behaviours.

Using classical laminate theory and the material properties given in Table 9.1, mechanical properties of a quasi-isotropic laminate with four bidirectional plies, quasi-isotropic laminate are calculated and given in Table 9.2. Since such bidirectional woven carbon fibre layers are commonly available in thicknesses as low as $0.08\,\mathrm{mm}$, a minimal thickness of $0.32\,\mathrm{mm}$ is assumed for all composite structures of the Electrobat. For larger thicknesses, the properties presented in Table 9.1 will only remain valid with increments of $0.16\,\mathrm{mm}$ or two plies. This way, the laminates can always be arranged symmetrically while remaining quasi-isotropic.

Table 9.2
Estimated quasi-isotropic composite properties used for the structural design of the Electrobat

Property	Symbol	Unit
Tensile strength	σ_t	770 [MPa]
Tensile modulus	E_t	42.3 [GPa]
Compressive strength	σ_c	477 [MPa]
Compressive modulus	E_c	42.3 [GPa]
Shear strength	τ	82.6 [MPa]
Shear modulus	G	16.5 [GPa]
Poisson's ratio	v	0.28 [-]

9.2. Wing Structure

In order to come up with a preliminary structural design of the wing, an analytical model has been developed. This model was used to compute and analyse the loads exerted on the wing, the resulting stresses and the failure criteria. This allowed for an iterative process in which the design of the wing could be optimised. In this section, the methodology of the model will only be briefly discussed. Further details on the model are presented in Appendix A.

9.2.1. Loading diagrams

This subsection will cover the methods used for obtaining the internal loading diagrams for the most critical load case. Required aerodynamic data such as C_L, C_D, and C_m distributions for the correct flight conditions are exported from XFLR5 and processed in the model.

Critical load case

The structures of the aircraft must be designed for $8\,\mathrm{G}$ / $-6\,\mathrm{G}$ with a single occupant and $6\,\mathrm{G}$ / $-4\,\mathrm{G}$ with two occupants. In these cases, the aircraft has MTOM's of respectively $876\,\mathrm{kg}$ and $966\,\mathrm{kg}$. In order to attain these g-loads, the wing will have to generate a lift force of $68.75\,\mathrm{kN}$ for the single occupant 8 G ultimate and $56.86\,\mathrm{kN}$ for the $6\,\mathrm{G}$ with dual occupants. The $8\,\mathrm{G}$ / $-6\,\mathrm{G}$ case is therefore assumed as most critical at the manoeuvring speed of the Electrobat, as the loading will be more concentrated at the wing tips, resulting in a larger bending moment at the wing root.

Force and moment per unit span distributions

The distributions of the lift, drag, and aerodynamic moment coefficients, as well as the centre of pressure locations along the wingspan for v = $150\,\mathrm{kts}$, were exported from XFLR5. Additionally, the C_{L_α} curve for the whole wing is given as input to the model. Based on this, the angle of attack required to generate enough lift for an $8\,\mathrm{G}$, sea level dive at $150\,\mathrm{kts}$ is determined to be $17.8\,\mathrm{deg}$. The C_L, C_D, and C_m distributions along the wing for this angle of attack are shown in Figure 9.1.

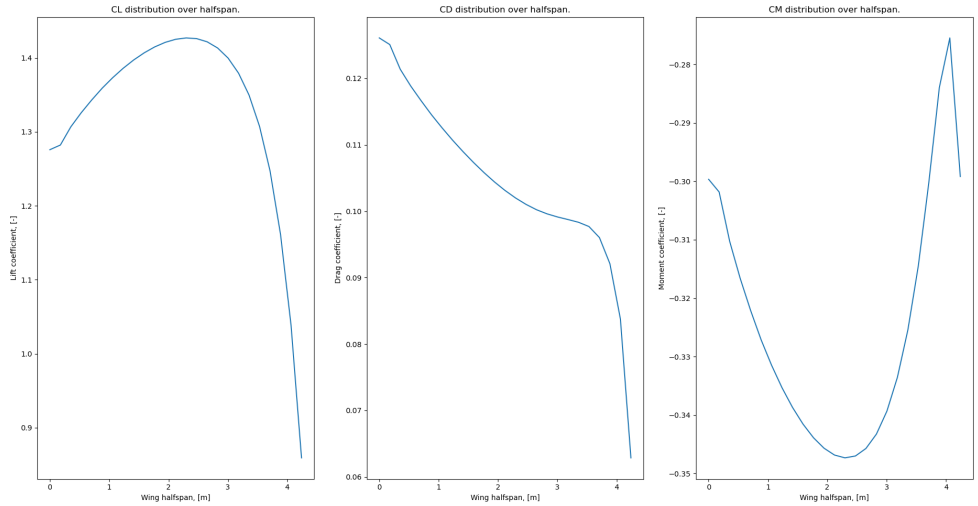

Figure 9.1: *Distributions of C_L, C_D and C_m over the wing*

The coefficients can be easily converted to force or moment per unit span by multiplying with the dynamic pressure and local chord length, as shown in Equation 9.1. The drag and pitching moments per unit are obtained in a similar fashion.

$$L'(y) = C_L(y) \cdot q \cdot c(y) \tag{9.1}$$

For the structural analysis, interest lies in the loads normal and tangential to the wing structure. Therefore, the unit force distributions are decomposed according to Equation 9.2 and Equation 9.3.

$$F'_N(y) = \cos(\alpha_a)\, L'(y) + \sin(\alpha_a)\, D'(y) \tag{9.2}$$
$$F'_T(y) = \sin(\alpha_a)\, L'(y) + \cos(\alpha_a)\, D'(y) \tag{9.3}$$

The spanwise distribution of these decomposed forces per unit span is plotted in Figure 9.2. In these figures, the weight of the batteries located at the root of the wing is accounted for, therefore steps in force per unit span are observed in the $F'_N(y)$ and $F'_T(y)$ plots.

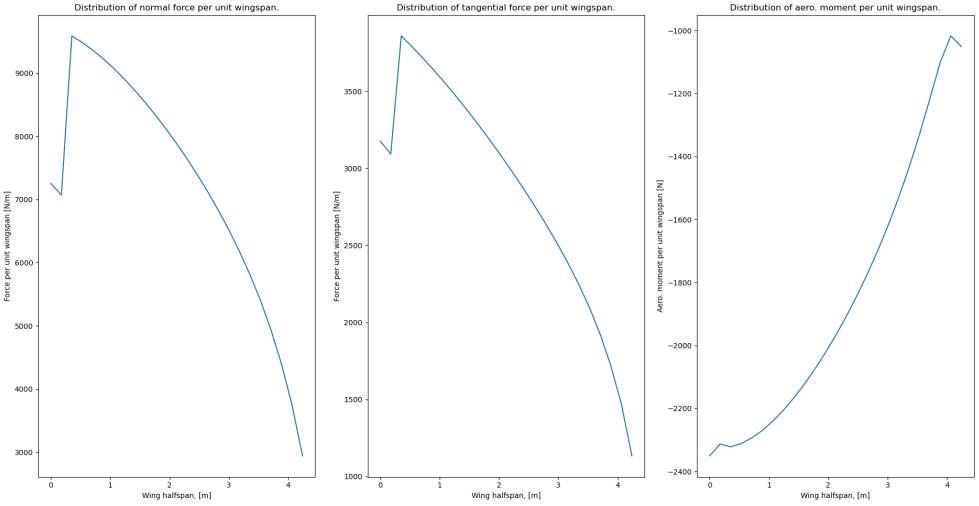

Figure 9.2: *Normal and tangent forces and aerodynamic moment per unit span distributions*

Internal shear forces and moment

The wing is modelled as a cantilever beam of length l_{span} onto which the distributed loads $F'_N(y)$ and $F'_T(y)$ are applied. The horizontal and vertical] shear force at any span y, respectively $S_x(y)$ and $S_z(y)$, are obtained

by integrating the distributed loads between y and l_{span}. As the tip of the wing is a free end, both $S_x(0)$ and $S_z(0)$ equal zero, resulting in Equation 9.4 and Equation 9.5. Their distributions over the wingspan are shown in Figure 9.3.

$$S_x(y) = \int_y^{l_{span}} F_T'(y)dy \tag{9.4}$$

$$S_z(y) = \int_y^{l_{span}} F_N'(y)dy \tag{9.5}$$

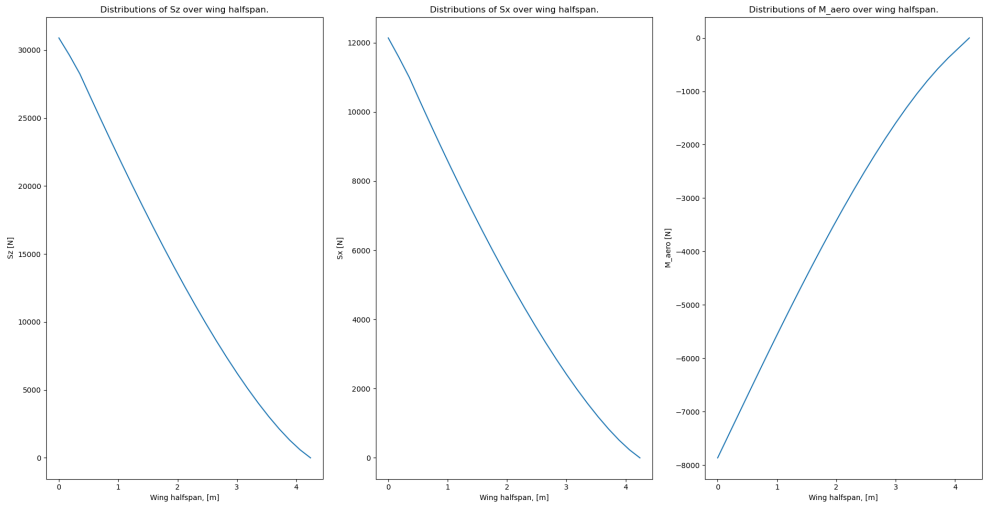

Figure 9.3: *Distributions of internal shear forces and moments over the wing*

Bending moment distributions

Finally, the internal bending moment distributions follow once more integrating the shear force distributions. Again, as the wing tip is essentially the free end of a cantilever beam, thus $M(L) = 0$. The resulting internal bending moment distributions over the wing are shown in Figure 9.4. As the vertical shear force creates an upwards bending of the wing, and thus compression in the positive first quadrant of the coordinate system, the bending moment M_x is as defined negative[38].

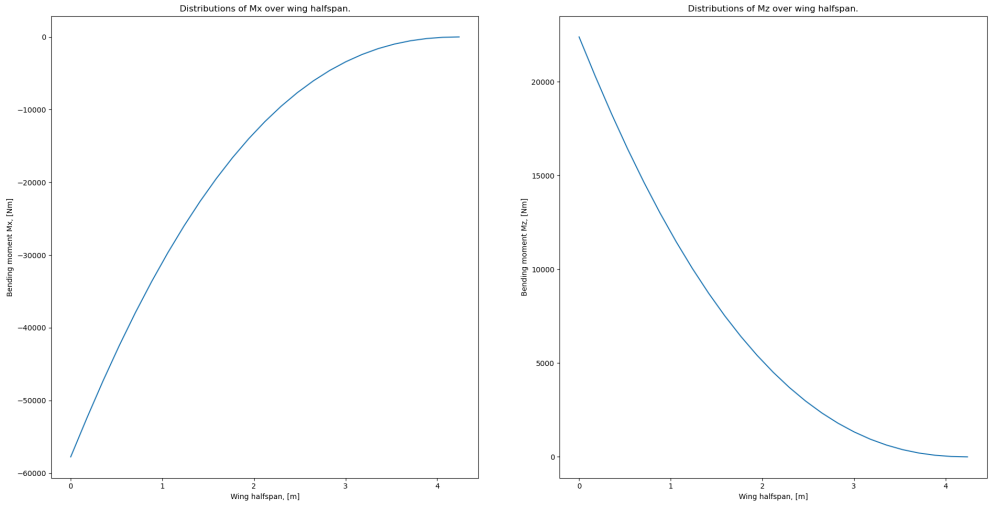

Figure 9.4: *Distributions of bending moments over the wing*

9.2.2. Wingbox layout

The load-carrying wing structure of the Electrobat is a full-composite three-spar, two-cell wingbox. The main spar is located at $30\,\%$ chord as this is the location of maximum airfoil thickness while being close to the centre of pressure. This spar will thus take up the largest part of the vertical load. The rear spar is located at $75\,\%$ chord, such that it coincides with the hinge line of the flaperon. Since the flaperon spans almost

the full wing, the aft $25\,\%$ chord is not considered structural along the full length of the wing. The front spar, located at $10\,\%$ of the chord, closes off the wing box and creates a two-cell design. Although adding some complexity, such a design can be lighter for the same torsional stiffness as a result of the shear flows of both cells counteracting each other in the centre spar [38]. The leading edge of the wing is therefore not considered structural. This has two primary reasons. First, it is less structurally efficient in bending due to reaching close to the neutral axis. Additionally, the leading edge could be damaged by a bird strike or impact of debris, so as a non-structural component, it poses less risk and is easier to repair or replace.

Next to this, the wing structure is designed to be symmetric over the x-axis. This means that top and bottom skins will be of equal thicknesses. Furthermore, the skin segments are simplified into straight line segments. Although leading to a slightly less optimised design, these two assumptions combined significantly decrease the complexity of the structural analysis, especially that of the shear flow and stresses. A cross-section of the wing at the root is presented in Figure 9.5, where the wing box is indicated in red.

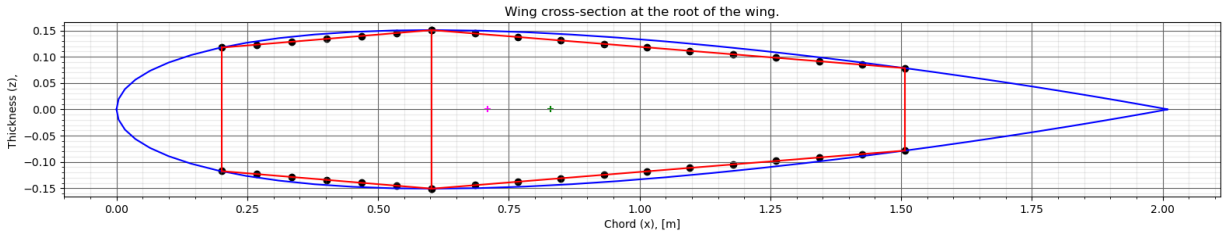

Figure 9.5: *Cross-section of the wing at the root*

9.2.3. Designing for failure modes

As commonly so for thin-walled wing structures, the two most limiting failure modes in the design of the Electrobat wing box were found to be spar web shear and skin compressive buckling [38]. To prevent these forms of buckling from occurring, the spar web and skins are split up into smaller 'panels' by the use of ribs and stringers.

The first step in determining the required locations of ribs was computing the shear stresses in each of the spar webs, based on an initial estimate of spar and skin thicknesses. In order to do so, the shear flow distributions had to be computed. For this, two methods were considered, namely structural idealisation and (numerical) integration of the shear flows. Ultimately, integration of the shear flow is chosen over idealisation as the importance of accuracy of the shear flow in the webs is essential for determining the rib placement. This outweighs the additional complexity of setting up the required integrals. If the structure was idealised, the shear flow in between the booms (and thus in the spar webs) would be assumed constant, thus neglecting the variance of shear stress through the height of the spars. Additionally, the skins and spar webs in between the booms would be assumed not direct-stress carrying, which is not applicable in the case of the full load-carrying structure that is being considered [38]. As the calculations of the shear flow require numerous elaborate steps, it is not further covered in this chapter. Instead, a full description of the process is provided in Appendix A, and Subsection A.0.3 to Subsection A.0.6.

With the shear flow known, the shear stresses are easily found by dividing the shear flow by the spar thicknesses, as shown in Equation 9.6. Then, based on Equation 9.7 and the constant K_s found in Figure 9.7, the initial maximum length of spar segments to prevent web buckling spacing is determined. In this figure, the ratio a/b is the aspect ratio between the length (a) and the height (b) of the spar web panel. It is assumed that the ribs constrain the spar web and skin panels in position, but that the edges of the panels are not fully constrained against rotation. Therefore, the curve for hinged edges is selected in Figure 9.7.

$$\tau = \frac{q}{t} \tag{9.6}$$

$$\tau_{cr} = Ks \frac{\pi^2 E}{12\,(1-v^2)} \left(\frac{t}{b}\right)^2 \tag{9.7}$$

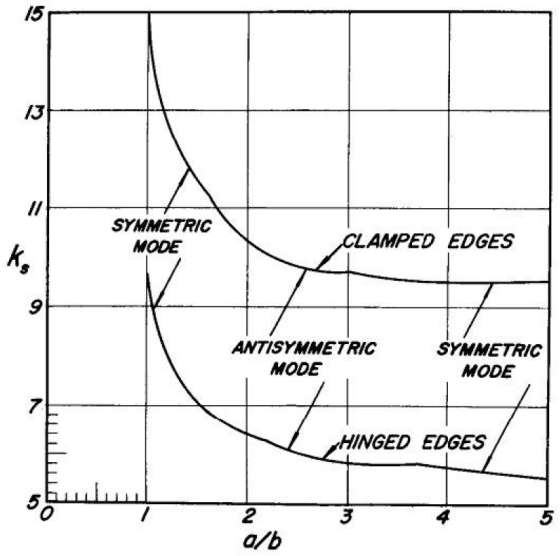

Figure 9.6: *Buckling coefficient for rectangular isotropic web under shear load [38]*

Given this initial rib spacing, values for the spanwise lengths of the skin panels are known, for each of which the bending stress in each of the skin panels is calculated with Equation 9.8. Similar to that of the web, the critical buckling stresses, and the required stringer spacing is obtained through Equation 9.9 and Figure 9.7 where again hinged (or in other words simply supported) edges are assumed. By setting the critical buckling stress equal to the bending stress, Equation 9.9 is solved for the required stringer spacing.

$$\sigma_x = \frac{I_{zz}M_x - I_{xz}M_x}{I_{zz}I_{xx} - I_{xz}^2}z + \frac{I_{xx}M_z - I_{zx}M_z}{I_{zz}I_{xx} - I_{xx}^2}x \tag{9.8}$$

$$\sigma_{cr} = Kc\frac{\pi^2 E}{12\,(1-v^2)}\left(\frac{t}{b}\right)^2 \tag{9.9}$$

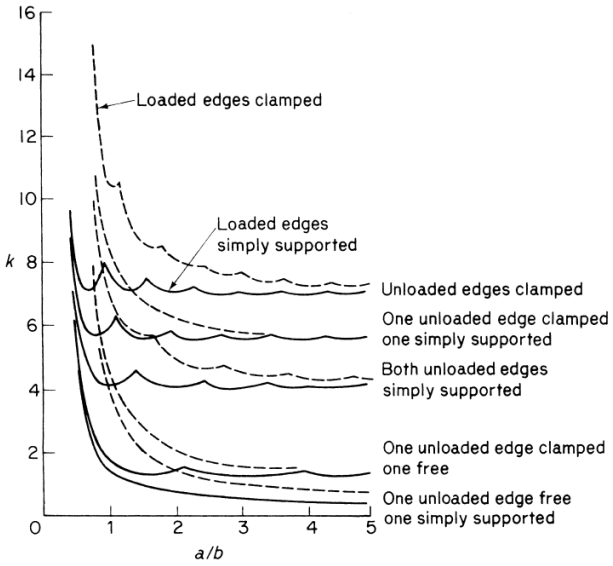

Figure 9.7: *Buckling coefficient for rectangular isotropic plates under compression [38]*

Two alternatives to using stringers have been considered. The first of these was the thickening of the skin panels, however, this results in a significantly heavier structure. This can be derived from Equation 9.9. If a skin thickness of $52\,\mathrm{mm}$ is assumed at the root of the wing where the distance between the main and rear spar is approximately $0.9\,\mathrm{m}$, then with the material properties given in Section 9.1 and a K value of approximately 4, the critical buckling stress of the skin panel is $0.75\,\mathrm{MPa}$. This lies far below the expected compressive stress at the root, thus buckling will occur. Doubling the thickness to $4\,\mathrm{mm}$ only improves the critical stress to $2.98\,\mathrm{MPa}$. However, for the same increase in cross-sectional area, around 25 z-stringers with $12\,\mathrm{mm}$ flanges of $2\,\mathrm{mm}$ thickness can be added. By splitting the skin in between the main and rear spar into effectively 26 narrow panels, the critical stress is increased to $504.08\,\mathrm{MPa}$. This extreme example thus

shows that adding stringers is more efficient than skin thickness for increasing the critical buckling stress.

The second considered alternative consisted of using composite sandwich panels, where the skin is effectively split into two and a foam or honeycomb core is added in between to give a thick, but light skin. However, as the relatively weak foam decreases the average material properties of the laminate significantly, such panels would have to be of significant thickness. At such thickness, the low compressive strengths of the core become a problem, as well as Equation 9.9 only being valid for thin plates [38]. Further research into this alternative is an advised post-DSE activity.

9.2.4. Final wing structure design

After a number of iterations with the described model, an optimised wing structure design was reached. This process started with setting initial values for skin, web, and stringer design parameters. When rough rib and stringer distributions were obtained, detailed iterations were performed to minimise the mass of the structure, while still meeting the 1.5x safety factor for all failure modes. The final wing structure design is shown in Figure 9.8 and Figure 9.9 where also the variation in skin thickness is visualised. Z-stringers have been selected over I-, J- or hat stringers due to their ease of manufacturing. The height of the Z-stringer, as well as the width of its flanges, is selected to be $12\,\mathrm{mm}$ and their thicknesses are set at $1.28\,\mathrm{mm}$. Further design parameters such as rib locations, spar thicknesses and amount of stringers along the wing are summarised in Table 9.3.

Table 9.3
Wing structure design parameters

Span section [m]	Front spar thickness [mm]	Main spar thickness [mm]	Rear spar thickness [mm]	Cell 1 skin top/bottom thickness [mm]	Cell 2 skin top/bottom thickness [mm]	Nr. of stringers top
0 - 0.3	2.08	2.72	2.56	1.92	2.24	19
0.3 - 0.65	2.08	2.72	2.56	1.76	2.24	19
0.65 - 1.1	2.08	2.72	2.40	1.76	1.92	19
1.1 - 1.65	2.08	2.56	2.24	1.6	1.92	19
1.65 - 2.7	1.92	2.56	1.92	1.28	1.6	19
2.7 - 4.24	1.44	1.92	1.44	1.28	1.6	11

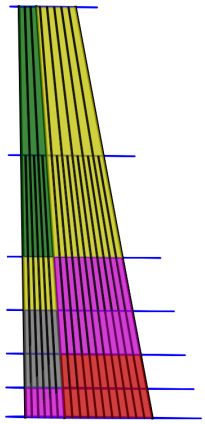

Figure 9.8: *Top-down view of the skin, rib, and stringer locations as well as the thickness variation*

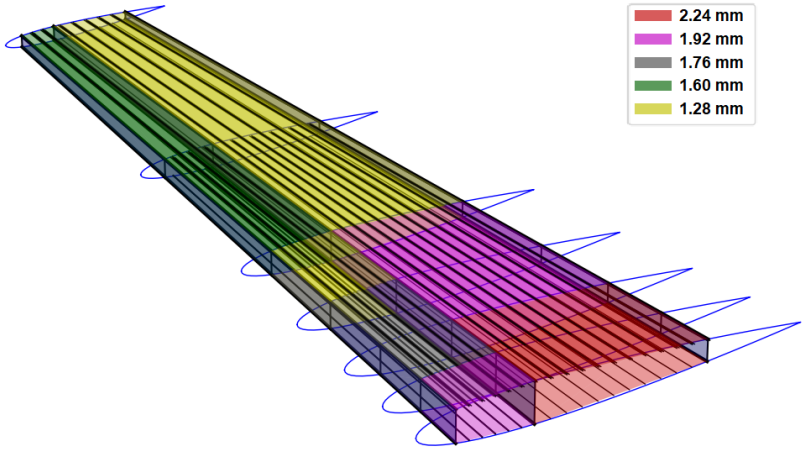

Figure 9.9: *Isometric view of the final wing structure*

The design shown in Figure 9.9 leads to an estimated mass of $87.2\,\mathrm{kg}$ for both halves of the wing combined. Since this excludes the weight of the flaperon at $25\,\%$ of the chord, its hinges and the non-structural leading edge, an extra $30\,\%$ is added to this estimate. An additional, $20\,\%$ margin is added on top of this to account

for local reinforcements needed around inspection hatches and to account for the landing gear attachment and cutout. This brings the estimated mass for the wing to $136\,\mathrm{kg}$.

The bending stresses over the wing for the load case described in Subsection 9.2.1 are shown in Figures Figure 9.10 and Figure 9.11. From these, it can be seen that the maximum compressive stress at the root reaches $69.7\,\mathrm{MPa}$. The maximum tensile stress at the bottom of the wing is $63.6\,\mathrm{MPa}$. These stay well below the ultimate compressive and tensile stress of the material, which were respectively $477\,\mathrm{MPa}$ and $770\,\mathrm{MPa}$.

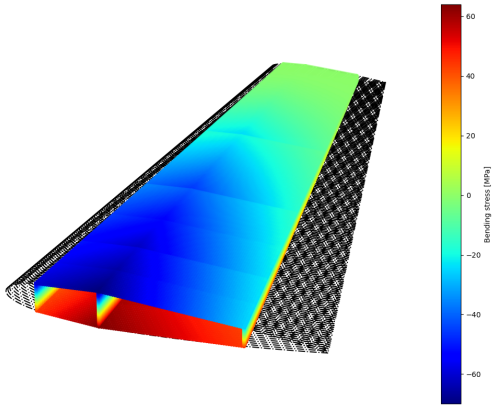

Figure 9.10: *3D bending stress distribution over the top of the wing*

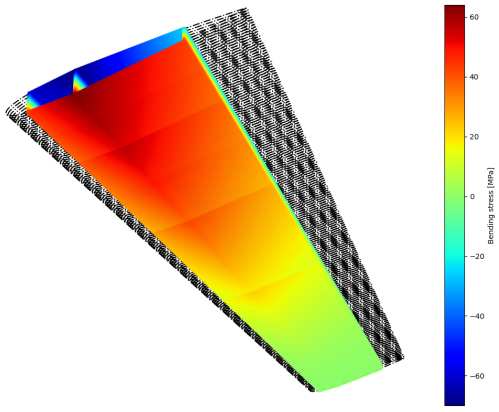

Figure 9.11: *3D bending stress distribution over the bottom of the wing*

As described in Subsection 9.2.3, the spar web and skin buckling were the most critical mode of failure for the design. The safety margins for these failure modes are plotted over the span in Figures Figure 9.12 and Figure 9.13, where the minimal overall safety factor equals 1.51 and occurs at $1.11\,\mathrm{m}$. Since the wing structure is designed to be symmetrical, the safety margins are equal for a $8\,\mathrm{G}$ / $-6\,\mathrm{G}$ load case. Therefore, only the $8\,\mathrm{G}$ load case had to be considered in order to meet the $8\,\mathrm{G}$ / $-6\,\mathrm{G}$ requirement.

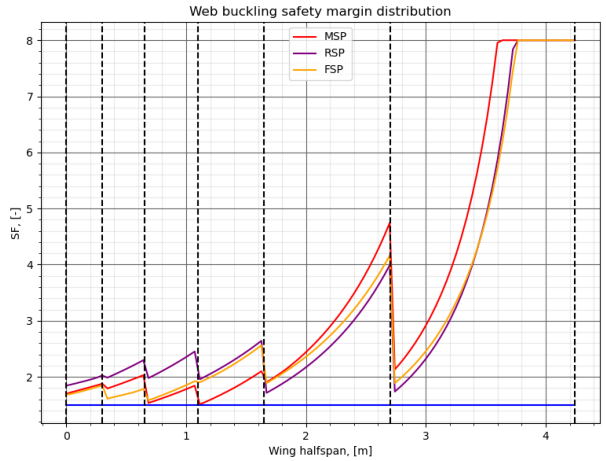

Figure 9.12: *Distribution of front, main, and rear spar web shear buckling safety margins*

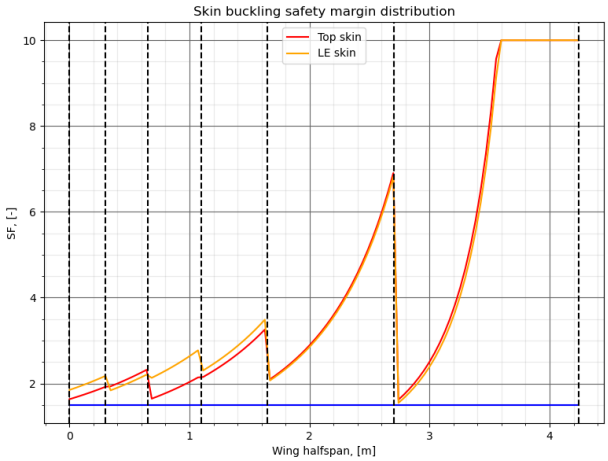

Figure 9.13: *Distribution of compression buckling safety margins of the skins*

Finally, the deflection profile of the wing is shown in Figure 9.14 where the tip deflection reaches $7.76\,\mathrm{cm}$.

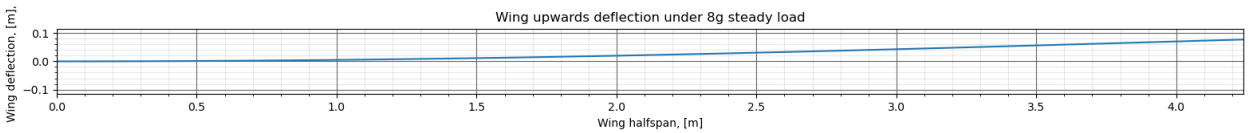

Figure 9.14: *Deflection of the final wing design under $8\,\mathrm{G}$ load*

To estimate the reduction in weight of this design compared to a traditional structure, a similar analysis has

been performed using 7075-T6 aluminium as a material. Including the assumed margins for the flaperon and reinforcements, the aluminium wing counterpart has an estimated mass of $218\,\mathrm{kg}$. Therefore, a weight saving of around $37.6\,\%$ has been realised by the full-composite wing.

9.3. Fuselage Structure

The required structural characteristics of the fuselage can be deduced by determining what sort of shear and bending loads the airframe will experience. The best way to determine such structural properties in the design phase is usually to perform a structural analysis via Finite Element Methods (FEM) - discretising the entire fuselage to the initial design details. By assigning the correct geometries, boundary conditions and loading conditions, one should be able to get reliable estimates on the order of magnitudes to the stresses the airframe will be subjected to. However, given the severely limited time and cost budget of this preliminary design project, performing detailed FEM on the fuselage falls outside the said budget, not to mention the verification and validation processes. Upon doing further research into how airframes are stress tested, one of the most common ways is to simply place the fuselage on a pivot point support or by splitting the fuselage into halved sections to mimic the deflection of either end of the fuselage as seen from the centre of gravity, where the CG is lifted by the wing. An example of this being performed physically is shown in Figure 9.15 and Figure 9.16.

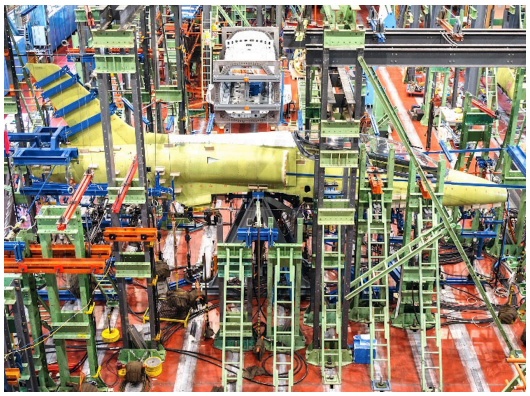

Figure 9.15: *Fuselage stress test of an L-39 Albatross with a pivot point[39].*

Figure 9.16: *Fuselage stress test at Gulfstream, done by clamping the midsection[40].*

The beam that is to represent the fuselage is split into two sections: front half and aft half. The split is made at the average location of the centre of gravity for the case where there is 1 occupant with MTO of $876\,\mathrm{kg}$. The distributed load shown in Figure 9.17 is computed by excluding the influence of the battery and motor, as they are not structurally integral components but are important to the stresses the airframe will experience. The battery, according to the fuselage design, is actually split into two portions where one is near the wing and the other is more forward towards the nose. However, for the ease of analysis, the battery is assumed to have a combined (assume total battery mass of $276\,\mathrm{kg}$ effect acting midway between the average CG and the nose at a distance of $1.96\,\mathrm{m}$ as measured from the nose. By removing these two components, the apparent centre of gravity shifts to roughly $4.78\,\mathrm{m}$, as measured from the nose. The overall weight, however, acts through the average location of the centre of gravity. The average location of the centre of gravity for the aforementioned case is between $3.79\,\mathrm{m}$ - $3.91\,\mathrm{m}$ as measured from the nose, see Table 6.7.

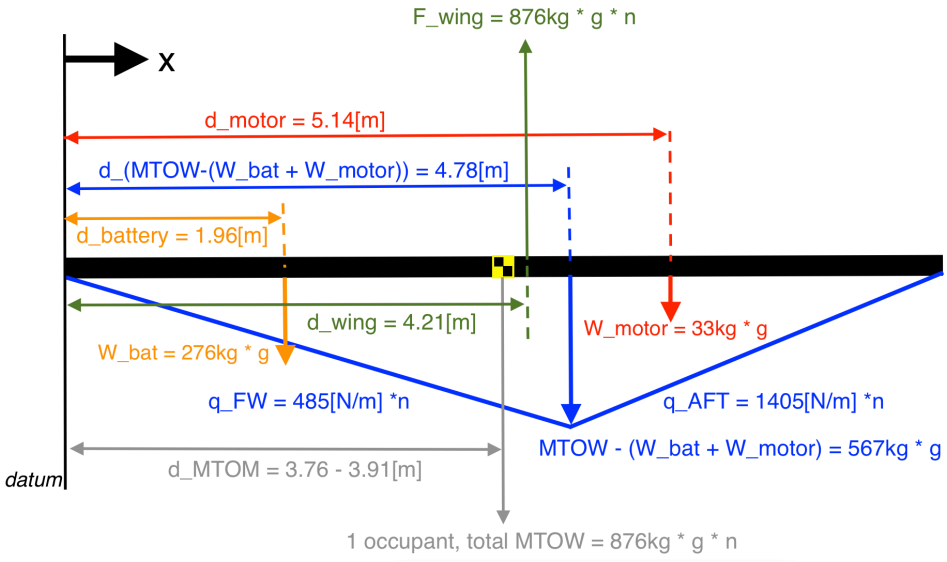

Figure 9.17: *Free body diagram of the simplified fuselage modelled as a beam (NOT TO SCALE)*

In the case of the Electrobat, the centre of gravity is located somewhere between $3.8\,\mathrm{m}$ and $4.0\,\mathrm{m}$ as measured from the nose. The n in Figure 9.17 is the load factor that the fuselage is under. Upon implementing a simple model of these beams, the following shear force and bending moment diagrams were plotted as shown in Figure 9.18 and Figure 9.19. Positive values of shear forces mean the forces are acting towards the ground. Positive values of bending moment before the average CG location means clockwise bending and counterclockwise bending after the average CG location.

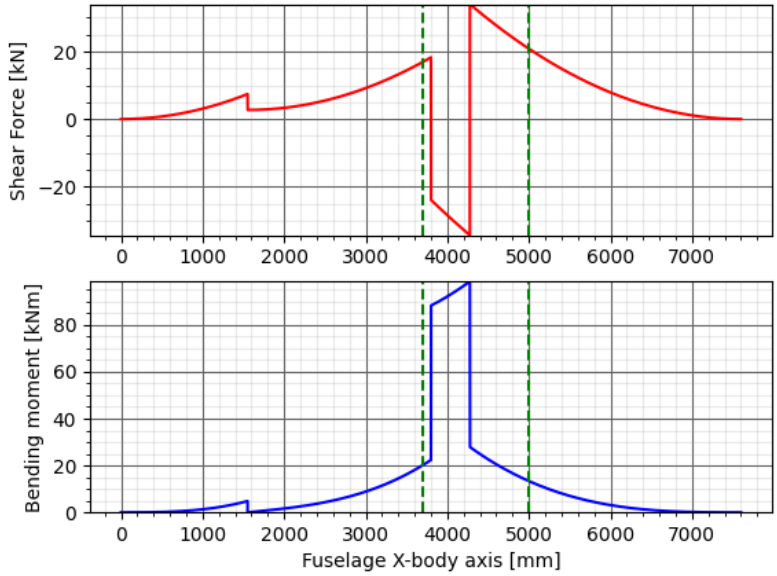

Figure 9.18: *Shear force and bending moment diagrams for the Electrobat at* $8\,\mathrm{G}$

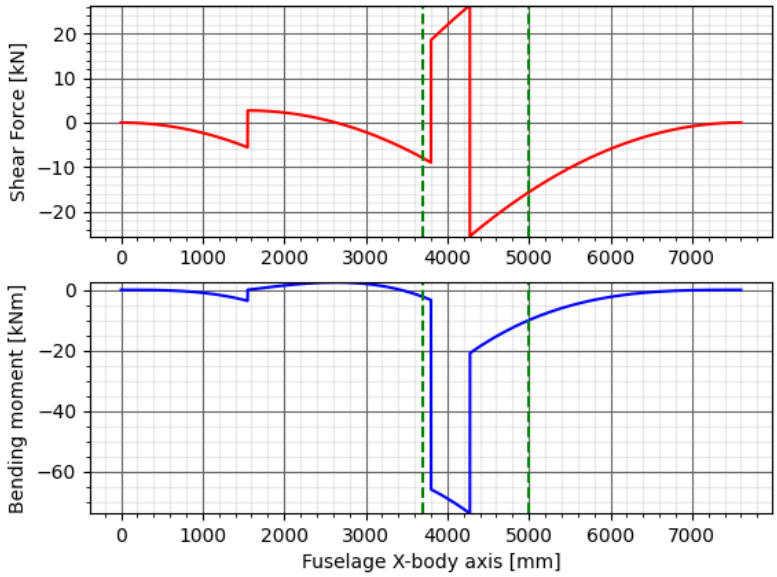

Figure 9.19: *Shear force and bending moment diagrams for the Electrobat at* $-6\,\mathrm{G}$

Accounting for a safety factor of 1.5, at $8\,\mathrm{G}$, the Electrobat experiences a maximum shear force of roughly $51\,\mathrm{kN}$ and a maximum bending moment of roughly $147\,\mathrm{kNm}$ in the vicinity of the wing-fuselage interface.

Figure 9.20: *Fuselage cross-section used for analysis, highlighted in orange (indicated with the green lines in Figure 9.18 and Figure 9.19.*

To ensure the structural integrity of the fuselage during the mission of the Electrobat. It is wise to analyse the loads at their highest possible loading, which is at $8\,\mathrm{G}$. It is also important to determine where, along the fuselage, the structure is most vulnerable and requires the most amount of stiffening. As previously mentioned, given the time constraint of this project, a specific section of the fuselage was to be chosen for further analysis. For the case of the Electrobat, based on the external design of the fuselage given in Section 7.3, the section of the fuselage right behind the cockpit and just before the engine was deemed to be the most critical. The stiffening of this section of the fuselage purely comes from the frames, stiffeners, and skin of the fuselage. This is illustrated in Figure 9.19, where the Macaulay's Step functions are plotted and the section that is to be further analysed is between the 2 green dotted lines. The said section (between the green dotted lines) is the fuselage section that will be discretised and analysed in Subsection 9.3.1 and Subsection 9.3.2. This section is shown from the side in orange in Figure 9.20.

Given the time of this design exercise, it was not possible to design the whole fuselage. Therefore, it was chosen to only do design the highest loaded part of the fuselage with a constant cross-section. As can be seen from the figure, the canopy is part of this cross-section. Due to time constraints, the canopy is assumed to be the same material as the other part of the fuselage, creating a closed cross-section. The fuselage design will thus deviate from how it would be implemented in a final design. However, the design in

this section will still give a clear picture of what a fuselage design would look like given the loads and induced stresses by these loads. Incorporating the canopy in the structural design will be a future consideration.

After the DSE, it will be wise to recompute the stresses for the fuselage by assuming the entire fuselage is one beam. When both the cantilever section of the fuselage is put together, the stresses in the analysed section will be significantly higher than what it is now, at least by $25\,\%$. The analyses conducted previously were simply to help understand what loading modes do to the stringers and skin of the fuselage experiences at that section. As a part of the future consideration, a safety factor of 2.0 is recommended.

9.3.1. Fuselage idealization

Fuselages are structural complex sections which need to be idealised to be able to design and analyse them. They commonly consist of a thin outer skin which is reinforced by stringers and frames to be able to cope with the stresses. The cross-section of the fuselage was idealised using the method from Megson [38]. In this method, the cross-section will be idealised in so-called booms. Booms are concentrations of areas along the cross-section. This idealisation will result in a cross-section as shown in Figure 9.21. The booms are placed at the locations of the stringers. The adjacent skin to the booms is then lumped onto the locations of the booms such that the booms carry all the stresses.

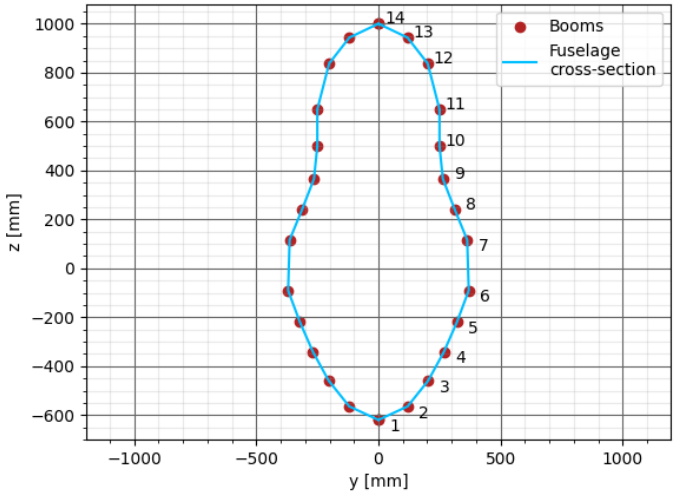

Figure 9.21: *Example of idealised cross-section of fuselage*

The area added to the boom because of an adjacent skin panel is given by Equation 9.10. In this equation t_D is the thickness of the skin mm, b the length of the skin panel mm and σ the stress MPa, j denotes the jth adjacent panel. The stress ratio $\frac{\sigma_j}{\sigma_i}$ is computed by taking the ratio of the distances of the booms to the neutral axis. The total area of each boom is then calculated by taking the sum of the stringer area, and the areas from the adjacent skin panels are calculated by Equation 9.10.

$$B_i = \frac{t_D b}{6}\left(2 + \frac{\sigma_j}{\sigma_i}\right) \tag{9.10}$$

Once the fuselage booms have been calculated, the shear and bending stresses can be calculated. The bending stress in each of the booms can be calculated by using Equation 9.8. From Figure 9.23 it can be seen that the z-axis is an axis of symmetry of the fuselage cross-section. Next to that, there is only a moment applied around the y-axis. The equation reduces to the simple equation shown below:

$$\sigma_x = \frac{M_y}{I_{yy}} \tag{9.11}$$

The moment of inertia of each boom can be found by multiplying the boom area with the distance to the

neutral axis, $\bar{y}$ squared. The total moment of inertia, I_{yy}, then equals the sum of all the moments of inertia of the booms.

Stringers can fail due to buckling when the stress induced by the moment exceeds the crippling stress of the stringer. The crippling stress of a flange of a stringer is calculated by Equation 9.12. In this equation, α and n are constants and equal to 0.8 and 0.6 respectively. σ_y is the yielding stress of the material, however, composites do not have yielding stress so for this the maximum tensile and compressive stresses are taken. For each flange, there are thus different crippling stresses for compression and tensile forces. The values of k_s and v are taken from Figure 9.7.

$$\frac{\sigma_{cc}^{(i)}}{\sigma_y} = \alpha \left[\frac{k_s}{\sigma_y} \frac{\pi^2 E}{12\,(1-v^2)} \left(\frac{t}{b}\right)^2 \right]^{1-n} \tag{9.12}$$

The crippling stress ratio is calculated for all flanges of the stringers. If the ratio from Equation 9.12 is greater than or equal to one, the crippling stress is taken to be the material maximum stress because material failure will happen before column buckling. If the ratio is greater than one, the crippling stress is calculated by Equation 9.13. Once the crippling stress of each of the flanges is calculated, the crippling stress of the stinger can be calculated by using Equation 9.14, in which A_i is the area of each of the stinger flanges in mm^2.

$$\sigma_{cc}^{(i)} = \left(\frac{\sigma_{cc}^{(i)}}{\sigma_y} \right) \cdot \sigma_y \tag{9.13}$$

$$\sigma_{cc} = \frac{\sum \sigma_{cc}^{(i)} A_i}{\sum A_i} \tag{9.14}$$

The formula for calculating the shear stress is given by Equation 9.15. This formula can be used because it is assumed that skin is only carrying skin shear stress. Next to that, only a force in the y-direction is applied.

$$q_s = -\frac{S_z}{I_{zz}} \sum_{r=1}^{n} B_r z_r + q_{s,0} \tag{9.15}$$

As the force is applied on the symmetry axis, the resultant shear flow, $q_{s,0}$ will be zero. The shear flow is analysed starting from the section between points 1 and 2, where the shear flow is set to be zero. The shear flow in the other panels will then be calculated by going over the fuselage section in a counter-clockwise direction. Due to the symmetry, only half of the fuselage will be analysed, so between points 1 and 14. The shear stress can be found by multiplying the shear flow from Equation 9.15 with the skin thickness.

Another failure mode of the fuselage is skin buckling. Unfortunately, due to time constraints, this failure mode was not addressed in this design iteration. This means that the placement of the frames will be left as a future consideration.

The above method is the discretisation and stress calculations of the fuselage in 2D. The fuselage will however be analysed in 3D. This is done by creating numerous 2D cross-sections behind each other, creating a 3D fuselage. Each of these individual cross-sections will then be analysed on bending stresses, shear stresses and column buckling of the stringers using the loads from Section 9.3.

9.3.2. Fuselage structural design

The first step of the design phase of the fuselage structure is choosing a type of stringer. For the design of the fuselage, the z-stringer was chosen, which is shown in Figure 9.22. The z-stringer was chosen because of the relatively easy manufacturability and the ability to inspect the stringer and fuselage from all angles. Next to that, it has good structural characteristics. To reduce the complexity of manufacturing, the two flange widths are set to be equal, meaning $b_1 = b_2$.

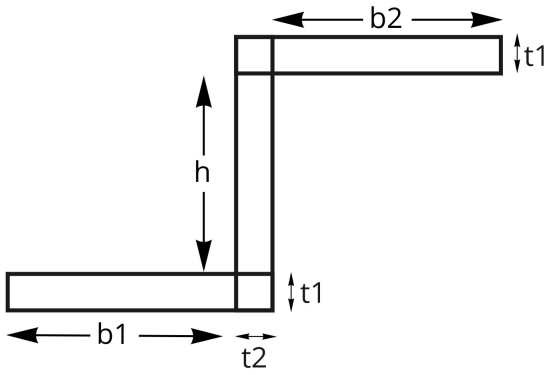

Figure 9.22: *Z-stringer layout*

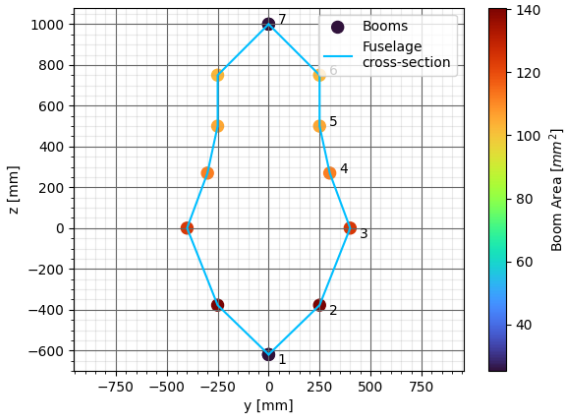

Figure 9.23: *Final design of fuselage cross-section*

Using the z-stringer and the material properties, the design of the fuselage was created using a Python script [1]. The design of the cross-section is shown in Figure 9.23. The cross-section has a total of 12 stringers which run through the whole part of the fuselage designed in this section.

Table 9.4 shows the result of the design of part of the fuselage. The design is a result of the loads for $8\,\mathrm{G}$ and $-6\,\mathrm{G}$ from Section 9.3. As can be seen, all sections have the same number of stringers, but their size changes over the sections. The weight of the fuselage is only the weight of the analysed parts. The skin thickness and weight of the fuselage are very low, which can be explained by the fact of not considering skin buckling in this analysis. Designing for skin buckling will increase the skin thickness and add frames to the structure, increasing the weight.

Table 9.4
Fuselage structural dimensions

		Section 1	Section 2	Section 3	Section 4
Range	[mm]	3696 - 3815	3815 - 4165	4165 - 4450	4450 - 4996
t_D	[mm]	0.32	1.28	0.48	0.32
$b_1\ (=b_2)$	[mm]	10	15	10	10
t_1	[mm]	0.80	1.60	0.96	0.80
t_2	[mm]	0.80	1.44	0.96	0.80
h	[mm]	10	20	10	10
$A_{stringer}$	[mm^2]	25.28	81.41	30.64	25.28
Stringers	[-]	12	12	12	12
Weight section	[kg]	0.27	3.04	0.93	1.24

With the given structural parameters, the stresses within the fuselage cross-section can be calculated. The bending and shear stresses throughout the fuselage are plotted in Figure 9.24 and Figure 9.25 respectively. The jumps in shear stress in Figure 9.25 are because of the change in skin thickness.

[1] URL: https://github.com/Niels-Prins/dseEflyer [Accessed 20 June 2022]

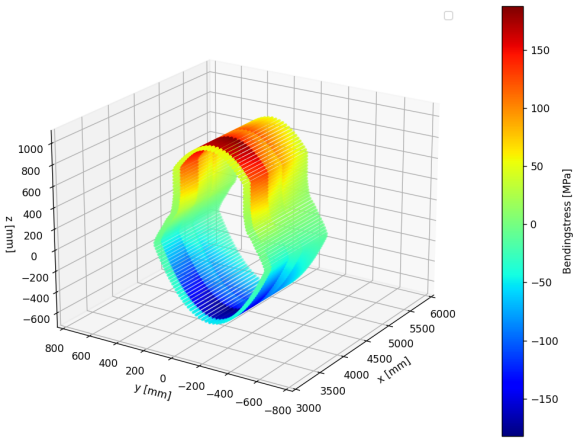

Figure 9.24: *Bending stress across the fuselage for* $8\,\mathrm{G}$

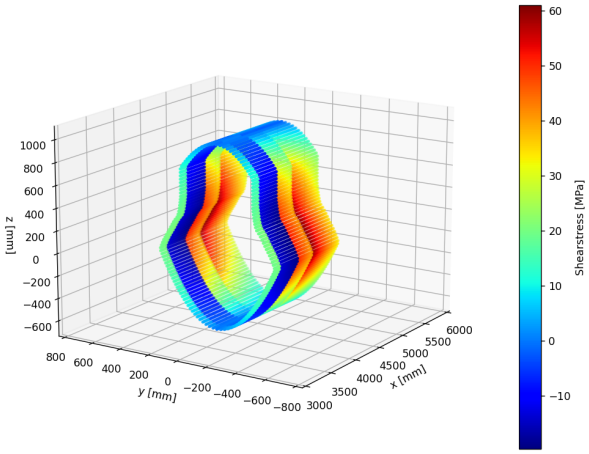

Figure 9.25: *Shear stress across the fuselage for* $8\,\mathrm{G}$

The most important requirement within the design of the fuselage is the requirement that the structure should be able to handle 1.5 times the limit load. Compliance with this requirement is shown in Figure 9.27. From this figure, it can be seen that the maximum material stress is always at least 1.5 times the actual maximum stress in the cross-section.

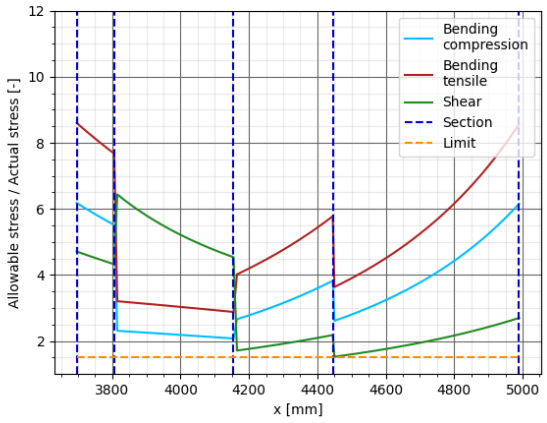

Figure 9.26: *Stress margin across the length of the fuselage at* $8\,\mathrm{G}$

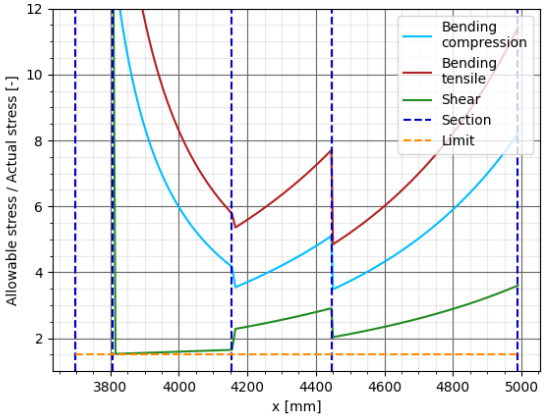

Figure 9.27: *Stress margin across the length of the fuselage at* $-6\,\mathrm{G}$

9.4. Verification & Validation

9.4.1. Wing model

The structural analysis and design of the wingbox has been performed using a Python model [2]. To ensure that the computations in this model are executed correctly, each unit of model was tested separately. This started off with the 3D discretisation of the wing geometry, which was checked through plots. In these the chords and thicknesses were checked to correspond to those in the XFLR model.

After this, unit tests were performed on the calculations of the geometrical properties, such as centroid locations and the cross-sections second moment of areas. Due to the simplifications made in the wingbox geometry, values for these parameters could be easily computed by hand using the methods described in Subsection A.0.2. At the root, tip and mid span of the wing the manually calculated values for the centroid location, I_{xx} and I_{zz} were found to deviate $< 1\%$ from those calculated by the model. This difference is assumed to be the result of round-off errors, thus verifying these units of the model.

[2] URL: https://github.com/Niels-Prins/dseEflyer [Accessed 20 June 2022]

Since the shear flows have been derived analytically before being coded into the model as functions, the derivations have been performed multiple times to verify their correctness. Then once implemented into the Python model, their output was checked in a number of unit tests and compared to manual evaluations of the formulas. Similar to the test of the geometrical properties, the manually evaluated shear flows deviated $< 2.5\%$ of those given by the model. This is also considered to be in the range of round-off errors, thus also these units are considered verified.

The last unit test that have been performed covered the implementation of the critical buckling stresses, given by Equation 9.9 and Equation 9.7. This was once again performed by comparing to manual calculations. Due to the simplicity of these equations however, no difference was found with the Python model.

With these units all verified individually, it can be said with sufficient confidence that that the overall results of the model are correct. In order to do a proper validation however, different methods must be used to make potential flaws are not repeated in the validation model. An ideal candidate for validation of the presented model would therefore be through a model made in Finite Element Analysis software, such as that of Dassault Systems Abaqus. Developing such a different model has however been deemed unfeasible given the time constraints of this DSE. Therefore this is given as a future recommendation.

9.4.2. Fuselage model

As mentioned before, the fuselage was modelled using Python code [3]. To ensure valid results were obtained, this model was verified and validated. The model was verified by calculation by hand. This was done for the previously shown cross-section as well for a different problem, which is shown in Figure 9.29. By verifying the model on two different problems, conclusions can be drawn with greater certainty. The verification was done by both comparing values and using graphs like Figure 9.24 to verify the stress distributions.

The methods were chosen for the model happen to be fully solvable by hand because of the simplicity of the formulas. Because of this, no flaws were found within the program, all the differences between the model and calculation by hand were zero. Therefore, in this subsection, no specific results will be given. Only the problems on which the model was verified will be explained.

The first output of the model that was verified is the calculation of the boom areas. This verification was done on the fuselage cross-section from Figure 9.23 and the closed beam section shown in Figure 9.28.

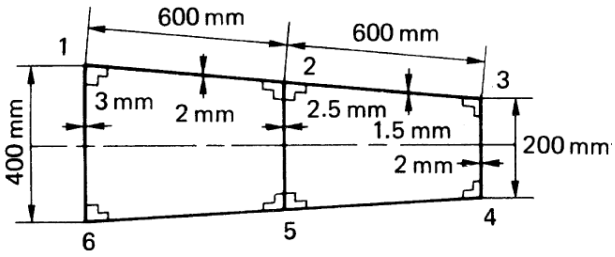

Figure 9.28: *Closed beam section for verification boom areas[38]*

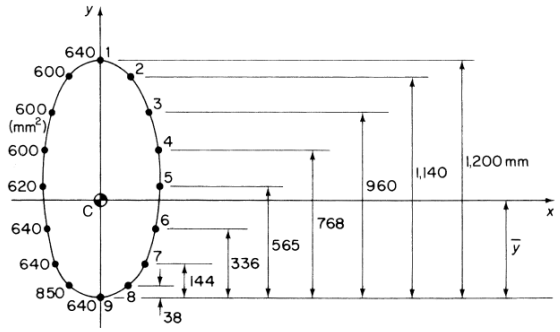

Figure 9.29: *Fuselage verification problem for bending, placed under a load of* $10\,\mathrm{kNm}$*[38]*

The problem shown in Figure 9.29 was placed under a moment of $10\,\mathrm{kNm}$ around the x-axis. This was done to verify the bending moment calculations. No discrepancies were found in this model verification. The next computation that was verified was the shear flow and stress, which was again done on the fuselage cross-section. Lastly, the weight of the fuselage cross-section was verified.

The method used for the fuselage design is a widely applied method for analysing simple structures like fuselages. Therefore, no validation was performed on the method by comparing the results with another method.

[3] URL: https://github.com/Niels-Prins/dseEflyer [Accessed 20 June 2022]

10

Stability and Control

In this chapter, the reference parameters of the Electrobat are iterated to ensure a stable and efficient design. Section 10.1 discusses the reference empennage to use as a starting point of the analysis. In Section 10.2 a static analysis is performed to check if this starting point is at least statically stable and controllable. Section 10.3 briefly discusses the program used to perform the dynamic analysis and Section 10.4 shows the results from this analysis. Additionally, the reasoning behind the final design is discussed in this section. Section 10.5 shows the final empennage design and Section 10.6 discusses the control system used in the Electrobat.

10.1. Initial Empennage Sizing

The stability and controllability of an aircraft are largely determined by the empennage and need to be designed in detail to ensure compliance with the performance requirements. The empennage determines performance characteristics such as the agility of an aircraft and the ability to recover from a spin. The design of this aircraft's empennage is created by the comparison of several reference aircraft that are presented in Roskam [1]. These aircraft all represent the single-engine propeller-driven aircraft category, to which the Electrobat can be best compared. Several driving parameters are given for the horizontal and vertical tail planforms and can be used to design the empennage. These parameters include: control surface fraction, aspect ratio and sweep angle for the horizontal and vertical tail. These parameters are shown in Table 10.8b and Table 10.1a for the horizontal and vertical tail, respectively. The given average parameters, together with the wing surface area as presented in Subsection 7.1.1, resulted in an initial horizontal and vertical tail planform. Most of the parameter values are the averages of the reference aircraft, as it is a starting point for the empennage design. The currently presented results have to be evaluated and iterated after the dynamic stability and controllability analysis to determine the optimal configuration.

Table 10.1
Average empennage planform parameters of reference aircraft in Roskam[1]

(a) *Horizontal tail parameters*

Parameter		Average value
V_h	[-]	0.67
S_h	[m^2]	3.18
$\frac{S_h}{S_w}$	[-]	0.21
Γ_h	[°]	0
i_h	[°]	0
AR_h	[-]	5.15
$\lambda_{c/4_h}$	[°]	5
λ_h	[-]	0.725
$\frac{S_e}{S_h}$	[-]	0.41

(b) *Vertical tail parameters*

Parameter		Average value
V_v	[-]	0.04
S_v	[m^2]	1.49
$\frac{S_v}{S_w}$	[-]	0.10
Γ_v	[°]	90
i_v	[°]	0
AR_v	[-]	1.65
$\lambda_{c/4_v}$	[°]	27
λ_v	[-]	0.45
$\frac{S_r}{S_v}$	[-]	0.36

10.2. Static Longitudinal Stability and Controllability

Using the average parameters of Section 10.1, a scissor plot can be constructed. This plot can quickly show the controllability and static stability of the aircraft as a function of CG location and $\frac{S_h}{S_w}$ ratio. This serves as a starting point for the analysis to see if the initial wing position gives a logical horizontal tail fraction. The stability curve is given by Equation 10.2 and the controllability curve by Equation 10.1 [3]. As can be seen in Figure 10.1, the design is not limited by either of these curves. The two curves even suggest a $\frac{S_h}{S_w}$ ratio of 0.1 can be used, as the CG range is small. The reason for this small CG range is that only the occupants can cause a CG shift, as the fuel and payload do not change and therefore do not have an influence. As said

before, the most optimal $\frac{S_h}{S_w}$ ratio is 0.1 This tail will have a low mass and produce minimal drag, it seems unreasonably small. This is later confirmed in the dynamic stability analysis in Section 10.4. Therefore, a $\frac{S_h}{S_w}$ ratio of 0.2 is chosen as a starting point for the horizontal tail.

$$\frac{S_h}{S_w} = \frac{1}{\left[\frac{C_{L\alpha_h}}{C_{L\alpha_{A-h}}}\left(1-\frac{d\varepsilon}{d\alpha}\right)\frac{l_h}{\bar{c_w}}\left(\frac{V_h}{V_\infty}\right)^2\right]}\bar{x}_{cg} - \frac{\bar{x}_{ac} - SM}{\frac{C_{L\alpha_h}}{C_{L\alpha_{A-h}}}\left(1-\frac{d\varepsilon}{d\alpha}\right)\frac{l_h}{\bar{c_w}}\left(\frac{V_h}{V_\infty}\right)^2} \tag{10.1}$$

$$\frac{S_h}{S_w} = \frac{1}{\frac{C_{L_h}}{C_{L_{A-h}}}\frac{l_h}{\bar{c_w}}\left(\frac{V_h}{V_\infty}\right)^2}\bar{x}_{cg} + \frac{\frac{C_{m_{ac}}}{C_{L_{A-h}}} - \bar{x}_{ac}}{\frac{C_{L_h}}{C_{L_{A-h}}}\frac{l_h}{\bar{c_w}}\left(\frac{V_h}{V_\infty}\right)^2} \tag{10.2}$$

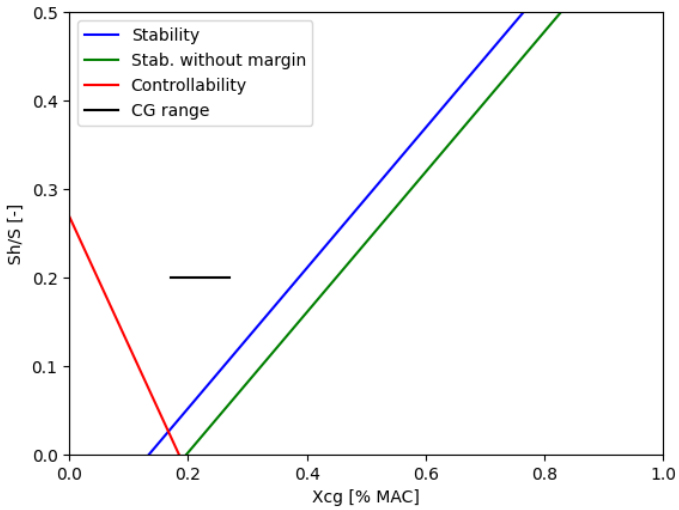

Figure 10.1: *Scissor plot for the Electrobat*

10.3. Dynamic Stability Analysis Program

The program that performs the dynamic analysis has been written in Python and consists of four classes, namely the Aerodynamic Surface, Aircraft, Fuselage, and Solver class [1]. The Aerodynamic Surface class translates the user inputs into Python variables and can calculate the forces and moments on this surface, given an initial condition. The Aircraft class combines these surfaces into a single aircraft and calculates the stability and control derivatives. The Fuselage class applies empirical corrections to the aircraft and wing surface. The Solver class transforms the full equations of motion into the state-space format and calculates the responses of the aircraft, given a control input. With these classes, the program can transform aircraft geometry directly into the expected dynamic response of the aircraft, thus greatly reducing the workload for the user. Changes in aircraft geometry only require a simple re-run of the program, instead of going through lists of equations to obtain the new derivatives. The workings of the program are explained in detail in Appendix B.

Verification
The program has been fully verified using Python unit tests and visual confirmation using plots and print statements [1]. The full description can be found in Appendix C.

Validation
To validate the program, its results are compared to those of the Cessna 172 aircraft. The primary reason to use the Cessna 172 is the fact that it is one of the few subsonic general aviation aircraft which has all the required information available. The full description can be found in Appendix D. The main conclusions from the validation are the underestimation of the aircraft drag, partly due to the inaccurate XFLR analysis and mostly due to the simplified fuselage model used in the program. The effect of this is a destabilised Phugoid

[1] URL: https://github.com/Niels-Prins/dseEflyer [Accessed 20 June 2022]

mode. Because the drag is underestimated, the aircraft is more stable in reality than in the program. Most of the remaining errors are caused by the approximation of the lifting surfaces and the CG location. To solve this, small changes to the input parameters are made, and the program shows convergence to the true values. The low-high wing correction for the spiral mode is deemed too excessive and is omitted in the analysis of the Electrobat, as both validation and an expert review implied the correction is incorrect.

Sensitivity Analysis

Like the other models used throughout this report, a sensitivity analysis has been carried out to ensure the program behaves as expected. Additionally, it helps to determine which parameters influence the dynamic stability the most. All parameters have been checked, of which the most influential ones have been given in Table 10.3 and Table 10.3. Only the Phugoid and Dutch Roll damping ratios and natural frequencies have been evaluated, as both of these modes have complex eigenvalues. As a reference, ζ is equal to $0.059-$ and an ω of $0.170\,\mathrm{rad/s}$ is used for the Phugoid. ζ is equal to $0.014-$ and an ω of $3.280\,\mathrm{rad/s}$ have been used for the Dutch Roll.

Table 10.2
Sensitivity analysis for the Phugoid mode

Parameter			+10%		-10%	
			ζ	ω	ζ	ω
S_w	16.165	[m^2]	-0.17	0.06	-0.68	0.12
S_h	3.353	[m^2]	0.68	-0.12	0.68	-0.18
i_w	0.500	[°]	-0.17	0.12	-0.17	0.12
i_h	-1.000	[°]	-0.68	0.29	-0.85	0.29
X_{CG}	-2.100	[m]	-5.08	2.29	-3.56	1.35
Z_{CG}	-0.700	[m]	0.34	-0.12	0.17	-0.12

Table 10.3
Sensitivity analysis for the Dutch Roll mode

Parameter			+10%		-10%	
			ζ	ω	ζ	ω
S_w	16.165	[m^2]	2.14	-0.10	1.43	-0.12
S_v	3.353	[m^2]	0.71	0.61	0.71	0.62
i_w	0.500	[°]	0.00	0.00	0.00	0.00
i_v	0.000	[°]	0.00	0.00	0.00	0.00
X_{CG}	-2.100	[m]	0.00	-0.01	0.00	0.00
Λ	1.733	[°]	0.00	0.00	-0.71	0.00

As can be seen from the tables, the program behaves as expected. 10% changes in wing and tail geometry only influence the outputs slightly. For the Phugoid motion, changes in CG location have a major influence on the overall stability compared to the other parameters. Again, this is something which is expected. For the Dutch Roll motion, the wing area seems to be of a larger influence compared to the other parameters. The dihedral does not seem to have any effect at all, which is unlikely. This is caused by the reference model, which only has $1.733°$ of dihedral a mere 10% change in this figure will not have a noticeable effect.

10.4. Dynamic Stability Analysis of the Electrobat

The outputs of the program for the Electrobat are given in Table 10.4. These outputs are generated using the empennage as defined in Section 10.1 as a first estimate. The wing planform, as described in Section 7.1, is assumed to be fixed. Other disciplines, like the propulsion and fuselage design, highly depend on their parameters and changes will greatly affect these sub-systems. To determine whether the stability of the Elecrobat is within bounds, the method as described in Appendix B is used. It is assumed the aircraft is a level II, category B and class I/IV, as it is light and required to be manoeuvrable.

With the average parameters, the aircraft was not longitudinally stable. The Phugoid mode was dynamically unstable, even though C_{m_α} was negative. $C_{m_{ac}}$ seemed to be the cause of the problems. After applying an incidence angle of $-4°$, the Phugoid motion became stable. With this as a basis, the reference parameters were iterated to reduce the horizontal tail area. This will directly result in less surface drag and a lighter

design. The second symmetric motion, the short period, is highly damped and well within limits. The eigenvalues and their acceptable bounds are given in Table 10.4, and it can be seen that Electrobat satisfies these bounds.

The asymmetric bounds were significantly more difficult to satisfy. Initially, the aircraft with the low-high wing correction included gave an enormous spiral instability. This suggested active fly-by-wire is required to satisfy the level II category. After validation, it showed that this correction was indeed too excessive and a reduction factor of 2 was applied. The spiral stability was still an issue after this change. An aerodynamic expert peer-reviewed the correction and was highly sceptical about its applicability, after which it was removed entirely from the dynamic analysis. With the current empennage parameters, the aircraft response as shown in Figure 10.2 can be expected. The eigenvalue figures which correspond to this response can be seen in Table 10.4.

The spiral instability is still slightly off the suggested target of $\lambda_{re} < 0.06$. This will be accepted for the following reasons. First, the suggested bound seems to be excessive when compared to reference aircraft. The Cessna Citation is known to be spirally unstable, and its responses are discussed in detail in [41]. Using their asymmetric stability derivatives, the asymmetric real eigenvalue is calculated to be 0.075. According to the reference table, this suggests a too unstable spiral mode, even though it is known this spiral is easily manageable by pilots in reality. The Electrobat has a real eigenvalue of 0.065, suggesting it has a more stable spiral mode compared to the Citation, and this is supposed to be a highly manoeuvrable aerobatic aircraft instead of a small business jet. Secondly, the Electrobat will implement a passive fly-by-wire system, as discussed in Section 10.6. If it seems this instability is undesired during flight testing, dynamic capabilities can be added to ensure an acceptable workload for the pilot, leading to a highly manoeuvrable and safely operable aircraft.

The Dutch Roll was close to neutrally unstable with the initial design parameters. As no dihedral is applied to ensure maximum manoeuvrability during both normal and inverted flight, the vertical fin had to be adapted to fit the design. Most aircraft on which the initial parameters are based have a dihedral applied to ensure stability, this requires a slightly larger vertical fin to ensure a stable Dutch Roll. As the Electrobat does not have dihedral applied, the vertical fin is assumed to be too large. Like the horizontal tail, the vertical tail parameters were iterated to reduce the area, resulting in a smaller tail and a converging Dutch Roll mode as depicted in Figure 10.2. The aperiodic roll mode is well-damped, both before and after the iterations, and is well within the suggested bounds of $\lambda_{re} > -0.30$.

Table 10.4
Eigenvalue parameters for the Electrobat

	λ_{re} [-]	λ_{im} [-]	ζ [-]	ζ_{req}[-]	ω [rad/s]	ω_{req} [rad/s]
Short-period	-0.86	2.52	0.32	0.20 - 2.00	2.38	0.37 - 5.96
Phugoid	-0.01	0.34	0.03	0.00 >	0.34	-
Aperiodic roll	-2.34	-	-	-	-	-
Spiral	0.07	-	-	-	-	-
Dutch Roll	-0.11	2.19	0.05	0.02 >	2.19	0.40 >

As the horizontal tail has a negative incidence angle and the aircraft remains stable at the stall speed, in theory, the aircraft will be recoverable from a stall. This has to be confirmed during flight testing. For now, it is assumed that the vertical tail positioning with respect to the horizontal tail along with its control authority is enough to recover from a spin, as described in Section 7.3. The reason for this is the limited time. It was decided a detailed stability analysis of the aircraft was more beneficial at this point than an in-depth spin analysis. Like the stall, the spin recovery has to be confirmed during flight testing as well.

The control rates of the aircraft were determined by the control derivatives as calculated by the program. The velocity, altitude, and mass input values were changed to get the roll, pitch, and yaw rates of the aircraft and can be seen in Table 10.5 below. It was determined that the mass of the aircraft between one and two occupants had a negligible effect on the roll, pitch, and yaw rates of the aircraft and were thus not added to the table. The take-off and landing configuration have the flaperons deployed and limit the deflection to one wing only, as the wing-up flaperon cannot deflect to a larger angle. The lower deflection angles and velocity result in lower control rates compared to the clean configuration, flying at $77\,\mathrm{m/s}$ and with a larger deflection of the control surfaces. With these control rates, the manoeuvrability requirements as stated by stakeholders in Section 2.2 are satisfied.

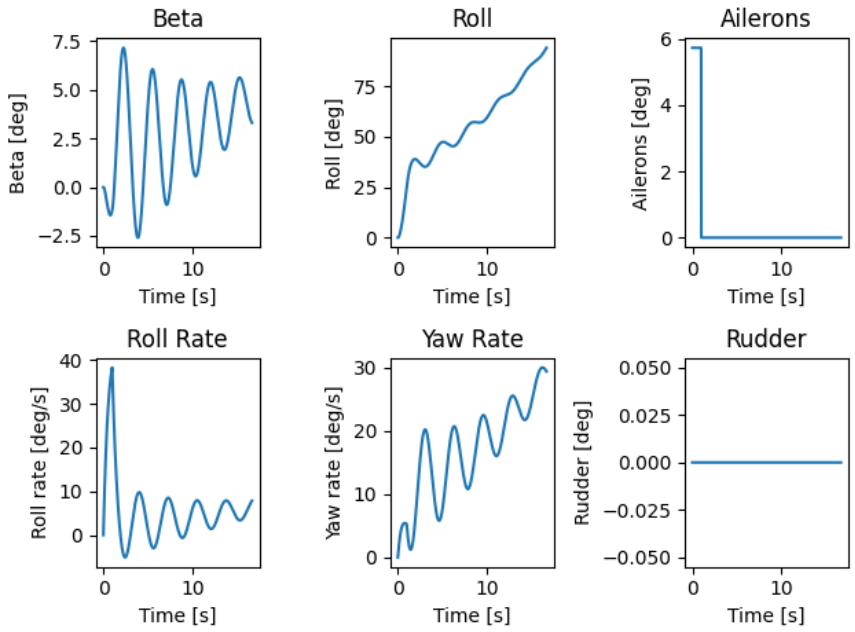

Figure 10.2: *Asymmetric response of the Electrobat*

Table 10.5
Control rates for different configurations and corresponding velocities

Configuration	Velocity [m/s]	Roll [deg/s]	Pitch [deg/s]	Yaw [deg/s]
Take-off / landing	33	115	102	97
Clean	77	571	484	427

10.5. Final Empennage Sizing

Combining the results from Section 10.4, the final empennage can be constructed. The horizontal tail and its parameters can be found in Figure 10.3 and Table 10.6, respectively. The final S_h/S ratio corresponds to 0.21, which is considerable higher than the scissor plot in Section 10.2 suggested. The vertical tail and its corresponding values are presented in Figure 10.4 and Table 10.7, respectively. The sweep angle, based on the information given by literature, is to delay the stall angle of the vertical tail [6]. This is desired for both crosswind landings and aerobatic manoeuvres, as large rudder deflections are required to execute them successfully.

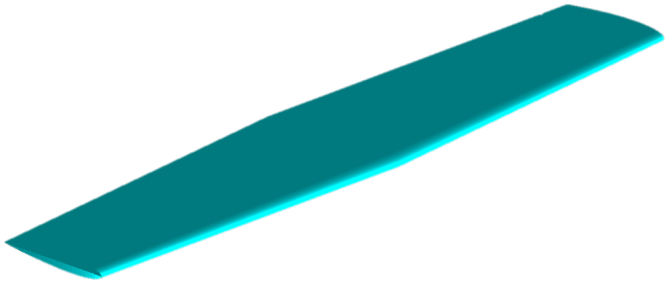

Figure 10.3: *Isometric view of the horizontal tail*

Table 10.6
Horizontal tail planform parameters

Parameter		Horizontal tail
airfoil_h	[-]	NACA 0012
S_h	[m^2]	2.62
b_h	[m]	3.67
AR_h	[-]	5.15
λ_h	[-]	0.72
Λ_{LE_h}	[°]	3.55
$\Lambda_{c/4_h}$	[°]	1.78
Γ_h	[°]	0
C_{r_h}	[m]	0.83
C_{t_h}	[m]	0.60
MAC_h	[m]	0.72
i_h	[°]	-4.00

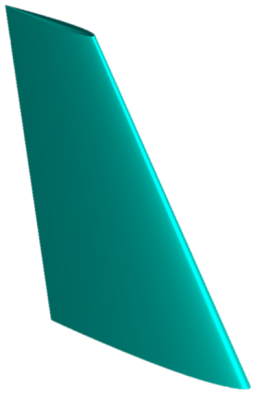

Figure 10.4: *Isometric view of vertical tail*

Table 10.7
Vertical tail planform parameters

Parameter		Vertical tail
airfoil_v	[-]	NACA 0012
S_v	[m^2]	1.23
b_v	[m]	1.42
AR_v	[-]	1.65
λ_v	[-]	0.45
Λ_{LE_v}	[°]	32
$\Lambda_{c/4_v}$	[°]	27.4
Γ_v	[°]	0
C_{r_v}	[m]	1.19
C_{t_v}	[m]	0.535
MAC_v	[m]	0.90
i_v	[°]	0

The calculated areas, chord, spanwise positioning and the maximum deflections of the control surfaces are presented in Table 10.8a. Using these values, the control rates as discussed in Section 10.4 can be reached. Therefore, each aerobatic manoeuvre can be executed successfully. Additionally, sufficient control authority will be available to recover from a stall and a spin, as the control surfaces remain wake-free due to the correct positioning as described in Section 7.3.

Table 10.8
Empennage control surface parameters

(a) *Elevator*

Parameter		Value
S_e	[m^2]	1.09
c_e	[% $\bar{c}$]	30
$b_{e,in}$	[% b]	11
$b_{e,out}$	[% b]	97
deflection_e	[°]	±30

(b) *Rudder*

Parameter		Value
S_r	[m^2]	0.44
c_r	[% $\bar{c}$]	40
$b_{r,in}$	[% b]	0
$b_{r,out}$	[% b]	91
deflection_r	[°]	±30

10.6. Control System

For this aircraft, a fly-by-wire control system was chosen, as it combined well with the other subsystems. The entire layout of the system, including the feedback loops, is given in Figure 10.5. The flight management computers are central to the control system. Computer A and B continuously compute each parameter independently and compare. If it becomes apparent that a duplicate system is not sufficient in terms of redundancy, a third computer can be added to ensure system integrity, as the failure of this subsystem will have catastrophic consequences.

During normal operations, the flight management computer receives various inputs. The sensors supply information to determine the aerodynamic forces used for feedback in the stick. The sensors will also provide information about the angle of attack for stall and G-load warnings. As mentioned before, these warnings must be suppressed in case of a disagreement between the computers. The desired state of the aircraft will be supplied by the cockpit controls and the current state of each sub-system by the sub-systems themselves. The fly-by-wire system does not calculate control deflections but simply transforms an electrical signal into a control surface deflection. Advanced fly-by-wire systems have dynamic control, allowing for automatic trimming of the aircraft and attitude protection, but this is beyond the scope of this project as it requires an in-depth technical analysis, which is not achievable within the given timespan.

A control gain will be implemented in the system, to make the aircraft appealing to both beginner and experienced aerobatic pilots. The flight management computers would simply restrict the maximum control deflections at the operating speed, making the aircraft feel more sluggish than it is. This helps beginner pilots not lose control over the aircraft and can be disabled below certain velocities to ensure full control authority during stall and spin.

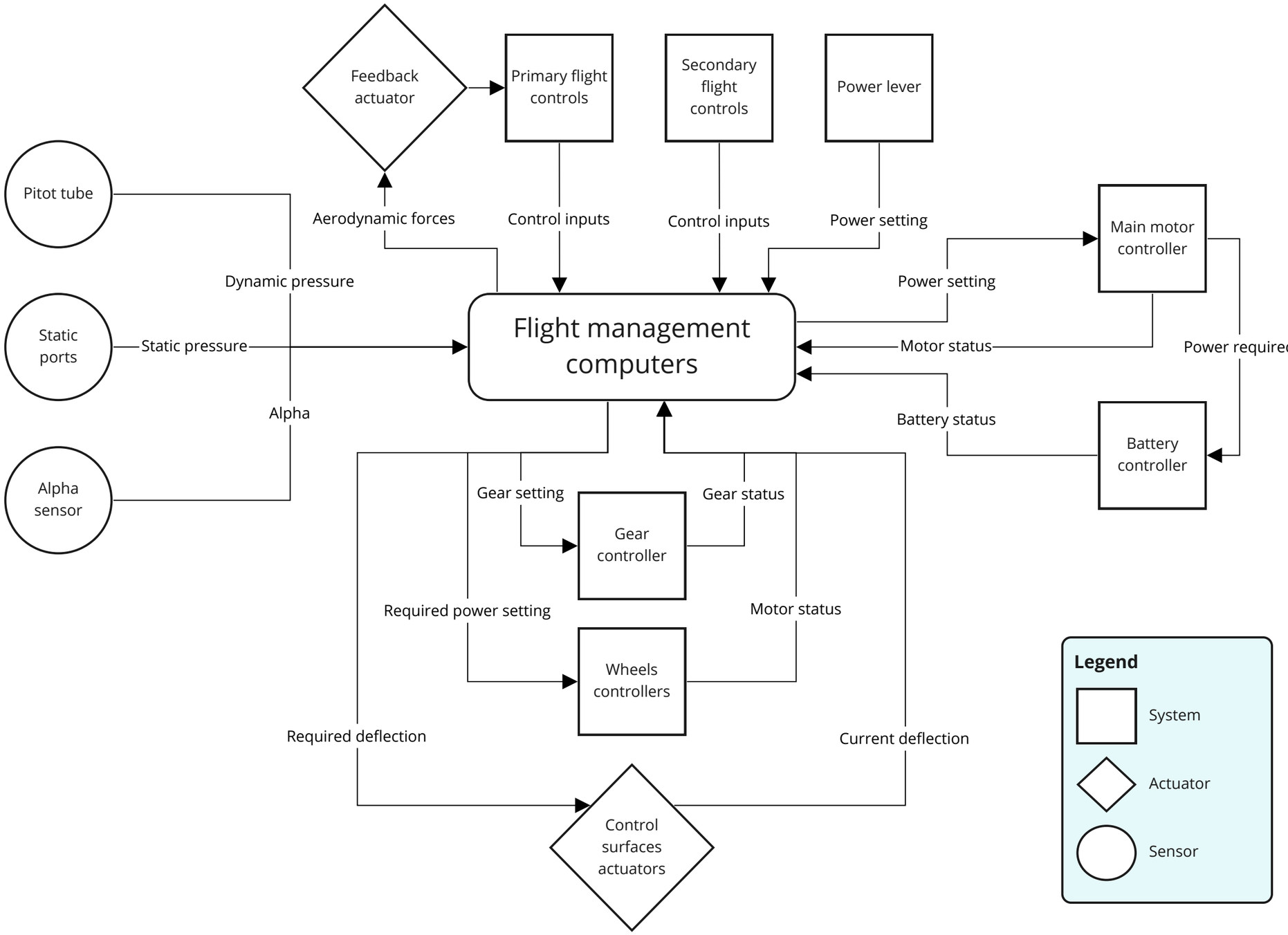

Figure 10.5: *Overview of the Electrobat control system*

11

Final Design Analysis

This chapter investigates whether the performance and cost requirements can be met with the current design. Section 11.1 discusses the performance of the aircraft, Section 11.3 performs a RAMS analysis, Section 11.4 checks if the budget requirement can be met, and Section 11.5 performs a budget breakdown for each subsystem.

11.1. Performance Analysis

In order to verify the compliance of the aircraft design with performance requirements and constraints, a performance analysis is performed. Here, the most critical phases of flight for an aerobatic aircraft are investigated. Namely, take-off, climb, cruise, manoeuvring and landing.

11.1.1. Take-off & Landing Performance

To model the drag during take-off and landing, Equation 11.1 has been used. For take-off, C_f corresponds to the rolling resistance coefficient, for landing, this value also includes the brake force coefficient. The values for C_D are given in Table 7.2. In order to solve the differential equation $\ddot{X} = \frac{F}{m} - \frac{D}{m}\dot{X}$, which is used to model the distances. The thrust force F is assumed to be constant and equal to $3{,}000\,\mathrm{N}$. The velocity component has to be linearised and has been done by solving Equation 11.2 for A. Subsequently, the ordinary differential equation has been solved using the Sympy module, first for $\dot{X}$, to give the total time and afterwards for X, giving the total ground distance. To obtain the take-off distance, an additional 2 seconds at take-off speed has been added to account for the climb to $50\,\mathrm{ft}$. For landing, an additional 4 seconds has been added to account for the flare and multiplied by a factor of $15\,\%$ to account for a grass runway, as suggested in the Extra pilot operating handbook [1]. This leads to a take-off distance of $243\,\mathrm{m}$ and a landing distance of $438\,\mathrm{m}$.

$$D = \frac{1}{2}\rho\dot{X}^2 S C_D + C_f m g \tag{11.1}$$

$$\int_0^{\dot{X}_{final}} D dX = \int_0^{\dot{X}_{final}} A\dot{X} dX \tag{11.2}$$

11.1.2. Climb & Glide Performance

The climb rate of an aircraft is important since it is required to climb after take-off and, in the case of an aerobatic aircraft, also during manoeuvres. Equation 11.3 below can be used to calculate the climb rate of an aircraft in case the thrust and drag are known at a particular altitude and velocity [42]. The thrust was assumed to be constant at sea level, and the drag was calculated with the help of preliminary equations and the data presented in Table 7.2.

The final climb rates that are achievable for the different configurations are presented Table 11.1. These are separated into two cases, one being the aircraft with one occupant and the second with two occupants. This influences the climb rates that can be achieved. The climb rates are relatively high compared to the constraint analysis, which was set to $14.5\,\mathrm{m/s}$. This difference can be explained by two design aspects. The first is that the mass used for the constraint analysis was higher compared to the final values used for this analysis. The second aspect is that the thrust is over-estimated for this analysis because the power is related to the RPM of the engine, which decreases when exceeding $5{,}000\,\mathrm{RPM}$, as can be seen in Figure 8.3. The same effect can be seen when flying at higher velocities.

$$R/C = \frac{V_\infty}{W}(T - D) \tag{11.3}$$

[1] URL: https://www.saluqimotors.com/products/ [Accessed 10 June 2022]

Table 11.1
Climb rates (R/C) with corresponding velocities (V_∞) and flight path angles (γ) for different configurations at maximum thrust

(a) *Two occupants (mass = 966 kg)*

Configuration	R/C [m/s]	V_∞ [m/s]	γ [°]
Clean	16.0	77	12.0
Take-off	9.3	51	10.5
Landing	5.7	33	9.9

(b) *One occupant (mass = 876 kg)*

Configuration	R/C [m/s]	V_∞ [m/s]	γ [°]
Clean	17.8	77	13.3
Take-off	10.6	50	12.2
Landing	6.7	33	11.7

The gliding performance can be calculated with the same formula as used for the climb rate calculations, but then with zero thrusts. The glide angle and ratio do not depend on the weight of the aircraft and are only of importance for the clean configuration. The reason for this is that an aircraft would like to glide as far as possible when an engine failure occurs. Extra drag from extended flaps or landing gear is thus not desired. The optimal glide angle and ratio were determined to be $4.75°$ and $11:1$, respectively, for a clean configuration with a free rotating fan.

11.1.3. Cruise Performance

It is important to evaluate the cruise performance, and this can be done by constructing a power curve. This power curve is given in Figure 11.1 and from this graph, it can be obtained that the Electrobat has excess power (subtracting the required power from the power available) for the complete range of flying velocities. The cruise speed is indicated by the green dotted line and this also shows that even above this velocity the Electrobat has enough power to fly at these higher velocities.

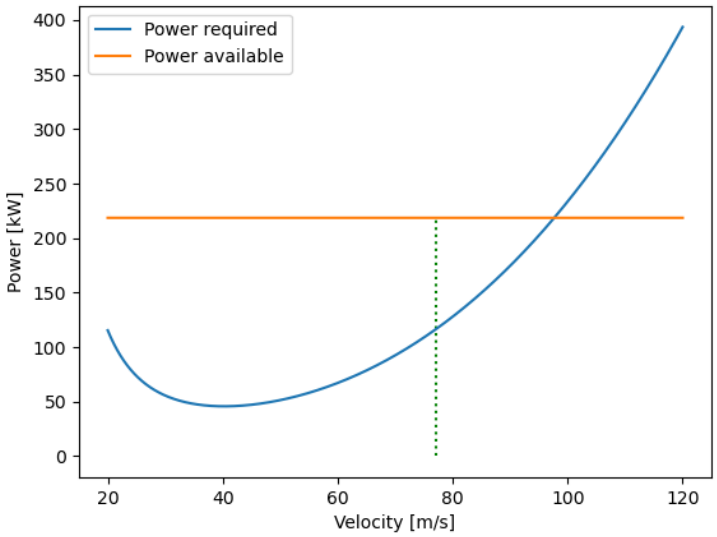

Figure 11.1: *Power curve of the the Electrobat*

11.1.4. Manoeuvres

The aircraft is required to perform a variety of manoeuvres, but to model each of them is beyond the scope of this report. It is assumed each manoeuvre consists of a looping plus a roll or yaw turn. For instance, the Immelmann consists of a half-looping plus a $180°$ roll. The control rates have been discussed previously, and this section will verify if the aircraft is able to perform the looping. The original differential equation is complex and has to be solved using numerical methods. Assuming the aircraft is able to perform the looping, the absolute velocity, $\dot{X}$, and $\dot{Z}$, is given by Equation 11.4 with $\theta = qt$. Thus, at $t = 2\pi$, the aircraft is at the original velocity, unless $\frac{T-D}{m}$ is negative. The lift during the manoeuvre is given by Equation 11.5, with $r = \frac{V}{q}$. The load factor is given by Equation 11.6 using the previously defined expressions for L, r and V. Using the thrust at cruise conditions, the aircraft can perform a $5\,\mathrm{G}$ looping without stalling at the top, as shown in Figure 11.2. The orange line represents the velocity at which the aircraft will stall, due to the increased load

factor, and the blue line represents the actual velocity. As can be seen, the load factor is not constant over time, which is due to its dependency on r and the gravity component, which changes over time. The X and Z positions used in the plot are obtained by integrating Equation 11.4.

$$V = V_0 - gtsin(\theta) + \frac{T - D}{m} \qquad \dot{X} = Vcos(\theta) \qquad \dot{Z} = Vsin(\theta) \tag{11.4}$$

$$L = \frac{mV^2}{r} + mcos(\theta) \tag{11.5}$$

$$n = \frac{V_0 q}{g} + 2cos(\theta) - 1 + \frac{\theta(T - D)}{mg} \tag{11.6}$$

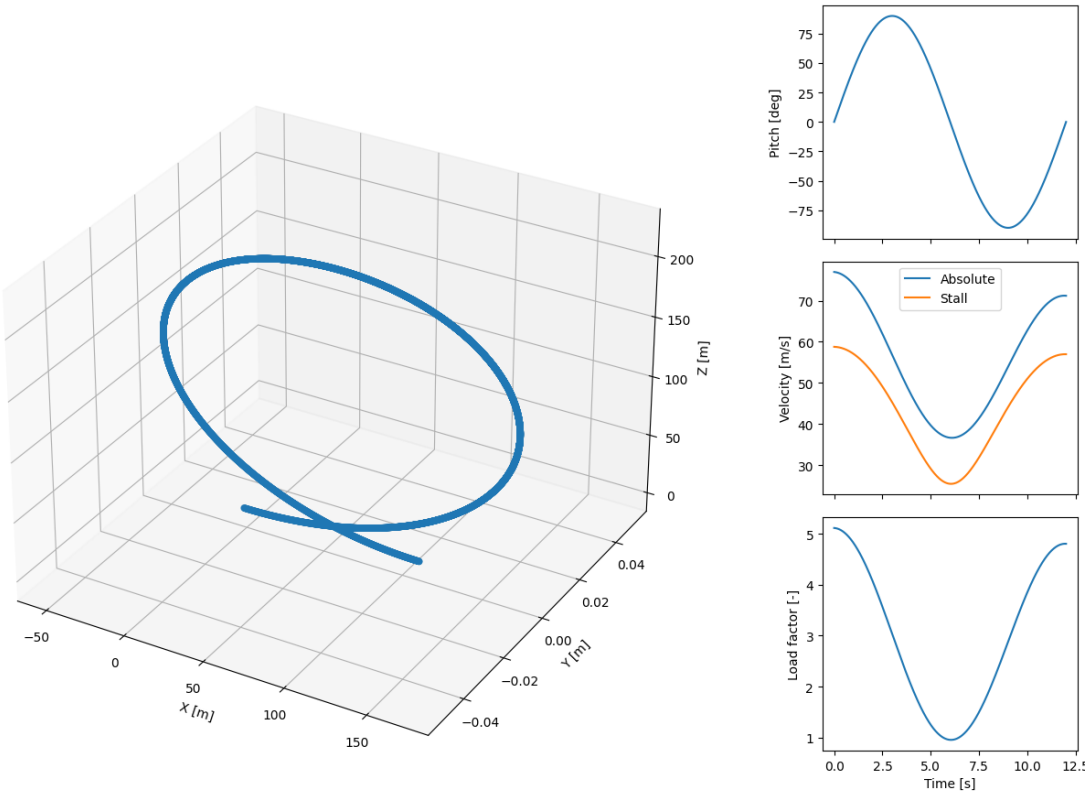

Figure 11.2: *Left plot depicting the flight path of the aircraft, right plots giving the pitch angle, absolute velocity and the load factor.*

For aerobatic turns, the same principle can be used for looping. The pilot rolls the aircraft $90°$ and then pulls to turn with the elevator. The aircraft will lose some altitude as the lift cannot be equal to the weight, but as the manoeuvre is short, this loss will be minimal. The same G-limits as for the looping apply. For a sustained turn, the lift does equal the weight and the induced drag will be significant to normal flight. Using the C_{D_0} and C_{D_α} as described in Subsection 7.1.3, the aircraft is capable of achieving a $3.1\,\mathrm{G}$ sustained turn.

11.2. Technical Risk Analysis

There are technical risks involved in every design. These risks should be identified and mitigated if possible to ensure that the aircraft works properly. Subsection 11.2.1 starts with identifying the technical risks of the Electrobat. This subsection is followed by Subsection 11.2.2, where mitigation strategies are explained for the identified risks. Subsection 11.2.3 ends this section by presenting the risk maps before and after the mitigation strategies have been implemented.

11.2.1. Risk Identification

The technical risks that have been identified for the Electrobat can be divided into ground and flight phases. Each risk is given a unique identifier, so the risks can later easily be referred to. The unique identifier is structured in the following way: risk (RI) is followed by technical (TE), explaining the type of risk. After this, either ground (GR) or flight (FL) are added as phase identification. After these, a more specific sequence flows to distinguish the risks even more. The more specific abbreviations for the flight and ground phase consist of; control (CO), long term (LO), control system (CS) and instruments (IN). An explanation and risk value are added to each risk. The latter is done by assigning each risk a value for probability and severity according to the definitions given in Table 11.2 and Table 11.3 respectively. Table 11.4 and Table 11.5 present the technical risks on the ground and during flight.

Table 11.2
Probability values and corresponding definitions for the technical risk

Probability	Definition	
1	Extremely unlikely	(25 years)
2	Unlikely	(10 years)
3	Occasional	(5 years)
4	Likely	(1 year)
5	Very likely	(monthly)

Table 11.3
Overview of severity values and corresponding definitions of technical risks for the ground phase and the flight phase

Severity	Ground phase	Flight phase
1: Minor	Inconvenient, still operable	Inconvenient but not affecting the operation
2: Moderate	Not operable for 1 day	Small influence on the performance of the operation
3: Significant	Not operable for 1 week	Requiring landing as soon as possible
4: Hazardous	Not operable for 1 month	Hazardous situation resulting in an emergency landing
5: Catastrophic	Not operable > 1 month	Catastrophic crash of the aircraft

Table 11.4
Technical risks during the ground phase with the effects, risk probability, severity and a unique identifier

Identifier	Description	Effect	P	S	RI
RI-TE-GR-01	The aircraft is not properly secured	The aircraft is damaged	4	1	4
RI-TE-GR-02	Engine does not start	There is no propulsion available	3	4	12
RI-TE-GR-03	Electrical systems do not work	The instrumentation in the aircraft is not working	3	2	6
RI-TE-GR-04	Door/canopy failure	The aircraft can not be closed properly	4	2	8
RI-TE-GR-05	Flight control surfaces are not working	The aircraft is not allowed to depart	1	3	3
RI-TE-GR-06	Damage due to exposed propeller	Propeller damage or injured personnel	1	3	3
RI-TE-GR-CO-01	Undercarriage failure	The aircraft is difficult or not controllable on the ground	3	3	9
RI-TE-GR-CO-02	Steering failure				
RI-TE-GR-CO-03	Brake failure				
RI-TE-GR-LO-01	Battery degradation	The flight duration reduces over time	3	1	3
RI-TE-GR-LO-02	Corrosion	The structure will degrade over time	2	1	2
RI-TE-GR-LO-03	Structural fatigue		2	4	8
RI-TE-GR-LO-04	Incorrect maintenance	The aircraft might be damaged	4	3	12

Table 11.5
Technical risks during the flight phase with their corresponding effects, risk probability, severity and a unique identifier

Identifier	Description	Effect	P	S	RI
RI-TE-FL-01	Engine failure	Insufficient thrust to fly	1	4	4
RI-TE-FL-02	Propeller failure due to impact of an object		2	4	8
RI-TE-FL-03	Communication failure	Contact with the ground is no longer possible	4	1	4
RI-TE-FL-04	Cable/hydraulic failure	Aircraft is no longer controllable	1	5	5
RI-TE-FL-05	Inadequately fastened internal components	Unpredictable causal faults, potentially affecting controllability	3	2	6
RI-TE-FL-06	Electrical failure	All electrically powered components fail - thrust, instruments, radio etc.	3	1	3
RI-TE-FL-07	Short circuit	Onboard fire hazard and a potential malfunctioning of electrically powered components	2	4	8
RI-TE-FL-08	Undercarriage failure - jammed landing gear, landing gear door does not open/close	Nominal landing procedures are compromised; Increased drag	2	4	8
RI-TE-FL-CS-01	HLD failure	The aircraft is more difficult to land	2	2	4
RI-TE-FL-CS-02	Ailerons failure	Aircraft loses aerodynamic roll/pitch/yaw control	1	5	5
RI-TE-FL-CS-03	Elevator failure		1	4	4
RI-TE-FL-CS-04	Rudder failure		1	5	5
RI-TE-FL-IN-01	Altimeter failure	Instrument data is no longer reliable	2	3	6
RI-TE-FL-IN-02	Airspeed indicator failure		2	2	4
RI-TE-FL-IN-03	Magnetic compass failure		1	1	1
RI-TE-FL-IN-04	Charge indicator failure		1	4	4

11.2.2. Risk Mitigation

This subsection describes the mitigation plans for the risks as defined in the previous subsection to lower the total risk. These mitigation strategies are presented in Table 11.6 and Table 11.7 for the ground and flight risks, respectively. The identifiers are given for the risks followed by the mitigation strategy, as well as the effect and changed probability or severity values. The effect of this change can be seen in the final risk value.

Table 11.6
Mitigation strategies for the technical risks during the ground phase and their corresponding effects

Identifier	Mitigation strategy	Effect	P	S	RI
RI-TE-GR-01	Recheck the harnesses and replace damaged harnesses	The aircraft doesn't get damaged from improperly secured harnesses	2	1	2
RI-TE-GR-02	Perform regular checks and maintenance on aircraft parts and systems	Any issues with the aircraft parts are discovered and can be fixed on time	2	4	8
RI-TE-GR-03			2	2	4
RI-TE-GR-04			3	2	6
RI-TE-GR-05			1	3	3
RI-TE-GR-06	Ducted propeller design	Propeller is not exposed	1	3	3
RI-TE-GR-CO-01	Perform regular checks and maintenance on aircraft parts and systems	Any issues with the aircraft parts are discovered and can be fixed on time	2	3	6
RI-TE-GR-CO-02			2	3	6
RI-TE-GR-CO-03			2	3	6
RI-TE-GR-LO-01	Charge and discharge the battery during maintenance to see extent of degradation.	Battery Endurance is monitored and can be replaced if degradation is too high	1	1	1
RI-TE-GR-LO-02	Check for leaks in the aircraft's internal structure. Replace panels that are starting to corrode	The aircraft structure remains intact for longer	1	1	1
RI-TE-GR-LO-03	Check for cracks in the aircraft's internal structure Replace panels that have cracks in them	Cracks in the structure do not propagate and cause severe damage	1	4	4
RI-TE-GR-LO-04	Allow maintenance to only be done by trained professionals	Reduces the chance of mistakes being made during inspections and repairs	3	3	9

Table 11.7
Mitigation strategies for the technical risks during the flight phase and their corresponding effects

Identifier	Mitigation strategy	Effect	P	S	RI
RI-TE-FL-01	Perform regular checks and maintenance on the propulsion system.	Propulsion problems can be fixed when discovered before flight	1	4	4
RI-TE-FL-02			1	4	4
RI-TE-FL-03	Perform regular checks and maintenance on the radio system. Have a backup communication system	Contact is always maintained with ground control	3	1	3
RI-TE-FL-04	Check and replace old or faulty cables or hydraulic systems	Prevents critical control failure during flight	1	5	5
RI-TE-FL-05	Perform regular maintenance on all aircraft subsystems. Perform stress tests on smaller subsystems	Ensures that internal components do not fail mid-flight	1	2	2
RI-TE-FL-06	Check for shorts and breaks in the electrical subsystems during maintenance	Prevents electrical failures mid-flight	2	1	2
RI-TE-FL-07			1	4	4
RI-TE-FL-08	Perform regular maintenance and checks on the undercarriage and all related subsystems	Prevents failure of the undercarriage during landing or take-off	1	4	4
RI-TE-FL-CS-01	Perform extensive pre-flight checks on all HLDs and control surfaces pre-flight. Perform regular maintenance on all HLDs and control surfaces	Any issues with these sub-systems are discovered before the aircraft takes off and can be fixed beforehand	1	2	2
RI-TE-FL-CS-02			1	4	4
RI-TE-FL-CS-03			1	3	3
RI-TE-FL-CS-04			1	4	4
RI-TE-FL-IN-01	Have backup instruments. Perform regular checks and maintenance on the instruments.	There is always a source of reliable data available to the pilot	2	3	6
RI-TE-FL-IN-02			1	2	2
RI-TE-FL-IN-03			1	1	1
RI-TE-FL-IN-04			1	3	3

11.2.3. Risk maps

This subsection presents the risk maps of the ground and flight risks before and after the mitigation strategies have been implemented. These are a visual representation of the risks from the risk tables given in the previous subsections. The risk map for the technical risks with and without the mitigation strategies implemented are presented in Figure 11.3a and Figure 11.3b respectively. The maps are colour coded where green areas indicate low risk, yellow areas medium risk and red areas high risk. It can be seen that the risks are reduced after the implementation of the mitigation strategies.

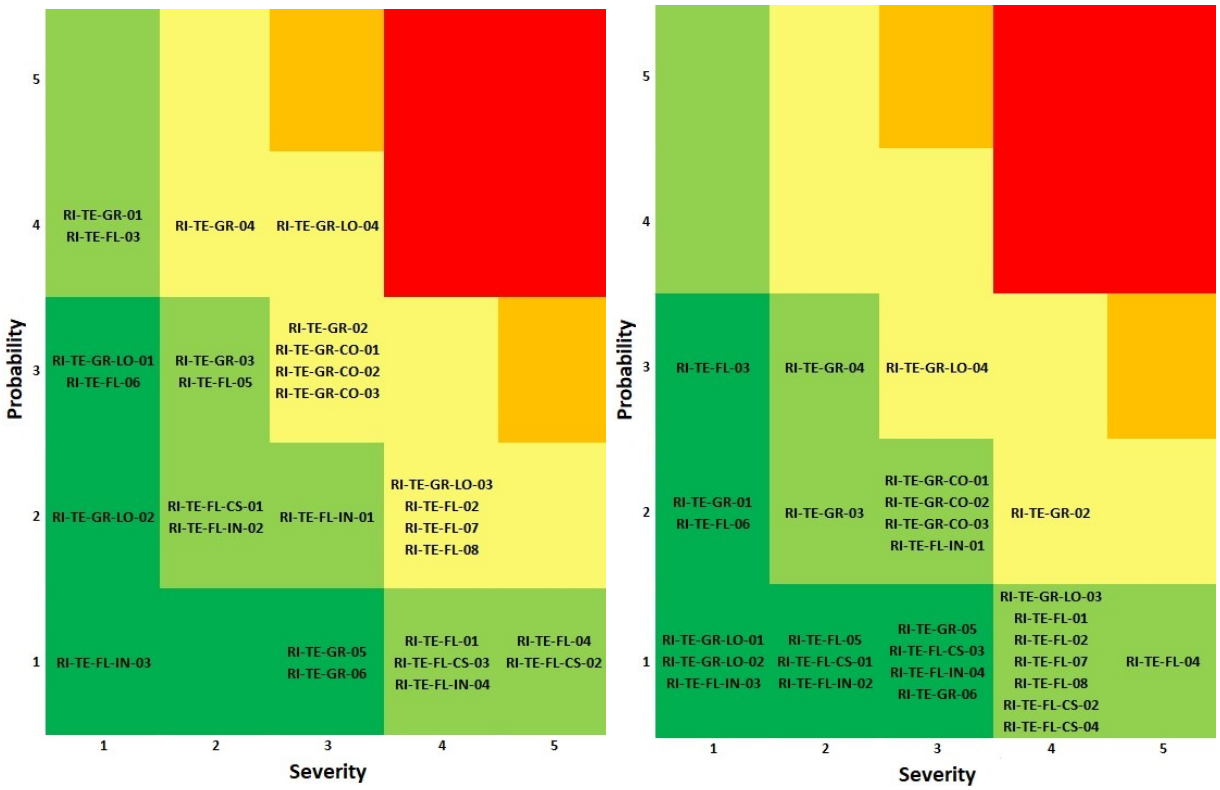

(a) *Technical risk map*

(b) *Technical risk map with mitigation strategies*

Figure 11.3: *Technical risk maps before (a) and after (b) mitigation strategies. Red indicates high risk, yellow medium risk and green low risk.*

11.3. RAMS Characteristics

When the aircraft enters its operation phase, the aircraft must have good operational performance. Future customers want to have an aircraft that would unburden them. To assess the operational performance, RAMS (Reliability, Availability, Maintainability, and Safety) characteristics can be used to give an estimation. The RAMS will only be applied to new technologies as conventional technologies are assumed to be working properly.

11.3.1. Reliability

Designing an aircraft on the limit will result in frequent failures, as the margins are small. This means that repairs have to be performed or that parts have to be replaced. The aircraft should be reliable to minimize downtime. As said before, only the new technologies will be considered.

Electric motor failure
High-performance electric motors are a new development in the aviation sector. These lightweight motors need to generate high amounts of continuous power in order to propel the aircraft forwards. Electric motors are already a proven technology in the automotive sector, which is promising for the aviation sector. There will always be a possibility of an engine failure, therefore the reliability of the aircraft decreases.

Ducted fan failure
Most conventional propeller aircraft use a single pull propeller. This design is well researched and there is a lot of experimental data. The ducted fan however is not widely used in aircraft, this technology is used mostly in drones. As the reference data for ducted fans are scarce, it is quite difficult to come up with a working design. Testing is necessary to ensure that the designed duct and propeller will perform as intended.

High performance batteries failure
As battery technology gets better, the power density will increase. This high power density needs sufficient cooling to keep the batteries in an optimal operating window. There could be a fire in the battery pack if the cooling system does not perform as expected. The batteries will go through extensive testing in order to

ensure the reliability of the battery pack.

11.3.2. Availability

The availability of an aircraft is the percentage of time the aircraft is available to fly. The three main reasons for the downtime of an aircraft are due to the recharging of the batteries, the maintenance of the aircraft and only being allowed to fly during the Uniform Daylight Period (UDP).

Recharging
In order to fly with maximum endurance, the battery should be fully charged ($95\,\%$ of total capacity). The recharge process will take place after every flight, where it will be plugged into fast chargers. These fast-charging stations have to be installed in the hangar to reduce the charging time of the aircraft. A requirement has been set up that the turnaround time, including charging, shall be 3 hours at most.

Maintenance
Maintenance of the aircraft will have a large impact on its availability. As said in Subsection 11.3.1, the aircraft should be reliable in the first place. However, maintenance is always necessary. Inspections after each flight are required to check if there are any visual faults. Next to this, weekly or monthly bigger inspections have to be performed in order to be sure that the aircraft is safe to fly. The estimated downtime of maintenance depends on what kind of faults have been detected that need a repair on replacement.

Operation during nighttime
Due to the strict certification rules of CS-23, it is simply not allowed to fly an aerobatic aircraft after UDP [43]. This will result in fewer flying hours in the winter and more available flying hours during summer. This, however, is a downside for every aerobatic aircraft and not only for the Electrobat.

11.3.3. Maintainability

In order to increase the availability of the aircraft, the recharge time should be lower or the downtime due to maintenance should decrease. The way to decrease the time due to maintenance is to design an easily maintainable aircraft. The maintainability is a measure of how well an aircraft is designed to be maintained. Again, just like in Subsection 11.3.1, only the new technologies are looked at.

Electric motor
The Saluqi P200T6 motor is a compact motor with an integrated inverter and cooling system. If there is a fault in one of these systems, it can be easily taken out for repairs as it is so small. If there is a spare motor around, it can be installed as a replacement. This would significantly reduce the downtime as the aircraft is able to operate sooner. In the meantime, the faulty engine can be repaired.

Ducted fan
A ducted fan, compared to a conventional propeller, will be more difficult to maintain as it is more difficult to reach. It is, however, more shielded against foreign objects, which makes the interval of inspection larger.

Batteries
In the design of the aircraft, maintainability with respect to the batteries was already taken into account. Therefore, the exchangeable batteries were chosen for the design. This will aid in the maintainability of the aircraft, as individual packs can be swapped if the performance is not up to standard.

11.3.4. Safety

Safety is an important aspect of the design of aircraft. Aviation became a lot safer in the last decades also due to the strict regulations from CS-23. As there are new and experimental subsystems in this aircraft design, the technology behind it must be tested thoroughly.

Battery fire
As the batteries used in the aircraft are high performing, they will generate a significant amount of heat. This heat dissipates through the installed cooling and the air flowing over the batteries. This will not guarantee however that a battery will not catch fire. This will be a dangerous situation as a fire can set off a chain reaction in the surrounding batteries.

Fan blade failure

If an unknown object enters the inlet, there is a possibility that a fan blade will break off. This blade should not cause any more damage to the aircraft, as it could result in a catastrophic failure. If the fan blade rips open a battery, an aforementioned fire could start. It is for this reason that the batteries are all placed upstream of the fan to mitigate this risk.

Short circuit
In an event of a short circuit, the electricity in the aircraft will shut off. As the aircraft uses a fly-by-wire system, it would then not be possible to control the aircraft. It is for this reason that there is redundancy incorporated in the battery pack. There are ten battery packs inside the aircraft that power the motor. These individual battery packs can be switched off or could be left out of the circuit in order to mitigate the short circuit. This allows for full control over the aircraft again, which is then able to land in a nearby airport or field.

Motor fire
The Saluqi motor has integrated cooling. The cooling capability of the Saluqi motor should be sufficient to not overheat. If this is the case, the pilot needs to find a place to land as quickly as possible, as the fire is behind the passenger. A firewall is incorporated between the engine and the cockpit to increase the safety of the occupants. Next to this, the aircraft can land on a grass field, therefore multiple emergency landing locations are possible.

Redundant motor
The Saluqi motor consists of four separate motors combined in a single unit. This is preferable for the overall safety of the aircraft, as the motor has a threefold redundant motor. In the event that an individual motor fails, there is still enough power left from the three motors to safely return to an airport to perform repairs to the motor.

11.4. Cost Analysis

Cost is an important factor to keep in mind during the design of an aircraft. The goal is to make this aircraft commercially viable. Therefore, it is necessary to keep the cost as low as possible in order to make it commercially interesting for potential customers. Next to this, a requirement has been established which states that the total production cost of the aircraft shall not exceed €595.000

11.4.1. Market Share

As mentioned in Chapter 3, the Electrobat is targeted at a market (+8 G/-6 G) in which no electric aircraft are available yet. Next to that, most aerobatic aircraft manufacturers are not publishing their annual delivered aircraft, making an estimation of the market size of combustion engine aerobatic aircraft difficult. Therefore, estimating the market share for the Electrobat is not possible. However, a target number of delivered aircraft within 5 years can be set. A target of 75 aircraft sold and delivered aircraft 5 years after completing the certification process is considered to be realistic. This number will be used throughout the cost analysis.

11.4.2. Cost Breakdown Structure

To know what the total cost consists of, it is useful to construct a cost breakdown structure (CBS). The CBS is an AND-tree, and it consists of all the individual sub-parts which contribute to the total cost of the aircraft. The CBS is constructed based on the cost estimation method for general aviation aircraft from Gudmundsson [6]. It is based on the DAPCA IV model, a widely used cost model for estimating aircraft acquisition costs for military aircraft based on Department of Defense data from the United States. The DAPCA IV model therefore greatly overestimates the cost for general aviation aircraft. This is why the model was altered to suit general aviation better by Professor Eastlake in 2000[44]. As can be expected, a lot has changed in the aviation industry since 2000, for example, the use of composites has become a lot more common. Therefore, the model was adjusted to better fit the current state of aviation by Gudmundsson. Recent research by Shariar et al., into the best method to estimate the cost of a general aviation aircraft in an early design stage, showed that the model by Gudmundsson is currently the best source available [45]. The model however was developed in 2012, and thus all the costs needed to be adjusted with the Customer Price Index (CPI) since then. This will result in greater uncertainty in the cost estimate, as not all resources for the aircraft have followed this price index.

The CBS can be seen in Figure 11.4. The model divides the cost into two main pillars, the fixed cost and the

variable cost. The fixed cost can be summarised as all the costs needed to design and certify the aircraft, as well as the construction of build plants. The variable cost is the cost of manufacturing one aircraft. This consists of the material and labour cost for one aircraft and is considered in the €595.000 requirement.

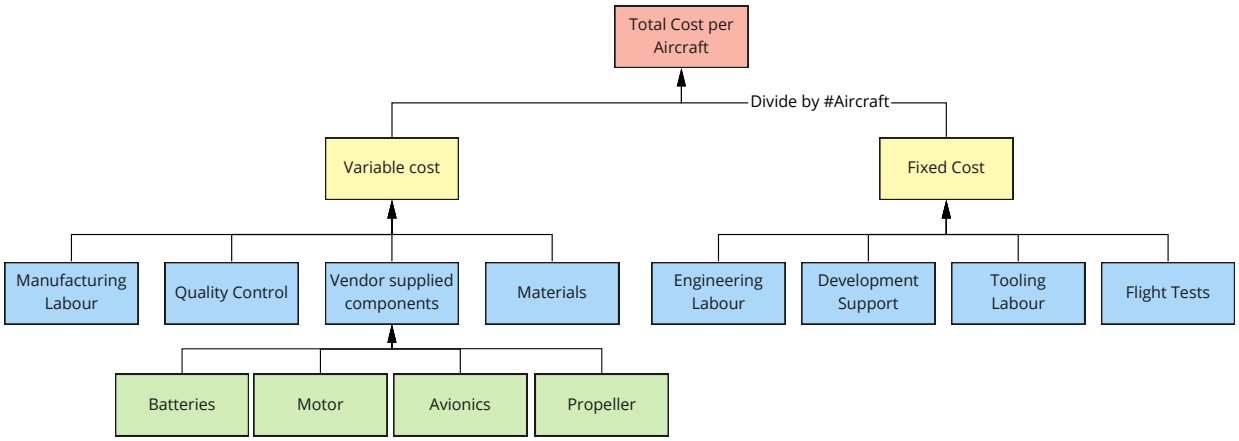

Figure 11.4: *Cost breakdown structure of the Electrobat*

The fixed cost is divided up into four components. The engineering cost is the cost of the man-hours for designing the aircraft. The development support cost is the cost of overhead, administration, logistics, human resources, facilities maintenance personnel and similar entities required to support the development effort, calculate and pay salaries. Tooling entails the cost of designing, fabricating, and maintaining jigs, fixtures, moulds, and other tools required to build the aircraft. For tooling, industrial, and manufacturing engineers are required for the design work and technicians to fabricate and maintain. The cost for the flight test program covers all the costs for the development and completion of the flight tests for certification. These costs are for example dependent on the number of prototype aircraft.

The variable cost is the cost to produce and deliver one aircraft, as mentioned before. The biggest expense for this is the manufacturing labour. Another big expense is the cost of quality control. This entails all the equipment and technicians needed to demonstrate that the produced aircraft complies with all manufacturing standards. Thirdly, the cost for all materials for the aircraft is covered in the variable cost. However, the cost of the propulsion system and avionics are not covered by the material cost since these expensive systems are often bought from an external supplier. Therefore, the cost for propulsion and avionics are covered by the fourth pillar in the variable cost, the vendor-supplied components.

Using these definitions and the formulas associated with them from Gudmundsson, the cost of the aircraft has been estimated [6]. The result of this is shown in Table 11.8. As can be seen, the requirement for the variable cost is met using this method, although there is uncertainty in the results given the large number of parameters that the cost is dependent on.

Almost all cost in Table 11.8 are taken from Gudmundsson [6]. For the materials, a full composite structure was used, which is taken into account by the method. The battery prices are taken from ELEO batteries, and equal €750 per kWh, resulting in a total price of €79.794. The price for the batteries will possibly reduce as batteries in higher numbers will be bought from the supplier. The same holds for the motor. The motor is a Saluqi P200T6 with a maximum power of $260\,\mathrm{kW}$. The price per kWh for the Saluqi motor is €300 when ordering a 100 pieces a year. However, in the current planning 15 motors will be bought per year, which is why a $20\,\%$ margin was added to the motor price. For the avionics, a Garmin GTN 750Xi might be used which cost €17.500 [2]. To incorporate this avionics system with the fly-by-wire system, additional systems are required. These systems are estimated to cost €15.000 which results in a total cost for the avionics and fly-by-wire of €32.500.

11.4.3. Direct Operating Cost

Next to the cost for the acquisition of the aircraft, the direct operating cost is a very important factor for a customer as this will be another big expense. A breakdown of the direct operating cost is shown in Figure 11.5

[2] https://www.garmin.com/en-US/p/606798 [Accessed 20 June 2022]

Table 11.8
Cost estimate of aircraft with 75 aircraft produced 5 years after certification

Component	# hours	Total Cost [€]	Cost per Unit [€]
Engineering (€119/hr)	85714	1.0184.108	135.788
Tooling (€79/hr)	88575	6.977.875	93.038
Development Support	-	939.938	12.533
Flight Tests	-	138.775	135.788
Total fixed cost	-	18.241.000	243.000
Manufacturing (€68/hr)	303575	20.778.947	277.053
Quality Control	-	5.402.526	72.034
Materials	-	2.705.185	36.069
Batteries	-	2.659.500	35.460
Motor	-	6.528.600	87.048
Avionics	-	2.437.500	32.500
Propeller	-	662.625	8.835
Total Variable Cost	-	41.175.000	549.000
Total	-	59.416.000	790.000

based on Gudmundsson [6]. Throughout these calculations, 250 flight cycles of $30\,\mathrm{min}$ per year were used, leading to 125 flight hours per year.

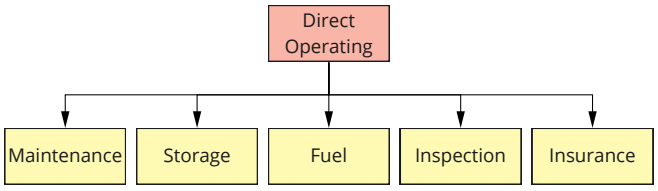

Figure 11.5: *Direct Operating Cost breakdown*

Maintenance cost
Electric aircraft require significantly less maintenance compared to conventional aircraft. The electric engine does not require any maintenance, just like the batteries. The fly-by-wire system also requires little maintenance. However, maintenance does need to be performed on other subsystems like the control surfaces and landing gear. The maintenance cost is dependent on a maintenance-to-flight hour ratio. This was taken to be 0.17[6]. With 125 flight hours per year and an hourly rate of €80 for a mechanic, the maintenance cost is calculated to be €13,60 per hour and €1.700 per year.

Storage
The aircraft needs to be stored at the main base. For this analysis, it is assumed that the monthly cost for storage is €350, leading to a total yearly cost of €4.200.

Fuel cost
Electric aircraft have the benefit of very low fuel costs compared to conventional aircraft, as electricity prices are low compared to jet fuel. In June 2022, $1\,\mathrm{kWh}$ cost €0,55 in the Netherlands[3]. The total battery capacity of the Electrobat is $59.1\,\mathrm{kWh}$, of which $85\,\%$ is used in each flight cycle, as explained in Section 8.3. This means that the cost of recharging the Electrobat after flight equals €27,63. This equals a fuel hourly cost of €55,26. this means that the total cost of electricity each year equals €6.907,50. A suitable option to reduce the electricity cost is to install solar panels on for example the roof of the hangar.

However, it should be noted that the battery capacity reduces over time, and they should be replaced after a certain number of cycles. As mentioned in Subsection 8.3.1, a conservative lifetime of 500 cycles is assumed for the batteries. This means that the batteries should be replaced after two years. With a battery cost of €35.460 and an expected 16 hours of labour hours needed, this means a cost of replacement of €36.740.

[3] https://www.overstappen.nl/energie/energietarieven/ [Accessed 20 June 2022]

Yearly this is a cost of €18.370, which equals an hourly cost of €146,96.

Inspection
The aircraft needs to be inspected by certified aircraft mechanics, to check for maintenance items. Within this method, this is considered separately from maintenance cost. These costs are taken to be €595 per year[6].

Insurance
Estimating the insurance cost is very difficult. It is dependent on the aircraft manufacturer, pilot experience, aircraft class and region, to only name a few parameters. Given the fact that the Electrobat is an innovative aircraft on the market with many uncertainties, insurance costs are not considered in this cost analysis.

Comparison with conventional aircraft
For comparison, the direct operating cost has been calculated using the same method for conventional aerobatic aircraft with a combustion engine, but still having a fly-by-wire system. The basic maintenance cost stays the same, however, the engine needs to be overhauled after a given amount of hours. For Lycoming engines, a commonly used engine, this is usually after around 1500 hours. This means that the engine needs to be overhauled after 12 years. If an engine overhaul costs around €12.000, this comes down to an hourly cost of €8 per hour[6].

The mean increase in cost will be the fuel. Aerobatic aircraft use on average $50\,\mathrm{L/hr}$ with a flight endurance between 25 and $45\,\mathrm{min}$[46]. Using an $30\,\mathrm{min}$ endurance and 250 flight cycles a year, like the Electrobat, this leads to yearly fuel consumption of $6{,}250\,\mathrm{L}$. In June 2022, The price of avgas at Lelystad Airport, a common airport for aerobatic aircraft, was €3,91 per L[4]. Using these numbers, leads to an hourly fuel cost of €195,50 and a yearly fuel cost of €24.438.

The cost for the other categories stays the same, the comparison is added to the third column of Figure 11.5.

Table 11.9
Direct Operating Cost Overview for 125 flight hours a year

	Electrobat [€/hour]	Combustion [€/hour]
Maintenance	13,60	21,60
Storage	33,60	33,60
Fuel	202,21	195,50
Inspection	4,75	4,75
Insurance	-	-
Total	253,91	255,45

Over the lifetime of the aircraft of fifteen years, this results in a total cost of €476.081 for the Electrobat and €478.875 for the conventional combustion engine aircraft. It must be noted that these costs can vary a lot over the course of 15 years as prices for electricity and aviation fuel are changing rapidly. Next to that, there might a significant difference in insurance cost between the two aircraft.

11.4.4. Market Price & Lifecycle Cost

As the unit price of the aircraft is known, the market price can be determined. Consequently, the lifecycle cost of the aircraft can be established. Commonly applied profit margins in general aviation are between 10% and 15%[45]. Given the relatively high price of the production of the aircraft, a profit margin of 10% was chosen to limit the total purchase price. This results in a market price of €871.000. This 10% is also the return on investment for the manufacturers, as the fixed cost was already incorporated in the total cost per unit in the aircraft.

Lifecycle Cost
For the customer, the lifecycle cost (LCC) of the aircraft is very important in the decision-making for an aircraft. The lifecycle cost is given by the purchase price, direct operating cost over the lifetime of the aircraft and the value of the aircraft at the end of life. This last parameter is not possible to estimate at this stage as the aircraft design is different from all others on the market. With the assumed lifespan of fifteen years, the lifecycle cost of the aircraft will be €1.347.000.

[4] https://www.lelystadairport.nl/pilot/brandstofprijzen [Accessed 15 June 2022]

11.5. Resource Budget Breakdown

The resource budget breakdown gives an overview of how the budget of a particular resource is allocated along with the different subsystems. The resource budget allocation is useful as it gives each department an estimate of what their subsystem may weigh, cost and consume power. Therefore, the breakdown is divided into a mass budget, a power usage budget and a cost budget. The values presented in the upcoming tables are obtained from the final design values discussed in previous chapters.

11.5.1. Mass budget

The mass budget represents the total mass of the aircraft. As the design is done in more detail, a better estimate can be given about the mass of every subsystem. The subsystems that are considered are propulsion, controls, structure, electronics, and aerodynamics. The batteries will fall under the electronics subsystem instead of the propulsion subsystem. The aerodynamics will only be the skin panels, as the wing box will fall under the structure of the aircraft.

Table 11.10
Mass budget of individual subsystems

Subsystem	Mass [kg]
Propulsion	107
Controls	50
Structure	285
Electronics	284
Aerodynamics	60
Empty mass	786

The total empty mass is $786\,\mathrm{kg}$. This value is budgeted according to the values found in the final design. The allocation can be seen in Table 11.12.

11.5.2. Power usage budget

In order to know where the power is used in the aircraft, a power usage allocation is constructed. The subsystems that consume power are the propulsion system, controls, and electronics. The propulsion system will consume the largest portion as it drives the ducted fan to propel the aircraft. The electronics controls will consume power in order to extend or retract the actuators to control the aircraft. This will be only a small amount of energy compared to the propulsion system. Then, the electronics will use power due to the onboard computer and the losses in the wire. This will, just like the controls, be a very small portion of the total power usage.

Table 11.11
Power budget of individual subsystems

Subsystem	Power usage [kW]
Propulsion	57.5
Controls	0.5
Electronics	1
Total	59

At this stage of the design, it is difficult to give value to the power usage of the controls and the electronics. It is expected that it will be around the values shown in Table 11.11.

11.5.3. Cost budget

As the aircraft will be commercially available, it is important to have a low-cost price in order to stand out with respect to the competition. Therefore, it is very important to have a good estimate for the budget breakdown of the aircraft. The subsystems that will be considered for the cost breakdown are propulsion, controls, structure, electronics, and aerodynamics. Next to these subsystems, the production is considered in this

breakdown. This is done because the production will contribute a large portion to the final cost of the aircraft, as it must be assembled to complete the aircraft.

Table 11.12
Cost budget of individual subsystems

Subsystem	Cost [€]
Propulsion	136.850
Controls	53.550
Structure	148.750
Electronics	166.600
Production	89.250
Total	595.000

12

Design Rationale

12.1. Sustainable Development Strategy

In modern engineering, sustainability should be encompassed in every aspect of the design: from the design process through usage, up to end-of-life. This is necessary for the market success of the product and its future usability. Sustainability may encompass environmental, economic and social aspects. Environmental sustainability considers the emissions and waste generated by a design throughout its conception, use and disposal. Economic and social sustainability considers the financial and social costs or benefits of a design. For brevity, the sustainability characteristics of the most critical design aspects, the carbon fibre airframe and lithium-ion batteries are discussed.

12.1.1. Production

According to Esfandiar Pakdel, the ”production of virgin carbon fibre is [an] expensive and energy intensive process” [47]. This is reflected by the significantly higher embodied energy (required for manufacturing) of carbon fibre compared with other structural materials such as aluminium or steel. vCFRP components present relatively high production PED of $821\,\mathrm{MJ/part}$ [36]. Additionally, carbon fibre production generates GHGs such as, ammonia, carbon monoxide, carbon dioxide and nitrogen oxide which may be collected and used as fuel or secondary manufacturing resources [47]. For vCFRP production GHG emissions amount to $37.0\,\mathrm{kgCO_2eq/part}$ [36]. Furthermore, the high cost of virgin carbon fibre at $40\,\$/\mathrm{kg}$ results in the material cost of vCFRP (50%vf) of $43.1\,\$/\mathrm{part}$ [36].

Contrasting, while recycled carbon fibres are reported to have inferior mechanical properties when compared with virgin carbon fibre composites, they constitute significant benefits [47]. The embodied energy of recycled carbon fibre is much less than virgin carbon fibre, depending on its recycling method [47]. For reference, the production GHG emissions of rCFRP components are similar or lower relative to GFRP with $8.7\,\mathrm{kgCO_2eq/part}$ [36]. The lowest production GHG emissions of rCFRP can be achieved at $4.4\,\mathrm{kgCO_2eq/part}$ [36]. The largest share of the production emissions is created by the production of matrix material, material processing, and final manufacturing [36]. The cost material cost of recycled carbon fibre is significantly less than that of virgin fibre at $2.2\,\$/\mathrm{kg}$ [36]. This results in material costs of rCFRP of $13.6\,\$/\mathrm{kg}$ when considering more expensive epoxy resin [36]. Material costs of rCFRPs using polypropylene and phenolic resins are estimated at $1.5\,\$/\mathrm{kg}$ and $2.3\,\$/\mathrm{kg}$, respectively [36]. These characteristics pose significant environmental benefits, and material cost-effectiveness while also permitting eco-friendly lightweight strategies.

Consequently, rCFRP is utilised in the implementation of a circular economy in the aircraft’s life cycle. Such a system allows maximum utilisation of materials and components throughout its lifetime by reducing, repairing, reusing, and recycling. A major proponent of material, cost and energy wastage may be eliminated prior to the conception of the aircraft with the implementation of LEAN manufacturing principles during production, and thus will be implemented in the aircraft’s production. This principle focuses on the minimization of waste while maximizing productivity, adding greater value to the final manufactured product. This may be envisioned in developing recycling methods for dry carbon fibre waste, which reportedly accounts for a significant $40\,\%$ of total carbon fibre waste [47]. The two most promising dry waste processing methodologies (as of 2021) include spinning hybrid yarns and developing non-woven products and prepregs [47]. The investigative scope of these methods is saved for future considerations. In order to satisfy the circular economy, still-useful used components shall be absorbed by the aircraft’s OEM and maintenance centres for inspection, repairs, and redistribution for reuse. Furthermore, if the useful lifetime of these parts is exceeded these centres shall recycle the material for the production of lower structural grade or interior components. Moreover, the recycling of the material shall not be limited to reapplication into the aircraft but may be used in the manufacturing of other components, for example, automobile parts, bike frames or furniture.

Production of lithium-ion batteries requires intensive lithium mining and refinement processes, which are slow, inefficient and chemically intensive. Additionally, lithium mining results in the extraction of approxi-

mately $50\,\%$ the available lithium from the mine [1]. This in combination with every tonne of mined lithium reportedly emitting 15 tonnes of CO_2 presents a great challenge for the sustainable production of lithium-ion batteries [2]. Furthermore, these effects are expected to be exacerbated as the global demand for lithium increases to $500\,\%$ of 2018 levels by 2050 [1]. Moreover, together Chile ($41.82\,\%$), Australia ($25.91\,\%$), and Argentina ($10\,\%$) account for $78\,\%$ of the worldwide lithium reserves making the production of lithium-ion batteries heavily reliant on these countries [3]. Similarly, $60\,\%$ of the world's cobalt is mined in the Democratic Republic of the Congo which has questionable human rights violations making its inclusion in the production supply-chain social unsustainable [2]. Therefore, during the development and production of the aircraft close attention will be paid to the novel, more efficient and sustainable methods of lithium and cobalt mining. When a better method presents itself raw materials will be sourced from it. Additionally, considerations for where lithium and cobalt are sourced will be made such as to ensure these materials are not sourced with questionable human rights violations. These could include the sourcing of materials from other countries or from certified mining companies.

12.1.2. Operations

The operational phase of the design dominates the life cycle cost, by mass-induced energy consumption [36]. As previously discussed in Section 9.1, vCFRPs have significant weight-saving properties beneficial for creating a high performance and reduced energy consumption design. The weight-induced power savings achieved outweigh the high cost of virgin carbon fibre materials, which enable vCFRPs to achieve $33\,\%$ life cycle cost savings [36]. Similarly, rCFRP materials are reported to "offer both cost savings and weight reductions relative to GFRP", ranging from 26 to $31\,\%$ life cycle cost reductions depending on the vf [36]. Furthermore, rCFRP components achieve weight reductions while reducing the impact of production due to low embodied energy, GHG emissions and cost-intensive recycling and recycled carbon fibre processing activities. This will allow significant savings and minimize wasted material and components through the implementation of the circular economy concept outlined previously. Therefore, vCFRPs will be used to exploit these weight-induced savings and thus also allow similar savings and environmental benefits of rCFRP components to be utilised in the circular economy of the aircraft.

Lithium-ion batteries offer the benefit of being able to cycle (charge-discharge) hundreds of times before no longer being usable, increasing their usable life span and reducing the waste of single-use batteries. Furthermore, due to their high energy density, they are able to store a greater amount of energy for the same weight as other batteries, which is crucial for high-performance aircraft. Additionally, lithium-ion batteries require less monitoring and maintenance reducing time and cost [4]. Operationally, particle emissions are removed by the use of electric motors. However, depending on a country's energy generation methods these particle emissions are offset by the local or regional power stations. In 2018, Dutch "electricity generation came primarily from gas ($52\,\%$) and coal ($27\,\%$)", while $16.5\,\%$ of electricity came from renewables according to [48]. Moreover, heating and electricity generation was found to be the largest source of energy-related CO_2 emissions $35\,\%$ [48]. However, "Climate Agreement measures would result in at least $70\,\%$ renewable energy share in electricity generation by 2030" [48]. Therefore, it is reasonable to assume that electricity usage of the aircraft may be practically emission-free by 2030, however as this would draw renewable electricity from the grid, non-renewable electricity usage would be allocated elsewhere. This issue may be addressed by airports investigating their own production of renewable energy [5]. An electric passenger car saves $4.6\,\mathrm{tons}$ of CO_2 on average yearly than a fuel-burning passenger car [2]. Therefore, within a couple of years the emissions saved by battery usage would break even with the emissions generated by producing the battery.

12.1.3. End-of-Life

According to the European directive 2000/53/EC, since 2015, it is required to recover and reuse $95\,\%$ of the total vehicle's components and recycle at least $85\,\%$ at the end of their life cycle [47]. This is reflected in the

[1] URL: https://www.suezwatertechnologies.com/blog/sustainable-lithium-mining-technology-behind-improving-yields-and-reducing-waste [Accessed 14 June 2022]
[2] URL: https://meche.mit.edu/news-media/how-much-co2-emitted-manufacturing-batteries [Accessed 14 June 2022]
[3] URL: https://www.statista.com/statistics/606014/distribution-of-world-lithiuim-reserves-by-country/ [Accessed 14 June 2022]
[4] URL: https://interestingengineering.com/clean-evs-and-dirty-lithium-mining-business [Accessed 14 June 2022]
[5] URL: https://www.airport-technology.com/features/sustainable-energy-the-airports-harnessing-green-energy/ [Accessed 13 June 2022]

user requirement that only $10\,\%$ of material is wasted at end of life. The basis for the methodologies aimed at targeting material waste are outlined in Subsection 12.1.1 and are further discussed here.

According to Esfandiar Pakdel, there are three main types of carbon fibre waste, off-cuts from production, prepreg residues or semi-finished products and fibres which can be reclaimed from parts [47]. Furthermore, three main carbon fibre recovery approaches exist namely, thermal, chemical and mechanical [47]. Of these, thermal pyrolysis and mechanical shredding, grinding, and milling are considered to be most economically and environmentally beneficial for industrial-scale carbon fibre recycling. Other recycling methods include high voltage fragmentation, electrohydraulic fragmentation and electrically driven heterocatalytic decomposition, however, the investigation of these methods is reserved for future consideration [47].

The use of recycled carbon fibre components in aircraft is still in infancy and further research and establishment of standards for carbon fibre recycling are required before such components could be integrated into structural aircraft components. Hence, the use of recycled carbon fibre components in the context of the circular economy of the design would be limited to non-primary structural components. This will include, for example, the control surfaces, interiors and more. Moreover, random structure injection moulded rCFRP parts can reduce both life cycle environmentally and cost impacts. Injection moulding parts however are limited to relatively small parts not appropriate for the manufacturing of large aircraft components. Additionally, due to reduce mechanical properties of recycled CF components their down-cycling forms an additional option. Their applications will be extended to include key chains, furniture, or electric scooters.

Lithium-ion batteries are generally safe as they do not contain highly toxic chemicals typically found in conventional batteries, allowing them to be safer to use and dispose of [4]. Furthermore, many main components in lithium-ion batteries can be recovered and reused [4]. Current recycling processes involve pyrometallurgy (smelting) of old batteries, which is an energy-intensive process and recover only cobalt, nickel and copper but not lithium or aluminium [6] [4]. Hydrometallurgy processing (chemical leaching) offers a less energy-intensive alternative and can recover lithium and copper in addition to the other metals but traditionally uses caustic reagents [6]. The materials recovered from the recycling process will be used to make new batteries, lowering manufacturing costs where material costs account for half the battery's cost [6]. More recycling means less virgin material mining and thus less environmental harm. Additionally, down cycling the lithium-ion batteries such that they can be repurposed for use in electric bikes, for example, can reduce battery waste.

Lastly, new research is being conducted into more efficient methods of lithium-ion battery recycling, for example, in May 2022 an NWO-XS grant was awarded to Professor Thijs Vulgt for research into "the use of novel solvents such as supercritical carbon dioxide and crown ether mixtures for better and more efficient lithium battery recycling" [7]. Such research inspires the potential for greater material savings and cost reductions. Therefore, once these more efficient lithium-ion recycling methods appear they will be implemented for the aircraft's batteries.

12.2. Requirements Compliance

The compliance matrix for the stakeholder and system requirements can be found in Table 12.1. Each requirement is abbreviated by its identifier, and next to it is the section where the requirement is satisfied. Some requirements were not addressed during the preliminary design, as they were beyond the scope of this project, or no estimation could yet be made with the limited information available. These requirements are marked with a 'TBD'. Table 12.2 gives the compliance matrix for the regulation requirements. Most of these are marked with 'TBD', as these can only be satisfied after flight testing. Note that the verification methods discussed in Chapter 4 have not been used to verify if the requirement is met. This table serves as an indication that the current design will be able to comply with the requirement. The actual compliance has to be verified during testing.

[6] URL: https://cen.acs.org/materials/energy-storage/time-serious-recycling-lithium/97/i28 [Accessed 14 June 2022]
[7] URL: https://www.tudelft.nl/2022/3me/nieuws/nwo-xs-grants-awarded-to-pe-research-on-smart-membranes-and-lithium-batteries [Accessed 14 June 2022]

Table 12.1
Requirements compliance matrix for the stakeholder and system requirements

Requirement ID	Compliance	Requirement ID	Compliance	Requirement ID	Compliance
EFLY-STK-COST-01	Section 11.4	EFLY-STK-ENV-04	Section 8.2	EFLY-CTRL-03	Section B.2
EFLY-STK-COST-02	Section 11.4	EFLY-PERF-01	Section 11.1	EFLY-CTRL-04	Section B.2
EFLY-STK-USE-01	Section 7.3	EFLY-PERF-02	Section 7.1	EFLY-CTRL-06	Section B.2
EFLY-STK-USE-02	TBD	EFLY-PERF-03	Section 8.3	EFLY-CTRL-08	Section B.2
EFLY-STK-USE-03	Section 8.3	EFLY-PERF-04	Section 11.1	EFLY-CTRL-10	Section B.2
EFLY-STK-USE-04	Section 8.3	EFLY-PERF-05	Section 11.1	EFLY-STR-01	Chapter 9
EFLY-STK-GPER-01	Section 11.1	EFLY-PERF-06	Section 11.1	EFLY-STR-02	Chapter 9
EFLY-STK-GPER-02	Section 7.1	EFLY-PERF-07	Section 11.1	EFLY-STR-03	TBD
EFLY-STK-GPER-03	Section 8.3	EFLY-PERF-08	Section 11.1	EFLY-STR-04	Chapter 9
EFLY-STK-GPER-04	Section 11.1	EFLY-PERF-09	Section 11.1	EFLY-STR-05	TBD
EFLY-STK-APER-01	Section 11.1	EFLY-PERF-10	Section 11.1	EFLY-STR-06	TBD
EFLY-STK-APER-02	Section 11.1	EFLY-PERF-11	Section 11.1	EFLY-EQP-01	Section 7.3
EFLY-STK-APER-03	Section 11.1	EFLY-PERF-12	Section 11.1	EFLY-EQP-02	Section 7.3
EFLY-STK-APER-04	Section 11.1	EFLY-PERF-13	Section 11.1	EFLY-EQP-03	Section 7.3
EFLY-STK-APER-05	Section 11.1	EFLY-PERF-14	Chapter 9	EFLY-OPER-01	Section 7.3
EFLY-STK-APER-06	Chapter 9	EFLY-PERF-15	Section 11.1	EFLY-OPER-02	Section 8.3
EFLY-STK-APER-07	Section 11.1	EFLY-PERF-16	Section 11.1	EFLY-OPER-03	TBD
EFLY-STK-APER-08	Section 11.1	EFLY-PERF-17	Section 10.4	EFLY-OPER-04	TBD
EFLY-STK-APER-09	Section 11.1	EFLY-PERF-18	Section 11.1	EFLY-OPER-05	TBD
EFLY-STK-APER-10	Section 11.1	EFLY-PERF-19	Section 11.1	EFLY-OPER-06	Section 8.3
EFLY-STK-SAFE-04	Section 10.4	EFLY-PERF-20	Section 11.1	EFLY-PROD-01	TBD
EFLY-STK-CPIT-01	Section 8.2	EFLY-PERF-21	Section 8.1	EFLY-PROD-02	Section 8.1
EFLY-STK-CPIT-02	Section 7.3	EFLY-STAB-01	Section 10.4	EFLY-ECON-01	Section 11.4
EFLY-STK-REG-01	TBD	EFLY-STAB-02	Section 10.4	EFLY-ECON-02	Section 7.3
EFLY-STK-REG-02	Section 8.2	EFLY-STAB-03	Section 10.4	EFLY-ENV-01	Section 8.3
EFLY-STK-ENV-01	Section 8.3	EFLY-CTRL-01	Section 7.3	EFLY-ENV-02	Section 12.1
EFLY-STK-ENV-02	Section 12.1	EFLY-CTRL-02	Section B.2	EFLY-ENV-03	Section 8.1
EFLY-STK-ENV-03	Section 8.1				

Table 12.2
Requirements compliance matrix for the regulations requirements

Requirement ID	Compliance	Requirement ID	Compliance	Requirement ID	Compliance
EFLY-REG-DOC-01	Chapter 9	EFLY-REG-PERF-12	Section 11.1	EFLY-REG-SAF-24	TBD
EFLY-REG-DOC-02	Section 5.1	EFLY-REG-PERF-13	TBD	EFLY-REG-SAF-25	TBD
EFLY-REG-DOC-03	Chapter 9	EFLY-REG-PERF-14	Section 11.1	EFLY-REG-SAF-26	TBD
EFLY-REG-DOC-04	Section 10.4	EFLY-REG-SAF-01	TBD	EFLY-REG-SAF-27	TBD
EFLY-REG-DOC-05	Section 7.1	EFLY-REG-SAF-02	TBD	EFLY-REG-SAF-28	TBD
EFLY-REG-DOC-06	Section 11.1	EFLY-REG-SAF-03	TBD	EFLY-REG-SAF-29	TBD
EFLY-REG-DOC-07	Section 11.1	EFLY-REG-SAF-04	TBD	EFLY-REG-SYS-01	TBD
EFLY-REG-DOC-08	Section 11.1	EFLY-REG-SAF-05	TBD	EFLY-REG-SYS-02	TBD
EFLY-REG-DOC-09	Section 11.1	EFLY-REG-SAF-06	TBD	EFLY-REG-SYS-03	TBD
EFLY-REG-DOC-10	Section 11.1	EFLY-REG-SAF-07	TBD	EFLY-REG-SYS-04	TBD
EFLY-REG-DOC-11	Section 11.1	EFLY-REG-SAF-08	Section 8.3	EFLY-REG-SYS-05	TBD
EFLY-REG-DOC-12	TBD	EFLY-REG-SAF-09	Section 7.3	EFLY-REG-SYS-06	TBD
EFLY-REG-DOC-13	Chapter 9	EFLY-REG-SAF-10	TBD	EFLY-REG-SYS-07	TBD
EFLY-REG-DOC-14	Section 11.1	EFLY-REG-SAF-11	TBD	EFLY-REG-SYS-08	TBD
EFLY-REG-DOC-15	Section 11.1	EFLY-REG-SAF-12	TBD	EFLY-REG-SYS-09	TBD
EFLY-REG-PERF-01	Section 8.3	EFLY-REG-SAF-13	TBD	EFLY-REG-SYS-10	TBD
EFLY-REG-PERF-02	TBD	EFLY-REG-SAF-14	Section 7.3	EFLY-REG-SYS-11	TBD
EFLY-REG-PERF-03	TBD	EFLY-REG-SAF-15	TBD	EFLY-REG-SYS-12	TBD
EFLY-REG-PERF-04	TBD	EFLY-REG-SAF-16	TBD	EFLY-REG-SYS-13	TBD
EFLY-REG-PERF-05	TBD	EFLY-REG-SAF-17	TBD	EFLY-REG-SYS-14	TBD
EFLY-REG-PERF-06	TBD	EFLY-REG-SAF-18	TBD	EFLY-REG-SYS-15	TBD
EFLY-REG-PERF-07	TBD	EFLY-REG-SAF-19	TBD	EFLY-REG-SYS-16	TBD
EFLY-REG-PERF-08	TBD	EFLY-REG-SAF-20	TBD	EFLY-REG-SYS-17	TBD
EFLY-REG-PERF-09	TBD	EFLY-REG-SAF-21	TBD	EFLY-REG-SYS-18	TBD
EFLY-REG-PERF-10	Section 11.1	EFLY-REG-SAF-22	TBD	EFLY-REG-SYS-19	TBD
EFLY-REG-PERF-11	Section 11.1	EFLY-REG-SAF-23	TBD	EFLY-REG-SYS-20	TBD

13

Outlook

This chapter will give an outlook on what will happen after the aircraft is designed. The aircraft will have to be produced to bring it out on the market. A production plan is written to outline the steps taken to produce an aircraft. This is discussed in Section 13.1. After this, the design and development logic is discussed in Section 13.2

13.1. Production Plan

After the design phase and performing multiple tests with experimental versions, it was possible to successfully showcase the safety and performance of the aircraft. Commercial production can start, now that the certification is acquired for the aircraft. The production of the aircraft will be done by the means of assembly. Assembly is the integration of several subassemblies to build the finalized aircraft. The main benefit is that the work on individual subassemblies can be performed in parallel and therefore increasing the work efficiency. There are two different divisions during assembly, namely a mounting and a manufacturing division. The difference between these divisions is the method used for joining the subassemblies. The mounting division shall make detachable and exchangeable joints. This is useful for parts that need to be replaced or detached more often than other parts like batteries, landing gear and the wings. The manufacturing division is the complete opposite, as the joining method is permanent. This is mostly used in joining the different parts of the fuselage together.

The different subassemblies that need to be joined together are:

- **Nose:** The nose will hold a large part of the batteries. These batteries will power the aircraft. This subassembly will be joined to the cockpit according to the manufacturing division.
- **Cockpit:** The cockpit will incorporate all the controls and will seat the pilot and potential passenger. The cockpit will also be joined utilizing the manufacturing division to the tail.
- **Tail:** The tail will consist of the duct and will provide support for the propulsion assembly. The combination of the nose, cockpit and tail is called the fuselage.
- **Empennage:** The empennage will consist of the horizontal and vertical tail of the aircraft. This subassembly will be joined to the tail through the manufacturing division
- **Wing**: The wing will be made in-house in a separate station. The wing will be joined to the fuselage according to the mounting division.
- **Exterior duct:** The exterior duct will provide the airflow to the propeller in the tail. This is joined to the fuselage using the mounting division.
- **Interior duct:** The interior duct will sit inside the tail. The interior duct will also hold the engine, driveshaft, propeller and stator. This is joined through the mounting division in the tail.
- **Undercarriage:** The undercarriage consists of the struts and the tyres on which the aircraft will land. The undercarriage will be joined utilizing the mounting division.

The wing should be detachable, as it is necessary for the transportation of the aircraft. The interior and exterior duct should be detachable as well, as it provides a way of easy maintenance of the motor and the propeller. To end, the undercarriage should be detachable because the wear on the tyres is high on concrete runways.

The manufacturing of these subsystems is reserved for future consideration as they are largely dependent on the detailed design of their sub-components. Despite this, it may be assumed that because composite

materials are used in the design similar manufacturing rigs like those used to create the fully composite airframe of the UL-39 will be used as seen in Figure 13.1.

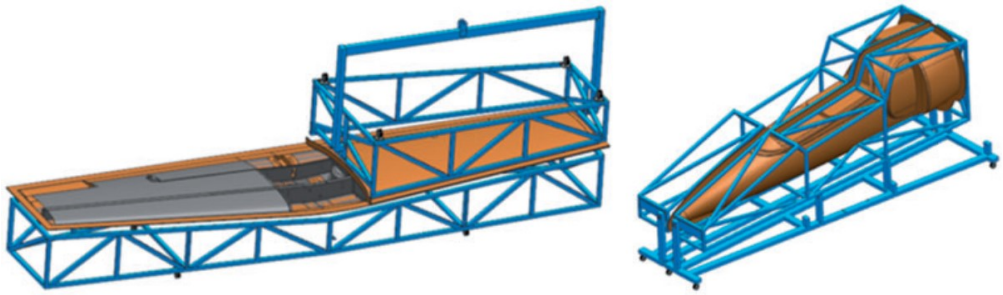

Figure 13.1: *UL-39 wing and fuselage manufacturing mould [17]*

13.2. Design and Development Logic

Following the DSE, the further design and development steps for the completion of the aircraft for eventual delivery to a customer are outlined in Figure 13.2. This includes the design steps performed during the DSE as well as the remaining design steps. Furthermore, considered within the development of the aircraft are testing, certification, and manufacturing of customer aircraft. Lastly, engineering support is to be provided to customers throughout the lifespan of the aircraft. This support includes considerations for component recycling and maintenance.

Additionally, the approximate time frame for these project development steps is depicted in Figure 13.3 giving a comprehensible overview of the entire project lifespan. The concept and definition phases incorporate the tasks performed during the DSE and post-DSE tasks of system development and detailed design. Within these phases, the design freeze milestone was reached where the aircraft's design was frozen and developed into detail. After the finalisation of the system development, the detailed definition freeze milestone is reached in which detailed design is fixed and the next development phase started. In the next phase, the design development is conducted. These include iteration steps of the design throughout the development. Furthermore, the design of tooling and the production process of the aircraft is developed and the test aircraft constructed. This then allows the testing of the structure and systems resulting in the third development milestone, the first engine test. Following this, the first flight milestone is achieved and the flight test and certification campaign begins. Simultaneous to the certification, the manufacturing of parts may take place, marking the final assembly start milestone. Here the customer aircraft are manufactured and assembled and the quality assurance checks are performed. After this the first delivery can be made, marking the final milestone. After this, continued engineering support is provided for the aircraft's customers.

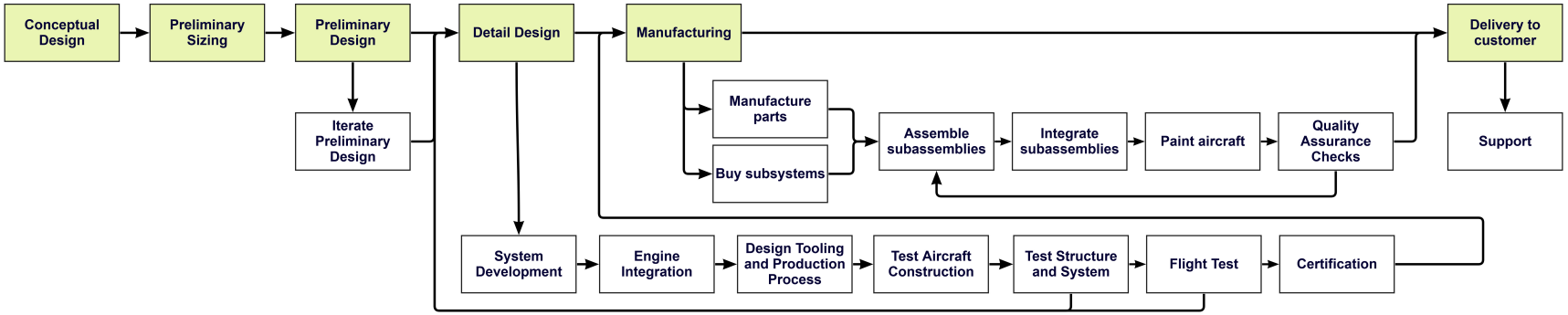

Figure 13.2: *Design and development logic diagram*

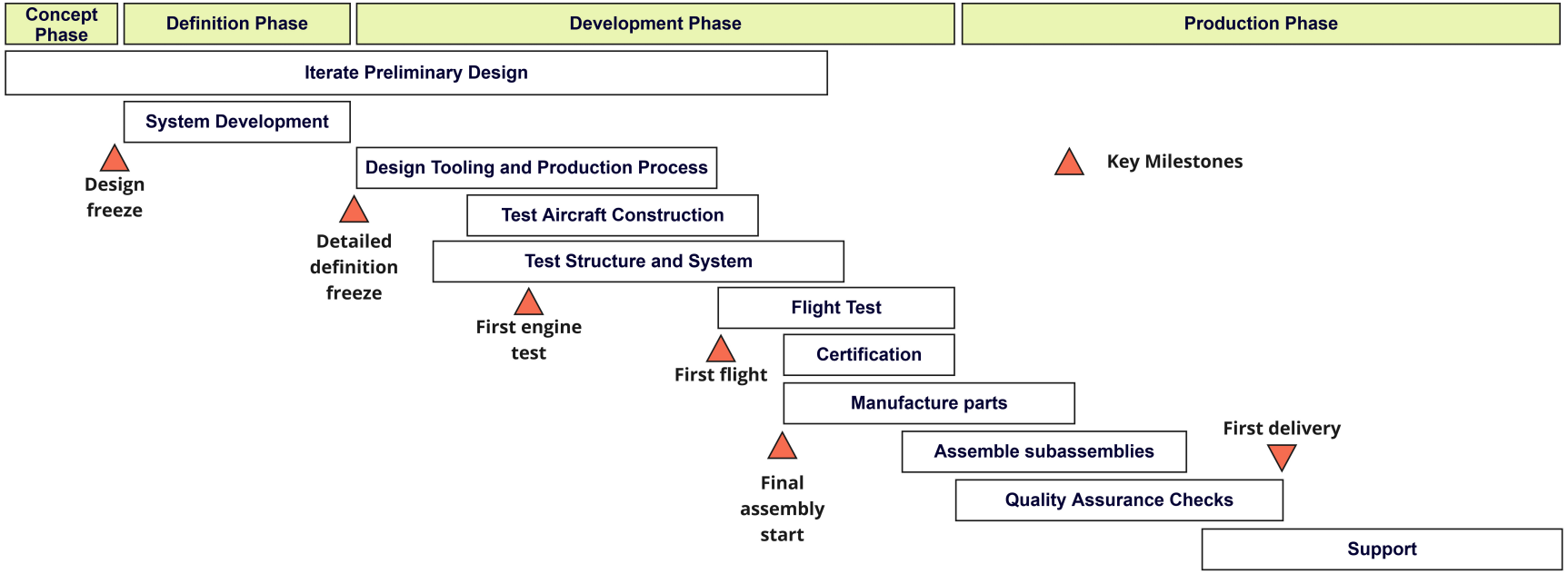

Figure 13.3: *Electrobat development timeline*

14

Conclusion and Recommendations

This chapter outlines the main findings and conclusions of the design process performed by the team. The conclusion itself is presented in Section 14.1 and the recommendations are given in Section 14.2.

14.1. Conclusion

With rising fuel prices and climate change due to air pollution, there is a demand for more sustainable air travel. With aerobatic aircraft, this effect is worsened as large combustion engines demand even more fuel compared to small aviation aircraft. With this in mind, a goal was set to fulfil the following mission statement:

To design an aerobatic electric aircraft capable of having a 40 minutes endurance including reserves and able to withstand +8 / -6 G, by 10 students in 10 weeks.

After an intensive conceptual and preliminary design process, the team was able to design an aircraft which, in theory at least, is able to fulfil this statement. The details of this multidisciplinary design are given throughout this report, but the final design is summarised in Table 14.1. The side view, front view and top view of the aircraft, with its dimensions, are shown in a three view plan in Figure 14.1. Key features of this design are the fully electric controls and ducted-fan propulsion system. Compared to competitors, it is highly manoeuvrable, has fighter like aesthetics and is capable of reduced noise emissions due to the duct.

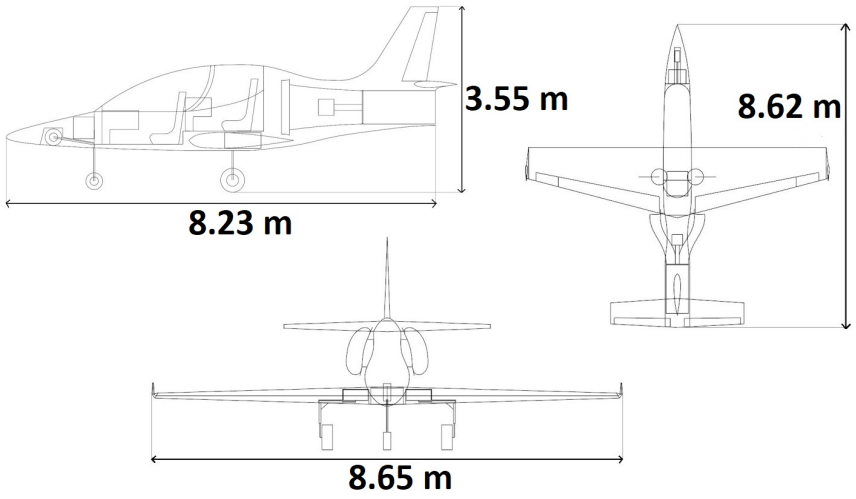

Figure 14.1: *Three view plan of the Electrobat*

Table 14.1
Final design parameters of the Electrobat

Parameter		Value
MTOM	[kg]	966
OEM	[kg]	786
Battery capacity	[kWh]	59.1
Battery recharge time	[min]	98
Never exceed speed	[kts]	187
Manoeuvring speed	[kts]	141
Stall speed	[kts]	50

Parameter		Value
Wing span	[m]	8.48
Wing area	[m^2]	12.30
Length	[m]	8.23
Height	[m]	3.55
Load factor (1 occupant)	[G]	+8/-6
Load factor (2 occupants)	[G]	+6/-4
Take-off distance	[m]	243
Landing distance	[m]	438

14.2. Recommendations

The project objective had to be achieved in no more than 10 weeks, a serious constraint for such a comprehensive project as this. Therefore, a detailed design would simply be unfeasible within the given time-frame, allowing for future recommendations and developments, each of which is discussed briefly in this section.

The aerodynamics parameters estimated using computational methods must be validated and checked with experimental wind tunnel testing. This would allow a more accurate estimation of the aerodynamic parameters such as lift, drag and moments of the aircraft to base further design iterations on. Additionally, this would allow the quantification of fuselage-wing and wing-empennage interactions. Furthermore, this would provide better insight into the interactions of the fuselage and duct.

For the propulsion, the thrust coefficient is obtained from the data of the UL-39. The UL-39 has a fan and one stator. As the aircraft has 2 stators and one fan, the thrust coefficient should be different as well. An accurate value for the thrust coefficient can only be obtained by building and testing the ducted fan. Next to the thrust coefficient, the noise calculation was determined by applying a reduction value due to the duct. This is a very rough estimate, as the duct has a totally different geometry than the data from the literature. To know how much noise is produced, an experimental aircraft must be build to test whether the aircraft meets the noise requirement.

The currently selected batteries by ELEO should be put to the test by simulating the power loads that the battery will nominally experience during the mission of the Electrobat. This indicate how much of the recommended battery capacity is actually spent during its mission. BY knowing this, the exact power density required for the Electrobat can be known. This may entail a lighter battery mass and could allow for the other subsystems to have higher mass allowance, such as a more powerful motor which may be heavier. Given the rapid advancements in battery technology, it is realistic to assume that the power density of the will increase in the future. This is already a noticeable phenomenon in the automotive industry.

Considering the structural design of the wing, a number of further developments can be made to reduce the weight of the wing. First, the composite laminates can be optimised by eliminating the set need for quasi-isotropic properties. This means optimising the directionality of the carbon fibre layers based on the load directions. As this invalidates the assumption of isotropic buckling behaviour, a research effort should be made towards accurately estimating the buckling behaviour of complex composites. Secondly, detailed analysis of the influence of the the landing gear cut-out as well as its attachment points is advised to improve the completeness of the design as well as the weight estimate.

The fuselage structure has only been designed partially and at a high level. The rest of the fuselage should be designed. Next to that, more loads should be considered, such as forces coming from the tail. The fuselage section was considered to be fully closed. This not the case as the canopy is present which will change the strenght of the fuselage. Lastly, skin buckling should be considered in the design.

As for the stability and control subsystem, the design has been evaluated using analytical methods. To ensure that the aircraft is indeed stable, the model should be evaluated using CFD or preferable wind tunnel testing. This is however more applicable in a later design stage. Additionally, the control rates might be optimistic, as they have been derived using steady state aerodynamic damping only. This has to be confirmed during testing as well. The capability of spin recovery has been determined using the positioning of the vertical fin with respect to the horizontal tail. A detailed method to determine the dynamics of the spin is described by Bandu N. Pamadi, but unfortunately insufficient time was available to perform the described analysis [49].

Bibliography

[1] J. Roskam. *Airplane Design: Preliminary sizing of airplanes*. Airplane Design. DARcorporation, 1985. ISBN 9781884885426.

[2] John F.Groeneweg. Aeroacoustics of advanced propellers, sept 1990. Small article for noise of ducted fans.

[3] Dr. F. Oliviero. Systems engineering & aerospace design, mrt 2022. Collection of slides from the course AE3211-I at the faculty of AE at TU Delft.

[4] M. Haddaoui. Development of a propeller source noise model. Delft University of Technology, 2019.

[5] H.H. Hubbard. *Aeroacoustics of Flight Vehicles: Theory and Practice. Volume 1: Noise Sources*. Defense Technical Information Center, 1991.

[6] S. Gudmundsson. *General Aviation Aircraft Design: Applied Methods and Procedures*. Elsevier Science, 2021. ISBN 9780128226476.

[7] Georgia Institute of Technology. *CARL Competition AeRobatic Light-sport*. AIAA, 2016.

[8] B.J. Holmes, United States. National Aeronautics, Space Administration. Scientific, Technical Information Branch, and Langley Research Center. *Flight Evaluation of the Effect of Winglets on Performance and Handling Qualities of a Single-engine General Aviation Airplane*. NASA technical memorandum. National Aeronautics and Space Administration, Scientific and Technical Information Branch, 1980.

[9] Alabama A & M University, R.E. Sheldahl, P.C. Klimas, Sandia National Laboratories, United States. Department of Energy, United States. Department of Energy. Office of Scientific, and Technical Information. *Aerodynamic Characteristics of Seven Symmetrical Airfoil Sections Through 180-degree Angle of Attack for Use in Aerodynamic Analysis of Vertical Axis Wind Turbines*. United States. Department of Energy, 1981.

[10] D.P. Raymer. *Aircraft Design: A Conceptual Approach*. AIAA education series. American Institute of Aeronautics and Astronautics, Incorporated, 2018. ISBN 9781624104909.

[11] André Deperrois. Theoretical limitations and shortcomings of xflr5, 2019. Rev. 1.0.

[12] L.M. Nicolai and G. Carichner. *Fundamentals of Aircraft and Airship Design*. Number v. 1 in AIAA education series. American Institute of Aeronautics and Astronautics, 2010. ISBN 9781600867514.

[13] B. Tillman, P. Tillman, and W. Woodson. *Human Factors Design Handbook*. McGraw-Hill Education, 1992. ISBN 9780070717688.

[14] Jan Roskam. *Airplane Design Part VI: preliminary calculation of aerodynamic, thrust and power characteristics*. Design, Analysis and Research Corporation, 1987. ISBN 9781884885525.

[15] Dhwanil Shukla & Narayanan Komerath. Rotor–duct aerodynamic and acoustic interactions at low reynolds number. *Experiments in Fluids*, 60(20), 2018.

[16] Ritschl. E Hanus. D, Theiner. R. Ultra and very light ducted fan propulsion system complex design optimisation. *International Congress of the Aeronautical Sciences*, 2004.

[17] R Theiner and J Brabec. Experience with the design of ultralight airplane with unconventional powerplant. *Proceedings of the Institution of Mechanical Engineers, Part G: Journal of Aerospace Engineering*, 232(14):2721–2733, 2018.

[18] R Poul and D Hanus. Composite axial flow propulsor for small aircraft. *Acta Polytechnica*, 45(4), 2005.

[19] F.M. de Piolenc and G.E. Wright. *Ducted Fan Design, Volume 1: Volume 1 - Propulsion Physics and Design of Fans and Long-Chord Ducts*. Ducted Fan Design. CreateSpace Independent Publishing Platform, 2001. ISBN 9781517645700.

[20] Christie John Geankoplis. *Transport Processes and Separation Process Principles (Includes Unit Operations), 4th Edition*. Pearson, 2003. ISBN 9780131013674.

[21] Internet Archive. Laminar and turbulent flow, June 2010.

[22] Hunter Rouse. *Elementary Mechanics of Fluids*. John Wiley Amp. Sons London, 1946.

[23] Ir. Wilfried Visser Prof. Ir. J.P. van Buijtenen. *Gas Turbines*. Faculty of Aerospace Engineering, TU Delft, 2011.

[24] Jing Zhang et. al. Aerodynamic benefits of boundary layer ingestion for distributed propulsion configuration. page 2, 2019. doi: 10.1108/AEAT-06-2018-0174.

[25] Frank Del Vecchio. Night flight in an a4b skyhawk. Air Facts: For pilots, by pilots, 2019.

[26] Abhishek Sharma. Design of inlet for boundary layer ingestion in a blended wing body aircraft. page 36, 2015.

[27] Noor Afzal. Friction factor directly from transitional roughness in a turbulent pipe flow. 2007. doi: 10.1115/1.2776961.

[28] Neil Dickson. Icao noise standards. *ICAO Symposium on Aviation and Climate Change, "Destination Green"*, 2013.

[29] DAVID HLAVÁČEK. Methods of ducted fan aircraft propulsion unit noise prediction. *TECHNICAL TRANSACTIONS MECHANICS*, 2013.

[30] Dittmar James H. Methods for reducing blade passing frequency noise generated by rotor- -wake-stator interaction. *Technical Memorandum*, (Report No. NASA TM-X 2669), 1972.

[31] Envia Edmane – Nallasamy M. Design selection and analysis of a swept and leaned stator concept,. *Technical Memorandum*, (Report No. NASA TM-1998- 208662), 1998.

[32] Cengiz. Aktürk, Ali – Camci. Axial flow fan tip leakage flow control using tip platform extensions. *Transactions of the ASME*, Vol. 132, 2010.

[33] G.J.J. Ruijrok. *Elements of avaition acoustics*. Delft University press., 1993.

[34] M. C. Y. Niu. *Composite Airframe Structures: Practical Design Information and Data*. Conmilit Press LTD., 1992. ISBN 962-7128-06-6.

[35] Rao K.P. Ravi Kumar G.V.V. Shama Rao N., Simha T.G.A. Carbon composites are becoming competitive and cost effective, 2018.

[36] et al. Fanran Meng. From aviation to aviation: Environmental and financial viability of closed-loop recycling of carbon fibre composite. Elsevier, 2020.

[37] Seneviratne W. Raju K. S. Tomblin J., Sherraden J. A–basis and b–basis design allowables for epoxy–based prepreg: Toray t700sc-12k-50c/2510, October 2002.

[38] T. H. G. Megson. *Aircraft Structures for Engineering Students*. Elsevier, 6 edition, 2017. ISBN 978-0-08-100914-7.

[39] David Oliver. The l-39ng successfully passed the fuselage strength test. European Defence Review Online, 2020.

[40] Charlotte Adams. Push it to the limit: Push it to the limit: Airframe structural test. Aerospace TechReview, 2020.

[41] Erwin Mooij et al. Ae3202 flight dynamics lecture notes, 2013.

[42] B.T.C. Zandbergen R. Vos, J.A. Melkert. Aerospace design and systems engineering elements i – ae1222-ii, feb 2020. Collection of slides from the course AE2111-I at the faculty of AE at TU Delft.

[43] European Union Aviation Safety Agency. Easy access rules for normal-category aeroplanes (cs-23) (cs amendment 5, amc/gm issue 1), March 2017.

[44] Charles N Eastlake et. al. Cost estimating software for general aviation aircraft design. 2000. doi: 10.18260/1-2--8243.

[45] Ali Shahriar, Azad Khandoker, Guido Gessl, Sabine Sint, M.A. Hamid, Abrar Tariq, and Al Rahman. Predicting the unpredictable: General aviation (ga) aircraft cost estimation evaluation. *Journal of Air Transport Management*, 102:102221, 2022. ISSN 0969-6997. doi: https://doi.org/10.1016/j.jairtraman.2022.102221.

[46] Aircraft Owners and Pilots Association. *The AOPA Aerobatic Certificate Courses Technical Companion Pitts S-2A Special*. Skybrary.earo, 2011.

[47] et al. Esfandiar Pakdel. Recent progress in recycling carbon fibre reinforced composites and dry carbon fibre wastes. Elsevier, 2021.

[48] International Energy Agency. The netherlands 2020. International Energy Agency, 2020.

[49] Bandu N. Pamadi. *Performance, Stability, Dynamics, and Control of Airplanes*. American Institute of Aeronautics & Astronautics, 2014. ISBN 9781624102745.

[50] John Anderson. *Fundamentals of Aerodynamics*. McGraw Hill Education, 2016. ISBN 978-1259251344.

[51] John McIver. Cessna skyhawk ii/100 performance assessment. *Temporal Images-http://www. temporal. com. au*, 2003.

[52] Marek Cel. Cessna 172 flight simulator data. pages 6–7, 2019. doi: 10.13140/RG.2.2.27040.51205.

[53] Coşku Kasnakoğlu. Investigation of multi-input multi-output robust control methods to handle parametric uncertainties in autopilot design. page 15, 2016. doi: 10.1371/journal.pone.0165017.

[54] Cessna Aircraft Company. *Pilot's Operating Handbook Cessna 172*, 1978.

[55] Catalin Nae. Vlm tool for ids integration. page 45, 2010. doi: 10.13111/2066-8201.2010.2.1.5.

A

Wing structural model

A.0.1. Wing discretisation

To reduce complexity and computational time, the wing has been discretised into a variable number of spanwise cross-sections, as shown in Figure A.1. For each of these spanwise sections, the applied loads, geometrical properties, shear flows, bending stresses and deflections are computed. In between the discretised sections, interpolation is used. The accuracy of the interpolation can be increased by increasing the number of spanwise sections, at the cost of extra computational time.

As described in Subsection 9.2.2, the simplified wing structure is assumed to be symmetric. This means that top and bottom skins are of equal thicknesses and stringer distributions are symmetrical over the x-axis, as shown in Figure A.2.

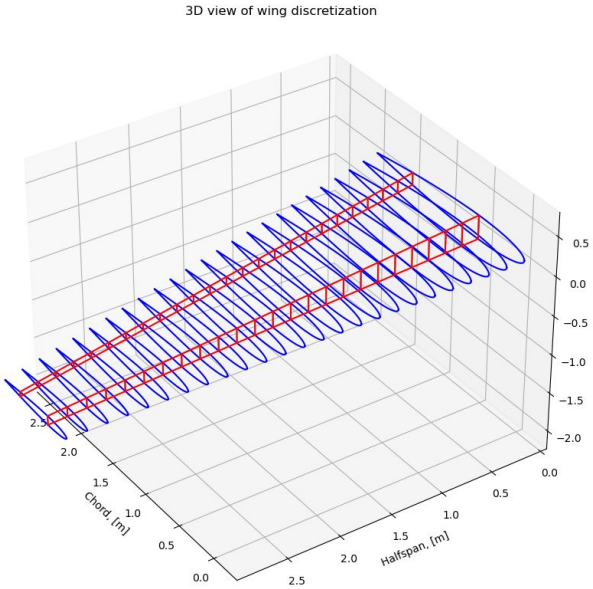

Figure A.1: *Spanwise discretization of the wing*

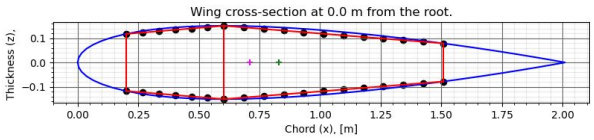

Figure A.2: *Cross-sectional discretisation of the wing*

A.0.2. Second moments of area

Due to the discretisation of the wing, the second moments of area can straightforwardly be computed for each of the spanwise cross-sections. First, the centroid is calculated according to Equation A.1. For this, the centroids of each of the line segments are taken at their centre.

$$\bar{x} = \frac{\sum_i A_i x_i}{\sum_i A_i} \tag{A.1}$$

Equations A.2 and A.3 are then used to determine the contributions of the spars to the second moment of areas, while Equations A.4 and A.5 are used to calculate those of the angled segments. Here β is the angle with respect to the (horizontal) x-axis. The stringers are added as point areas, therefore only accounting for their Steiner terms.

$$I_{xx} = \frac{th^3}{12} + Ad^2 \quad \text{(A.2)}$$

$$I_{zz} = \frac{ht^3}{12} + Ad^2 \quad \text{(A.3)}$$

$$I_{xx} = \frac{a^3 t \sin\beta^2}{12} + Ad^2 \quad \text{(A.4)}$$

$$I_{zz} = \frac{a^3 t \cos\beta^2}{12} + Ad^2 \quad \text{(A.5)}$$

A.0.3. Base shear flow distribution

To compute the shear distribution, two methods were considered, namely structural idealisation and (numerical) integration of the shear flows. Ultimately, integration of the shear flow is chosen over idealisation as the importance of accuracy of the shear flow in the webs is essential for determining the rib placement. This outweighs the additional complexity of setting up the required integrals. If the structure was idealised, the shear flow in between the booms (and thus in the spar webs) would be assumed constant, thus neglecting the variance of shear stress through the height of the spars. Additionally, the skins and spar webs in between the booms would be assumed not direct-stress carrying, which is not applicable in the case of the full load-carrying structure that is being considered [38].

The general equation for calculating the base shear flow along the length of an open section is given by Equation A.6.Here q_b is the base shear flow in $\mathrm{N/m}$; S_z and S_x are respectively the vertical and horizontal shear forces in N; I_{xx}, I_{zz} and I_{xz} are the second moment of areas in m^4, t is the skin/web thickness of the section in m; x and z are the considered coordinates in m as function of s w.r.t the cross-section centroid; s is the length along the section at which the shear flow is being evaluated in m and last but not least q_o is the shear flow in $\mathrm{N/m}$ at the origin of s.

$$q_b = -\frac{S_x I_{xx} - S_z I_{xz}}{I_{xx} I_{zz} - I_{xz}^2} \int_0^s t x ds - \frac{S_z I_{zz} - S_x I_{xz}}{I_{xx} I_{zz} - I_{xz}^2} \int_0^s t z ds + q_0 \quad \text{(A.6)}$$

To simplify the analysis, the structure is designed to be symmetrical over the x-axis. As a result, I_{xy} reduces to zero. Furthermore, the areas of the stringers are smeared out evenly over the skin panel that they are attached to. This increases the effective thickness of each section to account for the contribution of the stringers to the shear flow, but keeps the thickness along a section constant, allowing t to be taken out of the integrals. Combined, these simplifications result in two separate shear flow contributions as a result of a vertical and horizontal shear force, given in Equations A.8 and A.8.

$$q_{bz_i} = -\frac{S_z t_i}{I_{xx}} \int_0^s z ds + q_{bz_{i-1}} + q_{0_z} \quad \text{(A.7)}$$

$$q_{bx_i} = -\frac{S_x t_i}{I_{zz}} \int_0^s x ds + q_{bx_{i-1}} + q_{0_x} \quad \text{(A.8)}$$

To apply these equations to the considered closed, two-cell cross-section, two 'cuts' must be made in convenient locations. At the locations of these cuts, $q_{b_{i-1}}$ is assumed to be zero, therefore integrating the base shear flows of the two cells start there. A redundant shear flow (q_0) must however be added to correct for this assumption [38]. The computation of this redundant shear flow will be covered later in Subsection A.0.4. The sectioning of the cross-section is shown in Figure A.3 as well as the assumed positive shear flow directions.

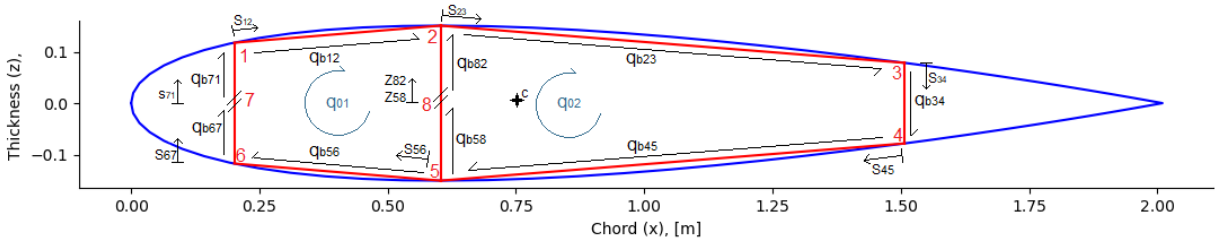

Figure A.3: *Definition of cross-section discretisation and positive shear flow directions*

Points 7 and 8 are convenient locations for making the cuts, as they lay on the symmetry axis. Therefore, for a horizontal shear force (Sx) the shear flow magnitude reaches zero as it crosses the symmetry axis. This means that no correcting redundant shear flow has to be computed for Sx, thus only for Sz.

With this all sorted, the base shear flow distributions are defined as follows:

Section 71: Since point 7 lays on the x-axis and s is defined in positive z-direction, z can simply be substituted

for s, giving Equation A.9. For $q_{bx_{71}}$, x can be substituted by $x = x_6 - x_c$ where x_6 is the x-coordinate of point 6 and x_c the x-coordinate of the centroid. This gives Equation A.10.

$$\begin{aligned} q_{bz_{71}} &= -\frac{S_z t_{71}}{I_{xx}} \int_0^s s ds \\ &= -\frac{S_z t_{71}}{2I_{xx}} \cdot s^2 \end{aligned} \tag{A.9}$$

$$\begin{aligned} q_{bx_{71}} &= -\frac{S_x t_{71}}{I_{zz}} \int_0^s (x_6 - x_c) ds \\ &= -\frac{S_x t_{71}}{I_{zz}} (x_6 - x_c) s \end{aligned} \tag{A.10}$$

Section 12: For $q_{bz_{12}}$, z is substituted by $z_1 + \frac{z_2 - z_1}{l_1 2} s$ where $l_1 2$ is the length of section 12, giving Equation A.11. Similarly, x is likewise substituted with $x_1 + \frac{x_2 - x_1}{l_{12}} - x_c$ to obtain $q_{bx_{12}}$ inEquation A.12

$$\begin{aligned} q_{bz_{12}} &= -\frac{S_z t_{12}}{I_{xx}} \int_0^s (z_1 + \frac{z_2 - z_1}{l_{12}} s) ds + q_{bz_{71}}(l_{71}) \\ &= -\frac{S_z t_{12}}{I_{xx}} (z_1 s + \frac{z_2 - z_1}{2l_{12}} s^2) + q_{bz_{71}}(l_{71}) \end{aligned} \tag{A.11}$$

$$\begin{aligned} q_{bx_{12}} &= -\frac{S_x t_{12}}{I_{zz}} \int_0^s (x_1 + \frac{x_2 - x_1}{l_{12}} - x_c) ds + q_{bx_{71}}(l_{71}) \\ &= -\frac{S_x t_{12}}{I_{zz}} (x_1 s + \frac{x_2 - x_1}{2l_{12}} s^2 - x_c s) + q_{bx_{71}}(l_{71}) \end{aligned} \tag{A.12}$$

Section 82: Since the shear flows of sections 12 and 82 come together in point 2, the shear flow in 82 must be computed before that of 23. In $q_{bz_{82}}$, ds can simply be substituted by dz. This gives Equation A.13. Similar to section 71, $q_{bx_{82}}$ is found in Equation A.22 by taking $x = x_8 - x_c$ while also substituting ds for dz.

$$\begin{aligned} q_{bz_{82}} &= -\frac{S_z t_{82}}{I_{xx}} \int_0^z z dz \\ &= -\frac{S_z t_{82}}{2I_{xx}} z^2 \end{aligned} \tag{A.13}$$

$$\begin{aligned} q_{bx_{82}} &= -\frac{S_x t_{82}}{I_{zz}} \int_0^z (x_8 - x_c) dz \\ &= -\frac{S_x t_{12}}{I_{zz}} (x_8 - x_c) z \end{aligned} \tag{A.14}$$

Section 23: Here, the shear flows of sections 12 and 82 come together and add to the shear flow created in section 23. The substitutions however are very similar to those in section 12 as can be seen from Equations A.15 and A.16.

$$\begin{aligned} q_{bz_{23}} &= -\frac{S_z t_{23}}{I_{xx}} \int_0^s (z_2 + \frac{z_3 - z_2}{l_{23}} s) ds + q_{bz_{12}}(l_{12}) \\ &\quad + q_{bz_{82}}(z_2) \\ &= -\frac{S_z t_{23}}{I_{xx}} (z_2 s + \frac{z_3 - z_2}{2l_{23}} s^2) + q_{bz_{12}}(l_{12}) \\ &\quad + q_{bz_{82}}(z_2) \end{aligned} \tag{A.15}$$

$$\begin{aligned} q_{bx_{23}} &= -\frac{S_x t_{23}}{I_{zz}} \int_0^s (x_2 + \frac{x_3 - x_2}{l_{23}} s - x_c) ds + q_{bx_{12}}(l_{12}) \\ &\quad + q_{bx_{82}}(z_2) \\ &= -\frac{S_x t_{12}}{I_{zz}} (x_1 s + \frac{x_2 - x_1}{2l_{12}} s^2 - x_c s) + q_{bx_{71}}(l_{71}) \end{aligned} \tag{A.16}$$

Section 34: Here, z and x are substituted with respectively $z_3 - s$ and $x_3 - x_c$ to give Equations A.17 and A.18.

$$\begin{aligned} q_{bz_{34}} &= -\frac{S_z t_{34}}{I_{xx}} \int_0^s (z_3 - s) ds + q_{bz_{23}}(l_{23}) \\ &= -\frac{S_z t_{34}}{I_{xx}} (z_3 s - \frac{s^2}{2}) + q_{bz_{23}}(l_{23}) \end{aligned} \tag{A.17}$$

$$\begin{aligned} q_{bx_{34}} &= -\frac{S_x t_{34}}{I_{zz}} \int_0^s (x_3 - x_c) ds + q_{bx_{23}}(l_{23}) \\ &= -\frac{S_x t_{34}}{I_{zz}} (x_3 s - x_c s) + q_{bx_{23}}(l_{23}) \end{aligned} \tag{A.18}$$

Section 45: The substitutions for this section are again similar to those of sections 12 and 23, resulting in Equations A.19 and A.20.

$$\begin{aligned} q_{bz_{45}} &= -\frac{S_z t_{45}}{I_{xx}} \int_0^s (z_4 + \frac{z_5 - z_4}{l_{45}} s) ds + q_{bz_{34}}(l_{34}) \\ &= -\frac{S_z t_{45}}{I_{xx}} (z_4 s + \frac{z_5 - z_4}{2l_{45}} s^2) + q_{bz_{34}}(l_{34}) \end{aligned} \tag{A.19}$$

$$\begin{aligned} q_{bx_{45}} &= -\frac{S_x t_{45}}{I_{zz}} \int_0^s (x_4 + \frac{x_5 - x_4}{l_{45} s} - x_c) ds + q_{bx_{34}}(l_{34}) \\ &= -\frac{S_x t_{45}}{I_{zz}} (x_4 s + \frac{x_5 - x_4}{2l_{45}} s^2 - x_c s) + q_{bx_{34}}(l_{34}) \end{aligned} \tag{A.20}$$

Section 58: Due to the junction formed in point 5, a different approach must be taken. In this junction, $q_{b_{45}}$ flows in while $q_{b_{58}}$ and $q_{b_{56}}$ flow out. This means that to compute $q_{b_{58}}$ from 5 to 8, $q_{b_{56}}$ must be known, while

$q_{b_{56}}$ itself can not be found without knowing $q_{b_{58}}$ first. Therefore, $q_{b_{58}}$ is computed in 'reversed' direction, namely from 8 (where the base shear flow is zero due to the cut) to 5. To compensate for the direction of the shear flow w.r.t. the definition in Figure A.3, an additional factor of -1 is added. Like section 82, ds can be substituted by dz in Equation A.21 while xds is substituted by $xds = (x_5 - x_c)dz$ in Equation A.22. The ranges of both integrals are set from z to 0.

$$q_{bz_{58}} = -1 \cdot (-\frac{S_z t_{58}}{I_{xx}} \int_z^0 z dz) = -\frac{S_z t_{58}}{2I_{xx}} z^2 \quad \text{(A.21)}$$

$$q_{bx_{82}} = -1 \cdot (-\frac{S_x t_{82}}{I_{zz}} \int_z^0 (x_8 - x_c) dz) = -\frac{S_x t_{12}}{I_{zz}} (x_8 - x_c) z \quad \text{(A.22)}$$

Section 56: Now that the base shear flows of sections 45 and 58 are known, that of section 56 can be computed. Here, the substitutions are once again very similar to those of sections 12, 23 and 45 therefore they are left out and Equations A.23 and A.24 are given directly.

$$\begin{aligned} q_{bz_{56}} &= -\frac{S_z t_{56}}{I_{xx}} \int_0^s (z_5 + \frac{z_6 - z_5}{l_{56}} s) ds \\ &\quad + q_{bz_{45}}(l_{45}) - q_{bz_{58}}(z_5) \\ &= -\frac{S_z t_{45}}{I_{xx}} (z_5 s + \frac{z_6 - z_5}{2l_{56}} s^2) \\ &\quad + q_{bz_{45}}(l_{45}) - q_{bz_{58}}(z_5) \end{aligned} \quad \text{(A.23)}$$

$$\begin{aligned} q_{bx_{56}} &= -\frac{S_x t_{56}}{I_{zz}} \int_0^s (x_5 + \frac{x_6 - x_5}{l_{56} s} - x_c) ds \\ &\quad + q_{bx_{45}}(l_{45}) - q_{bx_{58}}(z_5) \\ &= -\frac{S_x t_{56}}{I_{zz}} (x_5 s + \frac{x_6 - x_5}{2l_{56}} s^2 - x_c s) \\ &\quad + q_{bx_{45}}(l_{45}) - q_{bx_{58}}(z_5) \end{aligned} \quad \text{(A.24)}$$

Section 67: Finally, the last base shear flows are computed. Although a similar approach to that of 58 can be taken, it is considered simpler to evaluate $q_{b_{71}}$ in the positively defined direction, namely from 6 to 7. To do so, z is substituted by $z = z_6 + s$ to get Equation A.25. Last but not least, x is can be substituted by $x = x_6 - x_c$, from which Equation A.26 follows.

$$q_{bz_{67}} = -\frac{S_z t_{67}}{I_{xx}} \int_0^s s ds = -\frac{S_z t_{67}}{I_{xx}} \cdot s^2 \quad \text{(A.25)}$$

$$q_{bx_{67}} = -\frac{S_x t_{67}}{I_{zz}} \int_0^s (x_6 - x_c) ds = -\frac{S_x t_{67}}{I_{zz}} (x_6 - x_c) s \quad \text{(A.26)}$$

A.0.4. Redundant shear flow

The redundant shear flow due to the vertical shear force is calculated based on the relationship between the shear flow and rate of twist, given by Equation A.27. Here, $\frac{d\theta}{dy}$ is the rate of twist in $\mathrm{rad/m}$; A_c is the enclosed area in m^2 of the considered cell; G is the shear modulus in Pa; t the section skin/web thickness in m and last, q is the sum of the base and redundant shear flows in the section given in $\mathrm{N/m}$.

So far the base shear flow distributions have been irrespective of the location of the applied shear forces. Since the vertical shear force is primarily a result of the lift and drag forces, it is assumed to be applied at the location of the centre of pressure. To simplify the process, however, the vertical shear force is relocated to act through the shear centre, such that for both of the two cells, the rate of twist equals zero. Given that $\frac{1}{2A_c G}$ is constant in both cells, Equation A.27 reduces to Equation A.28 [38].

$$\frac{d\theta}{dy} = \frac{1}{2A_c G} \oint \frac{q ds}{t} \quad \text{(A.27)} \qquad 0 = \oint \frac{q ds}{t} \quad \text{(A.28)}$$

To ensure an equivalent force system, a torsion is added equal to the vertical shear force times its moment arm around the shear center: $T_r = Sz*(x_{sc} - x_{cop})$. This way, the shear centre can be calculated independent of the centre of pressure distribution. Additionally, any additional torsion on the cross-section can be added to this resulting torsion, reducing the need for separate computations. The shear flow due to this torsion will be covered in Subsection A.0.6.

From Equation A.28, a solvable system of two equations with two unknowns (q_{01} and q_{02}) is set up. Which can be written in the matrix form of Equation A.29. The constants A_{11}-A_{22} and B_1, B_2 are given in Equations A.30 to A.35. The values of B_1, B_2 are obtained through numerical integration.

$$\begin{bmatrix} A_{11} & A_{12} \\ A_{21} & A_{22} \end{bmatrix} \begin{bmatrix} q_{01} \\ q_{02} \end{bmatrix} = -\begin{bmatrix} B_1 \\ B_2 \end{bmatrix} \tag{A.29}$$

$$A_{11} = \frac{l_{56}}{t_{56}} + \frac{l_{67}}{t_{67}} + \frac{l_{71}}{t_{71}} + \frac{l_{12}}{t_{12}} + \frac{l_{82}}{t_{82}} + \frac{l_{58}}{t_{58}} \tag{A.30}$$

$$A_{12} = -\frac{l_{82}}{t_{82}} - \frac{l_{58}}{t_{58}} \tag{A.31}$$

$$A_{21} = -\frac{l_{58}}{t_{58}} - \frac{l_{82}}{t_{82}} \tag{A.32}$$

$$A_{22} = \frac{l_{23}}{t_{23}} + \frac{l_{34}}{t_{34}} + \frac{l_{45}}{t_{45}} + \frac{l_{58}}{t_{58}} + \frac{l_{82}}{t_{82}} \tag{A.33}$$

$$B_1 = \int_0^{l_{56}} \frac{q_{bz_{56}}}{t_{56}} ds + \int_0^{l_{67}} \frac{q_{bz_{67}}}{t_{67}} ds + \int_0^{l_{71}} \frac{q_{bz_{71}}}{t_{71}} ds + \int_0^{l_{12}} \frac{q_{bz_{12}}}{t_{12}} ds - \int_0^{z_2} \frac{q_{bz_{85}}}{t_{85}} dz - \int_{z_5}^{0} \frac{q_{bz_{58}}}{t_{58}} dz \tag{A.34}$$

$$B_2 = \int_0^{l_{23}} \frac{q_{bz_{23}}}{t_{23}} ds + \int_0^{l_{34}} \frac{q_{bz_{34}}}{t_{34}} ds \int_0^{l_{45}} \frac{q_{bz_{45}}}{t_{45}} ds + \int_{z_5}^{0} \frac{q_{bz_{58}}}{t_{58}} dz + \int_0^{z_2} \frac{q_{bz_{82}}}{t_{82}} dz \tag{A.35}$$

Finally, solving Equation A.29 gives the redundant shear flows in both cells.

A.0.5. Shear center

The shear centre is defined as the point around which the internal moment generated by the shear flows equals the externally applied moment. Since the cross-section of the structure has an axis of symmetry, the shear centre is known to be located somewhere along this axis [38]. The x-coordinate of the shear centre is calculated by equating the moment generated by the shear flow due to a vertical shear force to the externally applied moment. This evaluation can be done at any point in the cross-section. Therefore, the moments are evaluated about point 5, as the shear forces generated by sections 56, 58, 82 and 45 act through it and do not have to be considered. The following moment equilibrium of Equation A.36 is solved for ζ to obtain the location of the shear centre w.r.t. point 5.

$$-S_z \cdot \zeta = r_{67} \int_0^{l_{67}} (q_{bz_{67}} + q_{01}) ds + r_{71} \int_0^{l_{71}} (q_{bz_{71}} + q_{01}) ds + r_{12} \int_0^{l_{12}} (q_{bz_{12}} + q_{01}) ds + r_{23} \int_0^{l_{23}} (q_{bz_{23}} + q_{02}) ds + r_{34} \int_0^{l_{34}} (q_{bz_{34}} + q_{02}) ds \tag{A.36}$$

A.0.6. Shear flow distribution due to torsion

Finally, the last component of the shear flow distribution is computed, namely that due to torsion. For a two-cell structure, the relation between the applied torque and shear flows is given by Equation A.37 with two unknowns. A solvable system is obtained by introducing the rate of twist relations of Equations A.38 and A.39. The constants $A_{11} - A_{22}$ were already defined by Equations A.30 to A.33. As the rate of twist of both cells must be equal, this gives a solvable system with three equations and three unknowns [38].

$$T = 2A_{c_1} q_{tor_1} + 2A_{c_2} q_{tor_2} \tag{A.37}$$

$$G\left(\frac{d\theta}{dx}\right) = \frac{A_{11}}{2A_{c_1}} q_{tor_1} + \frac{A_{12}}{2A_{c_1}} q_{tor_2} \tag{A.38}$$

$$G\left(\frac{d\theta}{dx}\right) = \frac{A_{21}}{2A_{c_2}} q_{tor_1} + \frac{A_{22}}{2A_{c_2}} q_{tor_2} \tag{A.39}$$

For each spanwise cross-section, the applied torque taken for this calculation is the sum of the local torque on the wing and the torque as a result of the offset between the centre of pressure and the shear centre ($T_r = Sz * (x_{sc} - x_{cop})$).

B

Appendix Stability Program

This appendix focuses on explaining the program used for stability and control in detail. Each class used is discussed in detail, along with the assumptions made and the equations used.

B.1. Dynamic Analysis

The program that performs the dynamic analysis has been written in Python and consists of four classes, namely the Aerodynamic Surface, Aircraft, Fuselage, and Solver class. The Aerodynamic Surface translates the user inputs into Python variables and can calculate the forces and moments on this surface, given an initial condition. The Aircraft class combines these surfaces into a single aircraft and calculates the stability and control derivatives. The Fuselage class applies empirical corrections to the aircraft and wing surface. The Solver class transforms the full equations of motion into the state-space format and calculates the responses of the aircraft, given a control input. With these classes, the program is able to transform aircraft geometry directly into the expected dynamic response of the aircraft, and thus greatly reduces the workload for the user. Changes in aircraft geometry only require a simple re-run of the program, instead of going through lists of equations to obtain the new derivatives.

B.1.1. Fuselage Model

To model the fuselage, it is split into 3 sections. Namely, the nose, main and tail section. This may not be the true aircraft fuselage design, but this assumption greatly facilitates the calculation of the fuselage effects. Each variable used in this model, like the nose length, speaks for itself, except the sweep. This variable is best explained in Figure B.1. In this figure, both the nose and tail sweep are negative and must be given in degrees. The sweep angle between the section camber line and the reference aircraft can be measured or calculated. The sweep angle must always be 0 for the main section. In order to run the program, surfaces and the aircraft itself have to be defined as well, but an explanation of these parameters is beyond the scope of this report as it is more related to the usage of the program than the final design.

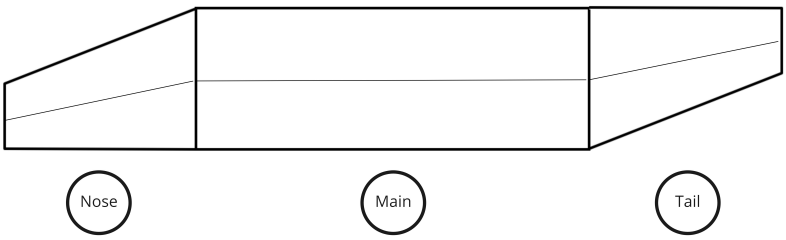

Figure B.1: *The sections of the fuselage model used in the program and the sweep angle. Note that both sweep angles are negative in this example*

B.1.2. Reference Frames

Without a proper understanding of the reference frames used, the program will most likely not make sense. The Aerodynamic Surface class can be used stand-alone, in which case the ϕ, θ, and ψ angles are provided by the user. These inputs are used to transform the velocity and acceleration vectors from the Earth reference frame to the Body reference frame using Equation B.1 for all surfaces, except the vertical surface [41]. When not used stand-alone, as it is being done in the program, all these angles are set to 0.

$$\textbf{out} = \begin{bmatrix} 1 & 0 & 0 \\ 0 & cos(\phi) & sin(\phi) \\ 0 & -sin(\phi) & cos(\phi) \end{bmatrix} \begin{bmatrix} cos(\theta) & 0 & -sin(\theta) \\ 0 & 1 & 0 \\ sin(\theta) & 0 & cos(\theta) \end{bmatrix} \begin{bmatrix} cos(\psi) & sin(\psi) & 0 \\ -sin(\psi) & cos(\psi) & 0 \\ 0 & 0 & 1 \end{bmatrix} \textbf{in} \tag{B.1}$$

In case a vertical surface is used, the Body reference frame is rotated by $90°$ around the X-axis called the Vertical reference frame, as depicted in Figure B.2. This is done by Equation B.2. For instance, a leading-edge translation of 5 meters on the Y body axis is seen as a translation of -5 meters on the Z vertical axis by the vertical surface. The same reasoning applies to all other input variables. Therefore, this transformation is done before the translation, as given by Equation B.1. A value of 1 is used for the rotation of the inputs. After the outputs of the vertical surface are determined, they are transformed back to the Body frame by the same equation, but then with a rotation value of -1.

$$\textbf{out} = \begin{bmatrix} 1 & 0 & 0 \\ 0 & 0 & rotation \\ 0 & -rotation & 0 \end{bmatrix} \textbf{in} \tag{B.2}$$

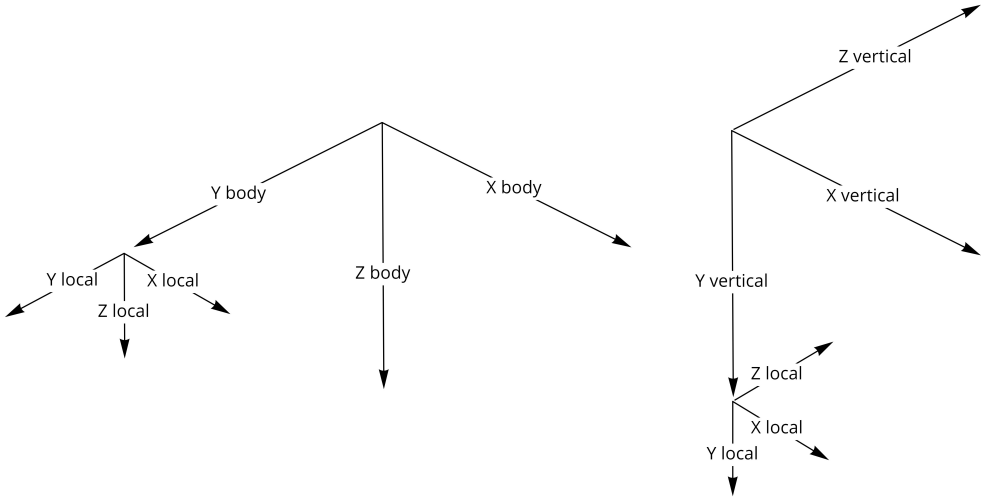

Figure B.2: *Reference frames for a horizontal surface (left) and vertical surface (right)*

The body frame used by the horizontal surfaces and the vertical frame, which is identical to the horizontal frame apart from the 90-degree shift, is given in Figure B.2. As discussed later, the forces are determined by a Riemann sum along the span of the surface. The reference frame used at the local coordinate at which the force is evaluated is translated along the span of the surface and is denoted with 'local' for clarity.

B.1.3. Aerodynamic Surface Class

As briefly explained previously, the main purpose of the Aerodynamic Surface class is to calculate the forces and moments for a single lifting surface given an initial state. This state is determined by the CG location and flight conditions. In order to accomplish this, certain steps have to be taken, and each step is discussed in this section. The equations given in this section are valid for a symmetric surface only. If desired, the equations can be found within the program as well, along with their asymmetric variants.

Assumptions
In order to be able to calculate the forces and moments with a relatively simple, linear, mathematical model, certain assumptions had to be made. Each of them is listed below, followed by a brief explanation of why the assumption is reasonable to make.

- The provided data contains no errors and has realistic values, e.g., no negative surface areas. As the program relies on a significant amount of variables, checking each of them in terms of their feasibleness is undoable. The responsibility lies with the user of the program. items C_L is constant along the surface span. As yet, no empirical method has been implemented to estimate the variation of α_i along the span. This will be considered in a future version of the program. Thus, for now, an elliptical lift distribution is assumed with constant α_i.

- Small-angle approximations are used, except for $\Lambda_{1/2}$. This greatly facilitates the verification of the code, as the equations are significantly smaller this way and the error induced is negligible.
- Only the aerodynamic effects due to turn rates are taken into account, complex effects like cross-flow along swept wings are neglected, as they are far beyond the scope of this program.
- Mach effects are neglected, and the flow is assumed to be incompressible. This implies the program should only be used for $\mathrm{Mach} < 0.3$.
- The surface does not have a geometric twist. This feature is relatively easy to implement and might be added in a future version of the program.
- The aerodynamic centre is assumed to be located at a quarter mean aerodynamic chord.

Initialisation

The initialisation step provides the basis for the other parts of the class to use. All variables provided by the user are loaded into the class and are transformed if necessary. It then calculates the AC location at $\overline{c}$. First, the Y position of the AC is determined using Equation B.3. At this location, $\overline{c}$ is calculated using Equation B.4. Lastly, the X and Z locations of the AC can be determined using Equation B.5 and Equation B.6 respectively. Note that for a vertical surface, the LE and CG positions have been transformed. The downwash and side wash values are also calculated in this part of the program, but for clarity, they are discussed in Subsection B.1.5.

$$Y_{AC} = Y_{LE} - Y_{CG} - \frac{b\,(1+2\lambda)}{6\,(1+\lambda)} \tag{B.3}$$

$$\overline{c} = c_r - c_r\,(1-\lambda)\,\frac{2|Y|}{b} \tag{B.4}$$

$$X_{AC} = X_{LE} - X_{CG} - \frac{c_r}{2} + \frac{\overline{c}}{4} + |Y| sin\,(\Lambda) \tag{B.5}$$

$$Z_{AC} = Z_{LE} - Z_{CG} - |Y| sin\,(\Gamma) \tag{B.6}$$

Local Velocity and Angles

This step of the program, along with the local forces, is done in succession per coordinate to obtain the total forces of the surface by a Riemann sum. For clarity, each part is discussed separately. First, the aerodynamic turn rate effects are calculated using Equation B.7 to Equation B.9. The dihedral effect is taken into account as well, given by Equation B.10 and Equation B.11. The local velocity is also correct for the fuselage in the case of the wing surface, but like the downwash and side wash effects it is discussed in Subsection B.1.5 for clarity. The final velocity is given by the initial velocity corrected for each effect previously discussed.

$$\dot{Z}_p = Yp \tag{B.7}$$

$$\dot{Z}_q = -X_{AC} q \tag{B.8}$$

$$\dot{X}_r = -Yr \tag{B.9}$$

$$\dot{Y}_\Gamma = -\frac{Y}{|Y|}\dot{Z}\Gamma \tag{B.10}$$

$$\dot{Z}_\Gamma = \frac{Y}{|Y|}\dot{Y}\Gamma \tag{B.11}$$

With the velocity vector now corrected for its local position, α, $\dot{\alpha}$, β, $\dot{\beta}$ can be determined using Equation B.12 to Equation B.15. The local velocity, absolute value of the velocity and angles are then passed to the local forces part of the program in order to determine the local forces.

$$\alpha = arctan\left(\frac{\dot{Z}}{\dot{X}}\right) \tag{B.12}$$

$$\beta = arctan\left(\frac{\dot{Y}}{\dot{X}}\right) \tag{B.13}$$

$$\dot{\alpha} = arctan\left(\frac{\dot{Z}+\ddot{Z}}{\dot{X}+\ddot{X}}\right) - \alpha \tag{B.14}$$

$$\dot{\beta} = arctan\left(\frac{\dot{Y}+\ddot{Y}}{\dot{X}+\ddot{X}}\right) - \beta \tag{B.15}$$

Local Forces

First, the local velocity, angles, and chord is calculated by the previously mentioned equation. α is then

corrected for the incidence angle provided by the user and control deflections. The deflection is provided by the program once the control derivatives have to be calculated, as discussed in Subsection B.1.4. $\frac{\delta\epsilon}{\delta\alpha}$ and $\frac{\delta\sigma}{\beta}$ are corrected for delay. The reasoning behind this is that when the aircraft accelerates, the new downwash or sidewash is temporarily delayed due to the distance between the downwash or sidewash body and the surface. The corrections are given by Equation B.16 and Equation B.17. α and β are then corrected with the respective corrected downwash and sidewash. Note that the sidewash delay in Equation B.17 is written as β, but after transformation, this will be α for a vertical surface. As the sidewash is only accounted for in the vertical tail, it is written as α in the program.

$$\alpha_{delay} = \dot{\alpha}\frac{X_{AC_{body}} - X_{AC}}{\dot{X}} \tag{B.16}$$

$$\beta_{delay} = \dot{\beta}\frac{X_{AC_{body}} - X_{AC}}{\dot{X}} \tag{B.17}$$

With the correct α, the C_L and C_D values are obtained by interpolation of the lift and drag curves provided by the user. The lift and drag is afterwards calculated by Equation B.18 and Equation B.19. Note the sweep correction factor implemented in the equations. This is an empirical correction obtained from [49] [41].

$$L_{local} = \frac{\rho}{2}V^2 C_{L_{local}} c_{local}\left(1 + \frac{Y}{|Y|} * \beta_{local} sin\,(2\Lambda)\right) \tag{B.18}$$

$$D_{local} = \frac{\rho}{2}V^2 C_{D_{local}} c_{local}\left(1 + \frac{Y}{|Y|} * \beta_{local} sin\,(2\Lambda)\right) \tag{B.19}$$

The lift and drag forces are then split into their normal and tangential components by Equation B.20 and Equation B.21. The small-angle approximation is not implemented here, as the equation is relatively simple, and the errors produced were too large to be acceptable. The components can then be used to find the forces in the Cartesian coordinate body frame by Equation B.22 to Equation B.24.

$$F_{normal} = cos\,(\alpha)\,L_{local} + sin\,(\alpha)\,D_{local} \tag{B.20}$$

$$F_{tangential} = sin\,(\alpha) * L_{local} - cos\,(\alpha)\,D_{local} \tag{B.21}$$

$$F_{X_{local}} = F_{tangential} \tag{B.22}$$

$$F_{Y_{local}} = -F_{normal}\frac{Y}{|Y|}\Gamma \tag{B.23}$$

$$F_{Z_{local}} = -F_{normal} \tag{B.24}$$

Forces and Moments

The final step in this class is to sum the forces and calculate the moments around the CG of the *aircraft*. Unfortunately, the local forces could not be integrated using the Scipy module, as it is a multivariable output function. It was therefore decided to use a simple Riemann sum with a small step size. An added bonus is the much faster runtime, compared to Scipy integration, with still an acceptable accuracy. The surface is integrated from $-\frac{b}{2}$ to $\frac{b}{2}$ for a symmetric surface and from $-b$ to 0 for an asymmetric one. To simplify the moment calculations, the forces are summed for the negative and positive coordinate sides separately. This implies the positive force sum will always be 0 for an asymmetric surface, as it has no positive coordinates.

For the moment calculations, the value of the positive side can then be subtracted from the negative side to find the net force at the AC per axis. With the distances from the AC to the CG known, the moments of these forces can be calculated. Additionally, the moment of the AC around the Y-axis is added by taking the average of the C_m curve provided by the user. This implies that the aerodynamic analysis, either in XFLR or another program, has to be done at the AC, otherwise this coefficient will be incorrect. The moment calculations per force are given by Equation B.25 to Equation B.30 and the AC correction by Equation B.31.

$$M_{Y_{F_X}} = Z_{AC}\left(F_{X_{left}} + F_{X_{right}}\right) \tag{B.25}$$

$$M_{Z_{F_X}} = -Y_{AC}\left(F_{X_{left}} - F_{X_{right}}\right) \tag{B.26}$$

$$M_{X_{F_Y}} = -Z_{AC}\left(F_{Y_{left}} + F_{Y_{right}}\right) \quad \text{(B.27)} \qquad M_{Z_{F_Y}} = X_{AC}\left(F_{Y_{left}} + F_{Y_{right}}\right) \quad \text{(B.28)}$$

$$M_{X_{F_Z}} = Y_{AC}\left(F_{Z_{left}} - F_{Z_{right}}\right) \quad \text{(B.29)} \qquad M_{Y_{F_Z}} = -X_{AC}\left(F_{Z_{left}} + F_{Z_{right}}\right) \quad \text{(B.30)}$$

$$M_{Y_{AC}} = \frac{\rho}{2} V^2 S_w \bar{c} C_{m_{ac}} \quad \text{(B.31)}$$

The final output of the program is a 3×3 matrix containing the forces per side and the moments. The rows correspond to X, Y and Z, the columns to the negative side force, positive side force, and the moment. In the case of a vertical surface, these outputs are post-transformed to represent the forces and moments in the body reference frame.

B.1.4. Aircraft Class

The main purpose of the Aircraft class is to calculate the stability derivatives of the provided aircraft. Like the Aerodynamic Surface, certain steps have to be taken in order to achieve this. Only a single assumption is made in this class, namely the interference factors between the loaded surfaces are neglected. In reality, the drag would be higher for combined surfaces instead of the independent sum, but this is beyond the scope of the program.

Initialisation
During the initialisation, all aircraft variables are loaded, and the mass variables are made dimensionless for the equations of motion matrices discussed in Subsection B.1.6. The equations to make the mass variables dimensionless are not discussed here and can be found in [41]. The applicability of a fuselage is checked and if this is the case, certain variables are corrected. Those corrections are discussed in Subsection B.1.5. A reference output is calculated using the flight conditions, which will be compared to the new output during the calculation of the stability derivatives.

Aircraft Output
The method to determine the entire output for the aircraft is relatively simple. For each surface located in the aircraft folder, an Aerodynamic Surface object is created. The results for each surface are summed, and the final matrix will correspond to the output of the entire aircraft. The Aerodynamic Surface output is a 3×3 matrix, but as the left and right side forces no longer have to be distinguished they are summed, and the final output matrix is 3×2 with the first column being the total forces and the second column the moments.

Stability & Control Derivatives
Like the aircraft output, the method to calculate the derivatives is relatively simple. The value for which the derivative has to be taken is increased slightly and the new output of the aircraft is compared to the reference and made dimensionless. Take C_{X_u} for example. This derivative is the change in F_X due to a change in $\dot{X}$. The program increases $\dot{X}$ slightly and calculates the new output. The reference output is then deducted from the new one and the difference is made dimensionless to get C_{X_u}.

For each derivative, a similar approach is taken. The main difference per derivative is the variable which is changed and the way it is made dimensionless. The flight dynamics lectures give the correct dimensionless equations, but can be rather ambiguous for certain derivatives [41]. Fortunately, extensive verification has been carried out in this part of the program to ensure it is correct.

The control derivatives are calculated similarly. Per control surface, as defined by the user, a small deflection is given and the Aerodynamic Surface object changes α of the surface accordingly. The outputs are then again compared and made dimensionless for the derivative. The program also prints the expected steady-state turn rates as given by Equation B.32 to Equation B.34.

$$p_{steady} = -\frac{C_{l_{\delta a}}}{C_{l_p}} \frac{2V}{b} \delta a \quad \text{(B.32)} \qquad q_{steady} = \frac{C_{m_{\delta e}}}{C_{m_q}} \frac{V}{\bar{c}} \delta e \quad \text{(B.33)}$$

$$r_{steady} = \frac{C_{n_{\delta r}}}{C_{n_r}} \frac{2V}{b} \delta r \tag{B.34}$$

B.1.5. Fuselage Class

It was decided to create a stand-alone class with all the empirical methods, called the Fuselage class. Its effects are embedded into the other classes, but each of them is discussed here. Verification has been done similarly. Unlike the other classes, the program can be run without this one. It has been created to model the fuselage in the greatest detail possible with empirical methods, but if suspicion exists about the correctness of the model, it can be run without. Secondly, not all aircraft have fuselages, like a flying wing, and the program must be capable to be run in this case. Like the other classes, a number of steps had to be taken, and each of them will be discussed next.

Assumptions
A certain number of assumptions had to be made in order to be able to model the fuselage, without asking for too many details from the user, and are summarised below.

- The wing surface is corrected to create a wing-fuselage surface, other surfaces remain uncorrected. It might be true that the horizontal tail experiences interference from the fuselage as well, but effects like these are neglected.
- The modelled fuselage does not experience structural deflections. Due to the bending of the fuselage, in reality, the tail will be slightly lower α than the wing, but effects like these are neglected as well.
- A 3-section fuselage is assumed, to have a nose cone, main section and a tail cone. The main section does not change in width nor height and is parallel to the X-axis of the aircraft. This assumption ensures the fuselage can be modelled with the few parameters given in the text file and does not require extensive knowledge of fuselage design, not details from the user.

Initialisation
Like the other classes, variables have to be loaded into the program, in this case from the fuselage text file provided by the user. It also calculates certain parameters which will be used repeatedly by the correction methods discussed next.

Empirical Corrections
The following empirical corrections are account for in this program, $C_{L_{\alpha_{wing}}}$, $C_{D_{0_{wing}}}$, $C_{m_{AC_{wing}}}$, $X_{AC_{wing}}$, C_{Y_β}, C_{l_β}, $\frac{\delta\epsilon}{\delta\alpha}$, and $\frac{\delta\sigma}{\delta\alpha}$. All these corrections can be found in [14, 49] and will not be discussed here. The C_{l_β} has been derived from aerodynamics to be used in the program and will be discussed in detail.

Although several references mention the effect of the fuselage on C_{l_p}, none of them provides methods to estimate this effect. The correction has been derived using aerodynamic equations from [1]. The fuselage is modelled as a cylinder, and $\dot{Y}$ of the aircraft acts as the free stream velocity which flows around the cylinder. A low wing will experience an increase in α on the left side and a decrease on the right side, acting destabilising as can be expected, assuming $\dot{Y}$, or equally β is positive. Each combination of elementary flows only applies to a specific fuselage type. The Rankine oval, which consists of a source and sinks flow, only works for fuselages where $w_{fuselage} > h_{fuselage}$ is true. The Kelvin oval is made of 2 counter-rotating vortices and only works in the opposite case, $w_{fuselage} < h_{fuselage}$. The doublet, comprised of a source and sink flow at a single position, holds when $w_{fuselage} = h_{fuselage}$. Each type is visualised in Figure B.3 with their respective flow fields. Unfortunately, the vertical lines in Figure B.3b could not be removed, it is due to the extreme velocity vectors at the centre of the doublet.

With the types of cylinders known to model the fuselage, it is still unknown how the cylinder can be modelled precisely to fit the fuselage. With the Rankine and Kelvin ovals, first, the location of the pairs has to be determined. This is done by solving Equation B.35 and Equation B.36 numerically using the FSolve method from the Scipy module. The ratio, which is solved in these equations, is equal to $\frac{location}{h_{fuselage}}$ for both ovals. This ratio is then multiplied with $h_{fuselage}$ to obtain the location. The doublet does not require a specified location, as it is always at the centre, and thus this step can be skipped. Please note that the program only

[1] URL: http://www.temporal.com.au/c172.pdf [Accessed 15 Jun 2022]

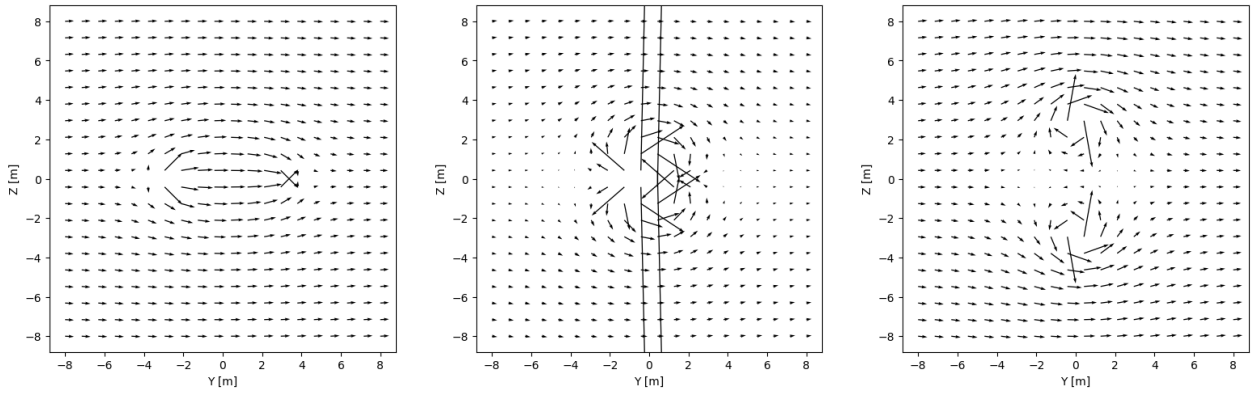

(a) *Rankine oval.* **(b)** *Doublet.* **(c)** *Kelvin oval.*

Figure B.3: *The aerodynamic methods used to model the fuselage*

solves the equations for the applicable cylinder, as is determined by the $\frac{w_{fuselage}}{h_{fuselage}}$ ratio, it never solves all 3 equations at once.

$$w_{fuselage}^2 = h_{fuselage}^2 \, ratio^2 + \frac{h_{fuselage}^2 \, ratio}{arctan\,(ratio)} \tag{B.35}$$

$$-\dot{Y}h_{fuselage} = \frac{h_{fuselage}^2 \, ratio^2 + w_{fuselage}^2}{2h_{fuselage} ratio} ln\left(\frac{1-ratio}{1+ratio}\right) \tag{B.36}$$

The strength is for the Rankine, Kelvin and doublet is determined by Equation B.37, Equation B.38, and Equation B.39 respectively. The derivations of both the position and strength equations are not given here, only the final results from the derivation. The potential flows, from which these equations have been derived, can be found in [50]. It can also be clearly seen that the doublet was by far the easiest to model.

$$strength_{Rankine} = \frac{\dot{Y}h_{fuselage}\pi}{arctan\left(\frac{location_{Rankine}}{h_{fuselage}}\right)} \tag{B.37}$$

$$strength_{Kelvin} = \frac{\left(location_{Kelvin}^2 + w_{fuselage}^2\right)\pi\ddot{Y}}{location_{Kelvin}} \tag{B.38}$$

$$strength_{doublet} = 2\pi\dot{Y}w_{fuselage}^2 \tag{B.39}$$

With the strength known, the flow field can finally be determined. In order to create Figure B.3 a grid was used with Y and Z values. In the program, the Y values are given by the span of the surface and Z is fixed. This Z value depends on the position of the wing with respect to the fuselage and is assumed to be at the bottom for a low wing, at the centreline for a mid-wing and the top for a high wing. In the case of a mid-wing, the velocity remains uncorrected, and the method returns the unmodified velocity vector. The Y and Z corrections in case of a Rankine oval are given by Equation B.40 and Equation B.41. Equation B.42 and Equation B.43 give the corrections in case of a Kelvin oval, and Equation B.44 and Equation B.45 give the corrections for the doublet. After validation of the asymmetric derivatives, which is discussed in Subsection D.0.3, it became apparent that this correction is too dominant. An empirical factor of $\frac{1}{2}$ has been applied to the $\ddot{Z}$ correction to better model this effect. Note that the subscript 'fs' refers to the free stream velocity, which in this case is $\dot{Y}$ before the correction.

$$\dot{Y}_{Rankine} = \dot{Y}_{fs} + \frac{strength_{Rankine}}{2\pi}\left(\frac{Y + location_{Rankine}}{(Y + location_{Rankine})^2 + Z^2} - \frac{Y - location_{Rankine}}{(Y - location_{Rankine})^2 + Z^2}\right) \tag{B.40}$$

$$\dot{Z}_{Rankine} = \frac{strength_{Rankine}}{2\pi}\left(\frac{Z}{(Y + location_{Rankine})^2 + Z^2} - \frac{Z}{(Y - location_{Rankine})^2 + Z^2}\right) \tag{B.41}$$

$$\dot{Y}_{Kelvin} = \dot{Y}_{fs} + \frac{strength_{Kelvin}}{2\pi}\left(\frac{Z - location_{Kelvin}}{Y^2 + (Z - location_{Kelvin})^2} - \frac{Z + location_{Kelvin}}{Y^2 + (Z - location_{Kelvin})^2}\right) \tag{B.42}$$

$$\dot{Z}_{Kelvin} = \frac{strength_{Kelvin}}{2\pi}\left(\frac{Y}{\left(Y^2 + (Z + location_{Kelvin})^2\right)} - \frac{Y}{Y^2 + (Z - location_{Kelvin})^2}\right) \tag{B.43}$$

$$\dot{Y}_{doublet} = \dot{Y}_{fs} + \frac{strength_{doublet}\left(Z^2 - Y^2\right)}{2\pi\left(Y^2 + Z^2\right)^2} \tag{B.44}$$

$$\dot{Z}_{doublet} = -\frac{strength_{doublet} YZ}{\pi\left(Y^2 + Z^2\right)^2} \tag{B.45}$$

B.1.6. Solver Class

The Solver class takes the stability and control derivatives and computes the symmetric and asymmetric responses of the aircraft, given a small control deflection. The equations of motion used have been derived in the flight dynamics notes, only the solution is presented here. During the derivation and linearisation, certain assumptions have been made, which can be found in it as well [41]. The method to transform the equations of motion into the state-space system is taken from the same reference and will be discussed as it has been implemented in the program as well. The calculation of the responses is done with the Control module and its methods will not be discussed, only the results in Section B.2.

The symmetric and asymmetric equations of motion are given in [41]. Both equations can be written in the format as given by Equation B.46. Multiplying both sides with $\mathbf{P}^{-1}$ gives the following relation given by Equation B.47. **A** and **B** represent the matrices required for the state-space system. The outputs of the state-space system are defined by Equation B.48. **C** is equal for both equations of motion and a 4×4 identity matrix. **D** is the control derivative matrix. In the program, this transformation is automated by using the Numpy module.

$$\mathbf{P}\dot{\mathbf{x}} = \mathbf{Q}\,\mathbf{x} + \mathbf{R}\,\mathbf{u} \tag{B.46}$$

$$\dot{\mathbf{x}} = \mathbf{P}^{-1}\mathbf{Q}\,\mathbf{x} + \mathbf{P}^{-1}\mathbf{R}\,\mathbf{U} = \mathbf{A}\,\mathbf{x} + \mathbf{B}\,\mathbf{u} \tag{B.47}$$

$$\mathbf{y} = \mathbf{C}\,\mathbf{x} + \mathbf{D}\,\mathbf{u} \tag{B.48}$$

With the state-space system in place, the eigenvalues can be easily determined with the Numpy module. The eigenvalues are used for verification of the code, and more importantly to determine the damping ratio and natural frequency of the mode, given by Equation B.49 and Equation B.50. These values can be used to describe the stability of the aircraft, as discussed in Section B.2. The state-space system is fed into the Control module, which calculates the outputs given an initial deflection. All those outputs will be discussed next in Section B.2.

$$\zeta = -\frac{\xi}{\sqrt{\xi^2 + \eta^2}} \tag{B.49}$$

$$\omega = \sqrt{\xi^2 + \eta^2}\sqrt{1 - \zeta^2} \tag{B.50}$$

B.2. Program Outputs

All the program outputs are stored in a new subdirectory called 'Results', located in the main folder. This folder will contain another subdirectory with the provided aircraft name, in which all results are stored. The 'Coefficients' folder contains both the symmetric and asymmetric stability and control derivatives stored in

a text file. The eigenvalues are stored as images and given in the 'Eigenvalues' folder. The image helps to quickly check if the eigenvalues are negative, unstable behaviour can be expected if they are positive. The modes, with their period, natural frequency and damping ratio are stored here as well as text files. The 'Responses' folder contains the plots of the dynamic stability of the aircraft.

From the graphs presented by the program, it immediately becomes apparent if the aircraft is dynamically stable or not. The AIAA provides an empirical method to determine the stability required based on the type of aircraft [49]. First, it distinguishes the kind of levels of quality, thereafter the category and classes of aircraft. Each part is described below.

- **Level I**, excellent flying qualities, minimal pilot workload.
- **Level II**, adequate flying qualities, some increase in pilot workload.
- **Level III**, the aircraft can be controlled safely, but unacceptable pilot workload without assistance.

- **Category A**, non-terminal flight phases that require rapid manoeuvring and precise flight path control, such as aerobatics and air-to-air combat.
- **Category B**, non-terminal flight phases that require gradual manoeuvring and flight path control, such as climb and cruise.
- **Category C**, terminal flight phases that require gradual manoeuvring and precise flight path control, such as take-off and landing.

- **Class I**, light, medium manoeuvrable aircraft.
- **Class II**, medium weight, medium manoeuvrable aircraft, such as short-haul transport aircraft.
- **Class III**, heavy, low manoeuvrability aircraft, such as cargo and large passenger aircraft.
- **Class IV**, low to medium weight, high manoeuvrable aircraft, such as fighters and aerobatic aircraft.

The program gives the eigenvalues for each mode, accompanied by its period, if applicable, damping ratio and natural frequency. With the applicable level, category, and class, the actual stability of the motion can be compared to the desired stability using the tables below. Table B.1 and Table B.2 give the required damping ratio and natural frequency for the short period mode. Note that n/α is defined by Equation B.51. Table B.3 gives the required damping ratio for the Phugoid mode. Table B.4 gives the required time constant for the aperiodic roll motion. The time constant is defined as $-1/\lambda_{aperiodic}$, with $\lambda_{aperiodic}$ being the real eigenvalue of the aperiodic roll mode. Table B.5 gives the required values for both the damping ratio and the natural frequency for the Dutch Roll mode. Finally, Table B.6 gives the maximum time to double the amplitude of the spiral mode.

Table B.1
Damping ratios for short-period mode

	$\zeta_{A_{min}}$ [-]	$\zeta_{A_{max}}$ [-]	$\zeta_{B_{min}}$ [-]	$\zeta_{B_{max}}$ [-]	$\zeta_{C_{min}}$ [-]	$\zeta_{C_{max}}$ [-]
Level I	0.35	1.30	0.30	2.00	0.35	1.30
Level II	0.25	2.00	0.20	2.00	0.25	2.00
Level III	0.15	-	0.15	-	0.15	-

Table B.2
Natural frequencies for the short period mode

	$\left(\frac{\omega^2}{n/\alpha}\right)_{A_{min}}$ [-]	$\left(\frac{\omega^2}{n/\alpha}\right)_{A_{max}}$ [-]	$\left(\frac{\omega^2}{n/\alpha}\right)_{B_{min}}$ [-]	$\left(\frac{\omega^2}{n/\alpha}\right)_{B_{max}}$ [-]	$\left(\frac{\omega^2}{n/\alpha}\right)_{C_{min}}$ [-]	$\left(\frac{\omega^2}{n/\alpha}\right)_{C_{max}}$ [-]
Level I	0.280	3.600	0.085	3.600	0.160	3.600
Level II	0.160	10.00	0.038	10.000	0.096	10.000
Level III	0.160	-	0.038	-	0.096	-

$$n/\alpha = \frac{\rho}{2W} V^2 S_w C_{L_\alpha} \tag{B.51}$$

Table B.3
Damping ratios for the Phugoid mode

	ζ_{min} [-]
Level I	0.04
Level II	0.00
Level III	-

Table B.4
Maximum allowed time constants for the aperiodic roll mode

Class	Category	Level I	Level II	Level III
I, IV	A	1.00	1.40	10.00
II, III	A	1.40	3.00	10.00
All	B	1.40	3.00	10.00
I, IV	C	1.00	1.40	10.00
II, III	C	1.40	3.00	10.00

Table B.5
Damping ratios and natural frequencies for the Dutch Roll motion

Level	Category	Class	ζ_{min}[-]	ω_{min} [rad/s]	$(\zeta\omega)_{min}$ [-]
I	A	I, IV	0.19	1.00	0.35
I	A	II, III	0.19	0.40	0.35
I	B	All	0.08	1.00	0.15
I	C	I, IV	0.08	1.00	0.15
I	C	II, III	0.08	0.40	0.15
II	All	All	0.02	0.40	-
III	All	All	0.02	0.40	-

Table B.6
Time in seconds to double amplitude for the spiral mode

Class	Category	Level I	Level II	Level III
I, IV	A	8	12	4
I, IV	B, C	20	12	4
II, III	All	20	12	4

C

Appendix Stability Verification

With the mathematical model in place as discussed in Appendix B, tests have to be performed to verify the model is implemented correctly. This has been done for each class separately. Within each class, variables are tested per part of the class. The variables and their test are summarised per part in separate tables. Only the major variables are tested, sub-variables on which these variables rely are not tested separately. If for example, the wing area test fails, the sub-variables on which this variable relies are checked for their correctness. This could be the wing span and wing chord for this example, which are loaded into the program from the provided files. With the major variables tested, the code is verified in its entirety. The type of test can be a visual check, by either a print statement or a plot, abbreviated with 'V', a recalculation by hand, abbreviated with 'R', or a simplified calculation, abbreviated with 'S'. The simplified calculations either rely on a simple example or a previously derived formula to check the variable for its correctness. Subsection C.0.1, Subsection C.0.2, Subsection C.0.3 and Subsection C.0.4 discusses the tests for the Aerodynamic Surface, Aircraft, Fuselage, and Solver class respectively.

C.0.1. Aerodynamic Surface Class

The Aerodynamic Surface class performs 5 major tasks. It initialises the surface to form a basis, transforms input data, calculates the local velocity, after which the local forces can be determined and finally everything is summed to form the forces and moments in the body frame. Additionally, each of these steps differs for each type of surface, a vertical surface requires an extra transformation compared to a regular one for instance. All the variables relying on the type of surface have therefore been checked multiple times. The aerodynamic centre location is an example of such a variable, as a Y shift in the body frame is represented in a Z shift in the vertical frame. If a variable had to be checked multiple times, this is denoted with 'Y' in the verification table, or else with 'N'. The variables and their testing method are summarised in Table C.1.

Table C.1
Verified variables for initialisation (left), local velocities and moments (middle) and inputs and outputs transformations (right)

	Method	Multiple
S	S	Y
AR	S	N
$\overline{c}$	S	Y
X_{ac}	R	Y
Y_{ac}	R	Y
Z_{ac}	R	Y
$\frac{\delta\epsilon}{\delta\alpha}$	S	N
$\frac{\delta\sigma}{\delta\beta}$	S	N

	Method	Multiple
V_{loc}	R	N
α_{loc}	R	N
$\dot{\alpha_{loc}}$	R	N
β_{loc}	R	N
X_{loc}	R	N
Y_{loc}	R	N
Z_{loc}	R	N

	Method	Multiple
angles	R	N
rates	R	N
V	R	N
$\dot{V}$	R	N
X	S	Y
Y	S	Y
Z	S	Y
m	S	Y
l	S	Y
n	S	Y

C.0.2. Aircraft Class

The Aircraft class performs 4 tasks. It creates the dimensionless aircraft from the provided surfaces, calculates the reference output and afterwards calculates the symmetric and asymmetric derivatives. The first 2 tasks fall under the initialisation category, the latter 2 are treated independently. Unlike the Aerodynamic Surface class, no different states for variables exist, and multiple checks do not have to be carried out. For the outputs, it is now assumed the Aerodynamic Surface class is correct and by printing those outputs a recalculation can be done by hand to check the derivatives.

Table C.2
Verified variables for initialisation (left), symmetric derivatives (middle) and asymmetric derivatives (right)

Parameter	Method
m_c	R
m_b	R
K_{XX}	R
K_{YY}	R
K_{ZZ}	R
K_{XZ}	R
ρ	R
V	R
$output_{ref}$	V & R

Parameter	Method
C_{X_0,Y_0,m_0}	R
C_{X_u,Y_u,m_u}	V & R
$C_{X_\alpha,Y_\alpha,m_\alpha}$	V & R
$C_{X_{\dot{\alpha}},Y_{\dot{\alpha}},m_{\dot{\alpha}}}$	V & R
C_{X_q,Y_q,m_q}	V & R
$C_{X_{\delta e},Y_{\delta e},m_{\delta e}}$	V & R

Parameter	Method
$C_{Y_\beta,l_\beta,n_\beta}$	V & R
$C_{Y_{\dot{\beta}},l_{\dot{\beta}},n_{\dot{\beta}}}$	V & R
C_{Y_p,l_p,n_p}	V & R
C_{Y_r,l_r,n_r}	V & R
$C_{Y_{\delta a},l_{\delta a},n_{\delta a}}$	V & R
$C_{Y_{\delta r},l_{\delta r},n_{\delta r}}$	V & R

C.0.3. Fuselage Class

The Fuselage class is independent, but its effects are embedded in the Aerodynamic Surface and Aircraft classes. It requires an Aerodynamic Surface object to calculate the effects and an Aircraft object to implement those effects. The downwash and sidewash effects are calculated in the Aerodynamic Surface class but are treated here as these effects, as the fuselage ones are calculated by empirical methods. The fuselage-wing interference caused by sidewash is derived from aerodynamics, but its effect has been scaled empirically, as initially, the effect seemed far too excessive to be realistic. Each generator, namely the Kelvin oval, Rankine oval and doublet has been verified by checking each stagnation point and the velocity at the top and bottom of the fuselage. The vectors of these velocities have also been plotted and checked visually for their correctness to ensure the fuselage is modelled correctly. All the tests belonging to the empirical correction methods have been summarised in Table C.3.

Table C.3
Verified variables for initialisation of the fuselage (left) and all the empirical corrections (right)

Parameter	Method
l_{fus}	R
S_{fus}	R
r_{fus}	R
S_{nose}	R
S_{main}	R
S_{tail}	R
S_{net}	R
S_{cross}	R
$k1 - k2$	R

Parameter	Method
$\delta\epsilon \backslash \delta\alpha$	R
$\delta\sigma \backslash \delta\beta$	R
C_L	R
C_D	R
$C_{m_{ac}}$	R
X_{ac}	R
C_{Y_β}	R
$Kelvin$	V & R
$Rankine$	V & R
$Doublet$	V & R

C.0.4. Solver Class

The Solver class takes the result from the Aircraft class and calculates the state-space system used to calculate the responses. The response calculations have been done by the Python Control module and can only be checked visually. It is assumed the calculations done by this module are correct. To check if the state-space system is calculated correctly, the derivatives from the Cessna Citation aircraft have been taken from the flight dynamics lecture notes and the state-space system is calculated manually using the Python Numpy module [41]. The eigenvalues are checked with the Sympy module. The state-space system is solved, and all the results are compared to those from the program.

D

Appendix Stability Validation

With the verification completed as described in Appendix C, it can be assumed no errors exist in the mathematical model of the program. Next is to determine how well the program can determine the stability derivatives, as this is the only important to the user. To do this, a proven example has been selected and analysed by the program, after which it has been compared to the actual derivatives provided by the reference. Subsection D.0.1 describes the model used for validation. Consequently, Subsection D.0.2 and Subsection D.0.3 discuss the accuracy of the symmetric and asymmetric derivatives calculated by the program.

D.0.1. Program Model for the Cessna 172 Aircraft

Finding an example aircraft which had both the geometrical and derivatives data available was an arduous task, but fortunately, the Cessna 172 aircraft has all the data available. Still, there were a few parameters which had to be approximated, due to the ambiguity of the sources from which the data was derived.Table D.1 shows the surface planforms used in the program, of which a few parameters are approximated, which are listed below.

- Wing planform, in reality, the Cessna has two wing sections, namely a straight root and a tapered tip section. The program cannot distinguish between the two, and an average single section has been approximated, of which the details are given in Table D.1.
- Tail planforms, only the surface areas, taper, and sweep were given. Using the scaled drawing, likely planforms fitting these areas have been derived.
- Leading edges positions, these have been derived from a scaled drawing as no exact positions were given.

Table D.1
Surface data for the Cessna 172 aircraft [51, 52]

Parameter		Wing	Horizontal tail	Vertical tail
S_w	[m_2]	16.165	3.353	1.274
b	[m]	10.922	3.350	1.400
c_r	[m]	1.729	1.250	1.300
$\overline{c}$	[m]	1.494	0.966	1.161
λ	[-]	0.712	0.600	0.400
$\Lambda_{1/2}$	[°]	0.000	0.000	22.550
Γ	[°]	1.733	0.000	0.000
airfoil_r	[-]	NACA 2412	NACA 0012	NACA 0009
airfoil_t	[-]	NACA 2412	NACA 0009	NACA 0006
LE_X	[m]	1.60	6.10	6.00
LE_Y	[m]	0.00	0.00	0.00
LE_Z	[m]	1.50	1.10	1.00

The true symmetric and asymmetric derivatives were gathered from two different sources, which evaluated the stability at different flight conditions. For this reason, Table D.2 has two different columns. The X location of the CG was given concerning the firewall of the aircraft, but again this had to be measured from the scaled drawing. No data was given for the Z location of the CG and is assumed to be close to the thrust axis of the aircraft. For these reasons, the CG locations are given as ranges in Table D.2.

Table D.2
Mass and flight data for the Cessna 172 aircraft [41, 52–54]

Parameter		Symmetric	Asymmetric
V	[m/s]	66.75	54.54
ρ	[kg/m^3]	1.060	1.060
m	[kg]	1200.0	1000.0
CG_X	[m]	2.0 - 2.2	2.0 - 2.2
CG_Y	[m]	0.0	0.0
CG_Z	[m]	0.6 - 0.8	0.6 - 0.8
I_{XX}	[kg m^2]	1285.3	1285.3
I_{YY}	[kg m^2]	1824.9	1824.9
I_{ZZ}	[kg m^2]	2666.0	2666.9
I_{XZ}	[kg m^2]	0.0	0.0

The fuselage data used to approximate the fuselage effects is given in Table D.3. The geometry has been tailored to fit the program and to be similar to that of the real fuselage. In each of these parameters, a small error is likely, but neglecting the fuselage in its entirety will result in far larger errors.

Table D.3
Fuselage data for the Cessna 172 aircraft [52]

Parameter	Nose section [m]	Main section [m]	Tail section [m]
Length	1.60	1.70	3.60
Height start end	1.00	1.60	1.60
Height end	1.60	1.60	0.50
Width start	0.80	1.10	1.10
Width end	1.10	1.10	0.40
Sweep	-9.00	0.00	-3.00

D.0.2. Symmetric Derivatives

All symmetric derivatives have been calculated using the Cessna 172 *symmetric* model and are compared to the true values in Table D.4. Each derivative will be discussed briefly in terms of its accuracy.

u derivatives

- C_{X_u}, extremely underestimated, indicating the drag estimation in the program is incorrect. The underestimation could be from the empirical fuselage drag estimation, but also due to the inaccuracies from the XFLR drag curve. Multiplying the entire drag curve before the fuselage zero drag correction by a factor of 3 shows convergence to the true value and suggests XFLR underestimates the drag of lifting surfaces. The drag underestimation destabilises the Phugoid motion, and thus the aircraft is likely to be more stable in reality.
- C_{Z_u}, underestimated, indicating the lift estimation in the program can be improved. Much like the drag, this is fully dependent on the accuracy of XFLR. Increasing C_{L_0} of the wing and horizontal lift slope by 0.05 already shows convergence to the true values. The implication of the lift underestimation is a longer period of the Phugoid motion.
- C_{m_u}, close to zero, as is expected. It is noted that the incidence angle of the horizontal tail greatly influences this derivative.

α derivatives

- C_{X_α}, extremely overestimated, and much like C_{X_u} this derivative shows convergence to the true value if the drag curves are multiplied by a factor of 3. The effect of this overestimation is identical to that of C_{X_u} as well, destabilising the Phugoid motion.
- C_{Z_α}, slightly overestimated and like C_{Z_u} dependent on the accuracy of the provided lift slope. Unlike C_{Z_u} though, this value depends on the slope of the curve and not C_{L_0}. Reducing the curve by 10 [%] shows convergence to the true value. Like C_{Z_u}, the effect is a longer Phugoid motion period.

- C_{m_α}, extremely overestimated. This derivative depends on the moment arms of the wing and the horizontal tail. As no exact data were available, these have been measured by hand from a scaled drawing from the reference location provided by the pilot operating handbook, as given in Table D.2. It is therefore likely errors have been made in the exact CG location. Shifting the CG backwards by 0.1 $[m]$ shows convergence to the true value. The effect is destabilising as the horizontal tail arm reduces. This is not considered an inaccuracy of the program, as the user will know exactly where the CG location is and this error will not be present.

$\dot{\alpha}$ derivatives

- $C_{X_{\dot{\alpha}}}$, close to zero, as is expected. The horizontal tail will provide slightly more lift and drag due to the downwash delay. It is likely that the reference assumed this effect to be zero.
- $C_{Z_{\dot{\alpha}}}$, close to the true value, indicating that the empirical formula for downwash is correct. After the lift slope modification suggested previously, this value also converges to the true value.
- $C_{m_{\dot{\alpha}}}$, same reasoning as for the $C_{Z_{\dot{\alpha}}}$ derivative.

q derivatives

- C_{X_q}, close to zero, as is expected. The reference must have assumed this effect to be zero. Due to the increased α at the horizontal tail, C_X has to change as well.
- C_{Z_q}, underestimated. Unlike the C_{m_α} derivative, this depends on the location of the horizontal tail and does not require a shift in the CG location, as this will change the moment caused by the wing as well. Shifting the tail backwards by 0.2 $[m]$ reduces the error, but no convergence towards the true value occurs. Fortunately, this error does not seem to affect the Phugoid motion much.
- C_{m_q}, same reasoning as for the C_{Z_q} derivative.

δe derivatives

- $C_{X_{\delta e}}$, same reasoning as for the C_{X_q} derivative.
- $C_{Z_{\delta e}}$, underestimated. The $\frac{\delta \alpha}{\delta e}$ value has been obtained using a flap deflection in XFLR. The percentage of chord and span used have been measured using a scaled drawing. It is therefore likely errors have been made, resulting in a less effective elevator compared to reality. Increasing $\frac{\delta \alpha}{\delta e}$ directly results in convergence to the true values and as the errors are made outside the program, it is not discussed further.
- $C_{m_{\delta e}}$, same reasoning as for the $C_{Z_{\delta e}}$ derivative.

D.0.3. Asymmetric Derivatives

All asymmetric derivatives have been calculated using the Cessna 172 *asymmetric* model and are compared to the true values in Table D.5. Each derivative will be discussed briefly in terms of its accuracy.

β derivatives

- C_{Y_β}, close to the expected value and no further comment can be made.
- C_{l_β}, overestimated. Initially, this value was greatly overestimated, leading to a highly spirally stable, but unstable Dutch Roll motion. This is mainly caused by the velocity (over)correction of the fuselage. This correction has permanently been reduced by a factor of 2 to reduce its impact on the global lateral stability. Apart from this, the only other parameters affecting this derivative are the wing sweep and wing dihedral. The dihedral has been confirmed to be 1.733 $[deg]$, but the sweep has been assumed to be 0 $[deg]$. Sweeping the aircraft slightly forward by 5 $[deg]$ as the scaled picture suggests reduces the error by 6 [%].
- C_{n_β}, overestimated. This derivative is mainly influenced by the tail arm and its size. As C_{Y_β} is close to the expected value, it is likely the error is made in the tail positioning as it has been derived from a scaled drawing. Moving the tail forward does indeed reduce the error in this derivative.

Table D.4
Symmetric derivatives for the Cessna 172 aircraft [41]

Parameter	Reference [−]	Calculated [−]	Difference [%]
C_{X_0}	0.000	0.000	0.0
C_{Z_0}	-0.310	-0.310	0.0
C_{m_0}	0.000	0.000	0.0
C_{X_u}	-0.093	-0.032	190.6
C_{Z_u}	-0.620	-0.420	47.6
C_{m_u}	0.000	-0.044	-
C_{X_α}	0.180	0.519	188.3
C_{Z_α}	-4.631	-5.538	19.6
C_{m_α}	-0.890	-1.888	112.1
$C_{X_{\dot{\alpha}}}$	0.000	0.029	-
$C_{Z_{\dot{\alpha}}}$	-0.850	-0.958	12.8
$C_{m_{\dot{\alpha}}}$	-2.600	-2.809	8.0
C_{X_q}	0.000	0.123	-
C_{Z_q}	-1.950	-1.596	22.2
C_{m_q}	-6.200	-5.156	20.2
$C_{X_{\delta_e}}$	0.000	0.038	-
$C_{Z_{\delta_e}}$	-0.430	-0.348	23.6
$C_{m_{\delta_e}}$	-1.280	-1.073	19.3

$\dot{\beta}$ derivatives

As no reference figures are given, no comparison can be made. The figures do seem to agree with the logic behind the derivative. As the sidewash effect reduces due to the delay, β decreases. This decrease is translated into a positive Y force and a negative moment around the Z-axis, as is reflected in the signs of the respective derivatives C_{Y_β} and C_{n_β}.

p derivatives

- C_{Y_p}, close to the expected value.
- C_{l_p}, relatively close to the expected value. This derivative is almost fully determined by the wing span and taper ratio. As both were obtained from the reference, nothing can be done to further reduce the error. The overestimation does indicate a more lateral stable aircraft compared to reality, and caution is advised when the design is on the limit in terms of stability.
- C_{n_p}, overestimated. This is likely because the program does not incorporate wing twist, as has been applied to the Cessna wing in reality. After programming in the wing twist manually, the error does reduce, but the effects were also immediately visible in the symmetric derivatives as C_{Z_u} decreased significantly, which was already underestimated.

r derivatives

- C_{Y_r}, close to the expected value.
- C_{l_r}, underestimated, but fortunately does not seem to affect the lateral stability much. The wing span and root chord seem to influence this derivative the most, and the reason for the error is therefore likely in the root chord, as it has been modified. The Cessna has two sections in reality and has been modified into a single section wing for the program to use. The change is minimal but is likely the cause for this error. If single section wings are used, this error is negligible.
- C_{n_r}, almost precisely the value it should be and will therefore not be discussed further.

δa derivatives

In general, these derivatives have been calculated correctly. The scaled drawings showed clearly the location and size of the ailerons, and they could therefore be programmed in with precision. As only a portion of the chord is used, XFLR is able to calculate the effects relatively accurately as well. If the user exactly knows

the aileron sizing, the error in these derivatives can be assumed to be negligible.

δr derivatives

The vertical tail is embedded into the end of the fuselage, and a relatively large fraction of the chord is used for the control surface. Both these factors made it difficult to estimate the correct vertical tail platform and lift curve and that is reflected in the control derivatives, which are extremely overestimated. Like the δa derivatives, it is certain that if the user implements the correct size, the error can be assumed to be negligible.

Table D.5
Asymmetric derivatives for the Cessna 172 aircraft [55]

	Reference [–]	Calculated [–]	Difference [%]
C_{Y_β}	-0.350	-0.373	6.6
C_{l_β}	-0.103	-0.143	38.8
C_{n_β}	0.058	0.083	43.1
$C_{Y_{\dot{beta}}}$	not given	0.100	-
$C_{l_{\dot{beta}}}$	not given	0.008	-
$C_{n_{\dot{beta}}}$	not given	-0.041	-
C_{Y_p}	-0.093	-0.097	4.3
C_{l_p}	-0.483	-0.584	20.9
C_{n_p}	-0.035	-0.059	68.6
C_{Y_r}	0.175	0.203	16.0
C_{l_r}	0.100	0.072	38.9
C_{n_r}	-0.086	-0.085	1.2
$C_{Y_{\delta_a}}$	not given	0.035	-
$C_{l_{\delta_a}}$	0.229	0.279	21.8
$C_{n_{\delta_a}}$	0.027	0.033	22.2
$C_{Y_{\delta_r}}$	not given	0.352	-
$C_{l_{\delta_r}}$	not given	0.032	-
$C_{n_{\delta_r}}$	-0.054	-0.156	188.9